GROWTH AND CHARACTERIZATION OF NITRIDE SEMICONDUCTORS ON CHEMICAL VAPOR DEPOSITED DIAMOND

by

Raju Ahmed, BS, M.S.

A dissertation submitted to the Graduate Council of
Texas State University in partial fulfillment
of the requirements for the degree of
Doctor of Philosophy
with a Major in Materials Science, Engineering, and Commercialization
May 2018

Committee Members:

Edwin Piner, Chair

Mark Holtz

Alexander Zakhidov

Casey Smith

Christopher Engdahl

FAIR USE AND AUTHOR'S PERMISSION STATEMENT

Fair Use

Duplication Permission

DEDICATION

I dedicate this work to my mother, Sheuly

ACKNOWLEDGEMENTS

First and foremost, I would like to thank and express my deepest gratitude to my advisor, Professor Dr. Edwin Piner for his continuous support, visionary guidance and graceful abilities to motivate. His unique style of guidance has shaped my critical thinking ability and has made my PhD experience worthwhile. I am very grateful to him for allowing me to work in his lab with excellent facilities and giving me the opportunity to explore the exciting research field of GaN-Diamond.

I would also extend my appreciation to Professor Dr. Mark Holtz, one of the best physicists I have ever met, for his collaboration, guidance and countless thoughtful discussions. I have always learnt something new about physics, and beyond, from each of our meetings. It has been an honor to work under his direction.

Thanks are due to two fine individuals, Dr. Casey Smith and Christopher Engdahl, for tolerating me and providing valuable support on various tools during this dissertation research. This research has been accomplished in a timely manner due to invaluable support from Dr. Smith on countless occasions. Help and support from Chris Engdahl regarding the diamond CVD tool was beyond my expectations. I would also like to thank my other committee member, Dr. Alex Zakhidov, for agreeing to serve on the committee when one of my previous committee members left Texas State University. Thoughtful academic discussions with Dr. Zakhidov has always motivated me.

I owe a special gratitude to my lab mate and longtime friend Anwar Siddique for

his continuous support and enduring my company throughout the last thirteen years. Without Anwar's cordial support in research and beyond, I would not have accomplished any of what I have now. I would also like to thank my other group member, and an excellent problem solver, Jonathan Anderson for his support on solving various research related problems on countless occasions.

A special thank you is also due to Dr. Holtz's group – Dr. Mohammad Nazari, Dr. Sandeep Sohal, Dr. Logan Hancock, Joyce Anderson, Peter Walker, Jaime Avila and Anival Ayala – for all of their help and cooperation, in research and fellowship.

I would like to thank the Texas State ARSC and NRSC technical teams and support staff, with special acknowledgement to Eric Schires, Dr. Dmitry Layashenko, Alissa Savage, Nate England, Aron Hoffman, Anthony Sherrow, John Miracle and Dean Koehne for the many hours spent training and answering my questions.

I would like to thank the MSEC program for providing financial support for my doctoral degree. Thanks are due to the outstanding faculty members of the MSEC program for delivering a unique and fulfilling doctoral education. I also gratefully acknowledge the US Army Research Office for partial funding of my PhD research.

I am extraordinarily grateful to all my family members for supporting me throughout my entire academic career. Their continual encouragement and unconditional support of my success throughout the course of my education is invaluable. Finally, and most importantly, I thank my wife, Nasrin. Without her love, support, sacrifice and constant motivation, none of this would have been possible.

TABLE OF CONTENTS

Page

LIST OF TABLES

Table **Page**

LIST OF FIGURES

Figure **Page**

ABSTRACT

Group III nitride semiconductor based devices have emerged as the best candidates for handling higher power and frequency in recent years. Performance of various devices such AlGaN/ GaN high electron mobility transistors, GaN lasers and GaN LEDs are often hindered by self-heating of these materials and poor heat removal capabilities of the substrate materials. Chemical vapor deposited (CVD) diamond has demonstrated the best heat removal capability, when employed as the substrate material for GaN based high power devices, due to its high thermal conductivity. Diamond is either grown directly on the backside or bonded with GaN using an adhesion layer to extract excessive heat from the near junction region of these devices. In both cases, thermal resistance associated with the interface of diamond and GaN limits the effectiveness of the diamond layer. In this work, single crystal GaN has been grown using metal organic chemical vapor deposition (MOCVD) directly on chemical vapor deposited diamond without any adhesion layer in a novel way which will mitigate thermal resistance between the near junction region of GaN devices and diamond substrate. The growth of GaN-on-diamond was achieved through a series of experiments and characterizations in various steps of the process.

Initial experiments were conducted to understand the effect of precursor stoichiometry of hot filament CVD (HFCVD) on diamond's morphology, phase purity and crystal structure. By varying the methane concentration in hydrogen in the range of

1.5-4.5%, it was found that film thickness, grain size, roughness and non-diamond carbon (NDC) of polycrystalline diamond increase with increasing methane concentration. X-ray diffraction and pole figure results indicate that diamond films grown with 4.5% methane exhibit preferential orientation in the <220> direction whereas films grown with 3.0% and 1.5% methane showed preferential orientation along <111>.

A process for photolithography and reactive ion etching based selective seeding of nano-diamond and selective deposition of CVD diamond was established on Si substrate which resulted in diamond feature size as small as 1 μm. Ultraviolet (UV) micro Raman stress mapping across selectively deposited diamond stripes with various widths revealed up to 0.9 GPa compressive stress in 1.5 μm thick diamond and a moderate (~150 MPa) tensile stress within 10 nm inside Si from the diamond-Si interface. UV Raman based measurements and finite element (FE) simulations indicated that the stress is thermal in origin which resulted from the mismatch of thermal expansion coefficients (CTE) between diamond and Si. The stress on Si was relaxed away from the diamond stripe which indicate global stress relaxation occurs when diamond is grown selectively.

Subsequently, the selective nano-diamond seeding and selective diamond growth process was developed for GaN substrate. Poor diamond coverage, poor selectivity and significant etching of GaN was observed when diamond was seeded on the bare GaN surface. To mitigate these problems, a thin SiN_x layer was deposited on GaN before selective nano-diamond seeding which resulted in enhanced coverage, excellent selectivity and complete protection of the GaN surface. To characterize the protection of

the GaN surface during CVD diamond growth, an MOCVD grown AlGaN/GaN wafer with ~25 nm AlGaN barrier layer on top of GaN was employed. The presence of the AlGaN layer after diamond deposition was confirmed form scanning electron microscopy (SEM), atomic force microscopy (AFM), Micro Raman and high-resolution x-ray diffraction (HRXRD) reciprocal space mapping (RSM) of the asymmetric (114) plane taken before and after diamond deposition.

Finally, selectively deposited diamond coated GaN wafers with various window sizes and orientations was used for epitaxial lateral overgrowth (ELO) of GaN on the windows. The effect of pressure (P), temperature (T), group V to group III molar ratio (V/III) and mask orientation on lateral growth was studied in detail to achieve complete coalescence of GaN over narrow diamond stripes. The best ELO process that resulted in complete coalescence of GaN over diamond mask was achieved using P=100 torr, T=1030 °C, V/III=7880 and GaN window on diamond mask oriented along $[1\bar{1}00]$. Cross-section SEM images indicated a continuous interface between ELO GaN and diamond. HRXRD data confirmed growth of c-axis (0002) oriented ELO GaN on overgrown region.

I. INTRODUCTION

The market size for radio frequency (RF) power electronic devices have demonstrated a rapid upsurge in recent years as the use of broad band internet and cellular technology have expanded significantly throughout the world[1]. Due to the increased requirement of reliable transmission of large quantities of data, increased capacity of these devices in terms of power and frequency are becoming more and more demanding[2]. Power electronic devices made of group III-Nitride semiconductors (GaN, AlN, AlGaN etc.) are the best candidates to meet the requirement of today's high power and high frequency operations due to their high electron density, large breakdown voltage and high electron velocity[3]. GaN based high electron mobility transistors (HEMT) have demonstrated off state voltage as high as 1100 V [4], extremely high output power (900 W at 2.9 GHz, 81W at 9.5 GHz for RF amplifier), extremely high frequency (f_T = 181 GHz at L_g =30 nm), high-power added efficiency PAE = 75% at P_{sat} = 100 W and broadband operation at 1.0–2.5 GHz with 50% efficiency[5][1].

III-Nitrides based optoelectronics is a matured technology and currently a multi-billion dollars industry[6]. Wide range of direct bandgap of various III-Nitrides and their alloys have enabled their application in successful production of light-emitting diodes (LEDs), laser diodes (LDs), photodetectors, and photovoltaics (PVs)[7]–[9]. Today's GaN based LEDs and lasers can produce high brightness green, blue, ultraviolet and white lights with great reliability[7]–[9]. Light extraction and quantum efficiency of III-Nitride based optoelectronics have been further enhanced through the growth of complex hetero-structure such as multiple quantum wells (MQW)[10], [11].

A continuous, multi-decade research thrust from federal and private organizations have been pushing the capability limit of GaN based power devices (mainly HEMTs) in terms of power and frequency. Although tremendous device performance has been achieved, reliable performance of GaN HEMTs are often hindered by a key limiting factor related to its thermal reliability under high operational power. Although GaN based HEMTs are expected to demonstrated power density exceeding 40 W/mm[12], only 5-7 W/mm have been achieved practically because mean failure time of these devices decreases significantly as power density increases[13]. Like any other modern semiconductor devices, the dimensional scaling of these devices has incrementally increased power dissipation where localized hot spots near the active region (channel layer under gate electrode) have heat fluxes above $1kW/cm^2$ and volumetric heat generation above $1kW/cm^3$[14][15]. Channel temperature as high as 350^o C has been reported for GaN on Si HEMTs[16]. Due to this excessive amount of heat generated at the active region of the device, mean failure time decreases significantly. Today's HEMTs operate at 150^oC with a maximum life time of 10^7 hours and the lifetime decreases exponentially as the device temperature increase linearly[13].

For GaN based HEMTs, the high electron density ($>10^{13}$ cm^{-2}) channel (<10nm thick) is located at the AlGaN/GaN interface and acts as the highest heat flux region during the active mode of the device[17][16]. Efficient extraction of this excessive heat from the active region has become the main challenge for the manufacturing of these devices. Self-heating at the active region causes losses in efficiency and output power density, decrease in electron mobility, and results in device degradation[18]–[20]. In case of GaN based optoelectronic devices, unwanted heating can lead to considerable losses in quantum

efficiency, changes in output wavelength, device lifetime, and material deterioration[10], [11], [21]–[23]. Currently Sapphire, Si and SiC are the most common substrate solutions where GaN based electronic devices are grown heteroepitaxially; albeit with many transition layers[24]. The poor thermal conductivity of transition layers and substrates along with interfacial thermal resistance impede the flow of heat from active region of this device.

A better thermal pathway from the hot active region is, therefore, a compelling need for the reliable operation of this device. Chemical vapor deposited (CVD) polycrystalline diamond has emerged as a promising substrate solution for GaN HEMTs due to its high thermal conductivity (800-2000 W/mK)[25][26]–[28]. Due to the polycrystalline nature of CVD diamond, historically, it is either attached with, or grown on, the backside of the GaN HEMT structure[26]–[30]. In both cases a low thermal conductive dielectric layer is employed as an adhesion layer[12]. Although GaN-on-diamond have demonstrated three times better thermal performance than any other substrate[12], the full advantage of diamond substrate have not been achieved due to this poor dielectric adhesion layer and excessive thermal boundary resistance associated with it. Compounding the problem, another limiting factor associated with CVD diamond is its poor thermally conductive high graphitic content nucleation layer which impedes efficient thermal conduction.

Since addressing every thermal resistance between the active region and nearby heat sink is necessary to achieve the full potential of GaN-on-diamond HEMTs, this research was focused on addressing these issues. Although primary focus of the research was GaN based power devices, other optoelectronics devices can also be benefitted from the outcome of the research. GaN was directly grown on diamond in a novel way to

minimize thermal boundary resistance where the self-heating active will be situated very close to diamond. Detailed materials characterization at each step of the complex fabrication process were necessary to achieve the novel GaN-on-diamond structure in a simpler way. A discussion on group III-Nitride semiconductors and diamond will be presented in next section along with various problems and challenges associated with the current GaN-diamond technology. Detailed layout of the research plan along with the organization of this dissertation will be presented at the end of the chapter.

1.1 Group III nitride semiconductors

Semiconductor materials consisting of Group III metal and nitrogen are called nitride semiconductors such as AlN, GaN and InN etc. [31]. The large bandgap, high breakdown field, good electron transport properties (an electron mobility as high as 3000 $cm^2V^{-1}s^{-1}$ and peak velocity approaching $5 \times 10^7 cms^{-1}$ for GaN at room temperature[32]) and favorable thermal conductivity make this materials attractive for high power/temperature electronic devices[3]. Along with these tremendous transport properties, the availability of heterostructures (particularly AlGaN/GaN) and the existence of a high-growth-rate and high-quality epitaxial method like Hydride vapor phase epitaxy (HVPE), Metal Organic Chemical Vapor Deposition (MOCVD) for producing very thin layers have made nitride semiconductors a viable choice for high power device fabrication[3].

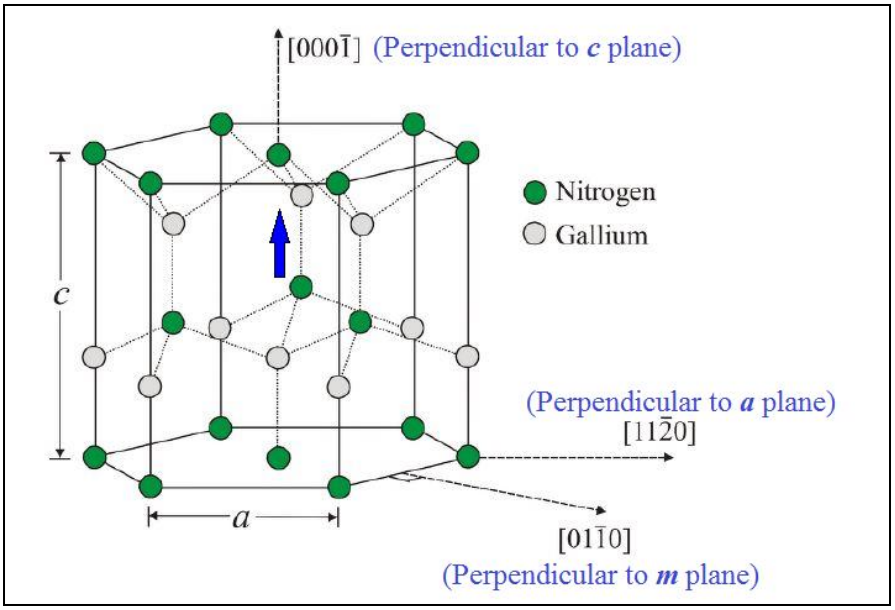

Figure 1. 1. The GaN (N-faced) Wurtzite crystal structure with three crystal planes.

GaN is the most important semiconductor among the group III nitrides because of its extraordinary electronic properties. GaN usually crystalize in two possible crystal structure, wurtzite hexagonal closed packed (HCP) and cubic zinc blend where wurtzite structure is thermodynamically more stable and is used to fabricate electronic devices. Fig.1.1 shows the wurtzite crystal structure of GaN (N-face) along with various crystal planes. Wurtzite crystal structure has five atoms (four Nitrogens and one Gallium or vice versa depending on polarity) per unit cell in a hexagonal Bravais lattice[33]. These types of crystals are described by three lattice parameters a, c and u representing the length of a side of the hexagonal base, the height of the hexagon and the III-N bond length along the c-axis, respectively.

An important feature of the GaN crystal is its non-centrosymmetric nature meaning that the crystal shows different layer sequencing of atoms when one moves from one side of the crystal to the other in opposite directions. GaN hexagonal closed packed (HCP) wurtzite structure shows this type of polarity along the typical growth direction *c* axis. i.e.,

along the axis normal to the hexagonal basal plane[34]. Due to lack of inversion symmetry, all atoms in a plane perpendicular to the *c*-axis are the same and alternating gallium and nitrogen. Therefore, Wurtzite GaN crystal have two distinct faces known as Ga-faced and N-faced which correspond to the (0001) and $(000\bar{1})$ planes, respectively. For an N-faced GaN, $[000\bar{1}]$ direction corresponds to a vector pointing from a Nitrogen atom to nearest neighbor Gallium atom as shown in Fig.1.1 and the convention is reversed for a Ga-faced structure. It is important to understand that an N-faced crystal may be terminated with Ga but that will never make it a Ga-faced crystal unless the crystal is physically flipped. In metal organic chemical vapor deposition (MOCVD) technique, GaN usually grows in the [0001] direction resulting in Ga faced crystal[33].

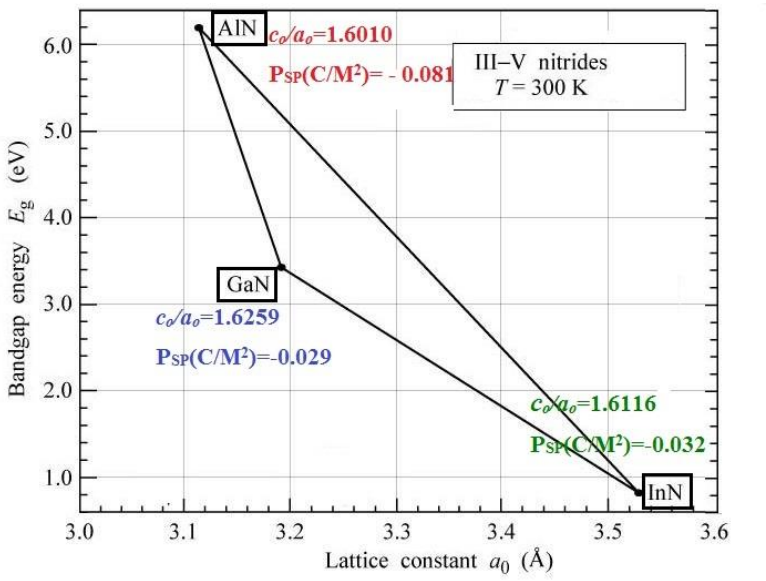

Figure 1. 2. Bandgap energy versus lattice constant a_o for group III nitride semiconductors along with spontaneous polarization**.**

Group III-nitride semiconductors form heterostructures when they are mixed as alloys thereby enabling the electronic properties of these heterostructure to be tailored. Ternary alloys use a notation with molar percentage x, e.g. $Al_xGa_{1-x}N$. Band-to-band transitions can occur without phonon involvement for group III-nitrides and its ternary alloys. The

bandgap of a ternary alloy $A_xB_{1-x}N$ can be described with Vegard's rule[35],

$$E_g^{AxB1-xN} = xE_g^{AN} + (1-x)E_g^{BN} - bx(1-x) \quad (1.1)$$

Where, b is bowing parameter of the alloy and has a value of 0.7, 1.4 and 2.5 for AlGaN, GaInN and AlInN, respectively. For the nitride ternary heterostructure, combining Al and In would give the possibility to engineer the band-gap between 6.2 eV to 0.7 eV by varying the amount of Al or In in the alloy as shown in Fig.1.2 [36]. This advantage of bandgap engineering allows the use of these materials for high power and high frequency electronic devices[32]. One most important feature of nitride heterostructures is formation of a two dimensional electron gas (2DEG). A 2DEG is a "gas" of electrons free to move in two dimensions, but tightly confined in the third and this tight confinement leads to quantized energy levels for motion in said direction[37]. Thus, the electrons appear to be a 2D sheet embedded in a 3D matrix. The formation and usefulness of the 2DEG will be further discussed in subsequent sections.

1.1.1 Polarization in group III nitride semiconductors

In the GaN crystal, individual atoms are electronically ionized. Large Gallium and small Nitrogen atoms are arranged irregularly with respect to each other, because of the difference in size[2]. Nitrogen is the most electronegative group V element having three electrons at the 2p orbital. Due to paucity of electrons in Nitrogen's outer most shell, electrons involved in the gallium-nitride covalent bond will be strongly attracted by the Coulomb potential of the N atomic nucleus. As a result, the iconicity of the covalent bond between Ga and N will be much higher than any other III-V materials and will result in an inherent electric field. Due to lack of inversion symmetry in the GaN crystal, the inherent

electric field will cause formation and subsequent maintenance of a permanent dipole moment which results in polarization of the material[33]. It is important to note that this type of polarization takes place when the lattice of the III-nitrides is in equilibrium, i.e. at zero strain and therefore it is called spontaneous polarization. The direction of the spontaneous polarization in wurtzite III-V nitrides is along the c-direction, $\vec{C}$ = [0001], which is beneficial for GaN high power transistor applications[3]. Spontaneous polarization is an inherent property of each type of III nitride semiconductor and depends on lattice parameters. The tetrahedral structure of nitride semiconductor has four bonds, of which only the bond along the c-axis contributes to the spontaneous polarization since the other three bonds counterbalance each other's effect. Thus, any change in the ratio of lattice parameters, i.e *a* and *c*, from its ideal value results in a spontaneous polarization. Fig.1.2 shows the variation in spontaneous polarization in the three binary nitride semiconductors due to change in the ratio of lattice constant a_o and c_o. The value of spontaneous polarization increase from GaN to InN and AlN as the non-ideality also increases (*u* increases, *c*/*a* decreases, and the difference from the ideal ratio of lattice constants of a closed packed hexagonal structure, *c*/*a*=1.633, increases as well)[38]. Bernardini *et al* [39] showed that the spontaneous polarization of relaxed alloys for a given composition depends linearly on the average *u* parameter, which indicates that spontaneous polarization differences between alloys of the same composition are mainly due to varying cation–anion bond length. This idea is supported by the fact that in binaries, the polarization depends linearly on the relative displacement of the cation and anion sub-lattices in the [0001] direction[38]. The spontaneous polarization of the random ternary nitride alloys is given to second order in *x* by (in Cm^{-2})[39]

$$P_{ABN}^{SP}(x) = xP_{AN}^{SP} + (1-x)P_{BN}^{SP} - bx(1-x) \quad (1.2)$$

The sign of P^{SP} is negative because the orientation of the spontaneous and piezoelectric polarization is defined by assuming that the positive direction goes from the metal (cation) to the nearest neighbor nitrogen atom (anion) along the *c* axis. The direction of P^{SP} is shown in Fig.1.3.

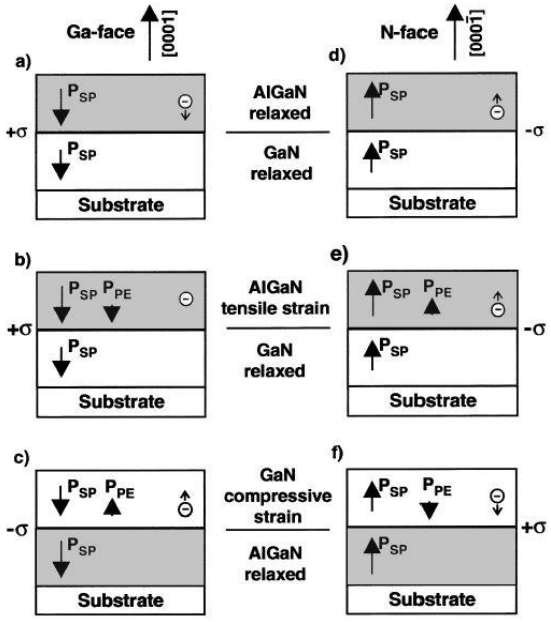

Figure 1. 3. Directions of the spontaneous and piezoelectric polarization and Polarization induced sheet charge density (+σ corresponds to accumulation of electrons and -σ corresponds to accumulation of holes) in Ga- and N-face strained and relaxed AlGaN/GaN heterostructures[17].

Apart from the spontaneous polarization, a piezoelectric polarization is also observed in nitride semiconductors. The epitaxial growth of semiconductor materials with different lattice constants causes mechanical strain in the final structure. AlGaN layer grown on GaN experiences this kind of strain due to having a smaller lattice constant than GaN. The piezo-electric properties of such materials cause additional polarization at the interface. As the wurtzite crystal belongs to C_{6v} point group, its piezoelectric tensor has three independent components. Two of these components measure the piezoelectric polarization P_{PE} induced

along the *c* axis or in the basal plane by the relation[17],

$$P_{PE} = \varepsilon_{33}\varepsilon_Z + \varepsilon_{31}(\varepsilon_x+\varepsilon_y) \tag{1.3}$$

Where, $\varepsilon_z = (c-c_0)/c_0$ is the strain along the *c* axis, the in-plane strain $\varepsilon_x = \varepsilon_y = (a-a_0)/a_0$ is assumed to be isotropic, e_{33}, e_{31} are the piezoelectric coefficients, and *a* and *c* are the lattice constants of the strained layer. The relation between the lattice constants in the hexagonal AlGaN system is given by[17]

$$\frac{c-c_0}{c_0} = -2\frac{C_{13}}{C_{33}}\frac{a-a_0}{a_0} \tag{1.4}$$

where, C_{13} and C_{33} are elastic constants. Using Equations (1.3) and (1.4), the amount of the piezoelectric polarization in the direction of the *c* axis can be determined by

$$P_{PE} = -2\frac{a-a_0}{a_0}\left(e_{31} - e_{33}\frac{C_{13}}{C_{33}}\right) \tag{1.5}$$

It is evident from equation (1.3) that the piezoelectric tensor is generated through the change in polarization induced by variations of the lattice constants *a* and *c* only. Any strain parallel or perpendicular to the *c* axis produces an internal displacement of the metal sub lattice with respect to the nitrogen which in turn changes the parameter *u* of the wurtzite structure. Therefore, the measured piezoelectric polarization is due to the effect of the change of the macroscopic lattice constants and to the associated change in *u*. For epitaxial layers under the same strain, the value of the piezoelectric polarization is increasing with strain from GaN to InN and AlN[17]. From the value of elastic constants of GaN and AlN, it is known for AlGaN/ GaN that the relation

$$\left(e_{31} - e_{33}\frac{C_{13}}{C_{33}}\right) < 0 \tag{1.6}$$

is valid over the whole range of composition. Thus, according to equation (1.5) and (1.6)

the piezoelectric polarization is negative for tensile and positive for compressive strained Al-GaN barriers, respectively[17]. Fig.1.3 shows that the spontaneous polarization for GaN and AlN are negative, meaning that for Ga (or Al)-face heterostructures the spontaneous polarization is pointing towards the substrate (as shown in Fig.1.3). Therefore, the alignment of the piezoelectric and spontaneous polarization is parallel in the case of tensile strain, and antiparallel in the case of compressively strained top layers[17]. Likewise, both the piezoelectric and spontaneous polarization changes its sign if the polarity flips from Ga-face to N-face. In Fig.1.3, the directions of the spontaneous and piezoelectric polarization are given for Ga-face, N-face, strained, unstrained AlGaN/ GaN, and GaN/AlGaN structures. For the present proposal, we will consider only tensile strained AlGaN grown on Ga faced GaN. The total polarization is the sum of spontaneous and piezoelectric, i.e. $P=P_{SP}+P_{PZ}$, since both of them are pointing toward the substrate for this strain situation.

The important effect of the polarization is accumulation of charge at the AlGaN/GaN heterostructure interface. The polarization induced charge density (ρ_P) can be calculated from the gradient of polarization in space using the equation, $\rho_P = \nabla P$. At the abrupt interface of a top/bottom type AlGaN/GaN heterostructure, polarization can decrease or increase within the bilayer which in turns causes a polarization sheet charge density. Such a polarization charge density for an AlGaN/GaN (Ga-Polar) structure is defined by the following equation[17],

$$\begin{aligned}\sigma(P) &= P(GaN) - P(AlGaN) \\ &= \{P_{SP}(GaN) + P_{PE}(GaN)\} - \{P_{SP}(AlGaN) + P_{PE}(AlGaN)\} \\ &= \{P_{SP}(GaN) - P_{SP}(AlGaN)\} + \{P_{PE}(GaN) - P_{PE}(AlGaN)\} \\ &= \sigma(P_{SP}) + \sigma(P_{PE})\end{aligned} \tag{1.7}$$

In the nitride semiconductor heterostructure, variations in composition, surface roughness,

or strain distribution will alter the local distribution of polarization induced sheet charge density. As shown in Fig.1.3, if the polarization induced sheet charge density is positive, free electrons will tend to compensate the polarization induced charge during the cooling process after growth[17]. The result of this accumulation is the formation of a 2DEG with a sheet carrier concentration n_S, assuming that the AlGaN/GaN band offset is reasonably high and that the interface roughness is low[17]. Alternately, a negative sheet charge density would cause an accumulation of holes at the interface resulting in 2DHG, but such a structure is challenging to realize empirically.

1.1.2 The AlGaN/GaN HEMT structure

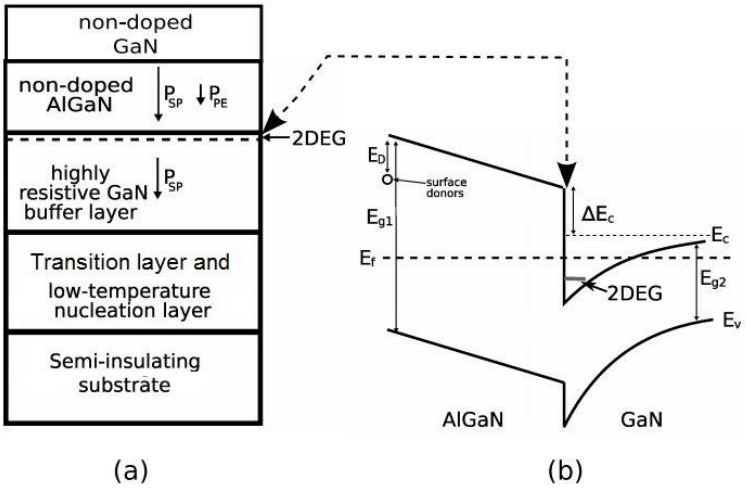

Figure 1. 4.(a) Schematic drawing of the standard AlGaN/GaN HEMT structure along with the direction of spontaneous and piezoelectric polarization in the structure and (b) corresponding band diagram[40].

Fig.1.4 (a) depicts various layers required for AlGaN/GaN HEMT heterostructures and in Fig.1.4(b), the formation of the corresponding 2DEG has been depicted. Fig.1.4(b) shows the energy-band diagram of a GaN-AlGaN heterojunctuion in thermal equilibrium where the AlGaN is grown on GaN. The AlGaN can be undoped or inherently n-type, while the GaN can be more lightly doped or even intrinsic. The strong electric field (as high as

3MV/cm[3]) resulting from the polarization discontinuities at heterointerfaces alter the energy band levels in the AlGaN/GaN materials. The piezoelectric and spontaneous polarization lead to a positive induced charge (+σ) near the AlGaN/GaN interface as shown in Fig.1.3 for a Ga-faced structure and electrons are attracted towards the interface to compensate for this positive charge. To achieve charge equilibrium, electrons from the wider-bandgap AlGaN flow into the GaN, forming an accumulation layer of electrons in the potential well adjacent to interface[2]. These electrons are collected on the GaN side of the heterojuction and move the Fermi level above the conduction band in the GaN near the interface as shown in Fig.1.4(b). The electrons are therefore confined in a narrow triangular potential well in the GaN conduction band. Quantum-mechanical results confirm that the energy of an electron contained in a potential well is quantized[37]. Thus 2DEG refers to the condition in which the electrons have quantized energy levels in one spatial direction (perpendicular to the interface), but are free to move in the other two dimension [41]. The formation of the 2DEG is a very important aspect of these types of heterostructures. The device named high electron mobility transistor (HEMT) was first designed on the basis of a 2DEG. The HEMT is actually a heterojunction device consisting of a wide-bandgap and narrow-bandgap material as shown in Fig.1.4(a). Actual device that is being used today has a similar structure as shown in Fig.1.5.

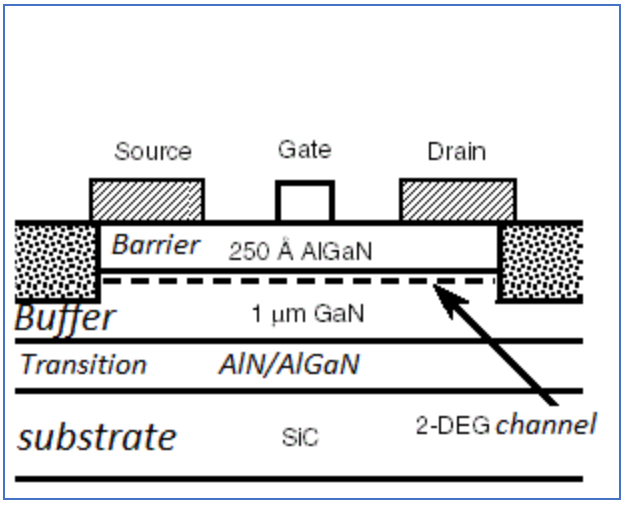

Figure 1. 5. Illustration of an AlGaN/GaN HEMT with different layer thicknesses.

Corresponding to Fig.1 4(a) and (5), the wider bandgap material is called the barrier layer, whereas the narrower bandgap material is called the channel layer. The channel layer is epitaxially grown on a relatively thick substructure that is normally called the buffer layer. The gate metal, which is deposited on the barrier layer, creates a Schottky barrier with the wide bandgap semiconductor. The source and drain contacts, on the other hand, are ohmic contacts and are connected with the channel layer. It is worth mentioning that due to very high crystalline quality of the top GaN layer and AlGaN barrier layer, high density charge carriers do not experience any ionized impurity scattering and exhibit higher mobility. For this reason, the HEMT is called 'high electron mobility device'. That means we get high electron concentration with high mobility in the highly conductive two-dimensional channel.

1.2 CVD diamond

Diamond for centuries has been appealing to humanity's imagination because it is a gem, fascinating, rare, and seemingly everlasting. Although the use of diamonds in jewelry may

be the most intriguing, it has found a wide range of applications in industry due to the CVD growth process. In particular, diamonds use in electronics has gained increased interest over the last two decades. The application of CVD diamond in electronics is two-fold. First, it becomes a wide band gap semiconductor material when doped with boron and used in harsh environment electronic device application. Secondly, the highest known thermal conductivity of CVD diamond (as high as 2,000 $Wm^{-1}K^{-1}$)[25] allows it to be used as an active or passive heat spreader in high power and high frequency electronic devices[42].

1.2.1 Crystal structure of diamond

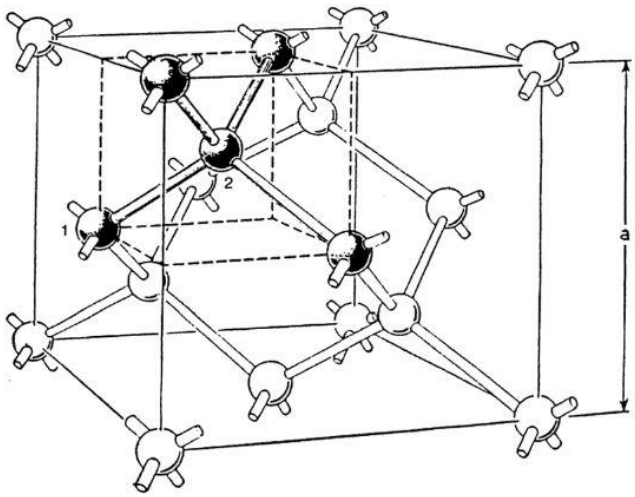

Figure 1. 6. Diamond crystal structure, showing the tetrahedral coordination and the short interatomic distance (1-2) of 1.54 A. The cubic unit cell with lattice parameter *a* is also depicted[43].

The crystal structure and chemical bonding of diamond has made this material an outstanding choice for many applications because carbon is the smallest atom that forms a three-dimensional network of covalent bonds. The structure shown in Fig.1.6 can be viewed as two interpenetrating face centered cubic lattices shifted along the body diagonal by (1/4, 1/4, 1/4) *a*, where *a* is the dimension of the cubic (mineralogical) unit cell[44].

Each carbon atom has a tetrahedral configuration consisting of sp^3 hybrid atomic orbitals. In any type of diamond, natural or synthetic, the carbon atoms make up this three-dimensional lattice in which each of their outer four electrons is shared with an electron of the four neighboring carbon atoms. Therefore, each carbon has four covalent bonds to four other carbon atoms forming a tetrahedral network, as shown in Fig.1.6. The resulting lattice is very compact with a density of 3.52 g/cm^3, and is called the diamond crystal structure[44]. The crystallographic direction perpendicular to the (1 1 1) plane of the unit cell shown in Fig.1.6 is the most common crystal growth direction and the (111) plane comprises 6-atom hexagonal rings arranged so that the adjacent atoms are alternately dislocated upward and downward from the plane[45]. The stacking sequence in the [111] directions is ABC ABC ABC, and lattice constant is 3.56 Å. The most important isomer of diamond is graphite which is also the most common form of carbon. In diamond growth, formation of graphite is often inevitable and therefore knowledge about the bonding and crystal structure of graphite is also a matter of significant interest in this research.

The structural property that is of great interest is the hybridization of covalently bonded carbon in diamond and graphite. Two possible hybridizations are found in carbon namely sp^3 and sp^2. As said earlier, sp^3 hybridization correlates to the diamond structure and this tetrahedral formation packs the carbon atoms together closely with four strong covalent bonds as shown in the highlighted bonds in Fig.1.6. These strong bonds create a uniform formation of a 3-dimensional network of carbon-carbon (C-C) single (sigma) bonds. In contrast, the sp^2 hybridized carbon atoms form a two-dimensional σ and π bond network to create sheets of carbon bonds, i.e., graphite. These sheets of graphite have strong bonds in-plane but their out of plane bonds are much weaker. These weak bonds

between sheets greatly reduce the overall thermal conductivity and mechanical strength of graphite.

A detailed description on various crystal plane formation during the CVD process of diamond will be presented in subsequent sections. In short summary, the interatomic distance of carbon in a tetrahedral network of diamond is very small (1.54 A) which results in an exceptionally high density of very strong bonds. Acoustic and thermal waves can propagate very fast and over long distances in diamond (tight bonding network) because they are little hindered by the light carbon atoms. As a result, high thermal conductivity and velocity of sound (phonon) in diamond is observed.

1.2.2 CVD Growth of polycrystalline diamond

The application of diamond in electronics has been possible because of the chemical vapor deposition (CVD) technique. Both single crystal and polycrystalline diamond films have been grown at industry scale using CVD. However, the present research will be focused on polycrystalline CVD diamond. CVD diamond can be grown on a wide range of substrate materials, along with diamond substrate. Si, Ti, SiO_2, SiN_x, etc. [45] have been reported as substrate materials for deposition of diamond in electronic device application. There are various CVD techniques available such as hot filament, microwave plasma, DC arc plasma, combustion flame, etc. [42]. However, the basic chemistry of the CVD process is somewhat similar in all techniques. In all the deposition techniques, diamond deposition utilizes a gas phase chemical reaction occurring above the substrate material. The high temperature and appropriate pressure activates gas phase carbon-containing precursor molecules which then goes through chemical dissociation to form diamond on seeded substrate. A general

description for hot filament is presented here since the present research will be focused on diamond growth in such a CVD chamber.

Nucleation

The first and most crucial step in diamond deposition is nucleation step. This step plays a significant role in optimizing the diamond properties such as grain size and orientation that are necessary for reduced thermal resistance[44]. CVD diamond growth on foreign substrates typically requires surface treatment in order to achieve a high nucleation density. Scratching the substrate surface with diamond powder was used historically for nucleation of diamond on a non-diamond substrate. A significant number of publications and industry applications have adopted this nucleation technique. Another popular approach that has been employed for almost two decades is seeding of the substrate with diamond particles through the use of a slurry of nano diamond dispersed in an appropriate solvent (alcohol, acetone, etc.) accompanied by ultrasonic agitation. This technique has demonstrated the highest nucleation density, as high as $1x10^{12}$ cm^{-2}.[46] Apart from mechanical scratching, many other seeding techniques such as photolithography, bias enhanced nucleation, ultrasonic polishing, etc. have also been used successfully. It is important to know that different nucleation densities greatly affect thermal conductance at the interface. Lower nucleation density can create voids at the interface, while overly high nucleation densities can create extremely small grains near the nucleation region that do not allow for coalescing into the high quality columnar grain structure that is desired for efficient thermal conduction. The most common methods for nucleation include: mechanical abrasion, by scratching the surface substrate with diamond powder, bias enhanced nucleation by applying a negative substrate bias voltage, ultrasonic polishing, and photolithographic

technique[47][48].

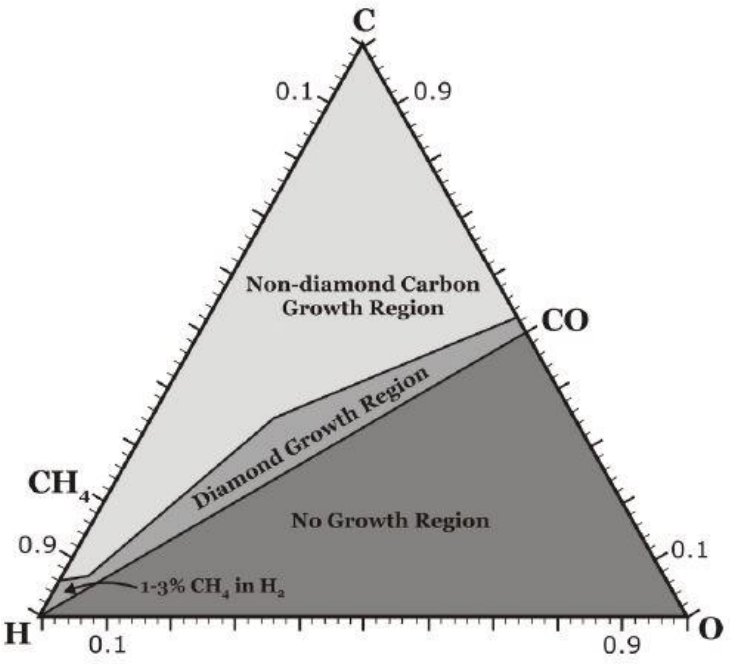

Figure 1. 7. Simplified form of the Bachmann triangle C–H–O composition diagram. No film growth is achieved below the CO tie-line and non-diamond carbon film is generally grown above the CO tie-line. Diamond is deposited in a narrow window close to the tie-line, which produces polycrystalline diamond films (Image adapted from[42]).

CVD growth

The CVD process involves mixing of three gases; hydrogen (H_2) with a small percentage of methane (CH_4) and an extremely small percentage of oxygen, in the chamber before diffusing to the surface. The gas ratio with the CVD process is extremely important and the chemical composition of the gasses in the CVD process must be precise. According to the Bachmann triangle, as shown in Fig.1.7, there is a narrow window for diamond formation.

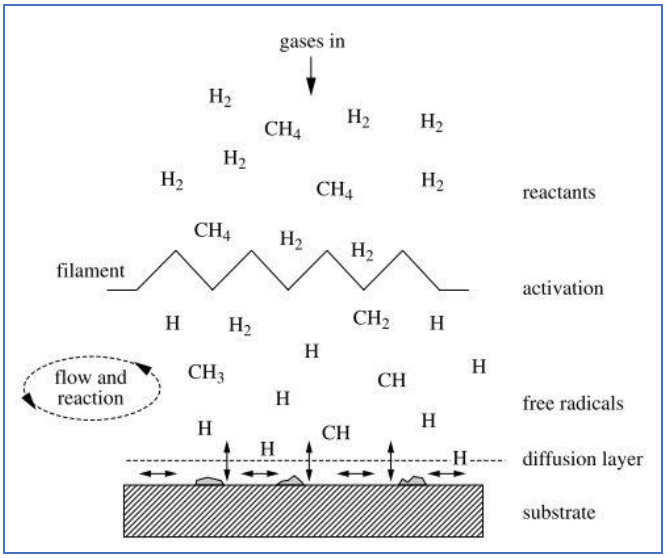

Figure 1. 8. Schematic of physical and chemical process occurring during CVD of diamond[42].

The gasses pass through an activation region (Hot filament of tungsten at 2200^{o}C) that provides energy to the gases, which cause the gas molecules to fragment into reactive radicals and atoms. The reactive radicles then strike the substrate as shown in Fig.1.8. Three different phenomenon can take place at this stage: 1) adsorb and react with the surface, 2) desorb back into the gas phase, or 3) diffuse close to the surface until a reaction site is found[15]. However, atomic hydrogen (or reactive OH in oxygen containing system) has been found to be the most active reactant in the entirre CVD process and performs multiple roles. These roles are: satisfying dangling bonds of sp^3 carbon temporarily to prevent forming sp^2 graphite, etching of any sp^2 graphitic carbon, scavenging any long chained hydrocarbon and reacting with neutral CH_4 molecule to form reactive radicasl[42].

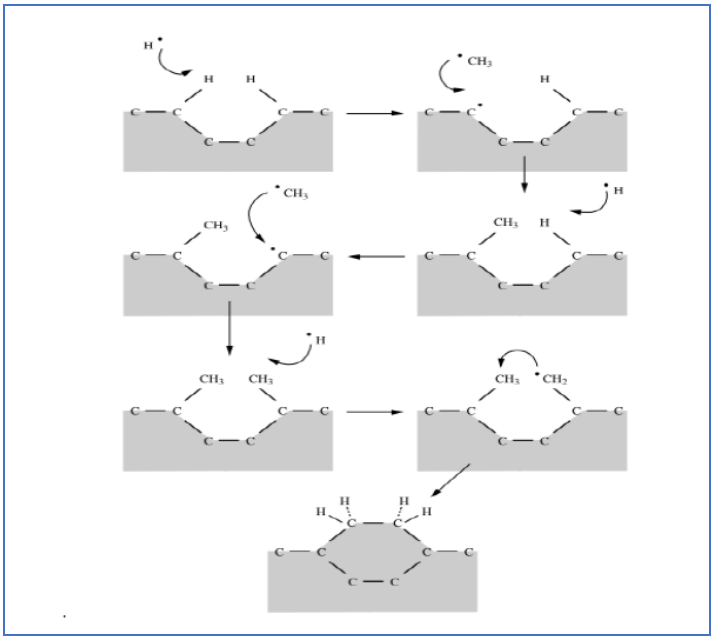

Figure 1. 9. Schematic of the reaction process occurring at the diamond surface leading to stepwise addition of CH_3 species and diamond growth[42].

Many theories have been proposed to describe the growth of diamond after nucleation[45]. Fig.1.9 depicts one of the most widely accepted theory for diamond deposition described by P. W. May[42]. After the nucleation process, the growth process can begin by saturating the surface with hydrogen. Atomic H attracts a surface H to form H_2 leaving behind a reactive surface site. The site will most likely react with a nearby H atom, returning to the original structure. However, a CH_3 radical may react with the surface site, which adds a carbon atom to the lattice. This process, as pictured in Fig.1.9, occurs continuously as the diamond growth continues. This is a stepwise addition of carbon atoms to the already existing diamond lattice, catalyzed by the presence of excess atomic hydrogen[42][15].

Controlling diamond quality

In CVD growth of diamond, the ultimate goal is to deposit high quality polycrystalline diamond films. Here, the term ‘quality’ in this context refers to three important parameters:

the ratio of sp^3(diamond) to sp^2-bonded (graphite) carbon, the composition (e.g. C-C versus C-H bond content), and the crystallinity. As the primary focus of the present research is the thermal property of diamond, "better quality" will be referring to a better thermally conductive diamond. Quality of diamond film is extremely dependent on gas chemistry in any given CVD technique as described in the Bachmann triangle in Fig.1.7. Besides, various CVD processes can deposit diamond at varied rates, the fastest being up to 1000 μm/hr while the slower methods deposit at 0.1μm/hr. The quicker methods lead to an overall poorer quality diamond inherently affecting the thermal properties. The overall challenge is increasing the growth rates to economically viable rates (100 μm/hr) without compromising film quality. The ultimate challenge lies in controlling the ratio of sp^3/sp^2 bonds since the greater the ratio, the higher the thermal conductivity of the material.

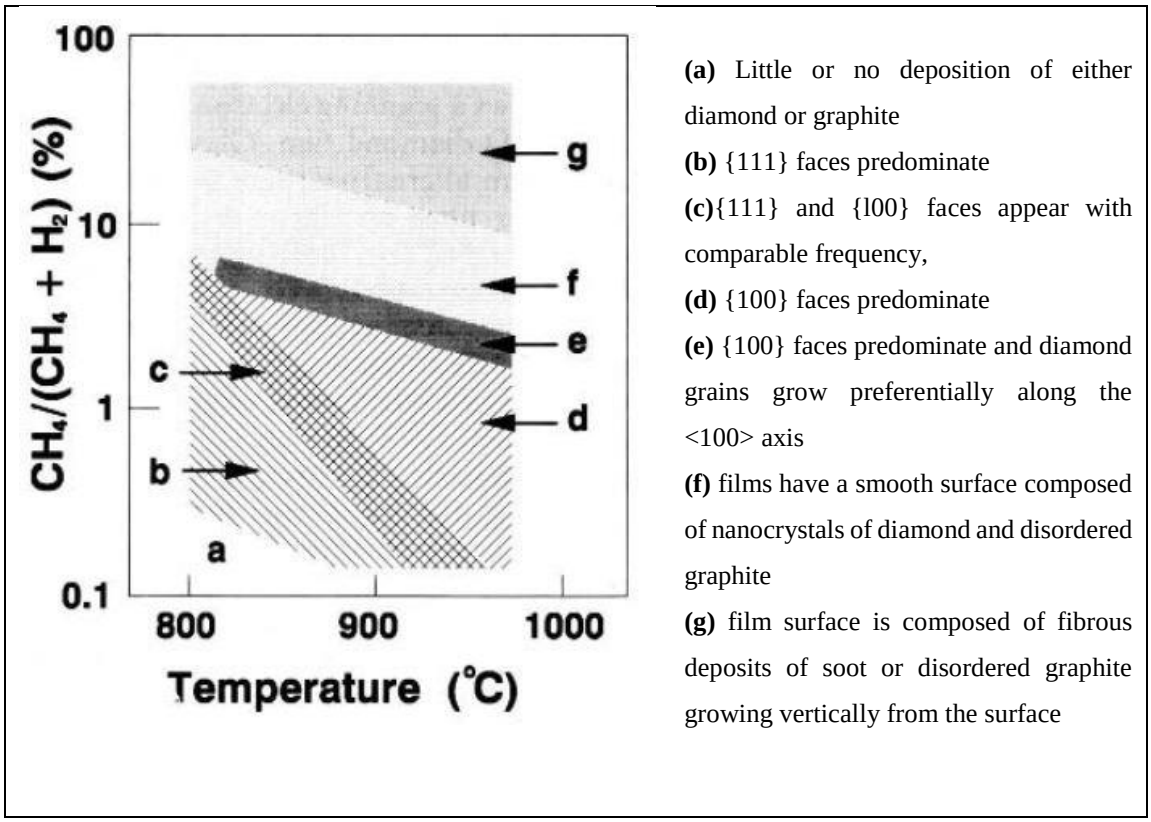

Figure 1. 10. Schematic diagram of diamond film crystallinity and morphology as a function of deposition temperature and methane/hydrogen ratio for CVD between 30-80 Torr (adopted from [45]).

Interestingly, the crystalline phases of CVD grown polycrystalline diamond are greatly dependent on the CVD process. Ashfold *et al.*[45] have reported an excellent study regarding the gas ratio and growth temperature dependence of crystalline phases that appear in polycrystalline diamond as shown in Fig.1.10. The preferential orientation of CVD diamond is an extremely important factor in terms of epitaxial growth of other materials on diamond. It is therefore established from Fig.1.10 that the control of gas ratio, pressure and temperature defines the crystallinity of polycrystalline diamond. It is important to note that diamond has grown at much lower temperature than the depicted value in Fig.1.10. Usually, under 'slow' growth conditions, low CH_4 partial pressure and low substrate temperature, triangular {111} facets tend to be most evident, with many obvious twin boundaries. Square and rectangular forms of {100} facets begin to dominate as the relative concentration of CH_4, in the precursor gas mixture, and/or the substrate temperature, is increased[45]. In microelectronic device application, be it active material or passive cooler, a smooth diamond surface with preferentially oriented crystal phases are always desired.

1.2.3 Thermal property of polycrystalline CVD diamond

Heat transport in any material is found to be governed by particle-involved mechanisms which try to restore thermodynamic equilibrium in the system subjected to a temperature gradient. Heat can be transported through both electron (especially in metal) and lattice vibration (phonon)[49]. In diamond, thermal conductivity is governed by lattice conductivity by phonon and phonon scattering. The crystal lattice of diamond consists of relatively low mass atoms and strong bonds as described in section 1.2.1. The strong bonds

pass along the phonons easily and because the carbon atoms are so light, they do not significantly interfere with the thermal waves. In diamond, phonons thus travel relatively long distances in a short time, in comparison to other materials. That is why diamond has such a high thermal conductivity. However, in polycrystalline diamond, the mean free path of the phonon is shortened by the various defects present in the crystal structure such as lattice defects, grain boundaries, isotopes, impurities, etc.

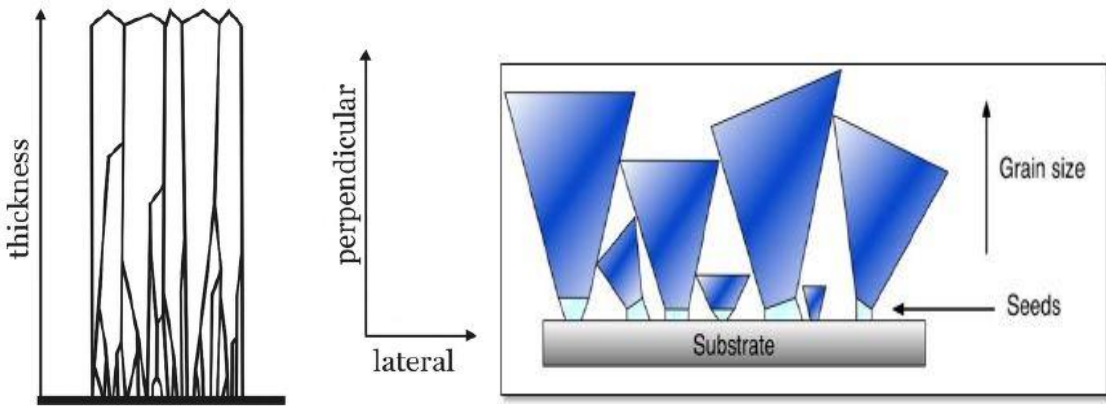

(a) (b)

Figure 1. 11. (a) Structure of a polycrystalline diamond film along with direction of heat flow [50] and (b) The grains grow from seeds on the surface of the substrate and take on a columnar structure[15].

As shown in Fig.1.11(b), polycrystalline diamond is grown from a large density of nuclei (or seed) on the substrate surface. As a result, the thermal conductivity may be highly anisotropic. A schematic cross section of polycrystalline diamond film in Fig.1.11(a) shows that only a few of many diamond seeds survive to grow along the vertical direction. Thus, the thermal conductivity measured through the thickness of the film (along the single crystals in perpendicular direction), may be significantly higher than in the lateral direction. This is due to the large number of grain boundaries that thermal phonons face when flowing laterally. Thus, the thermal conductivity is strongly affected by the grain size and grain

boundaries. It was reported by Ferrari et.al.[30] that the grain boundary consists of many hydrocarbon materials such as diamond like carbon, graphite and amorphous carbon. These materials are a significant source of localized thermal resistant. It is therefore evident that thermal conductivity of diamond is a strong function of a number of parameters, namely crystallite size, grain boundary, layer thickness and growth conditions. It is however important to note that despite being polycrystalline in nature, CVD diamond still has very high thermal conductivity. Recent reports show vertical thermal conductivity ~ 2,000 W/m-K[25] and lateral thermal conductivity ~ 800W/m-K[51] for polycrystalline diamond.

1.3. Research motivation

The main goal of the present research is to utilize the tremendous thermal conductivity of CVD diamond for thermal management of nitride semiconductor devices. The primary focus will be on the improvement of thermal performance of MOCVD grown AlGaN/GaN HEMT using CVD grown polycrystalline diamond. Research has been conducted over the last decade on this topic and significant results have been achieved. However, gaps remain between the achievement and expectation due to materials and device related issues. A brief overview of the research problems in the field will be presented in the following section.

1.3.1 Reliability of AlGaN/GaN HEMT

1.3.1.a. Reliability of AlGaN/GaN HEMT

AlGaN/GaN HEMTs are promising for power electronics applications such as power conditioning, microwave amplifiers and transmitters. Due to GaN's high breakdown voltage, these devices are expected to work in conditions that are not readily realizable

with other device technologies. These devices can operate in high drain operating voltage and low output capacitance per unit power which in turn leads to high power density and high peak efficiency[5]. For GaN based HEMTs, as noted earlier, the reported record device performances (not simultaneously achieved) include: high off state voltage of 1100 V [4], extremely high output power (900 W at 2.9 GHz, 81 W at 9.5 GHz for RF amplifier), extremely high frequency (f_T = 181 GHz at Lg =30 nm), high-power added efficiency PAE = 75% at P_{sat} = 100 W and broadband operation at 1.0–2.5 GHz with 50% efficiency[5][1].

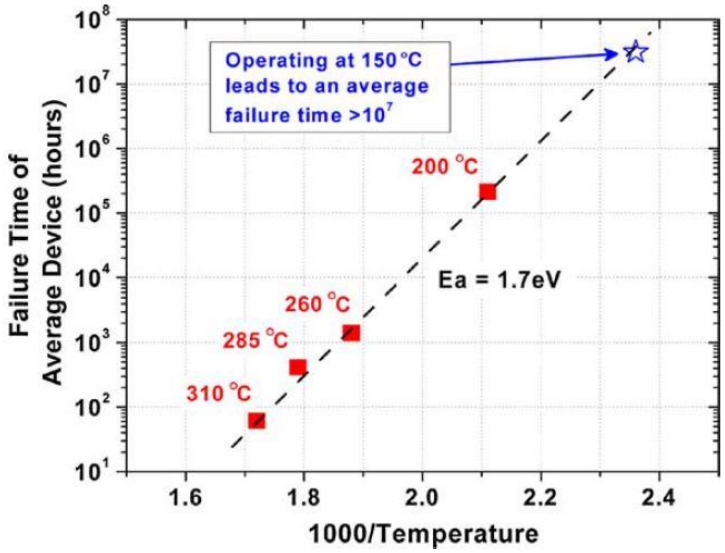

Figure 1. 12. Arrhenius plot showing a Mean Time to Failure (MTTF) plot for AlGaN/GaN HEMT [13].

As electronic devices scale smaller and GaN HEMT devices continue to increase in power dissipation over constant areas, power density continues to increase. This increased power density results in device self-heating that can lead to device failure. Thermal management is an area of great importance for these devices. In fact, inefficient thermal management is the main limiting factor for device performance and reliability [15]. GaN based HEMTs have been reported with power densities as high as 40 W/mm in RF and more than 7 W/mm in direct current (DC) [52]. In high frequency applications, these

devices have been reported to work at 300 GHz while operating temperature was above 200 ^{o}C[13]. However, practical HEMT devices operate only up to 5–7 W/mm in RF to prevent device failure due to prolonged excessive heating[53]. (Higher peak temperatures necessarily will decrease the time to failure in prolonged application with any device technology.) Mean time to failure (MTTF) is a useful parameter to define a device reliability. Fig.1.12 shows an Arrhenius plot for MTTF as a function of temperature for AlGaN/GaN based HEMTs. Device operation above 200 °C leads to an average failure time of greater than 10^5 hours, whereas devices operating at a peak temperature of 310 °C fails within less than 10^2 hours[13]. The maximum operating temperature limit for practical HEMT devices has been established below 200 °C due to this exponential decrease in reliability with increasing temperature. Therefore, self-heating problem and reliance on the conventional substrate materials (Si, SiC) through passive cooling techniques continue to limit the capability of GaN HEMT technology from their full potential. To reduce the gap between the expected power density and current practical power density, novel thermal management techniques are necessary.

1.3.1.b. Self heating of AlGaN/GaN HEMT and emergence of GaN-on-diamond technology

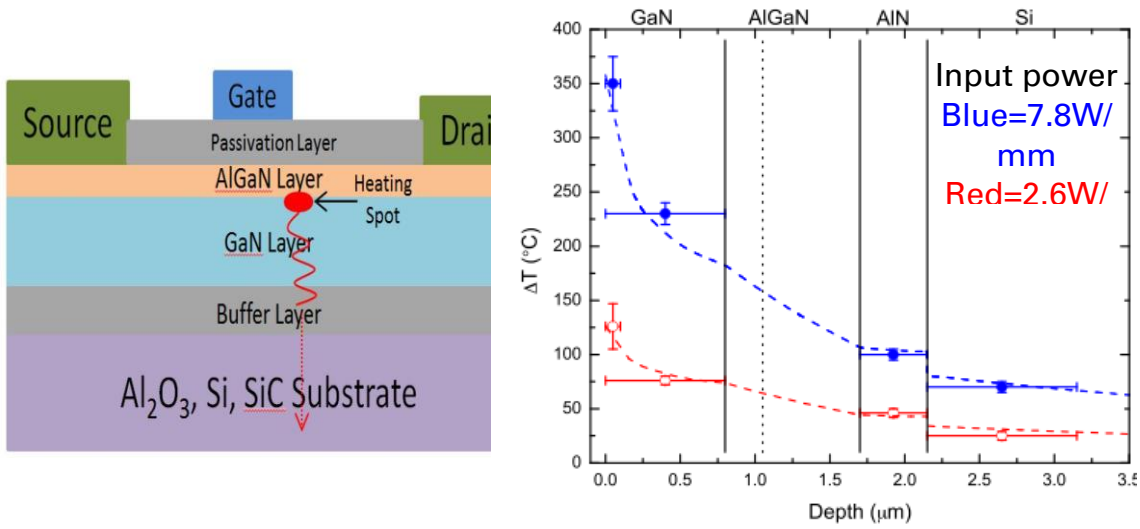

Figure 1. 13. (a)Schematic diagram of AlGaN/GaN HEMT with thermal pathway (adapted from [15]) (b) *Temperature rise* in different parts of AlGaN/GaN heterostructure at two different input powers obtained from Raman measurements along with COMSOL thermal simulation results (dashed lines)(adapted from[16]).

Thermal reliability of GaN HEMT devices are greatly affected by its self-heating. When a HEMT operates, excessive heat is generated at the active layer under the gate electrode as depicted in Fig.1.13(a). This excessive heat is required to dissipate efficiently and quickly in order to maintain operation and keep the device from failing. Efficient dissipation of the excessive heat from the active region depends on substrate material and its geometry. Higher thermal conductivity substrate and transition layer materials are required for efficient heat dissipation. However, thermal conductivity is not the only consideration while choosing a substrate. Many other factors such as coefficient of thermal expansion (CTE), lattice constants, thermal boundary resistance (TBR), electrical resistivity, and overall costs etc. must also be taken into account. Mismatch in CTE should be within the limit where thermal stress does not cause material degradation. Buffer layers are used to

minimize the lattice and CTE mismatches, and decrease residual stress. However, all these layers give rise to TBR which is unavoidable in current device structures. Materials with poor thermal conductivity along with high TBR used in typical AlGaN/GaN HEMT structures impede heat flow and cause device self-heating. Fig.1.13 (b) shows variation in temperature rise at various layer of an AlGaN/GaN heterostructure for two different input power densities. Here, input power density is calculated as the ratio of input power ($I_D.V_{DS}$) and channel length. It is clearly seen from Fig.1.13 (b) that the GaN buffer region (closest to heating spot and 2DEG) has the highest temperature rise compared to other regions. Other than thermal conductivity of GaN, one of the prime reasons for such a behavior is thermal boundary resistance between GaN and subsequent transition layers. In addition, the effect of self-heating is more severe as input power is increased which is a large drawback for advanced HEMT device design. It is important to note that self-heating induced temperature rise in AlGaN/GaN HEMTs is extremely dependent on layer stack geometry, composition, TBR and substrate material. Different research group have reported various results for self-heating induced temperature rise. For AlGaN/GaN HEMT grown on Si substrate, temperature rise as high as 300 ^oC have been reported for 2.8 W/mm input power[54]. For SiC substrate, maximum temperature rise of 192 ^oC under the gate region was reported by Arenas *et al.* [55]. Thickness of the GaN layer was also found to be crucial for self-heating induced temperature rise in AlGaN/GaN HEMTs. A temperature rise as high as 190 ^oC for a 150 nm GaN buffer layer was found by Hodges *et. al.* [56] and it was concluded that poor thermal conductivity of thin GaN (60 W/m.K) was responsible. The channel temperature rise due to self-heating directly affects the drain current (I_{DS}). In power amplifier application, the decrease in drain current reduces output power and thereby

reduces power added efficiency (PAE). PAE is given by[57],

$$PAE = \frac{P_{out}}{P_{DC}}\left(1 - \frac{1}{G}\right) \times 100\% \tag{1.8}$$

where G is gain performance, and depends on class of amplifier. In a comparative study between AlGaN/GaN HEMTs grown on Si and SiC, it was found that the drain current (I_{DS}) reduced by 100 mA/mm for a just a 20 µs long pulse (operation time) in a Si based device compared to that of a SiC based device[58]. In another study by Hilt *et. al* [59], the reduction of drain current in GaN/Si based device was found to be even more than 100 mA/mm compared to GaN/SiC based device, under DC operation. All these results indicate the effect of substrate on the self-heating of AlGaN/GaN HEMT and its overall reliability.

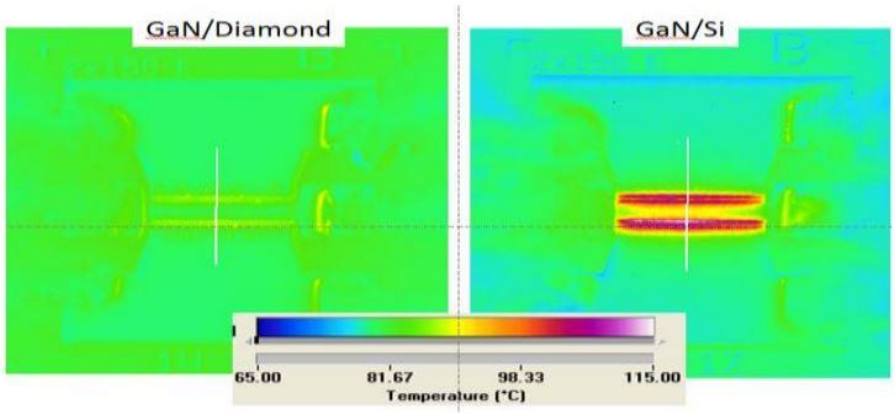

Figure 1. 14. IR thermal signature of AlGaN/GaN HEMT on diamond substrate (left) and on Si substrate during operation[12].

A majority of the present GaN HEMT technology is dominated by Si and SiC substrates for high power applications. In most cases, passive cooling is necessary to ensure reliable operation of HEMTs. However, passive thermal management systems greatly increase the overall size, weight, and power (SWaP) of the electronic system and make them expensive for portable purpose such as aerospace applications. To mitigate self-heating of

AlGaN/GaN HEMTs, scientist all over the world have been working since early 2000. In 2006, Jessen *et al.*[60] first demonstrated a working AlGaN/GaN HEMT on diamond substrate where the HEMT and CVD diamond were grown separately and then attached together using wafer bonder. This technology demonstration provided a pathway for future exploration of producing GaN based devices on polycrystalline CVD diamond substrates[12]. A significant amount of research in the field has been conducted over the last ten years. Due to the excellent device performance of GaN/Diamond wafers in high power application, DARPA initiated two round robin programs named Near Junction Thermal Transport (NJTT) in 2010 and Intra/Interchip Enhanced Cooling (ICECool) in 2012. These programs have explored the development of passive cooling approaches through integration of high thermal conductivity diamond in close proximity to the active transistor junction[12]. From modeling and experimental research outcomes of these programs, it was shown that a HEMT on diamond substrate could enable a 3x increase in areal heat dissipation without significantly increasing operational temperature. The CVD diamond deposition processes has allowed researchers to use high thermal conductivity diamond (as high as 2000 W/m-K) as a heat sink and heat spreader for GaN HEMTs. Fig.1.14 is infrared imaging showing the improvement in thermal management of GaN HEMT on diamond wafer compared to one on Si.

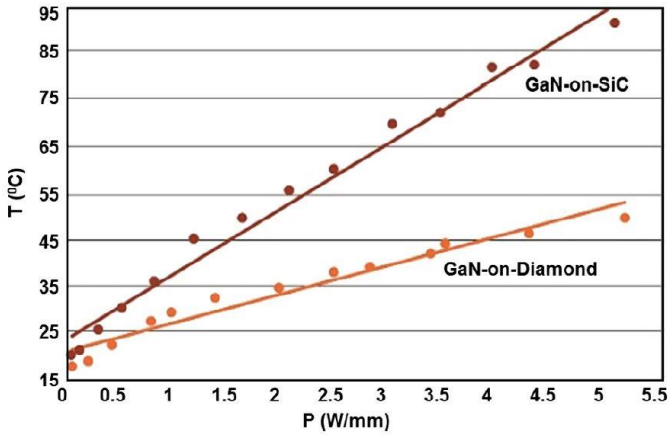

Figure 1. 15. Peak channel temperatures as a function of power density for GaN-on-diamond and GaN-on-SiC HEMT (adapted from [4] and Element Six corporation) .

The methodology for incorporating diamond in GaN HEMTs was to grow the AlGaN/GaN epilayers and diamond substrate separately, and then bond the two layers together by including a thin dielectric adhesion layer using the flip chip method[60]. Diamond manufacturer Element Six has demonstrated significant progress on GaN/Dia based RF devices and has published several papers and patents. Experimental and simulation results have confirmed that a GaN-on-diamond platform can significantly outperform GaN-on-SiC for RF applications by reducing thermal resistance and thereby increasing power density. Fig.1.15 shows that with GaN-on-diamond, a threefold improvement in RF power density has been achieved for a given channel temperature when compared to GaN-on-SiC[4]. Blevins et al.[12] from Air Force Research Lab (AFRL) have reported that the GaN/Diamond device yields 3.6X power per unit area (W/mm^2) compared to GaN/SiC devices.

1.3.2 Challenges to minimize self-heating using CVD diamond

It is undoubtedly true that the implementation of CVD diamond as a substrate material promises to increase the power and frequency of AlGaN/GaN HEMTs but further

development and optimization is critically necessary. Significant challenges still exist to reduce self-heating with this approach. As thermal conductivity of diamond is the main concern for the present research, a direct growth of GaN on diamond would be an excellent near-ideal solution to the current problem. However, researchers have developed the wafer transfer technology for attaching CVD diamond with GaN HEMT structure because crystalline III-Nitride materials cannot be directly grown on a polycrystalline diamond substrate. GaN HEMTs on single crystal diamond have not been substantially investigated due to two important reasons. First is the incredible cost and scarcity of large size single crystal diamond for substrates. Second, is the high lattice and CTE mismatch between GaN and diamond[61][24]. Specific challenges of the two approaches: a) direct growth of GaN on diamond and b) wafer transfer technology, are presented in the following sections.

1.3.2.a. Challenges in growing nitride semiconductors on polycrystalline CVD diamond

Growth of III-nitride semiconductors typically requires a crystalline substrate with manageable lattice and thermal expansion coefficient mismatches. As CVD diamond is typically polycrystalline, it is challenging to grow single crystalline, device quality III-nitride thin films on it. Furthermore, GaN, AlN, and AlGaN have a wurtzite crystal structure (shown in Fig.1.1), whereas diamond has a cubic structure (shown in Fig.1.6). Thus, the lattice mismatch between GaN and polycrystalline diamond must also be carefully considered. All these factors combine to make direct growth of III-nitrides on diamond difficult. To understand the feasibility of CVD as a substrate material for III-nitride growth it is necessary to know the associated challenges. Table 1.1 shows the various parameters of possible substrate materials for GaN growth.

Table 1. 1. Material properties of substrate materials, AlN buffer layer, and GaN layer [3][15].

Substrate	Lattice constant *a* (Å)	Lattice mismatch to GaN (%)	κ_L ($Wm^{-1}K^{-1}$)	CTE ($x10^{-6}$ K^{-1})	CTE mismatch to GaN (%)
GaN	3.189	0	130	5.59	0
AlN	3.112	2.5	290	4.15	26
Si(111)	5.430/√2	17	150	3.59	53
6H-SiC	3.08	3.5	490	4.3	23
Diamond	3.567	11	800-2000	1.5	73

It is clear from the table that even for single crystal diamond, the most significant challenges in growing GaN are the lattice and CTE mismatches. With a lattice mismatch between diamond and GaN around 11%, the growth of GaN on this substrate is expected to require a buffer structure, otherwise, poor material quality is expected. Additionally, the large CTE mismatch can induce a high tensile strain in the epilayer during cooling after growth[61]. Thus, cracks are likely to form thereby hindering HEMT device fabrication.

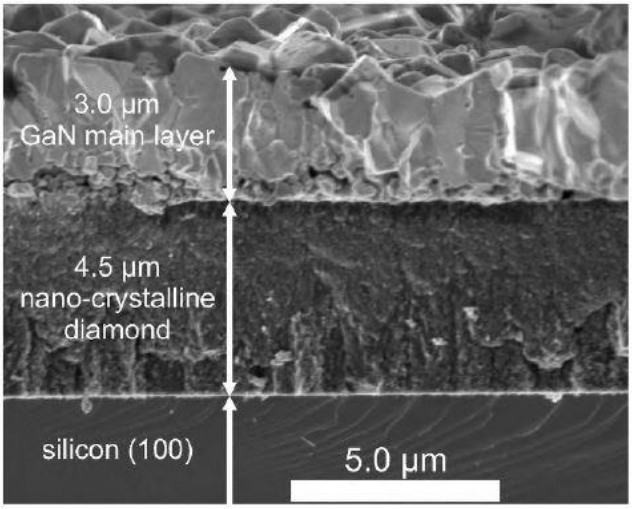

Figure 1. 16. SEM images of cross section of GaN grown on nanocrystalline diamond[62].

Interestingly, there are reports where a GaN HEMT was grown on (111) oriented single crystal diamond utilizing a multiple buffer layer of AlN and AlGaN[63]. However, the growth of GaN on single crystalline diamond is still a challenge and not many successful growth reports have been published. Drummel et. al[62] reported growth of GaN on

nanocrystalline diamond where GaN was found to be mainly polycrystalline in nature along with a preferred orientation in [0002] orientation. Fig.1.16 shows the cross section of GaN grown directly on nanocrystalline diamond.

Regarding the challenge of thermal stress, K. Hirama et al.[63] reported a large number of cracks in GaN during growth on a (111) oriented single crystal diamond substrate. GaN has a higher CTE than diamond and as a result a strong tensile strain is induced in GaN during cooling after growth. Since crack free relaxed GaN is required to facilitate device fabrication, it is currently not feasible to achieve a device, unless further progress can be made.

1.3.2.b. Complexities in wafer transfer technology

It is evident that GaN HEMT on diamond is the most promising approach to take advantage of diamond's tremendous thermal conductivity. At the same time, directly growing a GaN HEMT structure on polycrystalline diamond is a significant challenge. As a result, alternate approaches to fabricate GaN-on-diamond have been established. There are two common approaches[24].

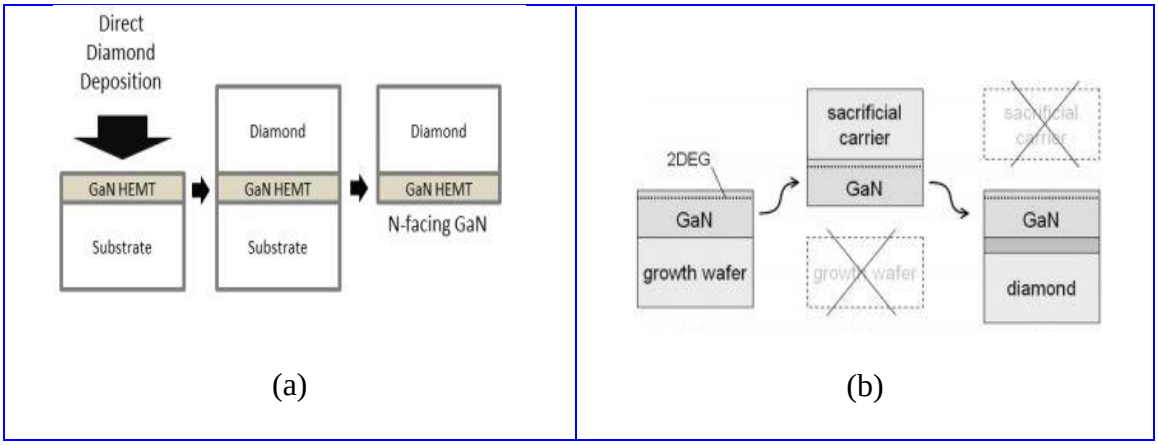

Figure 1. 17. (a) Direct growth of diamond on front side of GaN HEMT and etching backside to access N face GaN based HEMT [64] (b) Growth of CVD diamond on the backside of a AlGaN/GaN HEMT to make a free standing GaN HEMT on CVD diamond[28].

The first approach involves growing a thick (more than 50 micron) polycrystalline diamond layer on Si and separately growing the GaN HEMT on another Si or SiC wafer. Using a handle wafer attached on the GaN side of the HEMT wafer, its substrate and transition layers are etched from back side. Later the CVD diamond is attached to the backside of the HEMT wafer using a low temperature wafer bonding technique. Finally, the HEMT carrier wafer and the Si substrate, originally used to deposit CVD diamond, are removed[24].

The second approach shown in Fig.1.17(a) is a direct approach which involves growing 10–25-micron thick diamond directly on top of the GaN HEMT structure. A sacrificial handle wafer is attached with diamond using wafer bonder. The entire structure (including diamond and sacrificial wafer) is then flipped and everything except the GaN layer is removed from the backside. By this process, an N-face GaN wafer on CVD diamond is achieved. In addition to the two approaches, a modification of the second approach has also been developed. The process is shown in Fig.1.17(b). A sacrificial handle wafer is attached on top of the GaN HEMT wafer and then the backside material is removed. A dielectric adhesion layer is deposited to facilitate diamond seeding[65]. CVD diamond is grown on the backside and finally the sacrificial wafer is removed. The resultant wafer is a free standing GaN HEMT on CVD diamond.

Through various programs, including DARPA's NJTT, all these techniques have been implemented successfully. A 40-45% reduction of the operating junction temperature of a GaN transistor has been achieved and produced triple the practical RF power density[64]. However, these techniques still suffer from major drawbacks, discussed in the next section.

A. Problem associated with use of wafer bonder

In all three processes for making GaN-on-diamond wafers described in the previous sections, wafers go through complex wafer bonding processes. Due to the high lattice and CTE mismatch between GaN and Si, GaN HEMTs are grown with thick transition layers. As a result, wafers experience large thermal and lattice stresses. Wafer bow, wafer cracking, etc. often reduces the yield of these wafers. Furthermore, CVD diamond grown on any surface (GaN or diamond) creates excessive thermal stress on the substrate because of its small CTE. The wafer bonding technique usually involves a high force applied on wafers. The large stress results in bow and/or warps the wafers as they cool from the attachment temperature to room temperature. In some cases, the stress is sufficient to fracture the wafers[28]. Because of these extensive stress, reliable high yield GaN-on-diamond device processing is, to date, unfeasible.

B. Problem associated with low thermally conductive dielectric adhesion layer

GaN-on-diamond fabrication requires a dielectric layer as adhesion layer or as a seeding enhancer[53][66][67][25]. For direct bonding of GaN and diamond, a thin layer of SiN_x is usually employed as an adhesion prompter between GaN and diamond[67]. Likewise, a thin layer of dielectric (usually SiN_x) is deposited to enhance the seeding of nano diamond in GaN-on-diamond wafer transfer techniques as described in Fig.1.17(a) and (b). Thermal conductivity of such dielectric material is very poor. Thermal conductivity of such layer also depends on substrate, layer thickness, thermal boundary resistance and deposition technique. J. Cho *et al*. [68] reported the thermal conductivity of SiN_x layer grown on diamond varies in the range of 0.98 to 1.1 $Wm^{-1}K^{-1}$ for various film thickness between

24nm to 36nm. They also reported that the value of thermal conductivity varies between 0.94 and 1.0 $Wm^{-1}K^{-1}$ for similar films grown on GaN. It is important to note that thermal conductivity of the dielectric layer is a combined function of several factors, of which thermal boundary resistance is the most important. A detailed discussion on the effect of thermal boundary resistance on self-heating of GaN based HEMTs will be presented in section 1.3.2c.

C. Problem associated with graphitic content in diamond nucleation layer

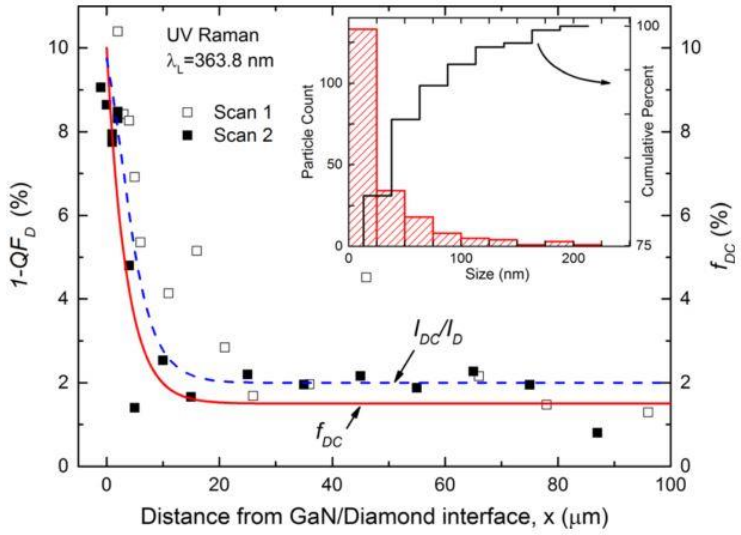

Figure 1. 18. Percentage of disordered carbon (DC) in diamond based on Raman intensity as function of distance from the GaN-Diamond interface. Inset is a histogram of TEM image analysis of DC average particle size (Image adopted from[69]).

Present strategies to fabricate GaN on diamond devices (strategies shown in Fig.1.17) involve either diamond growth on top of the device passivation layer or on the back side after removing the substrate. As previously discussed diamond grows from nanocrystalline seeds through a complex nucleation process where many seeds cannot grow vertically or does not result in diamond formation. The nucleation process is very complex and some of

these ‘unsuccessful’ seeds form sp^2 bonded carbon or diamond like carbon[45]. These materials have incredibly low thermal conductivity compared to diamond that impedes heat flow. Unfortunately, in current GaN-on-diamond devices heat has to diffuse across the nucleation region of the diamond film which results in a poor overall thermal conduction. This nucleation layer is therefore one of the most important factors that control the CVD diamond’s thermal conductivity. Many inconsistent results are published in the literature about the in plane thermal transport in the first micron of polycrystalline diamond showing values ranging from ~ 10 to few hundred W/m K[51]. In a recent study, Nazari *et. al.* [69] reported 10% disordered carbon or diamond like carbon (DLC) in diamond at the GaN-diamond interface where average particle size was less than 20 nm. Although a clear understanding of the thermal transport through the thin nucleation layer of diamond-substrate interface is not established, it is undoubtedly true that the thermal impedance caused by this layer is a significant challenge in realizing the full potential of GaN-on-diamond devices[51][69][47].

1.3.2.c. Thermal boundary resistance

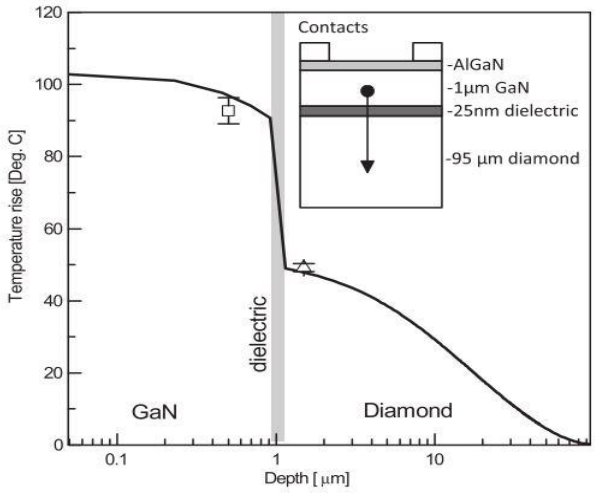

Figure 1. 19. Experimental and simulation result of temperature rise in various layers of a GaN-on-diamond HEMT, showing effect of TBR_{eff} caused by the thin dielectric layer[25].

It has been established through experiment and simulation that the main attribute that impedes effective heat spreading capability of GaN-on-diamond HEMT is thermal resistance at the interface of the various layers, i.e., GaN-transition layer or GaN-dielectric and GaN-diamond[25][66][70][71]. This thermal resistance is mainly caused by 'effective thermal boundary resistance' (TBR_{eff}) at the interface between the GaN layer and the substrate[66]. Fig.1.19 shows the effect of TBR_{eff} in GaN-on-diamond HEMT caused by, mainly, the GaN-dielectric-diamond interface. The AlGaN/GaN-on-diamond HEMT shown in Fig.1.19 was a non-gated structure and a source drain bias of 40 V was applied. A schematic cross section of the device structure with various layer thickness is also shown as an inset.

Thermal boundary resistance (TBR) can be defined as the inverse of thermal boundary conduction across an interface and given by, $TBR = [\frac{Q}{A.\Delta T}]^{-1}$, where, Q is heat flow across an interface, A is the area that the heat is passing through, and ΔT is temperature difference between the two sides of the interface. However, for the case of GaN HEMTs grown on foreign substrate and then transferred to diamond, there are multiple layers and multiple interfaces which make the effective thermal boundary resistance calculation more complex than this simple expression. In AlGaN/GaN HEMT, TBR_{eff} is associated with interfaces between materials, the dielectric interlayer used for diamond growth seeding, the adhesion layer if used, the high defect density, and small grain transition region near the nucleation surface[66]. Fig.1.20 is a cross section transmission electron microscope (TEM) image of a GaN-on-diamond wafer showing the various interface region layers that contribute to TBR_{eff}.

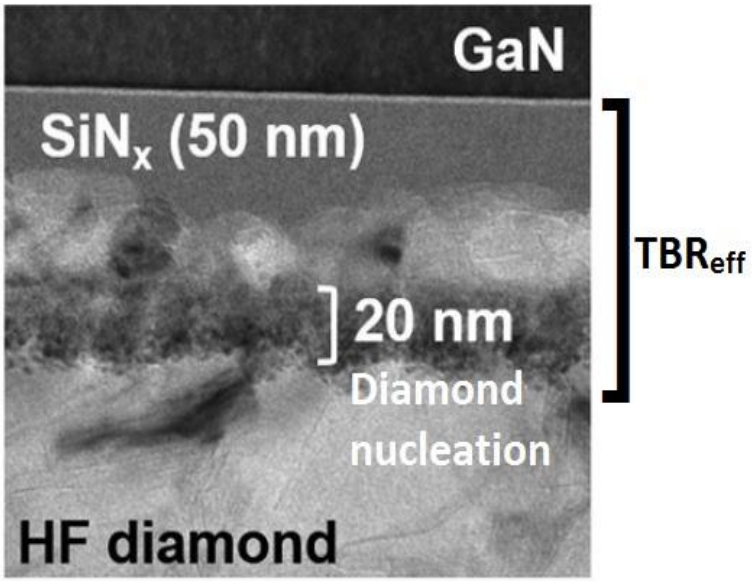

Figure 1. 20. TEM image of effective thermal boundary resistance regions in a GaN-on-diamond system prepared by removing substrate from the back side of HEMT structure and growing diamond on the back side with dielectric interlayer[66].

For the structure shown in Fig.1.20, the TBR_{eff} can be calculated using the following equation[72],

$TBR_{eff} = R_{th}(GaN) + R_{th}(GaN - dielctric) + R_{th}(dielectric) + R_{th}(NCD) + R_{th}(dielectric - diamond)$ Where, R_{th} is thermal resistance and NDC stands for non-diamond carbon at the nucleation layer. Furthermore, the thermal resistance of the dielectric layer R_{th} can be defined as the ratio of the layer thickness and dielectric constant of the dielectric[68]. It is important to recognize that the formation of GaN-on-diamond is dependent on many factors such as diamond nucleation density, inter-grain voids, non-diamond carbon in the nucleation region, dielectric layer, and growth techniques in the diamond. Therefore, large variation in TBR_{eff} ranging from 10-50 m^2K/GW have been reported for GaN-on-diamond[16][66][65][73]. Table 1.2 shows variation in thermal conductivity and TBR_{eff} for GaN-on-diamond wafers grown by various methods.

Table 1. 2. Variation in thermal conductivity of diamond and thermal boundary resistance between GaN and diamond[66].

	$k_{diamond}$ (W/m-k)	TBR_{eff} (m^2K/GW)
34nm seeding Opaque HF diamond	620 ± 50	25 ± 3
100nm seeding Translucent MW Diamond	1500 ± 300	50 ± 5
28nm seeding Translucent MW Diamond	1500 ± 300	12 ± 2

It has been noted that a thin dielectric layer is essential for seeding and adhesion of diamond onto GaN[60][66][25][53] and the most common dielectric material used for GaN-on-diamond HEMT is SiN_x. Due to its low thermal conductivity, SiN_x creates a large thermal resistance ranging from 5-50 m^2K/GW (for various thicknesses)[65]. The thermal conductivity and thermal resistance of such a thin dielectric layer depends on the thickness and dielectric constant of the layer, given by $R_{th}(SiNx) = \frac{d_{SiNx}}{k_{SiNx}}$ [68]. From the equation of TBR_{eff} given above, it is seen that TBR_{eff} is directly proportional to the thickness of dielectric layer when other parameters are held constant. This relation was found to be valid for most of the reported TBR_{eff} values in literatures[16][66][65][73]. The most significant result was reported by H. Sun *et al.*[66], where a linear relation between TBR_{eff} and SiN_x thickness was observed. Therefore, it is clear that TBR_{eff} of GaN-on-diamond system can be significantly reduced by minimizing the thickness or ideally removing (if possible) the dielectric layer.

Despite various problems associated with the GaN-on-diamond implementation discussed so far, fabricated HEMTs are still 3-4 times more thermally efficient than existing GaN on Si or SiC technology. However, realization of the full potential of GaN-on-diamond is impeded by the many factors associated with fabrication and materials

properties. GaN-on-diamond's true potential can only be achieved with either directly growing the GaN HEMT on the diamond substrate or growing high quality, defect free diamond on GaN. Implementation of such a strategy would result in GaN HEMTs capable of working at the highest power density of any semiconductor material.

1.4. Proposed solution

From the background study presented above, it is clear that self-heating is one of the most significant roadblocks in the way of realizing the full performance potential of GaN HEMTs. Therefore, this research was focused on solving self-heating in the GaN-diamond system. The fundamental research approach is to directly grow the GaN layer on diamond. This approach takes advantage of three different technologies, namely GaN (or generally Nitride semiconductor) growth on Si substrate, epitaxial lateral growth of III-nitride semiconductor with non-crystalline mask and selective deposition of CVD diamond. These three techniques have unique application in three different fields and their combination results in a straight-forward and effective solution to the complex fabrication of GaN-on-diamond wafers.

The research involves three main steps:

1) Growth of relaxed GaN layer on Si substrate using AlN nucleation layer and AlGaN transition layer,
2) Selectively deposition of CVD diamond on the GaN wafer,
3) Regrowth of GaN on the openings of the selectively deposited diamond wafer and epitaxial lateral overgrowth of GaN

The GaN-on -diamond wafer produced in above three steps can be used for depositing

AlGaN/GaN HEMT, LEDs and lasers. The proposed fabrication process is shown in Fig.1.21.

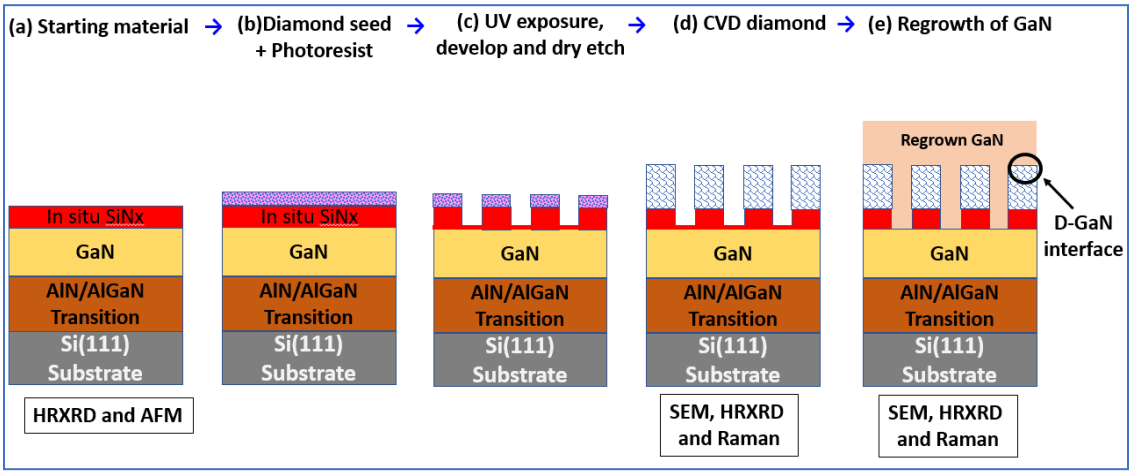

Figure 1. 21. Proposed fabrication steps for growing GaN on CVD diamond. Various characterization methodologies between different steps are also noted.

The current state of the art process for GaN-on-diamond fabrication suffers from several issues such that the resultant devices cannot perform to their full potential. The most significant problems associated with fabrication is complexity of wafer transfer or flip chip technology. For the materials, poor thermal conductivity and thermal boundary resistance of the dielectric layer impedes the flow of heat from the active region of the devices. An effective solution to all those problems has been presented through this research plan. This methodology will result in GaN deices (HEMTs or LED, Lasers etc.) grown directly on diamond with the following advantages:

i. The active layer or 2DEG in direct contact with the diamond which will result in very efficient heat removal from the active region.

ii. No poor thermally conductive nucleation layer or graphitic carbon adjacent to the GaN surface resulting in no or very small thermal resistance between GaN and diamond.

iii. No dielectric adhesion layer between GaN and diamond which will facilitate the full benefit of highly thermally conductive diamond for heat extraction from the active region.

iv. Eliminate the problem associated with thermal boundary resistance, which is presently the fundamental problem with GaN-on-diamond HEMTs.

v. No permanent wafer bonding is required which will result in reduced process complexity and overall cost.

1.4.1 Background on the proposed solution

The growth of GaN in MOCVD is an established technique but selective deposition of hot filament CVD diamond on nitride semiconductor poses significant challenge due their decomposition at CVD environment[74]. Direct growth of diamond on GaN has been reported using HFCVD[75] and PECVD[48], and significant surface damage/etching was observed in both cases. The presence of atomic hydrogen in the plasma was responsible for etching in the case of microwave PECVD. For HFCVD, the etching effect is even more severe because of the simultaneous impacts of the hot filament temperature and energetic hydrogen atoms. A protective layer is therefore necessary to protect the underlying III-Nitride layers during diamond deposition[76]. Plasma enhanced CVD grown SiN_x has been used as such a dielectric layer in this dissertation research.

Photolithography based selective deposition of CVD diamond on Si and SiO_2 was first demonstrated by Masood et. al.[77]. Selective deposition of CVD diamond on GaN has been achieved by via low temperature PECVD diamond deposition followed by a reactive ion etching to pattern the diamond in many of the reported results[76] [78][79].

Significant etching and damage of the underlying Nitride layers were observed and the processes had low throughput.

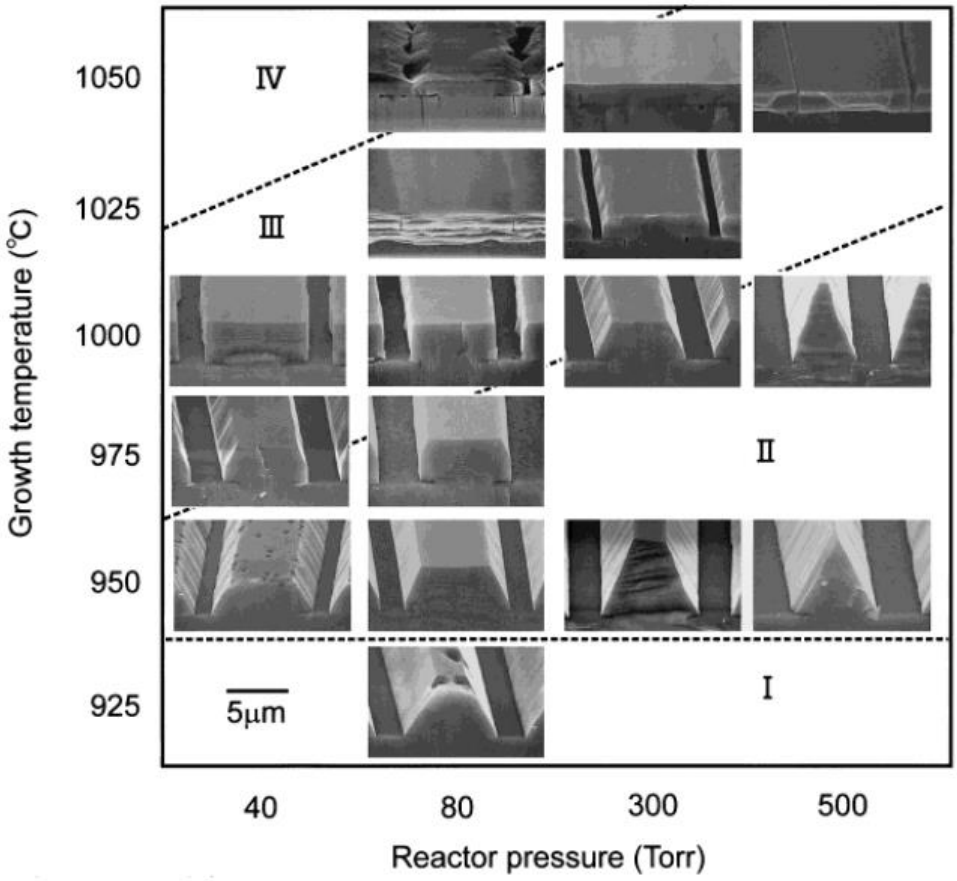

Figure 1. 22. SEM images showing morphological change in MOCVD grown ELO GaN on SiO_2 mask for various reactor pressures and temperatures[80].

Epitaxial lateral over growth (ELO) of GaN was first reported by Kato et. al[81] and the process has been extensively used in GaN optoelectronics due to its effectiveness in producing low defect GaN[80][82]. In ELO, GaN is overgrown through the mask opening of a patterned dielectric coated GaN wafer. Hiramatsu et. al.[80] has reported a detailed study on the effect of various growth parameters on lateral growth of GaN on dielectric mask. The growth anisotropy of ELO GaN in various crystallographic

orientations is a strong function of four main factors namely group V to group III mole ratio (V/III), pressure, temperature and mask orientations[83]. As seen from Fig. 1.22, lateral growth can be enhanced by using low pressure and high temperature growth. A wide range of V/III (1000-5000) value have been reported for enhanced ELO[83][84]. ELO of GaN on 200 nm SiO_2 mask was first reported in 1997 by Kapolnek, *et al*[83] where the ELO growth rate anisotropy was found to be a strong function of both the temperature and ammonia flow. Increased lateral growth was achieved by increasing the group V to group III molar ratio (V/III) or total ammonia partial pressure or, by increasing the growth temperature, and thereby increasing the decomposition efficiency of the ammonia[83]. ELOG of GaN on SiO_2 has also been reported by Chen *et al* [85] and the process resulted in GaN with high crystalline quality. For this process, the full width at half maxima of GaN (0002) peak was found to be 376 arc second. High quality GaN grown through ELOG on SiN_x mask[86] and sapphire mask[87] have also been reported recently. ELO of GaN on diamond has never been reported before. The ELO of GaN reported in this dissertation is expected to produce high quality electronic devices since the defect density on ELO region can be as small as 10^7 cm^{-2} [3] whereas a standard HEMT available in market has a GaN layer with defect density ~10^9 cm^{-2}[88].

1.5 Dissertation overview and research objectives

During this dissertation research, significant efforts were given mainly in optimization of steps (b)-(e) of Fig. 1.21. Initially, growth optimization of CVD diamond in HFCVD were performed by changing various growth parameters. Effect of gas stoichiometry on crystal structure and quality of HFCVD were studied using X-ray diffraction and Raman

spectroscopy. Selective deposition of CVD diamond on various substrate were achieved through optimization of photolithography based seeding technique. Raman spectroscopy and finite element analysis based stress measurement of diamond structure grown on Si were performed before moving to the Nitride based substrates. Selective seeding and HFCVD of diamond on Nitride semiconductors were achieved through carefully conducted experiments. Finally, epitaxial lateral over growth of GaN on selectively deposited diamond coated GaN wafer were performed through optimization of several growth parameters such as group III to group V molar ratio, temperature, pressure and mask window orientations.

In Chapter Two, an overview of various deposition tools and measurement techniques utilized in this dissertation are presented. The basics chemical vapor deposition (CVD) and metal organic CVD have been presented along with a brief description of specific tools used for this research. Physical principals of various characterizations technique along with a brief tool specific description have also been presented. Methods and accomplishments in the context of data analysis and simulation has also been described in some detail, highlighting finite element (FE) analysis of thermal stress using appropriate model.

In Chapter Three, a systematic CVD growth study and associated characterization results have been presented to understand effect of gas stoichiometry on the quality and crystal structure of polycrystalline diamond. Texture formation and preferred orientation of polycrystalline diamond films were studied using diamond films grown under various conditions and various thickness. XRD Pole figure, Raman Spectroscopy and scanning electron microscopy were employed to understand the effect.

Chapter Four highlights a focused study of stress distribution across selectively grown CVD diamond stripes on Si. UV Raman Spectroscopy based stress measurement was accompanied by EF analysis of an appropriate model to understand the origin of the stress.

Chapter Five presents a detailed study on selective deposition of HFCVD diamond on AlGaN/GaN HEMT structure. Optimization of seeding and CVD growth parameters to eliminate surface damage of Nitride semiconductors have been presented with detailed structural and morphological characterization results.

In chapter Six, a systematic study on MOCVD based ELO of GaN on selectively deposited diamond coated GaN wafers have been reported. Effects of various growth parameters on ELO of GaN have also been reported with associated characterization results. Growth parameters associated with successful ELO process has been reported in detail.

Finally, chapter Seven provides a summary of the dissertation and addresses conclusions of the work. Based on the knowledge gained through this dissertation research, five potential future research projects have been suggested and briefly discussed.

II. GROWTH, PROCESSING, CHARACTERIZATION AND ANALYSIS TECHNIQUES

In this chapter, a brief overview of the two-main chemical vapor deposition (CVD) techniques viz. hot filament CVD (HFCVD) and metal organic CVD (MOCVD) has been described because this dissertation research was conducted using them for growing polycrystalline diamond and nitride semiconductors respectively. A detailed discussion on selective seeding approach developed for the research has been presented in detail. Details regarding standard equipment employed and typical characterizations for each of materials will be provided. A brief discussion on the general physics and working principle of each of the characterization tools have also been presented. In addition to materials growth and characterization, finite element analysis of thermal stress was also performed during the dissertation research. A brief description of the simulation works performed in this research has been presented here as well.

2.1 Chemical vapor deposition

In any CVD process, there are five main steps involved for successful film deposition[89]. The steps are: a. flow of gases into the chamber and the flow is directed to wafer surface, b. adsorption of gas molecules with the wafer surface, c. surface chemical reaction of the gas molecules resulting in solid product (film material), d. desorption of the byproducts and e. removal of byproducts from the chamber. The reactant gas is often mixed with carrier gas (such as nitrogen, hydrogen or argon) to prevent gases from reacting prior to reaching the wafer surface. The gas delivery is controlled by mass flow controllers (MFCs). The gas delivery system to a CVD chamber vary depending on reactor geometry. There are

two main types of gas delivery systems are available for CVD namely horizontal flow and vertical flow. Vertical flow reactors usually result in best film uniformity in terms of thickness and roughness. CVD tools used for this dissertation had a showerhead gas delivery systems and substrates were rotated to improve uniformity. The gas flow inside the CVD chamber creates a thin layer above substrate surface called the 'boundary layer' through which reactant gas must traverse to incorporate on the substrate[89]. To achieve successful film deposition and minimum gas phase reactions, gas molecules must penetrate the boundary layer. Gases that are unsuccessful to penetrate the boundary layer are pumped out by the pumping system. In addition, the pumping system also controls the resident time of gas molecules inside the boundary layer by controlling the chamber pressure. However, gas phase reaction is sometime desirable in some special CVD process. For example, in case of CVD of diamond (discussed in detail later) dissociation of methane into methyl radicals takes place in gas phase which is essential for diamond deposition.

Various types of surface reaction can take place in a CVD process. Pyrolysis, reduction, oxidation and photolysis are some of the most common CVD reactions. Energy in the form of heat or plasma is necessary for the surface reaction. Various types of CVD systems are available based on types of energy source. In case of CVD tools used for dissertation, mainly heat was the source of energy. Once the gas reactants adsorbed to the surface, they keep migrating across the surface until a chemical reaction takes place. The location where chemical reaction takes place is called 'nucleation site'. Further chemical reaction take place at these nucleation sites and they expand. Expanding neighboring nucleation sites will then merge together resulting in 'coalescence' of individual nucleation sites. The bulk film grow in a uniform fashion until the deposition is complete.

The byproduct gases of the surface chemical reaction leave the wafer surface through desorption. The removal of the byproducts from the surface is necessary for uniform and desired film deposition. The temperature of the wafer surface plays another important role here. It breaks the bond between the byproduct and wafer surface and provide sufficient energy for them to traverse through the boundary layer. Once the byproduct is out of boundary layer, the exhaust pumping system pumps them away. The uniformity, growth rate, morphology and physical properties of CVD films are greatly affected by the five steps described above.

2.2.1 Hot filament CVD for diamond deposition

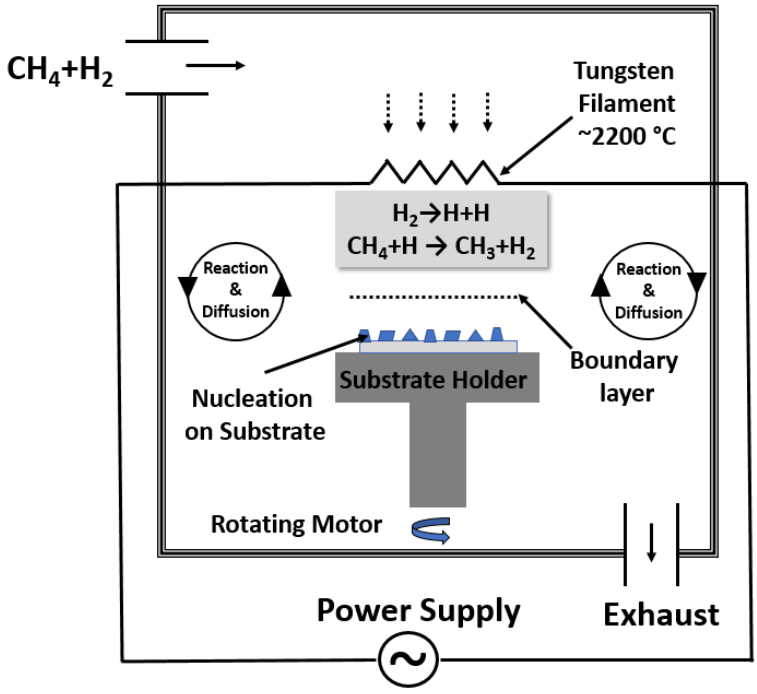

Figure 2. 1. Schematic diagram of hot filament CVD reactor used for this dissertation to deposit diamond.

Hot filament CVD is the oldest and one of the most widely used techniques for diamond deposition. was first developed by Matsumoto and co-workers at NIRIM, Japan[90], [91]. The basic setup for a HFCVD system requires a vacuum chamber, a pump capable of working at sub-atmospheric pressure, gas feed and metallic wire connected with heating power supply. A simplified schematic diagram of the HFCVD used for this research is shown in Fig. 2.1. The metal filament array is placed several millimeters above the substrate. At maximum power, these filaments can be as hot as ~2200 °C while glowing and the corresponding substrate temperature becomes 700-800°C which is necessary for diamond deposition. To achieve uniform diamond deposition, the substrate is required to be coated with 'nano-diamond seed'. There are various techniques for substrate seeding with nano-diamond seeds. Details about seeding will be presented in a later section. The

seeded wafer is then loaded into the chamber and diamond starts to deposit on the nucleation sites initially. The deposition process continuous as more and more energetic hydrogen traverses the boundary layer and take part in surface reaction. Complete coverage of the substrate surface takes place when these individual grains meet each other and coalesce. Most widely accepted model for hot filament diamond deposition process has been presented in previous chapter. As shown in Fig.2.1, diamond grains are deposited on nucleation sites through the chemical reaction between methane and energetic atomic hydrogen. Hydrogen molecules break into highly energetic atomic hydrogen as they come in contact of the hot filament. These energetic atoms break the methane into methyl radicals and the dissociation process continues until it produces carbon atoms that make chemical bond with nano diamond seeds on the surface[92]. Methane in the diamond deposition process serves another important purpose of metal wire carburization[93]. The carburization of the tungsten wire results in increase in wire resistance and that give rise to increase in total voltage and power. It is worth mentioning that the carburization process is slow and that result in slow growth rate at the beginning of HFCVD process. Besides, each set of new wire is required for every deposition because the metal carbides become extremely fragile when they are cool down and breaks off from the array.

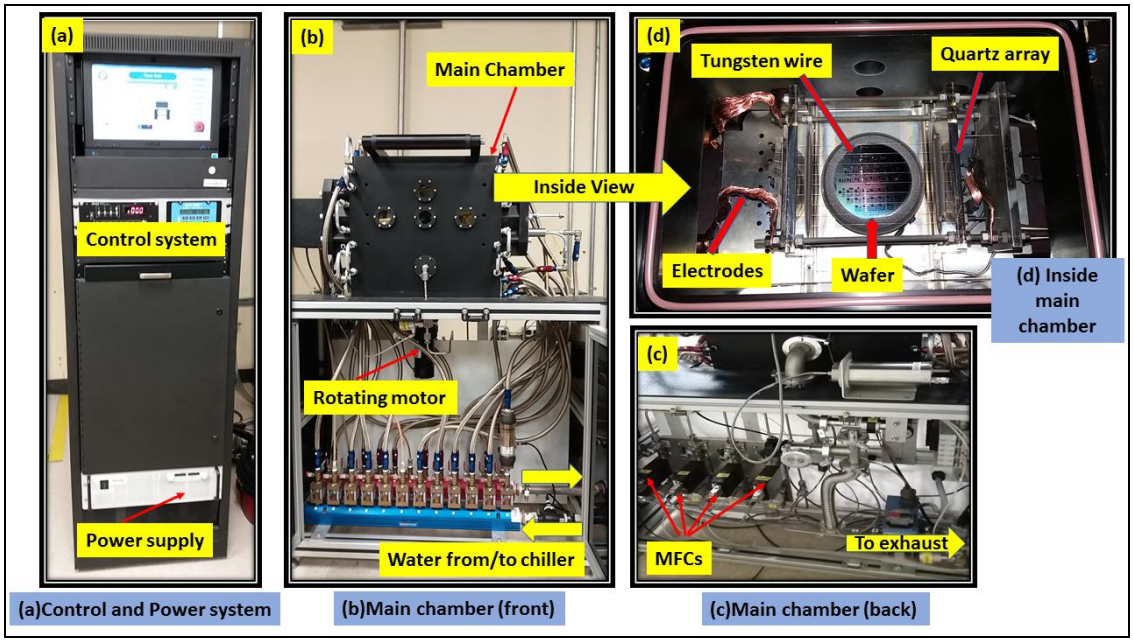

Figure 2. 2. Different parts of Hot filament CVD reactor at Texas State University (a) computer control system and power supply, (b) front side of the main chamber showing water circulating system, (c) backside of main chamber showing MFCs and exhaust line and (d) the inside view of the main chamber right before diamond deposition showing the quartz array with 9 tungsten wires and a selectively seeded diamond wafer loaded on the substrate holder.

Hot filament chemical vapor deposition (CVD) reactor used in this dissertation research was purchased from Crystallume Inc. Various parts of the CVD tool is shown in Fig. 2.2. A custom-built control software system of the tool as shown in Fig. 2.2 (a) allowed editing recipe and modifying various parameters for any specific growth. The substrate holder is made of Molybdenum and connected with a rotating motor which rotates the substrate during deposition for uniformity in deposited films. In addition, the whole chamber is cooled by chilled water as seen in Fig. 2.2 (b). As described in previous chapter, 1-3% methane gas in hydrogen was used as process gas to deposit CVD diamond with very small (3 standard cubic centimeter per minute or sccms) amount of oxygen. The flow of gases was controlled by Mass flow controller (MFCs) as seen in Fig. 2(c). The diamond growth process for this dissertation was optimized using nine tungsten wires of diameter 0.25mm

separated by 1mm. The array is visible in 2.2 (d) over a nano-diamond seeded 100mm wafer. The HFCVD reactor is capable of depositing diamond with maximum 107A current and 66 Volts of voltage.

The growth rate of the HFCVD is a complex function of several parameters such as methane concentration, current, tungsten wire to substrate separation and pressure. With higher methane concentration, high growth rate is achievable but the quality of diamond become poor. Besides, higher methane concentration results in faster carburization of the tungsten wire resulting in faster and uniform growth rate. Increasing filament current increases the surface temperature and results in increased growth. The pyrometer reads the surface temperature through the quartz window on the back side of the reactor. Increase of pressure can increase the growth rate due to increased resident time of the reactants. Substrate to wire distance is basically another knob to control the surface temperature and thereby growth rate. The HFCVD reactor used for this research was capable of growing diamond with 0.5-4.5% (10-90sccm) methane in hydrogen (2 SLM). Diamond growth rate using the reactor can be varied between 0.2 μm/hour and 1.5 μm/hour.

2.2.2 Metal organic CVD for III-Nitride deposition

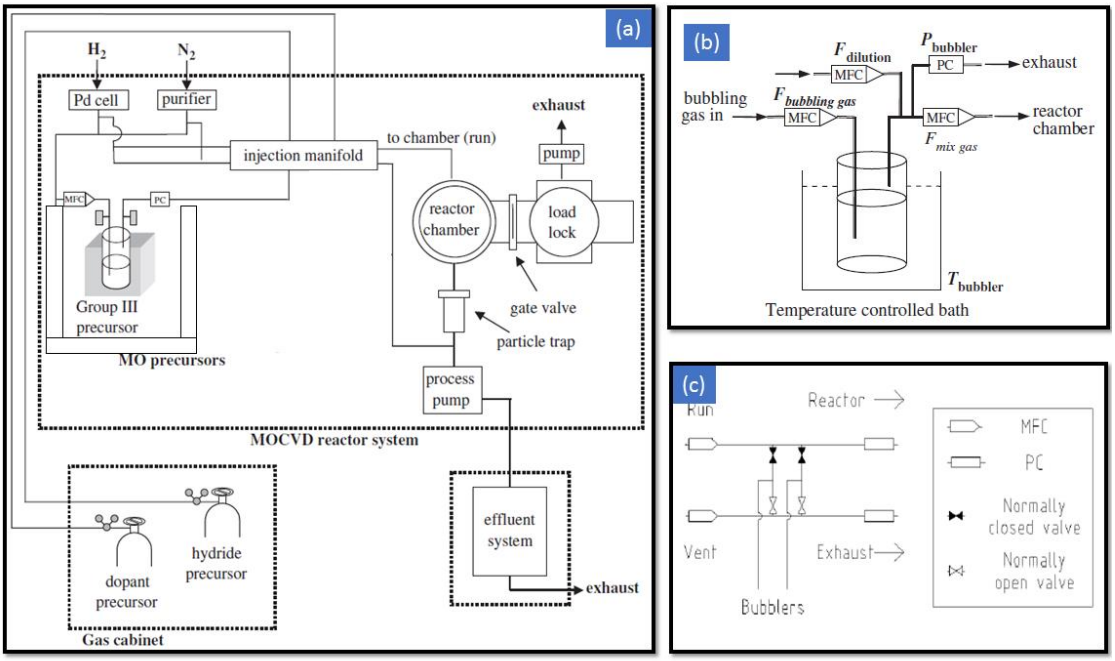

Figure 2. 3.(a) General schematic diagram of an MOCVD system showing main components only [89] (b) Schematic diagram of a bubbler used for organometallic precursors and (c) run vent manifold used for MOCVD reactor [94].

MOCVD is a non-equilibrium semiconductor film deposition technique which involves gas phase transport of organometallic precursors (OM), hydrides (source of nitrogen such as ammonia) and carrier gases onto a heated substrate where the precursors are pyrolyzed and film is deposited[95]. However, MOCVD growth involves very complex chemistry and the growth is influenced by reactor system conditions, especially the reactor chamber geometry. MOCVD reactor system design requires the integrated consideration of hydrodynamics, thermodynamics and kinetics because it critically affects the structural, electronic and optical qualities of material itself and uniformity, controllability and run-to-run repeatability of the growth process[89].

The components of a general MOCVD reactor system can be grouped into several

parts. However, basic MOCVD reactor system must have three major components as shown in Fig. 2.3 (a): (i) the gas delivery system, (ii) the reactor growth chamber and (iii) exhaust system. Most modern MOCVD system has another component for safety system.

The detail chemical reaction occurring in MOCVD are very complicated; however, the process can be represented by a very simple formula for a reaction of III-V employing metal-organic precursors and hydride precursors[89],

$$R_3M(g) + EH_3(g) \rightarrow ME(s) + 3RH \uparrow (g) \qquad (2.1)$$

where M is a Group III metal atom, e.g., Ga, Al or In; R is an organic radical, typically CH_3(methyl) or C_2H_5 (ethyl); E is a Group V atom e.g., As, P or N; and H is atomic hydrogen. The main difference of MOCVD compared to other CVD process stems from the use of organometallic precursors. Compound semiconductors such as GaN, AlN and their alloys can be grown in MOCVD by using precisely controlled MFC and PCs. A simplified schematic diagram of a basic MOCVD system and its various parts are shown in Fig. 2.3. In MOCVD of group III-Nitrides, precursors and their transports are completely different than a conventional CVD. MOCVD of III-V compound semiconductors generally employs mixtures of Group III metal-organic and Group V hydride precursors in a carrier gas. Typical carrier gases are H_2, N_2, or mixture of H_2 and N_2, and the precursors are transported by one or more carrier gases and injected into an open-tube process chamber[89].

For growth of III-Nitrides, ammonia anhydrous is most common nitrogen source which is a liquid in room temperature but has high vapor pressure and can be delivered directly into the reaction chamber as a gas. OM precursors are usually either liquid or solid at room temperature and atmospheric pressure which prevents them from being delivered

directly to the chamber. Most common OM precursors used for MOCVD of III-Nitrides are trimethylaluminum (TMA) (liquid at room temperature), trimethylgallium (TMG) (liquid at room temperature), and trimethylindium (TMI) (solid at room temperature). The OM precursors come in a sealed metal container because of their pyrophoric nature. The special metal container is called 'bubbler' as shown in Fig. 2.3 (b). Since OM precursors are either liquid or solid at room temperature, they are kept in temperature controlled bubbler and a carrier gas is flowed into the bubblers where it enters through a dip tube submerged in the OM. After carrier gas bubbles through the OM liquid precursors, they become saturated with the vapor phase of the OM above the liquid surface. Unless the gas flow rate is too high, the bubbling action sets up an equilibrium between the condensed phase and the vapor phase. The equilibrium vapor pressure of OM at any given temperature T (K) is given by following equation,

$$ln\, P_{Eq,T} = -\frac{A}{T} + B \tag{2.2}$$

Where A and B are constants. The, saturated carrier gas with OM precursor vapor is carried into the growth chamber via special tubing. The flow rate of OM materials in moles per minutes can be calculated using$P_{Eq,T}$ and is given by,

$$Q_{OM}(mol/min) = \frac{P_{Eq,T}}{P - P_{Eq,T}} \times \frac{F_{bubbling-gas}(sccm)}{C_{STP}(cm^3/mol)} \tag{2.3}$$

where, $F_{bubbling-gas}$ is the OM containing carrier gas flow rate in sccm and $C_{STP} = 22400\ (cm^3/mol)$ at room temperature and atmospheric pressure. Due to the exponential temperature dependence of the $P_{Eq,T}$ of OM in equation 2.2, the bubblers are kept in chilled baths to very carefully and accurately regulate their temperature in order to maintain consistent delivery. Besides, the use of MFC and PC make the bubbler system more robust

for precise control of gas flow. In addition, OM flow can be diluted with carrier depending on the application using a more complex double dilution manifold as shown in Fig. 2.3(b). The hydride (Ammonia) can be treated as an ideal gas and the flow rate is calculated using following simple equation:

$$Q_{NH_3}(mol/min) = \frac{F_{NH_3}(sccm)}{C_{STP}(cm^3/mol)} \tag{2.4}$$

The ratio Q_{NH_3}/Q_{OM} calculated from equations (2.3) and (2.4) is called the well-known 'V/III' for MOCVD of any III-V semiconductor[89]. V/III is a universal representation of the molar ratio of OM and hydride which affects the properties of deposited film. However, the V/III value for any specific material is reactor specific and same value may not always result in same film properties. Hydrogen is most widely used carrier gas because high purity can be achieved using a palladium (Pd) cell. At ~400 °C, Hydrogen molecules breaks into atomic hydrogens as it passes through the Pd cell and forms molecules after that. Due to the smallest size of hydrogen atom, no other particles/impurity such as H_2O, CO_2 or CO can pass thorough the Pd cell. Due to availability of highly pure hydrogen through the use Pd cell, hydrogen is used as carrier gas for most of the III-Nitride semiconductors except the one involving Indium because of hydrogen has negative effect on Indium incorporation[96].

In MOCVD of III-Nitrides, multiple layers of materials are deposited and abrupt interfaces between layers is necessary for this purpose. The flow from bubbler to the reactor is therefore controlled in a precise way by linking a normally closed valve to a normally open valve in a configuration known as a run/vent manifold illustrated in Fig. 2.3(c). Initially, flow starts in the vent line which bypasses the reactor and valves are activated when flow to the reactor is necessary for a specific layer of semiconductors[94]. In the

switching manifold, the individual precursor gas flows are switched, combined and routed into either the growth chamber or the vent/exhaust line, while maintaining a differential pressure of nearly zero between the ‘‘run’’ and ‘‘vent’’ line so that the gas flow switching transient is minimized and does not strongly affect the growth process[89]. In the MOCVD, flow rates through the bubblers into the manifold are typically less than 200 sccm. Therefore, a second MFC with a higher flow rate is placed on the line upstream of the valves to provide gas to push the OM material to the chamber quickly, and to provide sufficient flow rate so that the flows into the reactor chamber can be tuned for uniformity across the wafer[94]. Pressure controllers are placed downstream of the manifold to balance the pressure between the vent and run lines to prevent a pressure surge when the valves are activated[94].

For a vertical flow MOCVD reactor, the main growth chamber consists of three main parts: gas shower head top plate, chamber sidewall and the bottom plate. The precursor and process gases are injected through the specially designed shower head and dispersed uniformly across the substrate. The electrical heater element is placed on the bottom plate which is also connected with a rotational feed through that links a shaft to a motor outside the chamber. The bottom plate is also connected with the exhaust system that is connected with the system pump. All the components of the main chamber except the heater element is water cooled to minimize damage during the high temperature deposition. Inside the main chamber, substrate is supported on a susceptor that sits on top of the motor shaft above the heater and is rotated to facilitate uniform film deposition. The susceptor (also called platter) is made of SiC coated graphite. The graphite helps transferring heat from the heater to the wafer and the SiC coating provide interness during the deposition of nitride

semiconductor. A new platter is used for each run and can be cleaned using concentrated sodium hydroxide. The heater element is controlled by a thermocouple and surface temperature is measured using a pyrometer.

The process pump and throttle valves are used to regulate the pressure inside the chamber. Control of pressure is an important factor because it affects the growth and uniformity of deposited materials. For MOCVD, typical pressure is 30-500 torr depending on the design of the reactor. The advantage of MOCVD over other high vacuum deposition is its capability to deposit at much higher temperature and no necessity of expensive high vacuum pumps. However, due to the higher-pressure operation, in situ characterization such as RHEED cannot be used. The other important part of the MOCVD system is the load lock(LL) system which is isolated from the main chamber by a gate valve and used for loading/unloading wafer to/from main chamber using a transfer arm. The LL is pumped and purged with nitrogen before loading wafer or transferring wafer to the main chamber.

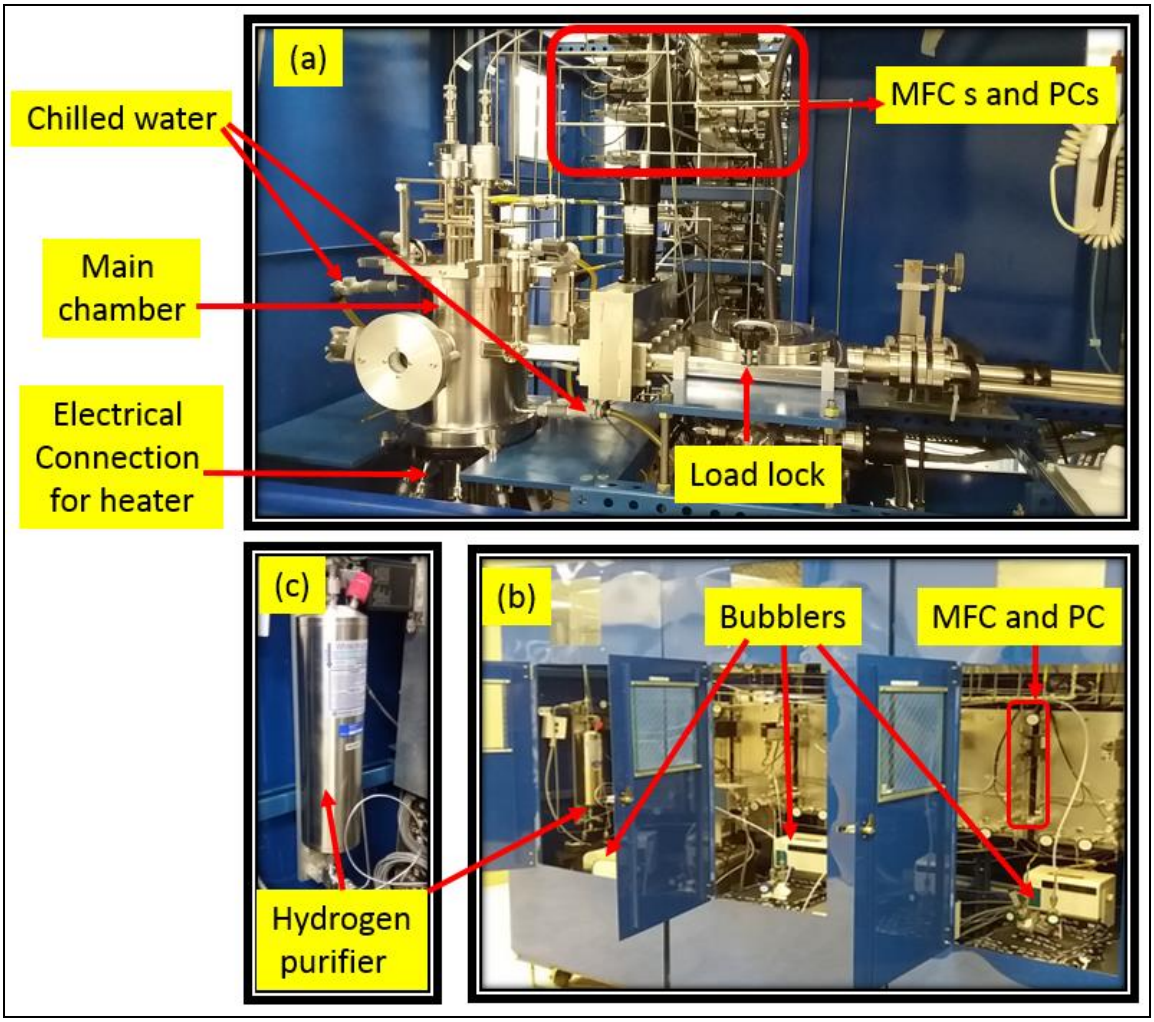

Figure 2. 4. Various parts of MOCVD reactor at Texas State University (a)Main deposition chamber, (b) Bubblers and associated MFC and PCs, (c) Magnified view of the hydrogen purifier.

The MOCVD reactor used for this dissertation research is shown in Fig. 2.4 which was donated by Nitronex corporation Inc. and was installed at Texas State University in 2014. As seen from the figure that the design is much complex than the simple design shown in Fig. 2.3. However, main components of the MOCVD as described before has been identified in the figure. The main chamber and LL is seen in Fig 2.4 (a) along with pyrometer, water lines and electrical feed through. The bubbler and purifiers are housed in a separate chamber as seen in 2.4 (b) and (c) and connected with the main chamber through

the run/vent manifold containing MFCs and PCs. Initially a Pd cell was used for hydrogen purification but later it was replaced by the purifier shown in Fig. 2.4 (c) because the PD cell was damaged. The ammonia and hydrogen gas cylinders are stored in a separate gas cabinet. Each gas storage unit has adequate safety system involving metallic case and exhaust system. There is a main pump and two other pumps connected with the reactor (no shown in figures).

Hydrogen is used as carrier gas and nitrogen is used for purging. Hydrogen, nitrogen, and ammonia are delivered in high pressure cylinders. All cylinders are connected to regulators that reduce the pressure from the cylinder pressure, which is 2400 psi for full hydrogen and nitrogen cylinders. From there the gases, with the exception of hydrogen, pass through chemical purifiers and a second set of regulators further reduces the pressure. All these gases are connected with the main chamber and exhaust through run/vent manifold.

The growth parameters for various nitride semiconductors are different in terms of V/III, Pressure and temperature. A process has been developed through previous research efforts to deposit AlGaN/GaN HEMT on Si using this reactor. The detailed growth parameters are described below:

To despite AlGaN/GaN HEMT, extremely high quality GaN crystal with very low defect density is necessary. To achieve such GaN on Si, growth starts with AlN followed by two transition layers of AlGaN alloy. Finally, a thick GaN buffer layer is deposited on top of which the AlGaN barrier layer is deposited. The process has been established for a Si (111) wafer due to its smaller lattice mismatch with hexagonal crystal of nitride semiconductor. After heating the substrate to ~1020 °C, first ammonia is turned on for few seconds for

nitridation of the Si. This nitridation is extremely important for nucleation of nitride semiconductor on Si surface[97]. Pressure for growing various layers are kept at 100 Torr. Around 420nm AlN nitride is deposited at ~1020 °C as the first layer using TMA and ammonia with a V/III value of 9433. The flow rate for TMA and NH_3 are 30.3 µmole/min and 0.295 mole/min respectively for this layer. This AlN layer has very high roughness and later a ~550nm thick transition layer (TL1) with composition $Al_{0.5}$ $Ga_{0.5}$ N is grown on top of it at ~1000 °C. The V/III value for TL1 is 5530 with TMG flow of 29.75 µmole/min, TMA flow of 23.5 µmole/min and 0.295 mole/min of NH_3. The second transition layer (TL2) with thickness of ~300nm and composition $Al_{0.25}$ $Ga_{0.75}$ N is grown at ~980 °C using V/III value of 4850. Corresponding TMG and TMA flow rates are 45.5 and 10.2 µmole/min with same amount of NH_3 used in TL1. GaN buffer layer is deposited at ~ 975 °C with three steps, by varying TMG flow while keeping the NH_3 flow constant. V/III for three GaN buffer layers are 1906, 1906 and 7880 respectively. The total thickness of the GaN buffer layer is ~800nm. The ~25nm $Al_{0.25}$ $Ga_{0.75}$ N barrier layer is deposited with vary small flow (TMG= 31.2 µmole/min, TMA=3.5 µmole/min and NH_3=0.07 mole/min) and V/III is 2011 at ~1000 °C. The ~3nm top GaN cap layer is deposited with TMG= 76.5 µmole/min, NH_3=0.29 mole/min and V/III=3815 in 6 seconds. It is important to note that the temperature reported here are based on pyrometer reading and may not be exactly accurate because pyrometer measured thickness based on reflectivity from surface which can be different when film thickens.

Growth of GaN on Si surface is similar to the process explained above with only exception that this wafer does not have barrier or GaN cap layer. 100mm wafers were used for every wafer and cross wafer uniformity in terms of thickness and surface roughness

was achieved for each run. For epitaxial lateral overgrowth of GaN on diamond masked GaN wafers, a systematic study involving variation of pressure, temperature and V/III were conducted. detail of the study will be presented in chapter 6 of this dissertation.

2.2 Selective deposition of diamond on various substrates

As proposed in previous chapter, selective deposition of CVD diamond on various substrate is the heart of this research. Selective diamond deposition requires selective seeding of nano diamond on substrate surface. Photolithography based selective deposition of CVD diamond was first reported by Masood et.al [77]. We repeated the process in the Texas State University cleanroom but did not achieve desired result at first few trials. The facilities and tools used for selective diamond seeding in the Nano fabrication Research Service Center (NRSC) at Texas State University is shown in Fig. 2.5 (a)-(d). After several failed attempts of selective seeding and growth, we modified the process in several steps for various types of substrates. Specifically, we developed and optimized selective deposition of CVD diamond on Si, SiO_2, SiN_x, AlN and GaN surface. SiN_x for this dissertation was deposited using a PECVD reactor as seen in Fig. 2.5(a). SiO_2 was deposited using thermal oxidation process in the NRSC. The modified selective seeding process is shown in Fig. 2(e) and is described for Si surface in following section.

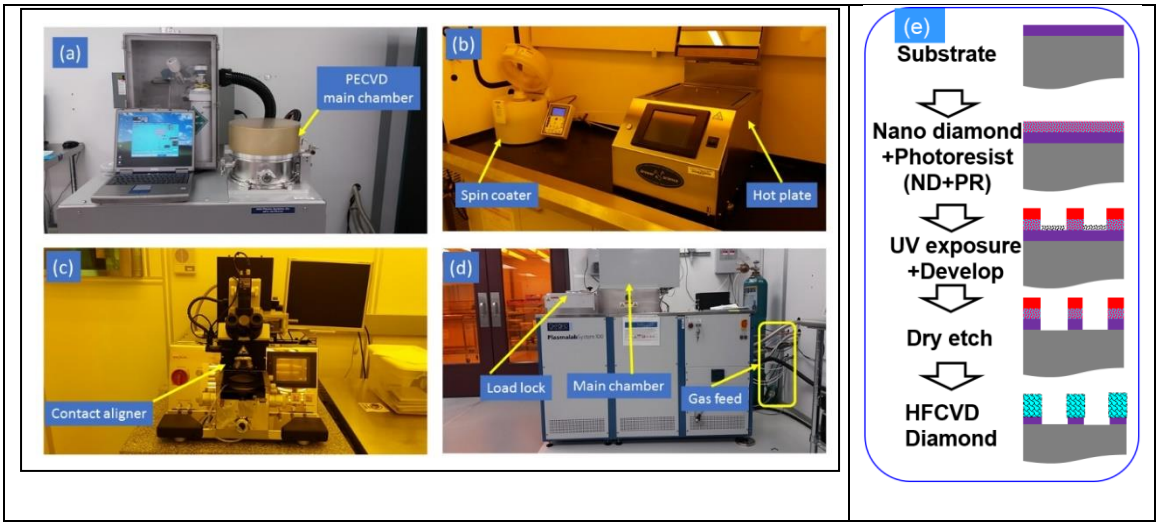

Figure 2. 5. Various tools and facilities inside NRSC of Texas State University used for selective seeding of nano diamond on substrates (a) Plasma enhanced PECVD (b) spin coater and hot plate for photolithography (c) SuSS Microtech contact aligned equipped with I -line sources and (d) Oxford Plasma lab System 100 reactive ion etcher and (e) is the process flow for selective seeding of nano-diamond seeds on any substrate.

Selective deposition of CVD diamond stripes on Si (100) wafer was started with patterning the wafer with nano diamond seeds using standard photolithography technique. After a series of trial and optimization of various parameters, the following seeding and growth was established. Dimethyl sulfoxide (DMSO) based nano diamond suspension (ND) with 5 wt% nano diamond seeds (seed size ~4nm and average aggregate size of 20 nm-30nm) was used as seed source which was mixed with photoresist S1813. A 5mL photoresist solution containing 2.5 mL of S1813, 2 mL of DMSO and 0.5 ml of ND was then sonicated in ultrasonic bath for 30 min. Energy provided by ultrasonic bath helps breaking the cluster of nano diamond seeds which is often much bigger than 20nm [46]. Since DMSO's freezing point is 18.5 °C, the solution was then pre-heated at 60 °C for 1 min to avoid any non-uniformity or striation effect during spin coating. Care should be taken in this step since heating at a higher temperature might crosslink the photoresist. It is important to note that the cleanroom temperature and humidity was always maintained at 18-23 ^{o}C and 65-

70% respectively since both parameters were found to be affecting the uniformity of photoresist dispersion on our wafer. The photoresist was then spun on the wafer and soft baked at 115°C for 90 seconds using a Laurel spin coater (Fig. 2.5 (b)) and a Brewer Science hot plate (Fig. 2.5 (b)). UV exposure was performed using a SUSS Microtech contact aligner shown in Fig. 2.5 (c). MIF 300 developer was used for developing the exposed wafer. At this stage, photoresist and majority of nano diamond seeds were cleared from the exposed regions. To get absolute selectivity and to clear any remaining seeds from the exposed regions, the wafer was then plasma etched in an Oxford Reactive Ion Etching (RIE) chamber (Fig. 2.5 (d)). RIE/ICP power was 150W/1500W and chamber pressure was 20mTorr. To etch any native oxide along with remaining seeds from exposed region, a mixture of 45 sccm of CF_4 and 5 sccm of O_2 was used as etching reagents [98]. The etch rate for SiO_2 using this chemistry was found to vary between 0.6nm/s to 1.5nm/s depending on deposition/growth technique of SiO_2. Since no oxide was intentionally deposited on the wafer, a 10 seconds Ar plasma breakthrough followed by another 10 seconds reactive ion etching with CF_4 and O_2 was sufficient to etch all the materials (residual nano diamond and native oxide). Fig. 2.6 (a) and (b) show the effect of RIE on clearing remaining seeds from exposed region after developing.

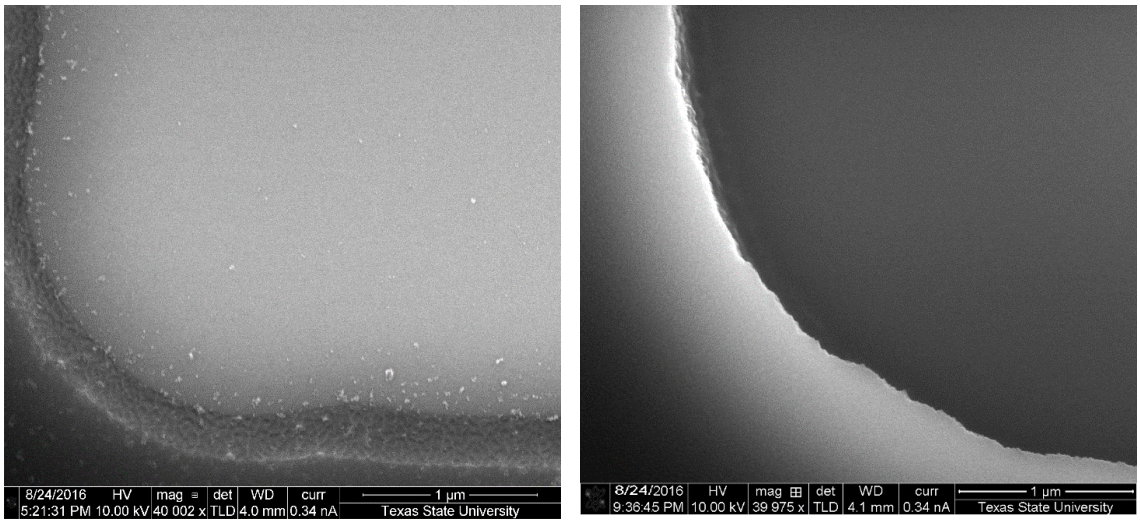

(a) (b)

Figure 2. 6. Effect of RIE on clearing any remaining seeds from UV exposed and developed regions (a) before RIE (b) after RIE .

The selective seeding process was straight forwards for Si and SiO_2 but showed significant problem when other surfaces such as SiN_x and Nitride semiconductors were used. The photoresist dispersion was badly hampered and non-uniformity and poor coverage of photoresist was observed on the wafer. To solve this problem, the seeding process was modified. Initially, a thin layer of ND containing photoresist layer was spun on the surface using the same dilution described before. The solution was heated at 115°C for 150 seconds before dispensing on the wafer and then spun at relatively lower speed (2500rpm) for 25 seconds. The heating of solution resulted in better uniformity of the resist layer but showed another problem. The layer of photoresist was ~500nm thin and too low for UV exposure. The smallest possible dose time of UV exposure with our contact aligner was 0.1 second and the ~500nm layer was completely overexposed with this exposure. To solve this problem, we then deposited a thick layer of photoresist on top the ~500nm ND containing resist layer. This time exposure and develop was successful. Reactive ion etching and

diamond deposition parameters were varied depending on type of film. It is worth mentioning that a customized photolithography mask was designed for the selective deposition of CVD diamond on various substrate with a minimum feature ~1µm to observe the smallest diamond feature that we can deposit using the selective deposition technique. Fig. 2.7(a) shows the layout of the mask designed using KLayout software. Fig. 2.7(b) shows magnified view of a panel of 10 µm sized features on the mask and Fig.2.7 (c) shows SEM image of diamond film deposited using the newly designed mask. A focused discussion on selective seeding and deposition of diamond on Si, SiN_x, GaN and AlGaN layer will be presented in chapter 4 and 5 of this dissertation. In addition, the details of the selective seeding, PECVD SiNx deposition and etching parameters are presented in appendix section of this dissertation.

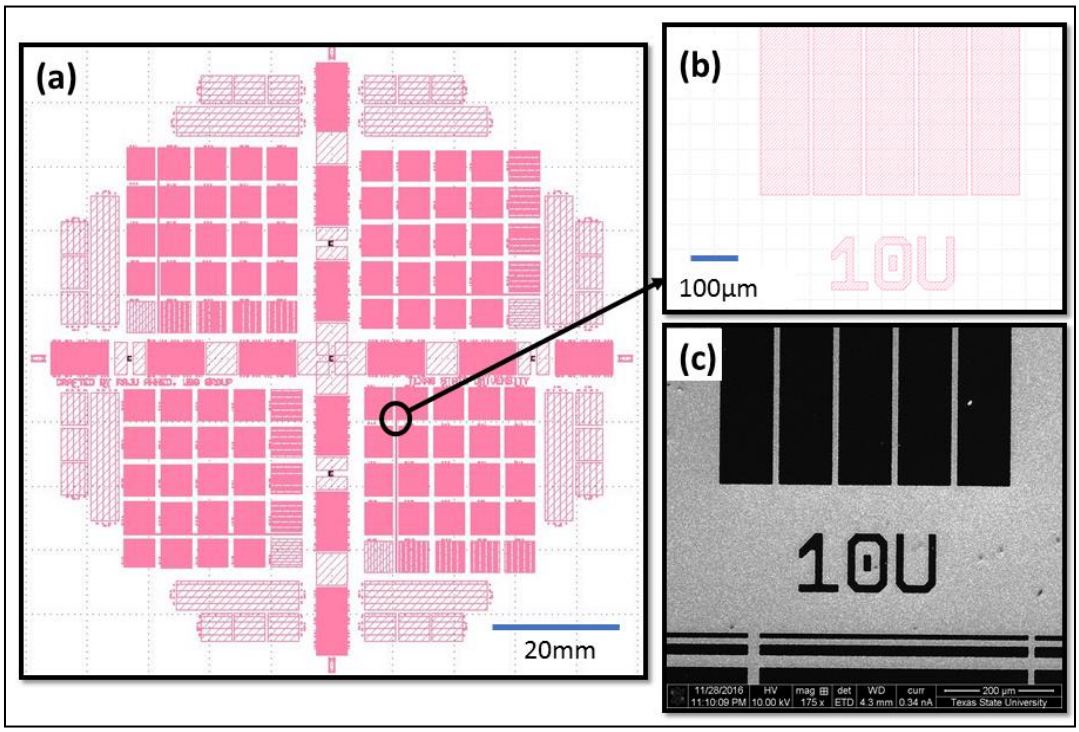

Figure 2. 7. (a) Layout of photolithography mask designed using Klayout for selective seeding of nano diamond, (b) magnified view of a region with 10µm diamond stripes and (c) plane view SEM image of the region with diamond feature same as (b) after selective seeding and diamond deposition.

2.3 Characterization techniques

The diamond films and GaN films deposited during this research were characterized using several morphological and structural characterization tools. A brief discussion on each of the tools are presented in following section.

2.3.1 Scanning electron microscopy

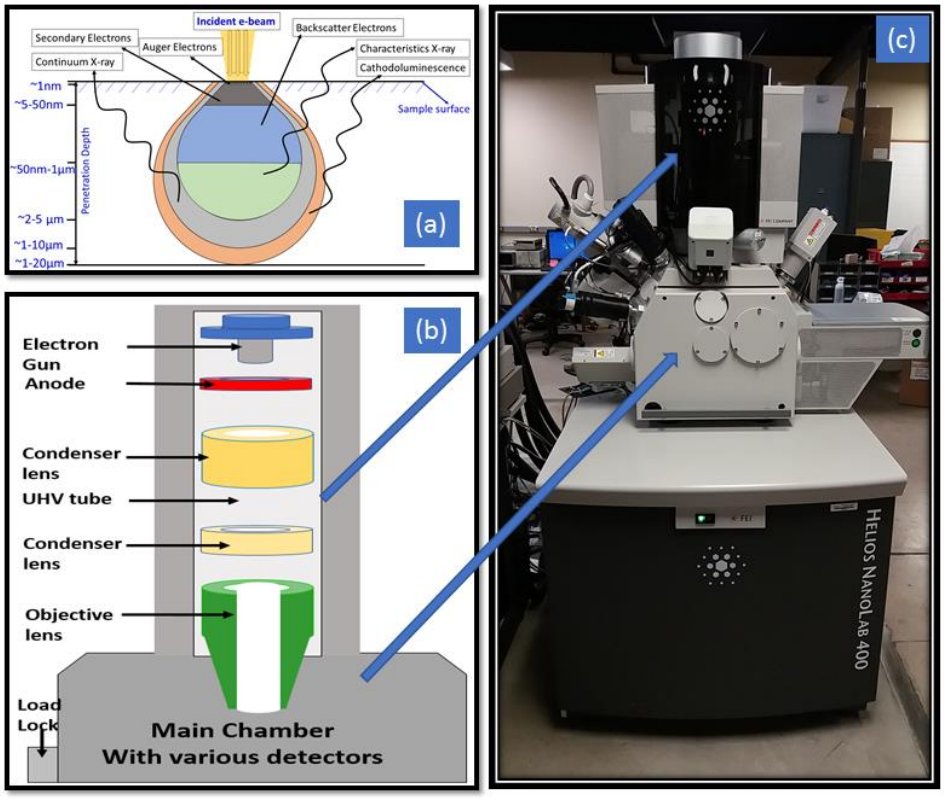

Figure 2. 8. (a) Schematic view of interaction volume of incident electron on a sample surface with penetration depths (b) Schematic view of an SEM chamber and (c) FEI HELIOS NanoLab SEM at Texas State University.

Scanning electron microscope (SEM) is a versatile characterization tool that permits the observation and analysis of heterogeneous organic and inorganic materials on a micro meter to nanometer scale[99]. Although SEM is primarily used for imaging, it has a wide range of application in other microanalyses. In SEM, the area to be micro analyzed is

irradiates with a finely focus electron beam which maybe swept in a raster across the surface or static. Due to the interaction of the electron with the specimen surface, various types of signals may come out from various depth of the material such as secondary electron, backscatter electron, characteristics X-ray and other photons of various energy. Fig. 2.8(a) shows such an interaction volume of the electron beam and various signals that comes out from various depths. In modern day SEM, there are dedicated detectors to detect each of these signals. These signals are obtained from a specific location of a sample and are used to examine many characteristics of the sample i.e. topography, crystallography, composition etc.

Fig. 2.8 (b) shows the schematic of a SEM system and Fig. 2.8 (c) shows the FEI HELIOS NanoLab SEM at Texas State University. The imaging signals in SEM mainly come from low energy secondary electron and backscattered electron since they vary primarily because of topographical changes. Two dedicated detectors namely Everhart-Thornley detector (ETD) and through the lens (TLD) are mainly used for topographical imaging and they can detect both secondary electrons (SEs) and backscattered electrons (BSEs). Usually, for lower resolution imaging in field free mode, the ETD is employed. For high resolution imaging TLD is always used in immersion mode of the SEM. The images produced by detecting SEs provide valuable information about the topography of the sample whereas image produced by detecting BSEs give much more information about the composition of the sample. Each of the detector has its own application in specific samples. Some advanced detecting option such as solid-state detector (vCD), down hole visibility are also available in SEM to image at low accelerating voltage.

The electron beam used in SEM can be generated either by a field emission or a thermionic

emission. In case of field emission, electrons are generated by placing a pointed cold cathode filament in a high potential electric field, which makes ejection of electrons away from the filament and directs them toward the sample. For thermionic emission, a very strong current is passed through a conducting filament. This current generates a beam of electrons which are directed toward the sample surface because of an anode placed right in front of electron gun as shown in Fig. 2.8(b). It is important to note that regardless of the method of generation, the electron beam must be created under a high vacuum to collimate the beam and prevent premature electron scattering[100]. The beam is then directed towards sample through a column of "electromagnetic lenses" as shown in Fig. 2.8(b). These lenses are basically electromagnetic coils which collimates, condenses and focus the beam of electrons on the sample surface. In addition to these coils, another pair of scanning coils can deflect the electron beam which enables raster scanning of electrons on sample for two-dimensional imaging. Since the SEM chamber works at UHV ($<10^{-6}$torr), a lower beam energy can reduce the image artifacts by reducing sample damage and charging effects. With the SEM shown in FIG. 2.8 (c), with electron beam energy as low as 1.5kV is capable of yielding operation resolution down to 1nm given that any insulating sample is properly grounded[101]. In addition to the general imaging, this SEM is equipped with Energy dispersive X-ray (EDX) capability. Electron beam deposition, Electron beam lithography, focus ion beam (FIB) are some of its other capabilities. This SEM was the primary tool for the characterization of deposited diamond and GaN films. In addition, FIB cross section of the deposited films were also performed using this tool.

2.3.2 X-ray diffraction

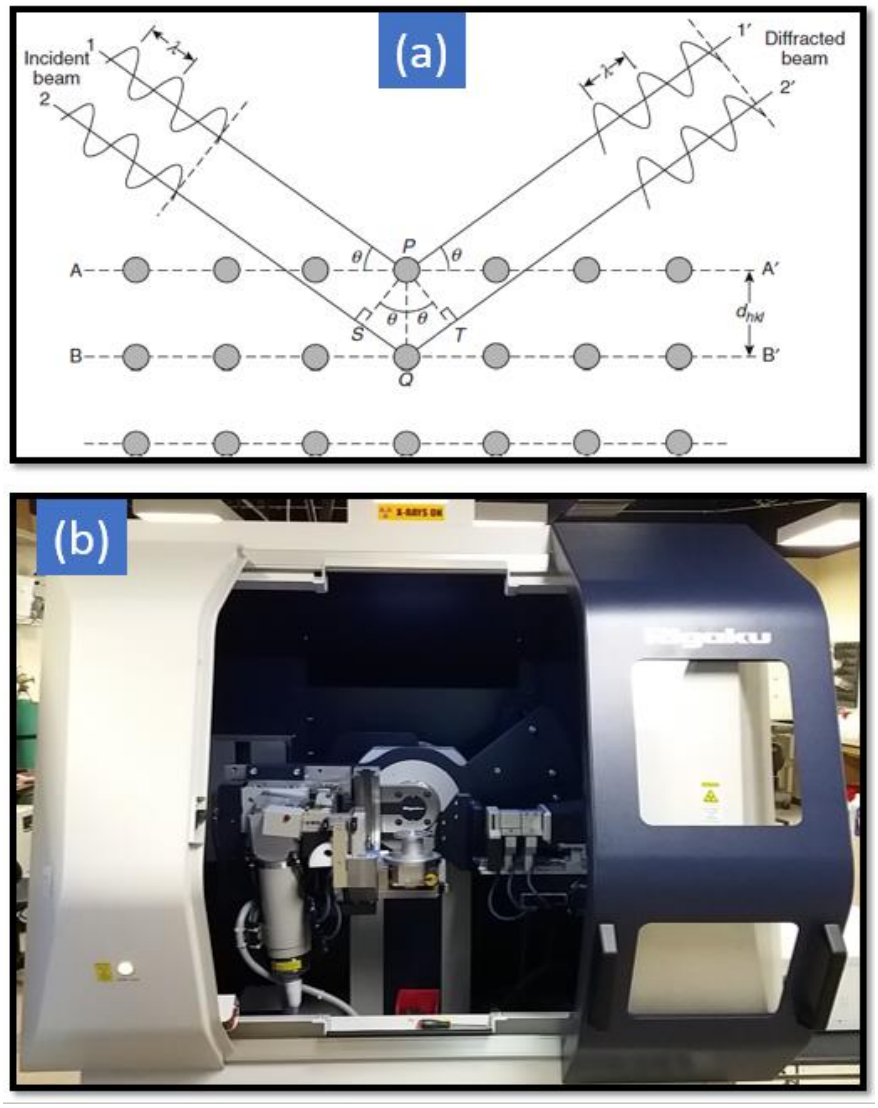

Figure 2. 9. (a) Schematic representation of Bragg's law where λ is x-ray wavelength, n is an integer, θ is the incident angle and d_{hkl} is the lattice spacing of the (hkl) crystal plane[102] and (b) Rigaku SmartLab XRD system at Texas State University.

One of the most fundamental studies used to characterize the structure and composition of materials is X-ray diffraction. This technique uses the principle that waves interacting with atomic planes in a material will exhibit the phenomenon of diffraction. A schematic of the diffraction process is shown in Fig. 2.5 (a). X-rays incident on a sample are scattered off at an

equal angle. At certain angles of incidence, x-rays scattering off of neighboring parallel planes of atoms will interfere destructively. At other angles, these waves will interfere constructively and will result in a large output signal at those angles. The XRD technique is based on Bragg's principle[103]. Bragg reflection is a coherent elastic scattering in which the energy of the X-ray is not changed on reflection. If a beam of monochromatic radiation of wavelength λ is incident on a periodic crystal plane at an angle θ and is diffracted at the same angle as shown in Fig. 2.9(a), the Bragg diffraction condition for X-rays is given by given by,

$$2dSin\theta = n\lambda \tag{2.5}$$

Where *d* is the distance between crystal planes and *n* is the positive integer which represents the order of reflection. Equation (2.5) is known as Bragg law. This Bragg law suggests that the diffraction is only possible when $\lambda \leq 2d$[104]. The X-ray spectrum for any material is plotted as x-ray intensity versus 2θ graph. The obtained spectrum is analyzed by comparing with the x-ray crystallographic library or database to obtain the orientation and composition of the layers in the grown structure. The lattice constants and many other structural properties such as crystal quality, strain, defect etc. can be accurately evaluated using the XRD. To study the structural properties of the films deposited during this dissertation research a Rigaku SmartLab XRD system was employed as shown in in Fig. 2.9 (b). The wavelength used for the measurements was Cu K_α, λ = 1.5418 Å and the x-ray tube operates at 40 kV and 44 mA.

In addition to standard θ/2θ scan, several other types of scans were employed to study the diamond and Nitride semiconductors. To study the quality of crystal and defect in crystal, a rocking curve (ω scan of a specific plane) was performed. An extended rocking curve between 2θ =33.5° and 37° of AlGaN/GaN revealed the (0002) planes of these materials which was often used as quick determination of crystal quality. To observe thin AlGaN barrier layer, reciprocal space mapping or a coupled ω/2θ scan around an

asymmetric plane (114) was performed. A reciprocal space map reveals the distribution of the lattice parameter, associated with this peak, along these directions. It can be used to visualize strain distributions in thin films. To study any preferential orientation in polycrystalline diamond films, pole figure analysis was also performed. Pole figure analysis was performed by around any specific brag plane by varying the rotation of the sample stage (φ scan) between 0° and 360° for each tilt angle χ between 0° and 90°.

2.3.3 Atomic force microscopy

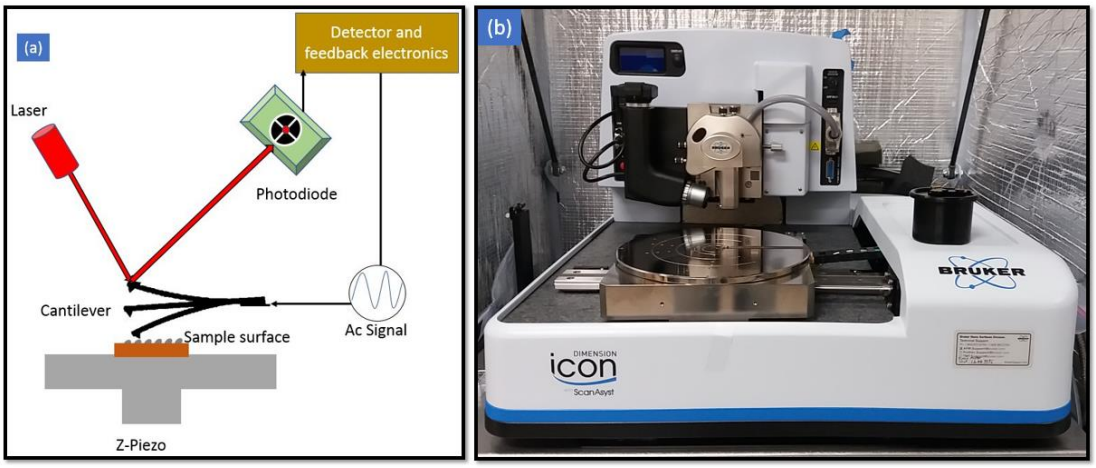

Figure 2. 10. (a) Schematic diagram of an AFM system (b) The Bruker dimension ICON AFM at Texas State University.

Atomic force microscopy (AFM) is one of the most common scanning probe metrology techniques that allows atomic scale topological imaging of surfaces. The simplest mode of AFM is the physical profile mode as shown in Fig. 2.10 (a) where an atomic scale stylus (tip) is either dragged along a surface, giving rise to the topography of the surface or the tip only briefly touches the surfaces and then retracts. The working principle of AFM is based on atomic interaction (attraction or repulsion) of a sharp tip and sample surface[105], [106]. Vertical deflection of cantilever takes place due to weak interaction force (Van der

Waals force) when tip is very closed to the sample surface[102]. A laser beam pointing on the tip is reflected back to the photodiode and the feedback resulting from these small forces (order of nano-Newton) returns a map of the surface where topological variation as small as single atoms can be resolved[102][106][107].

The AFM used for this dissertation was Bruker dimension ICON as shown in Fig. 2.1(b). Most of the measurements were performed in tapping mode and scan assist mode. Various parameters can be controlled before and during AFM measurement. The most important parameters affecting quality of AFM imaging are the feedback parameters: amplitude set point, and proportional/integral gains. The gain parameters determine the sensitivity of control over the surface features. For example, high gain parameters result in high noise. These parameters were varied in order to maximize the agreement between the trace and retrace lines. The lines must directly overlap as much as possible and all the parameters are considered only when the lines are overlapped. Besides, cantilever tuning is another important factor that affects the measurement accuracy. However, the scan assist mode of the ICON AFM was very robust in terms of optimization. In this mode, no parameter except the spring constant and peak force are required any change. These parameters too are automatically optimized resulting in AFM faster imaging. Most important parameter obtained from an AFM image is the root mean square roughness given by[107],

$$R_q = \sqrt{\frac{1}{L}\int_0^L |Z^2(x)|dx} \tag{2.5}$$

where, Z(x) is the function that describe the surface profile analyzed in terms of height (Z) and position (x) over the evaluation length L. In addition to RMS roughness, AFM has

sveral other applications such as determining defect in Nitride semiconductor, measuring small step height on sample surface etc.

2.3.4 Surface Profilometer

Figure 2. 11. The DektakXT stylus profilometer of ARSC at Texas State University.

Surface profilometry is performed by moving a diamond tipped stylus over the sample surface, with this technique the tip and the sample surface are in direct contact with each other [108]. Electromechanical signals control the vertical and lateral position of the stylus based on parameters set by the user such as; scan length, distance, speed, and stylus contact force. The stylus is linked up to a Linear Variable Differential Transformer (LDVT), which produces and processes electrical signals that correspond to topological variations of the sample. Small surface variations in the vertical displacement of the stylus can be detected. After being converted to digital format, these surface variations are stored for display and

analysis. Surface profilometers have some distinct advantages over AFM, however AFM resolution is still superior. A DektakXT Stylus Profilometer from Bruker as shown in Fig. 2.11 was used in this research to obtain thickness of samples. For hard to soft surface measurements, the stylus force can vary between 1 mg to 15 mg.

2.3.5 Raman spectroscopy

Raman scattering is an inelastic light scattering process that involves absorption of incident high intensity laser light by a polarizable sample and causes a transition from the ground electronic state to an excited or virtual state. The energetic system then goes through a radiative relaxation via a transition from the virtual state to a lower energy electronic state by spontaneous emission of a photon and either creating (Stokes process) or absorbing (anti-Stokes process) a vibrational quantum of energy (a phonon in crystals)[109]. The emitted photon has a shifted energy from the incident excitation photon energy ($h\omega_L$) by the phonon energy. In conventional Raman spectroscopy, only Stokes processes are studied because of their higher intensities. The Raman spectra of intensity versus emission photon energy exhibits peaks at energy $E_s=h\omega_s$ which corresponds to the vibrational energies involved in the process[49]. Note that in Raman spectroscopy, change in vibration energy is written as inverse of wavelength as $1/\lambda$ (cm^{-1}) $=\Delta E/hc$ where $\Delta E= h\omega_L- h\omega_s$. Not all the vibration gives Raman peak. This is dictated by Raman selection rule [49].

The Raman selection rule can be derived from the kinematics of inelastic light scattering determined by conservation of energy and momentum. The energy and momentum conservations are given by[110],

$$\hbar\omega = \hbar\omega_1 - \hbar\omega_2 \tag{2.6}$$

$$\boldsymbol{k} = \vec{q} = \overrightarrow{k_1} - \overrightarrow{k_2} \tag{2.7}$$

$\hbar\omega$ and $\hbar k$ represents energy and momentum where ω and k are frequency and wave vector of crystal excitation. Since equation (2.7) is a vector sum, the magnitude of **k** depends on direction of scattering. For forward scattering, the value is minimum. For first order inelastic scattering such as Raman scattering, the difference in wave vectors $\mathbf{k_1}$ and $\mathbf{k_2}$ is small and the range of **q** is very small. This is only possible at the zone center of the first Brillouin zone. Thus, a Raman scattering will only take place if the optical vibration is zone centered or $\boldsymbol{k}$=0. A complete version of equation (2) can be given by[110],

$$\boldsymbol{k} = \vec{q} = \overrightarrow{k_1} - \overrightarrow{k_2} + \vec{K} \tag{2.8}$$

Where, K is the reciprocal space vector or the separation between zone centers. That means a Raman scattering will take place when the difference between the wave vectors of two excitations is very small and they are close to zone center so that the momentum is conserved. It is important to note that, the zone center optic vibration refers to those which retain the full symmetry of the crystal and have having non-zero energy at the zone center[49].

Raman spectroscopy is a powerful diagnostic tool for the evaluation of chemical vapor deposited (CVD) diamond films[111] and Nitride semiconductors[112]. This technique can be used to asses a number of properties such as stress, crystallite perfection, phase purity, crystallite size and thermal conductivity etc. of diamond films. It is evident from the discussion in previous chapter that CVD diamond film is polycrystalline by nature and are subject to a number of imperfections compared to single crystal diamond. An ideal cubic diamond has a single Raman-active first order phonon mode at the center of the

Brillouin zone[113]. The sharp Raman lines can be used to recognize cubic diamond against a background of graphitic carbon and also to characterize the graphitic carbon. The volume of non-diamond carbon can be given by[114]

$$f_{DC(D)} = \frac{V_{DC}}{V_{DC} + V_D} = A\frac{I_{DC}}{I_{DC} + I_D} \tag{2.9}$$

Where f_{DC} is the volume fraction of non-diamond carbon or disordered carbon (DC), I is the intensity and A is a constant having value of 1.13 for polycrystalline CVD diamond[114]. Usually, the volume fraction f_{DC} is calculated as percentage. The small shift in the peak wave number have been related to the stress state of deposited films[113]. Several researchers have reported various equation for the stress measurements[111]. It is important to note that the biaxial stress depends on the orientation of the polycrystalline diamond. According to Prawer et. al.[111] the biaxial stress can be given by,

$$\sigma_{xx(GPa)} = k\Delta\omega \tag{2.10}$$

where, $\Delta\omega$ represents the diamond peak shift from single crystalline diamond peak ω_o and k is the Raman stress factor. Interestingly, stress in Nitride semiconductors can also be measured using equation (2.10). The full width at half maxima (FWHM) of the Raman peak varies with mode of preparation of the diamond and has been related to degree of structural order. The peak broadening can also be used to extract the residual stress on the film. The intensity ratio of the diamond peak and non-diamond peak gives important information about the phase purity of the deposited film[115].

2.3.5.a. Ultra violet Micro Raman spectroscopy

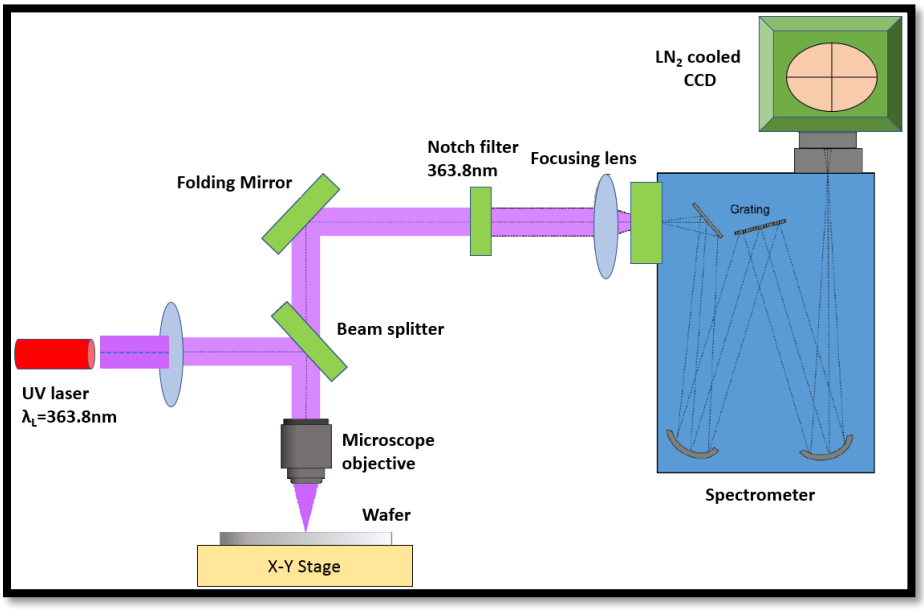

Figure 2. 12. Schematic diagram of the UV Raman set-up at the optical characterization laboratory, Texas State University (adopted form[116] and then modified).

Schematic diagram of a typical setup for UV Raman spectroscopy is shown in Fig. 2.12. Laser excitation and collection of Raman signals are accomplished by using objective, beam splitter and notch filters. In a back scatter geometry, laser excites the sample surface and generate Raman signal along with reflected laser signals. The holographic notch filter in front of the spectrometer excludes unwanted signal coming from the laser and allows only Raman signals. The collected Raman signal then enters the spectrometer where it is dispersed by a diffraction grating and directed toward the exit slit at a specific wavelength closed to the laser wavelength. The signal detection is accomplished by a combination of photo multiplier tube and charge-coupled device (CCD) array detectors. The CCD was liquid nitrogen cooled during all measurements.

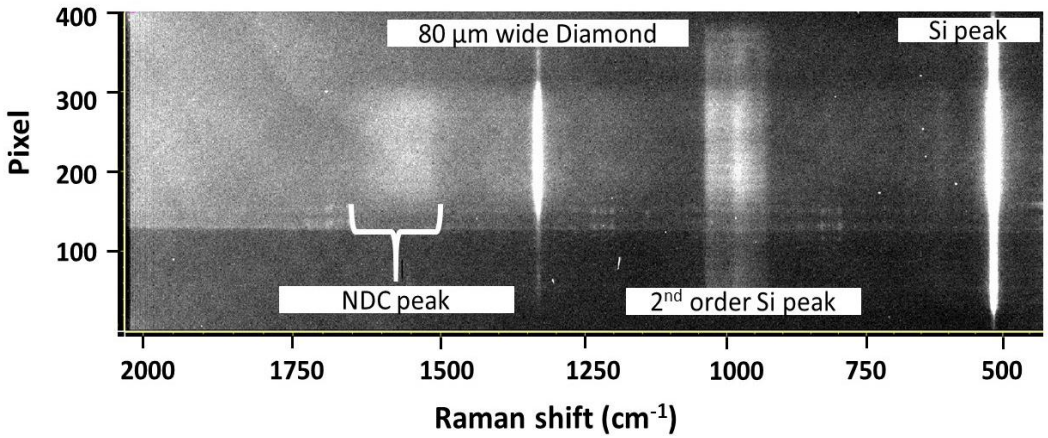

Figure 2. 13. Raman spectra collected in hyperspectral image mode from an 80µm wide Diamond stripe on Si.

The UV Raman system in the Optical characterization lab of Texas State University was modified to obtain Raman signal using a laser line instead of laser beam. In this mode, a laser line beam is used for excitation instead of a point and one spectrum is collected for each pixel[117]. The laser excitation for the micro Raman system used for characterizing present samples was 363.8nm excitation from an argon-ion laser focused on the sample through a Powell lens. The Powell lens can be visualized as a prism with a small radius at one edge, which operates as a cylinder lens with radius of curvature decreasing from center to edge. Due to such a geometry, a monotonic decrease in divergence takes place from center to edge of the lens resulting in a nearly uniform intensity along its length. The non-uniformity in beam intensity along the line can be less than 10% [118]. Powell lens converts the point beam into a laser line and Raman measurement were carried out using a 10× objective for a nominal line size of ~192µm. This laser line corresponds to 400 pixels in the charged coupled device (CCD) detector and each pixel corresponds to one Raman spectra. The Raman system was calibrated at the beginning of the measurement with a neon lamp.

Raman spectra collection from a reference Si wafer and diamond anvil cell were performed at the beginning and at the end of each measurement session to observe any change in Raman shift and there by verifying measurement accuracy. In addition, for each measured sample, a new wavenumber calibration was made using the reference Si wafer and diamond anvil cell with Raman shift of 520 cm^{-1} and 1332 cm^{-1} respectively. The laser power for the UV excitation was ~ 35μW and laser heating was negligible when focused on a 192 μm line[119]. However, acquisition time for Raman spectra collection were varied from 60 to 600 seconds to see any effect of laser heating on shape and position of Si and diamond peak position and no variation was observed. Since, thickness of the deposited diamond was small, a 600 seconds acquisition time was used for collecting Raman spectra. Ultraviolet laser was used for the current research for two reasons. The first one is small background from diamond which allows simultaneous observation of Si (520 cm^{-1}), Diamond (1332cm^{-1}) and NDC peaks (1500-1600 cm^{-1})[120]. The second reason is related to stress measurement for Si. Since the goal of the research was to measure stress on Si near the Diamond-Si interface, ultraviolet laser is a superior choice because its penetration depth is around 10-15nm in Si[121]. The Raman spectra collection was performed in image mode and the software (Winspec) generated a 400×1340 pixels image which covered the at least 192 μm in spatial space and relative Raman shift between 400 cm^{-1} and 2000 cm^{-1}. Fig. 2.13 shows typical Raman spectra in image mode for capturing relative Raman shift across an 80 μm wide diamond stripe grown on Si. To increase signal to noise ratio of spectra collected in hyperspectral mode, a pixel binning was performed. As a result, the signal to noise ratio increased and the spatial resolution for each spectra were increase to ~2μm. The five-pixel binned spectra were then converted into ASCII file which was

then used for fitting individual peaks for Si, diamond and NDC. Lorentzian peak fitting was performed for all spectra across a diamond stripe and peak position, width and intensity were recorded for them. The error of evaluating the centerline frequency was estimated to be ±0.1 cm^{-1} which corresponds to very small stress for both diamond and Si. Later, stress calculations were performed for Si and diamond across the diamond stripe. Stress evaluation of Si or diamond using Raman spectroscopy is performed based on frequency change of optical phonons due to applied strain. Detail explanation on stress dependence of Raman mode for Si and Diamond will be discussed in results and discussion section.

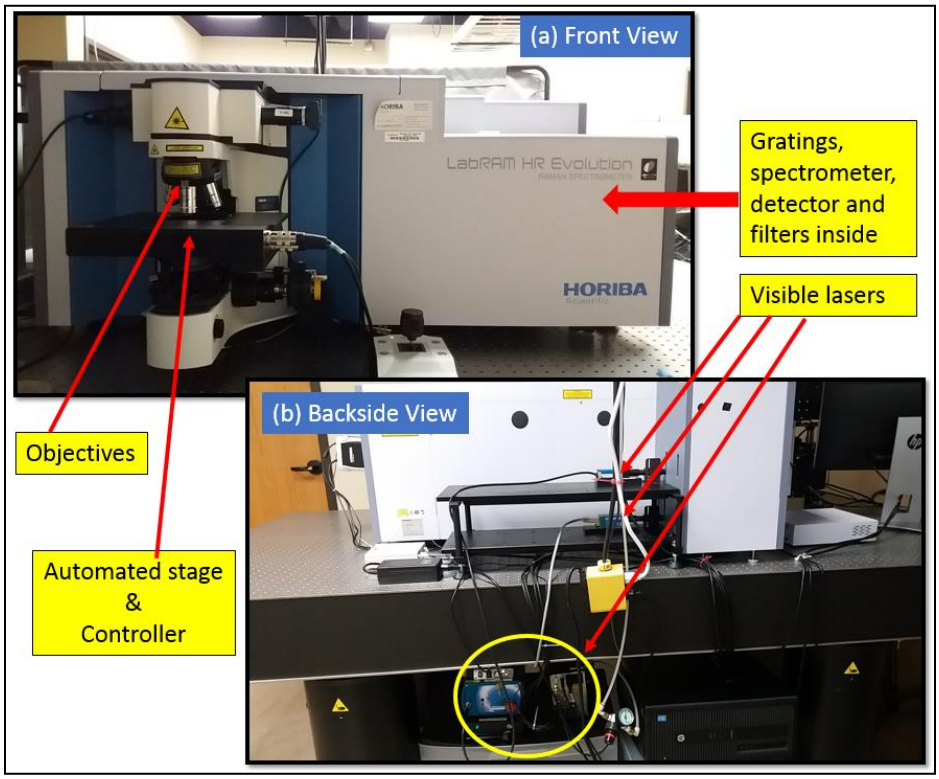

Figure 2. 14. The LabRAM HR evolution visible Raman system (HORIBA scientific) of ARSC at Texas State University (a) front side view showing objective and x-y stage and (b) backside showing various visible wavelength laser assembly.

2.3.5.b. Visible Micro Raman spectroscopy

In addition to the UV Raman setup described before, a visible Raman system from

HORIBA scientific (LabRAM HR Evolution) was also used for this dissertation. Fig. 2.14 shows the image of the visible Raman system at Texas State University. The visible system works in the same principle as UV with only difference in laser wavelength. For visible Raman measurements, 532nm laser excitation was used for specific reason. Visible lasers are better for nitride semiconductors because of low background compared to UV lasers[112].

2.4 Finite element simulation of thermal stress

Finite element analysis of thermal stress was performed by simulating an appropriate model (2D and 3D) created using structural mechanics module of COMSOL Multiphysics 5.3a. The model assumes that a thin layer of material (CVD Diamond) is deposited on substrate (Si) at a temperature of 750^{o}C (CVD diamond deposition temperature). At this temperature both the epitaxial film and the substrate are stress-free. The temperature of the system is then reduced to 20 °C (room temperature), which induces thermal stresses in the film/substrate assembly. The FEM simulation for stress was performed in a continuum model approach based on solving Hooke's law, given by,

$$\sigma_{ij} = D\left(\varepsilon_{ij} - \varepsilon_{ij}^{th} - \varepsilon_{ij}^{o}\right) + \sigma_{ij}^{o} \tag{2.11}$$

with thermal strain,

$$\varepsilon_{ij}^{th} = \alpha_{ij}\left(T - T_{ref}\right) \tag{2.12}$$

where, ε_{ij}, σ_{ij} and α_{ij} are the components of strain, stress and coefficient of thermal expansion tensors respectively, D is the elasticity matrix in a linear approximation and independent of ε_{ij}, and T_{ref} is the reference temperature at which the thermal stress is zero (for our case, it was room temperature or 20^{o}C). For an isotropic approximation, the D matrix in Eq. (1) is independent of thermal strain and can be derived from only two

quantities, the Young modulus and the Poisson ratio[122]. In our simulation, we used plane strain approximation in the solid mechanics interface where the materials are restrained from moving in the z direction. The assumption is then that the z-component of the strain is zero. Models were created and stresses were simulated for various width of the epitaxial diamond film with nominal thickness 1.5µm (same as our grown sample). Model was created for a continuous film on the full thickness of Si substrate (500µm) and the computational domain was extended from edge to edge of Si wafer. The fixed constraint was placed at the bottom edge of Si wafer and prescribed displacement was always in horizontal axis (x-y plane). The fixed constraint points at the bottom left corner acted like a fixed-in-space point, while all other boundaries were left free for a fictitious deformation (the grid itself was not deforming). Since we tried to see the stress at 10nm in Si, extremely fine mesh was build where the grid size was 1nm. However, we used a laser line of length ~192µm corresponding to 400 pixels, therefore many grids were covered by a single pixel or Raman spot (~480nm).

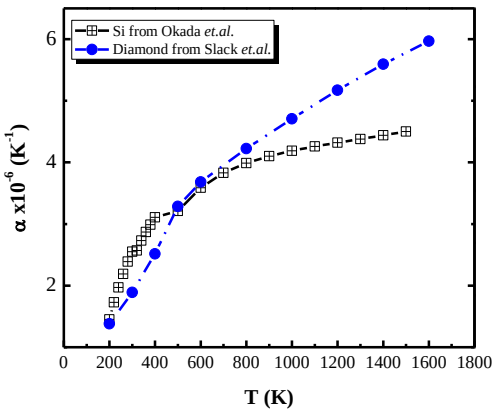

Figure 2. 15. Temperature dependent thermal expansion coefficient of Si (adopted from Okada *et.al.* [123]) and CVD diamond (adopted from Slack *et.al.*[124]) used in the FEM simulation.

Thermal stress simulation was performed using structural mechanic module of COMSOL

assuming that thermal stress is formed instantaneously when the heated sample is cooled down to room temperature rapidly. As a result, the software calculates the mechanical stress at an instantaneous temperature drop without the need to solve heat transfer. Although the software assumes that the coefficient of thermal expansion (CTE) is constant for these temperature drop, CTE values for Si and Diamond are extremely temperature dependent[122]–[124] as shown in Fig. 2.. Besides, the difference in CTE between Si and diamond as shown in Fig. 4 is relatively low at the deposition temperature. Due to this reason, Jirásek *et al.*[122] used the integral mean value incorporating the temperature dependence of CTE for diamond and Si in their model. However, in our model, due to availability of the option, instead of using a constant value of CTE, an interpolation function (of temperature) generated by literature suggested values as shown in Fig.2.15 was used as the value of CTE for Si and diamond. This approach is more appropriate because the reliability of the simulation results is highly dependent on the reliability of the CTE data. In addition, CTE of CVD diamond is highly dependent on film quality and morphology of CVD diamond. Qadri *et.al*. [125] reported that CTE of CVD diamond is higher than single crystal diamond depending on level on NDC in diamond. Due to this fact, we have used a relatively higher value for CTE of CVD diamond reported by Slack *et. al.* [124] as shown in Fig.4. Young modulus of CVD diamond has strong dependence on growth techniques and growth chemistry and a wide range of values have been reported by various groups. To study the sensitivity, we varied young's modules between $9x10^{11}$ Pa to$1.2x10^{12}$ Pa but no significant change in stress was observed. We created our model by using reported value of density, Poisson's ratio and Young's modulus of CVD diamond as reported by Hess *et.al* [126] but these values were optimized for best fit with experimental

values later. The optimized values of density, Poisson's ratio and Youngs modulus of CVD diamond were found to be 3500 kg/m^3, 0.1 and 1.05x10^{12} Pa respectively. For Si, temperature dependent CTE were published by many groups but Okada *et.al* [123] (shown in Fig. 4) had shown a validation of their finding by comparing it with a calculation based result. We therefore, used this result as an interpolation function for CTE of Si in the model. It is important to note that calculation of thermal strain should be performed only along the prevailing direction of strain which in our case is along (110) for a Si (100) wafer. Therefore, young's modulus of Si for only (110) direction has been used in the model as suggested by Hopcroft *et.al.*[127]. Since we used single crystalline Si, we used 2329 kg/m^3, 0.28 and 1.7x10^{11} Pa as density, Poisson's ratio and Young's modulus respectively for Si as reported in[128].

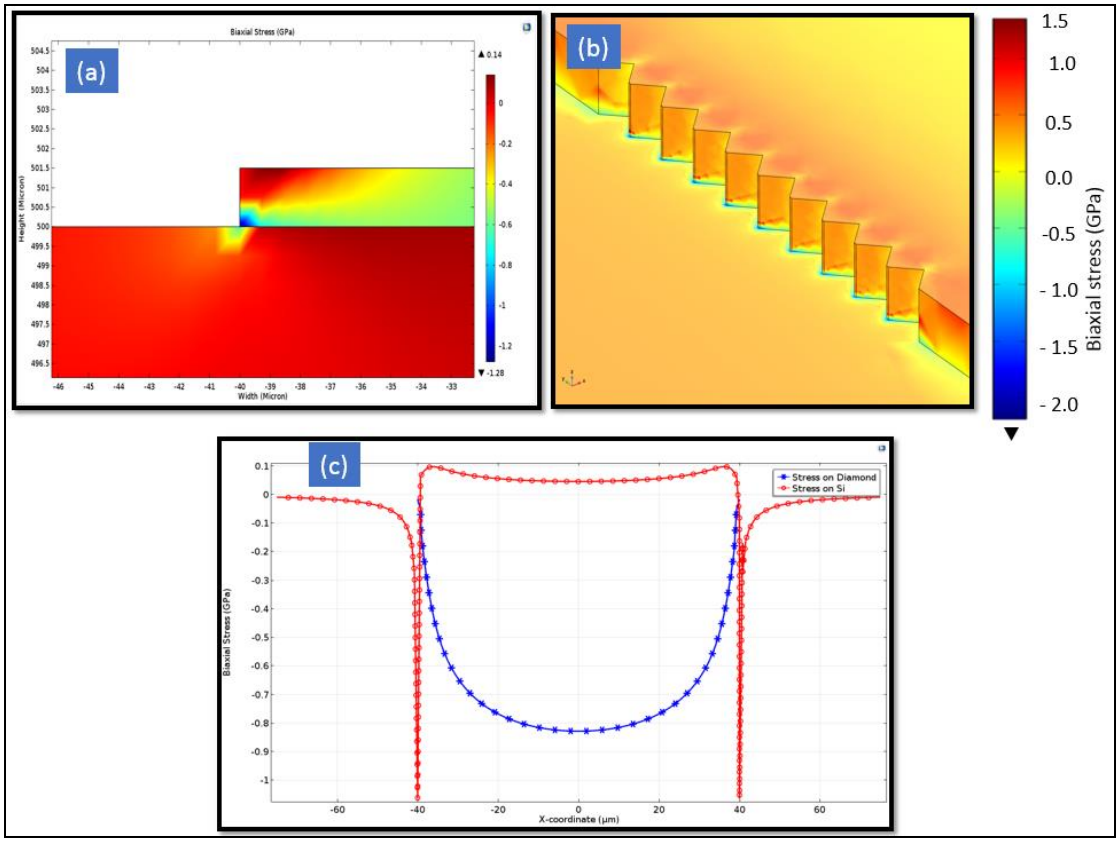

Figure 2. 16. Biaxial thermal stress simulation results of a diamond stripe grown on Si using COMSOL 5.2. (a) Stress distribution at the edge of diamond stripe simulated using 2D model (b) Corresponding 3D simulation result for a structure with ragged edge and (c) 1D representation of thermal stress in diamond (blue) and at ~10nm inside Si obtained using a 1D cutline at select depths from (a).

Fig. 2.16 (a) and (b) depicts the of biaxial stress distribution in diamond and Si simulated for a 1.5µm thick and 80 µm wide diamond stripe grown on Si in 2D and 3D respectively. In Fig. 2.16(b), both compressive (negative) and tensile (positive) biaxial stress can be seen in the silicon substrate as well as in the diamond film. In 3D model, the edge of the stripe was intentionally made ragged to mimic the actual diamond feature which has very ragged edge. To observe actual stress profile, two horizontal cut lines were taken inside diamond and at ~10nm inside Si respectively. 1D stress profiles along these two cut lines are shown in Fig. 2.16 (c). Clearly visible from the figure that the highest compressive stress is calculated at the center of diamond stripe (blue graph). For Si, however, tensile stress was

very small with sharp compressive stress at the edges (red graph). A detail discussion on such simulated stress profile experimental stress calculated using Raman stress mapping has been presented in chapter 4.

III. EFFECT OF PRECURSOR STOICHIOMETRY ON MORPHOLOGY AND TEXTURE FORMATION IN HOT FILAMENT CVD DIAMOND FILMS GROWN ON SI (100) SUBSTRATE

In this chapter, the effect of stoichiometry on morphology, structural and electronic properties of polycrystalline diamond prepared by hot filament chemical vapor deposition (HFCVD) technique have been reported. Polycrystalline diamond films on 100mm Si (100) substrate were deposited in HFCVD chamber at ~720-750 °C using a mixture of methane and hydrogen. The gas mixture was varied between 1.0% to 4.5% methane while keeping the deposition time the same in one experiment whereas the deposition time was varied to keep the thickness of the films the same in another experiment. Diamond film thickness measured by surface profilometer and cross-sectional scanning electron microscopy, average grain size measured from scanning electron microscopy and surface roughness measured from atomic force microscopy indicated an increase in thickness, grain size and surface roughness with increasing methane concentration in hydrogen. Raman spectroscopy results indicated that non- diamond carbon percentage is an increasing function of methane concentration for the selected range. The preferentially oriented polycrystalline nature of the deposited films was observed by x-ray diffraction (XRD). From the XRD pole figure data, it was found that only diamond films deposited with 4.5% methane is preferentially oriented in the <220> direction whereas films deposited with all other methane concentrations showed texture along the <111> direction.

3.1 Introduction

Polycrystalline chemical vapor deposited (CVD) diamond thin film has gained increased interest as a semiconductor for harsh environment electronics, micro electromechanical

systems (MEMS) and as a heat spreader layer for high power electronics due to its wide bandgap, high hardness and excellent thermal conductivity[129][130][131]. The application of CVD diamond in electronics has been enabled by its tunable electronic and microstructural properties. For example, the power density in high power RF transistors, such as GaN based high electron mobility transistors (HEMTs), has been increased by a factor of ~3 with diamond employed as a substrate material due its excellent thermal conductivity, enabling the function of a passive heat spreader[60][12]. Among all methods for diamond deposition, hot filament CVD (HFCVD) is commonly employed due to its relatively simple design, low capital cost and the ability to efficiently scale. Diamond growth via HFCVD involves dissociation of methane (CH_4) in the presence of highly energetic hydrogen atoms activated by the high filament temperature at low pressure (5-100 torr) [92][132]. The effects of various growth parameters such as concentration of CH_4 in H_2, chamber pressure, substrate temperature and filament to substrate distance have significant effects on the structural and electronic properties of deposited diamond films.

In any application, whether as an active material or a passive heat spreader, CVD diamond's performance is highly dependent on its structural properties. Crystalline orientation, grain size, surface roughness and non-diamond carbon (NDC) percentage are some of the most important factors affecting its electrical and thermal properties[129][133][134]. Since electron and phonon transport are greatly dependent on crystalline orientation and any preferential orientation, these factors significantly affect CVD diamond's electrical and thermal properties[135]. For example, electron emission is feasible from the {111} facet of diamond [136], thermal conductivity in the <100> direction is higher than that in <111> and <110> directions [137], [138] and refractive

index and extinction coefficient of (100) films are better than that of (111) films [139].

Polycrystalline materials having completely random orientation is said to have no texture. On the other hand, if the crystallographic orientations are not random, but have some preferred orientation toward certain direction, then depending on percentage of preferred orientation it can be categorized to have weak, moderate or strong texture along that direction[140]. Prior research has shown that formation of preferential orientation (in other word texture formation) and grain formation in CVD diamond films are tunable by changing growth parameters and growth duration[135]. Several research groups have reported the effect of gas stoichiometry and process parameters on morphology and diamond quality [141][142][143]. Yang *et al.* [144] have reported lower gas pressure resulting in the preferred formation of <110> textured diamond. Anaya *et al.* [134] have recently demonstrated the effect of grain size and crystallographic orientation of CVD diamond on its thermal conductivity. C.J. Tang *et al.* [131] have reported deposition of very smooth and highly <100> textured diamond film without any substrate bias in microwave plasma CVD using a gas mixture of $CH_4/H_2/O_2/N_2$. T. Liu *et.al* [135] have demonstrated that the methane concentration in hydrogen has one of the most significant effects on forming highly <110> textured CVD films. However, there is no report where the effect of constituent gas stoichiometry have been studied on morphology, quality and texture formation of CVD diamond, simultaneously[141].

Since morphology and crystallographic orientation of CVD diamond film is highly dependent on growth parameters, we have investigated the effect of gas stoichiometry and growth duration on structural, morphology and crystallographic orientation in CVD films. Two sets of CVD films were deposited with varying CH_4 to H_2 ratio on 100mm Si (100)

wafers. One set with fixed growth time and the other with fixed thickness. A discussion on <111> and <220> texture formation during CVD growth is also presented.

3.2 Experimental

To achieve high nucleation diamond density and process uniformity, a spin coating based seeding approach was adopted for the present research. Mirror polished 100mm Si (100) wafers were seeded with nano diamond particles. Dimethyl sulfoxide (DMSO) based nano diamond suspension (ND) with 0.5 wt% nano diamond seeds (seed size ~4 nm and average aggregate size of 20-30 nm) was used as the seed source which was mixed with S1813 photoresist. A 5.0 mL photoresist solution containing 2.5 mL of S1813, 2.0 mL of DMSO and 0.5 mL of ND was then sonicated for 30 min. The energy provided by the ultrasonic bath helps break the larger clusters of nano diamond seeds (> 20 nm) [46]. Since DMSO freezes at 18.5 °C, the solution was pre-heated at 60 °C for 1 min to avoid non-uniformity or striation effect during spin coating. The photoresist was then spun on the wafer and soft baked at 110 °C for 90 seconds. This technique resulted in seeding density of 10^{11}-10^{12} cm^{-2}. The photoresist coated wafers were then loaded into the HFCVD chamber. The HFCVD system is a custom-built shower head design (Crystallume Inc.) where 9 tungsten wires with 0.25 mm diameter were used with a separation of 1 cm. The peak power drawn by the filament array was maintained at 6 kW which resulted in a filament temperature of 2200 °C. A 6 mm filament-substrate separation resulted in uniform diamond growth with a substrate temperature of 720-750 °C. It is well known from the C-H-O phase diagram proposed by Bachmann et.al.[145] that diamond grows in a narrow window of 1-3% CH_4 in H_2. This range of methane concentration is greatly affected by the addition of oxygen,

however, and there are reports where diamond films were deposited with methane concentration as high as 7.5% [146]. Therefore, in our experiments, the methane concentration was varied from 1.5% to 4.5% (with corresponding CH_4 flow rates of 30-90 sccm) while keeping the H_2 flow rate at 2000 sccm. A small amount of O_2 (3 sccm) was also flowed into the chamber to maintain a low sp^2 bonded carbon concentration in the deposited films [147]. The HFCVD chamber pressure was kept at 20 torr for all experiments.

In the first experiment, three diamond films were grown with 1.5, 3.0 and 4.5% CH_4 in H_2, respectively, while keeping the deposition time constant (8 hours). Morphology and thickness of the films were characterized using scanning electron microscopy (SEM, FEI Helios 400), atomic force microscopy (AFM, Bruker Dimension ICON) and Surface profilometer (DektakXT). Raman spectroscopy of the samples was performed in a Horiba Raman system equipped with a visible laser (λ = 532 nm) and a spot size of ~2 μm. X-ray diffraction (SmartLab XRD system, Rigaku Corporation) measurements analyzed the texture of the films with Cu Kα radiation (λ = 1.540562 Å). Based on the wide angle θ-2θ XRD scan results, pole figure measurements were performed around diamond (111) and (220) peaks because of their relatively higher intensities. Pole figure data were collected using the Schulz method combined with a parallel beam [148]. Each pole figure was measured at a fixed scattering angle (2θ) and was obtained by a series of β (or φ) scans (azimuthal rotation around the normal to the surface of the sample by 0 to 360°) at different tilt angles (α or χ), between 0 to 90° with a step size of 3°. Pole densities were plotted in stereographic projection with obtained diffracted intensity data as a function of polar and azimuthal angle χ and φ, respectively.

The first three wafer experiment had different thicknesses because the growth rate of CVD diamond is a strong function of gas chemistry. Therefore, to observe the effect of methane concentration on morphology and texture formation, decoupled from film thickness, we deposited a second set of two diamond wafers (1.5% and 4.5% methane concentration) with the identical thickness of the sample grown in first experiment with 3.0% methane by adjusting the deposition time. The characterization scheme for this second experiment was the same as the first.

3.3 Results

3.3.1 Morphology and thickness

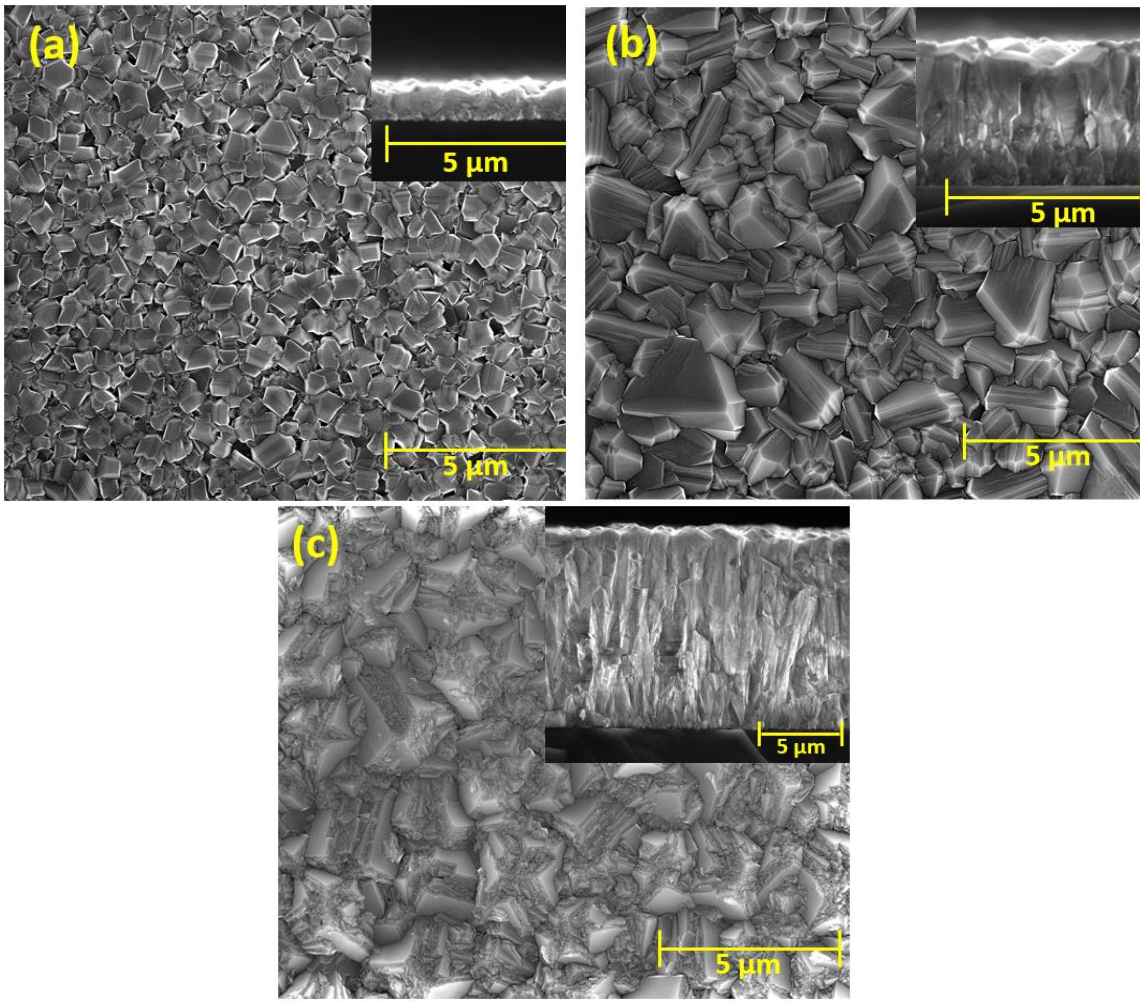

Figure 3. 1. SEM micrographs of Experiment 1 diamond films deposited for 8 hours with (a) 1.5% methane, (b) 3.0% methane and (c) 4.5% methane. The insets are the corresponding cross section SEM images.

Fig.3.1 (a)-(c) show plan-view SEM images of experiment 1 diamond films after 8 hours growth, taken at the middle region (~ 30 mm from the center) of each 100 mm wafer. The insets are corresponding cross-section SEM images obtained by cleaving the wafers. Excellent uniformity across the wafer in terms of diamond coalescence was achieved for all methane concentrations (CH_4:H_2= 1.5%, 3.0% and 4.5%). Grain structure variations

were strongly correlated to methane concentrations. Average grain size and thickness of the films are shown in Table 3.1 and in lower panel graphs of Fig.3.5 (A) and (C)respectively. It is seen from Table 3.1 and Fig.3.5 that grain size and film thickness vary greatly as a function of methane concentration. As seen from Table 3.1 and lower panel graph of Fig.3.5(A), a 3.0% increase in methane concentration from 1.5% to 4.5% resulted in a film thickness increase from ~1 µm to ~11 µm for same 8 hours growth time. Corresponding grain size increase was ~ 300 nm to ~1600 nm.

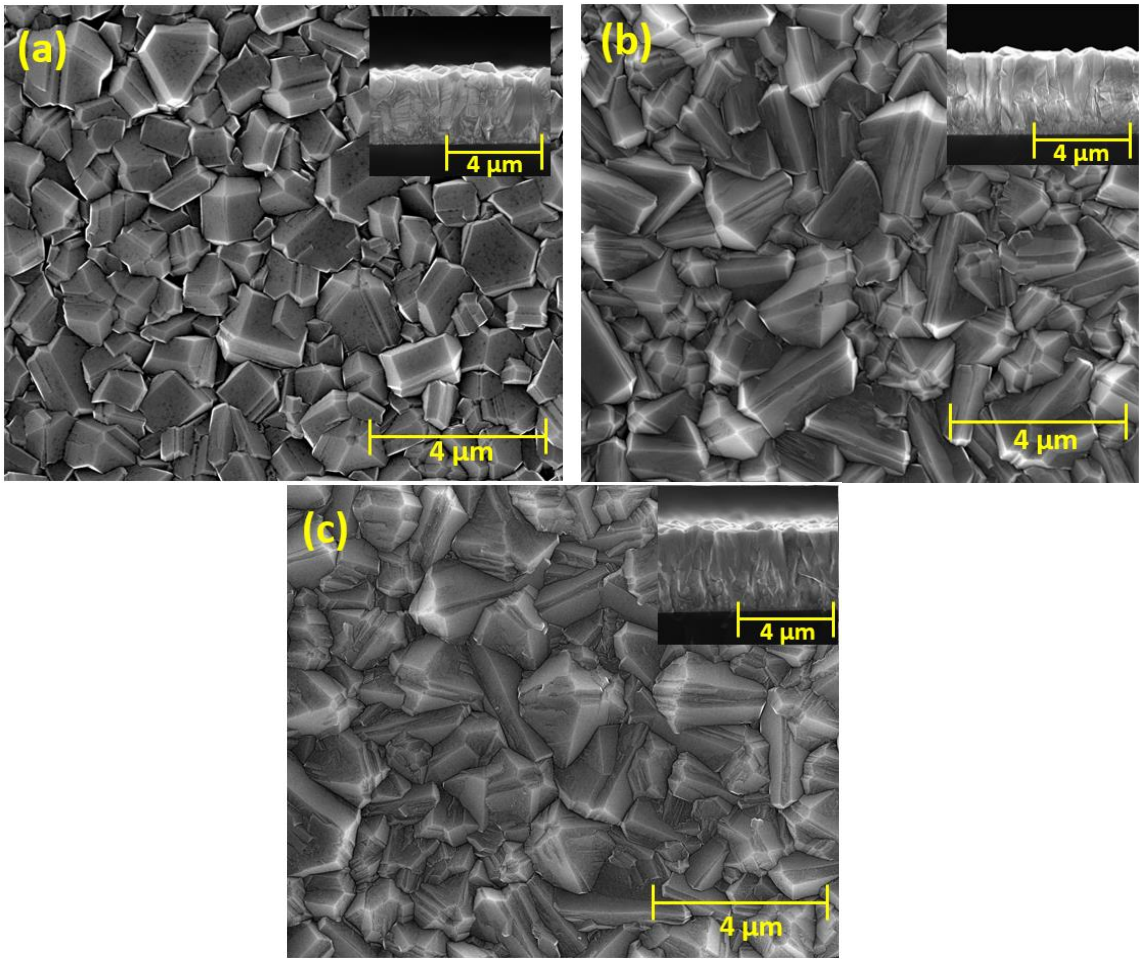

Figure 3. 2. SEM micrographs of Experiment 2 diamond films deposited with (a) 1.5% methane for 20 hours, (b) 3.0% methane for 8 hours and (c) 4.5% methane for 4 hours. The insets are their corresponding cross-section SEM images.

The across-wafer thickness variation is shown in Table 3.1. Growth rate variation across the wafer can be a result of several factors including seed density variation during spin coating of photoresist containing seeds across the wafer or variation in gas flow during CVD. Considering the middle zone thickness, the growth rates of CVD diamond films are ~130-140nm/h, ~480-500nm/h and ~1370-1420 nm/h for 1.5%, 3.0% and 4.5% methane concentrations, respectively. To achieve diamond films with similar thickness for all methane concentrations, we selected the 3.0% methane sample for reference and adjusted the diamond deposition time for 1.5% and 4.5% conditions in order to conduct Experiment 2. Calibration runs (not shown) indicated that growth rate was not a linear function of time. But rather, for 1.5% methane, 20 hours growth time was required to achieve similar thickness to 8 hours, 3.0 % methane, while for 4.5% methane, 4 hours growth was required. Fig.3.2(a)-(c) shows the SEM images of grain structure of Experiment 2 (with identical thicknesses) and insets of each figure shows the corresponding cross section SEM images. The variation in thickness and grain size at the middle region of the wafers produced in Experiment 2 is shown in the top panel figures of Fig.3.5(A) and (C).

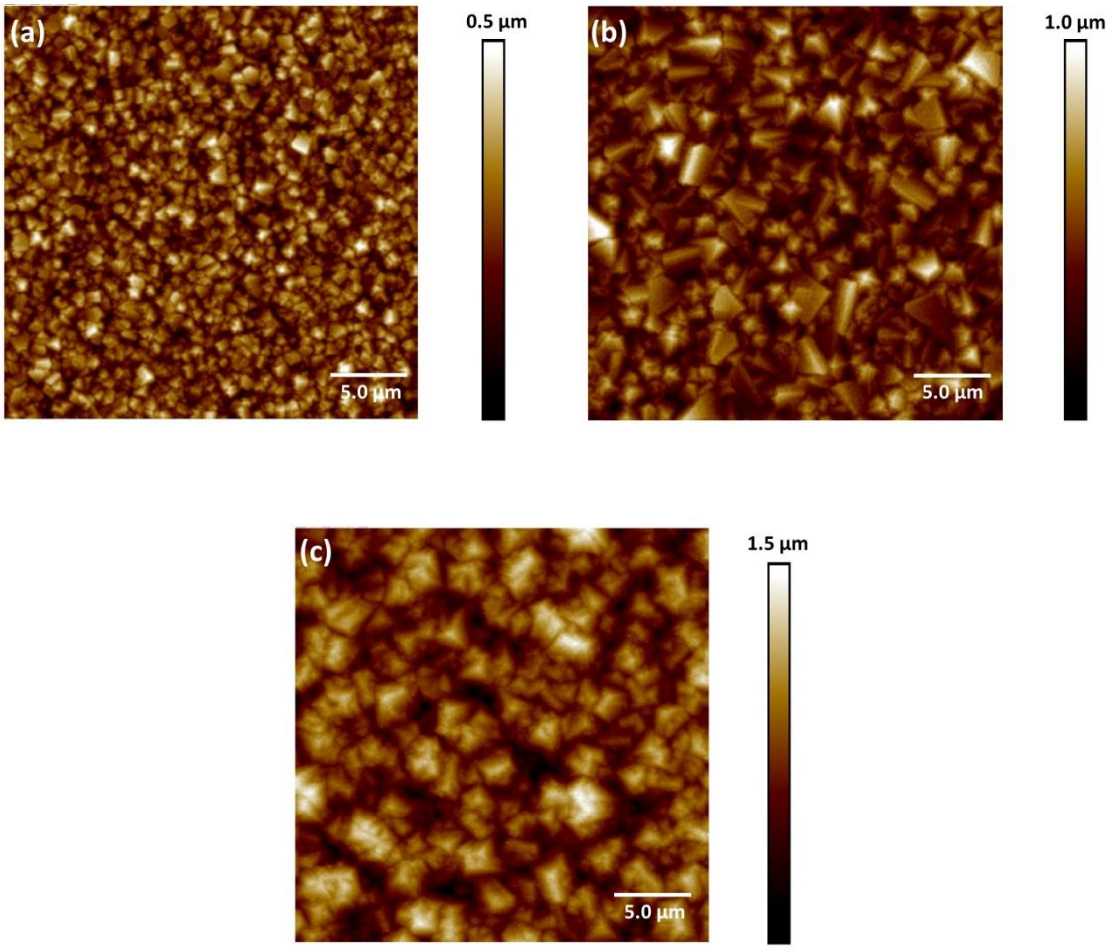

Figure 3. 3. AFM topography taken at wafer middle zone of CVD diamond wafers deposited with (a) 1.5%, (b) 3.0% and (c) 4.5% methane.

It is worth mentioning that control of thickness in hot filament CVD is difficult because of the very rough surface of the deposited film and non-uniform filament temperature rise for various methane concentrations [149]. Figure 3.3 (a)-(c) show AFM images from Experiment 1 (after 8 hours growth). The root mean square (RMS) roughness for each sample taken from a 25 µm × 25 µm region is shown in Table 3.1 and in bottom panel of Fig.3.5 (C). Note the linear increase in the contrast scale bar of the AFM images in Fig.3.3 and corresponding RMS roughness increase in Table 3.1 and Fig.3.5 (B). Roughness was found to be an increasing function of methane concentration for sample grown for 8 hours.

Interestingly, as seen from Table 3.1 and top panel of Fig.3.5(B), for samples with similar thicknesses in Experiment 2, diamond films grown with 3.0% methane showed highest RMS roughness followed by films with 4.5% methane.

3.3.2 Raman spectroscopy

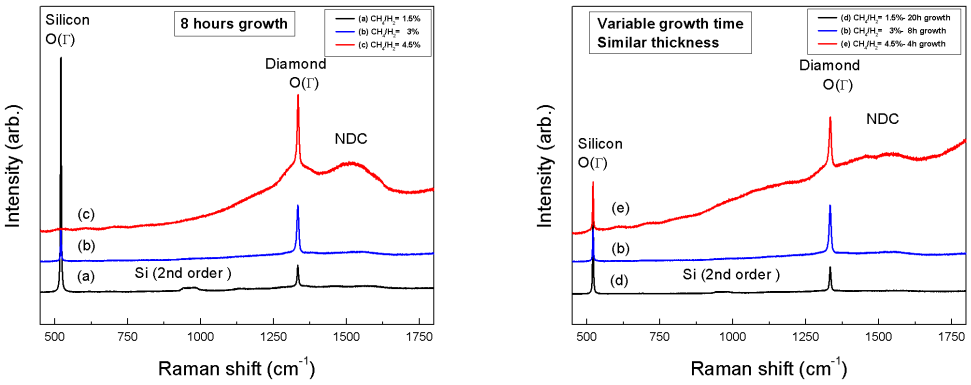

(a) (b)

Figure 3. 4. Visible Raman spectra at 30 mm of CVD diamond wafers deposited with 1.5, 3.0 and 4.5% methane grown for (a) Experiment 1, 8 hours and (b) Experiment 2, similar thickness.

The visible Raman spectra of Experiment 1 diamond samples, grown for 8 hours, are shown in Fig.3.4(a). There are two strong, sharp peaks identified as Si O(Γ) and diamond O(Γ). The peak confirming the presence of diamond phase was found to be at 1332.89 cm^{-1}, 1333.42 cm^{-1} and 1333.69 cm^{-1} for diamond films grown with 1.5%, 3.0% and 4.5% methane, respectively. The blue shift in diamond peaks with higher methane percentage can be a result of intrinsic stress in the film that may come from increased thickness. The broad peak centered at ~1550 cm^{-1} is referred to as "G band", or non-diamond carbon (NDC) phase, and was visible for all three Experiment 1 diamond films. This broad peak represents the vibration of sp^2 bonded carbon atoms in a hexagonal lattice and have been reported as E_{2g} vibration of graphite [144]. Fig.3.4 (a) also shows that the intensity of NDC

peak increases as the percentage of methane increases in diamond. This NDC band can be a result of defects, intrinsic stress and/or the amount of graphitic impurity in diamond. The volume fraction of diamond in these samples can be calculated from the ratio of integrated intensities (area under curve after background correction) of diamond peak (I_D) and summation of diamond peak and diamond like carbon peak (I_{DC}). Table 3.1 and bottom panel graphs in Fig.3.5 (D) shows the change in diamond phase with increasing methane concentration. Diamond phase reduced from 57% to 18% when methane concentration was increased from 1.5% to 4.5%, for 8 hours growth. The intensity of Si O(Γ) peak has decreased with increasing methane concentration due to increased diamond thickness.

The visible Raman spectra for Experiment 2 diamond films, with identical thicknesses, are shown in Fig.3.4(b). The data indicate that NDC phase is an increasing function of methane concentration for films with similar thickness, analogous to Experiment 1. Table 3.1 and top panel graph of Fig.3.5 (D) show the volume fraction of diamond phase in Experiment 2 films. 1.5% methane concentration resulted in the highest diamond phase, 77%, for a ~3.38 μm diamond film, whereas 4.5% methane resulted in 36% diamond phase for similar thickness. Such an increase in NDC phase with increasing methane concentration have been reported by other researchers [92] [146] [150].

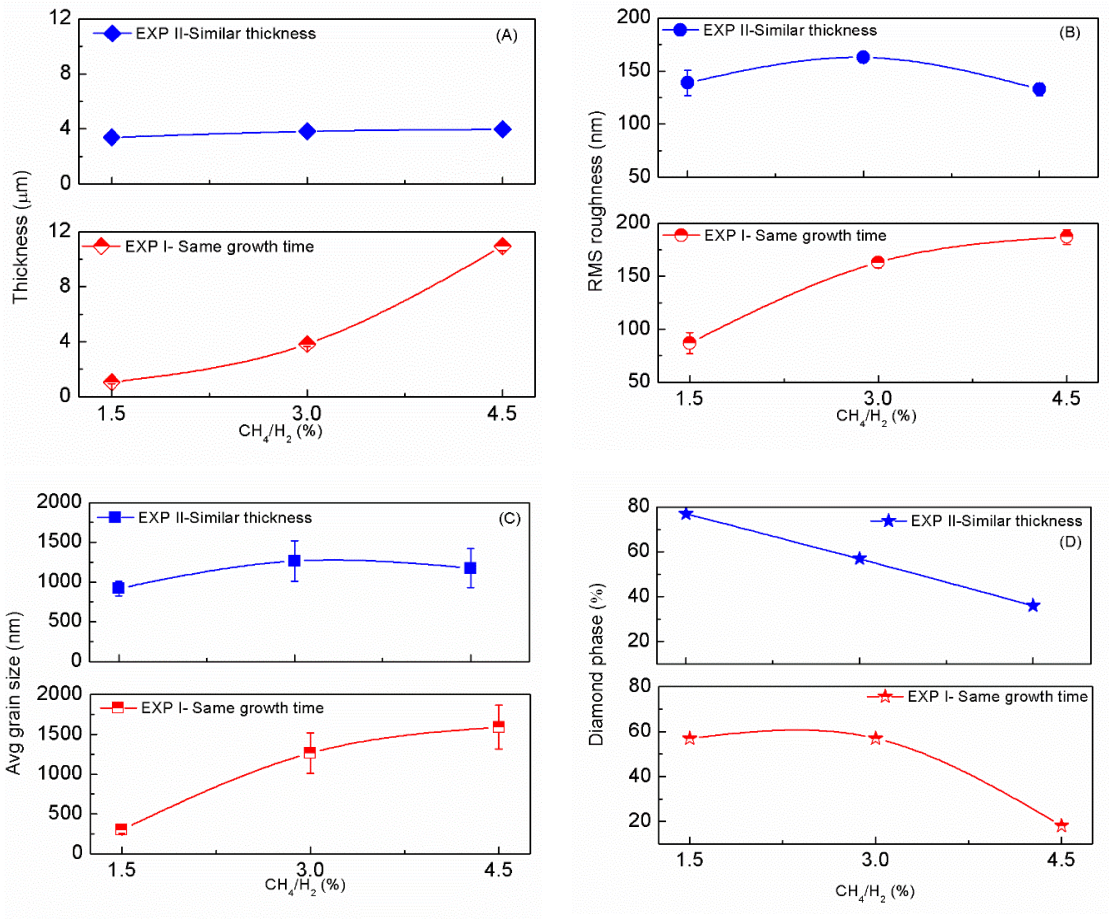

Figure 3. 5. Variation in morphology and diamond quality (at middle region of the wafer) due to change in methane concentration for two sets of experiments;(A) Thickness (B) RMS roughness (C) Average grain size and (D) Diamond phase (sp^3) percentage in diamond films. Deposition time was 8 hours for Experiment 1 and variable deposition time were employed in experiment 2 wafers to achieve similar diamond film thickness.

3.3.3 XRD and pole figure

Omega-2theta XRD of Experiment 1 diamond films is shown in Fig.3.6(a). Data were collected from the middle region of each wafer. Three major diamond peaks, namely (111), (220) and (311), were visible at ~ 43.9°, 75.3° and 91.5°, respectively. Other peaks are attributed to the Si (100) substrate. It is important to note that peak positions were varied slightly from sample to sample due to thickness variation and compressive stress [133] [151]. It is well known that compressive stress in diamond film decreases as film thickness

increases [152][153]. The relative intensity of (111) and (220) peak has changed significantly as the methane concentration was increased. Specifically, the intensity of the diamond (111) peak was highest for diamond film grown with 3.0% methane, whereas the intensity of the diamond (220) peak was highest for film grown with 4.5% methane. For 1.5% methane, the intensity of the diamond (111) peak was lowest because of reduced thickness. It is clear from Fig.3.5(a) that between diamond films grown with 3.0% and 4.5% methane, the integrated intensity of (111) peak compared to that of (220) have been reduced for 4.5% methane. This result gives an impression that diamond film with 4.5% methane may have a preferential orientation toward (220) whereas diamond film with 3.0% methane may have such a preference toward (111). However, such comparison may not be accurate because these films had different thickness and the relative variation may have come from thickness of diamond film.

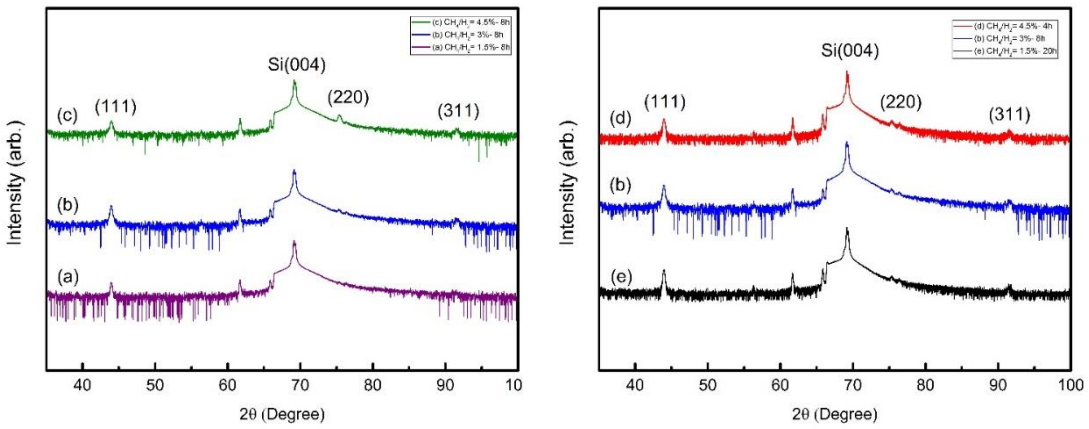

(a) (b)

Figure 3. 6. X-ray diffraction spectra taken at 30 mm from CVD diamond wafers deposited with 1.5, 3 and 4.5% methane grown for (a) 8 hours and (b) variable duration to achieve similar thickness.

To understand the true effect of methane concentration on texture formation in our CVD diamond films, Experiment 2 was undertaken, as described before. Fig.3.6(b) shows the omega-2theta XRD patterns of diamond films of identical thicknesses, grown with various

methane concentration. Measurements were taken at the middle region of the wafer. In this case, the relative integrated intensity of (111) peak is lowest for diamond films grown with 4.5% methane compared to the other films. No differences were visible in relative integrated intensities of (220) and (311) peaks for various diamond films in Fig.3.6(b).

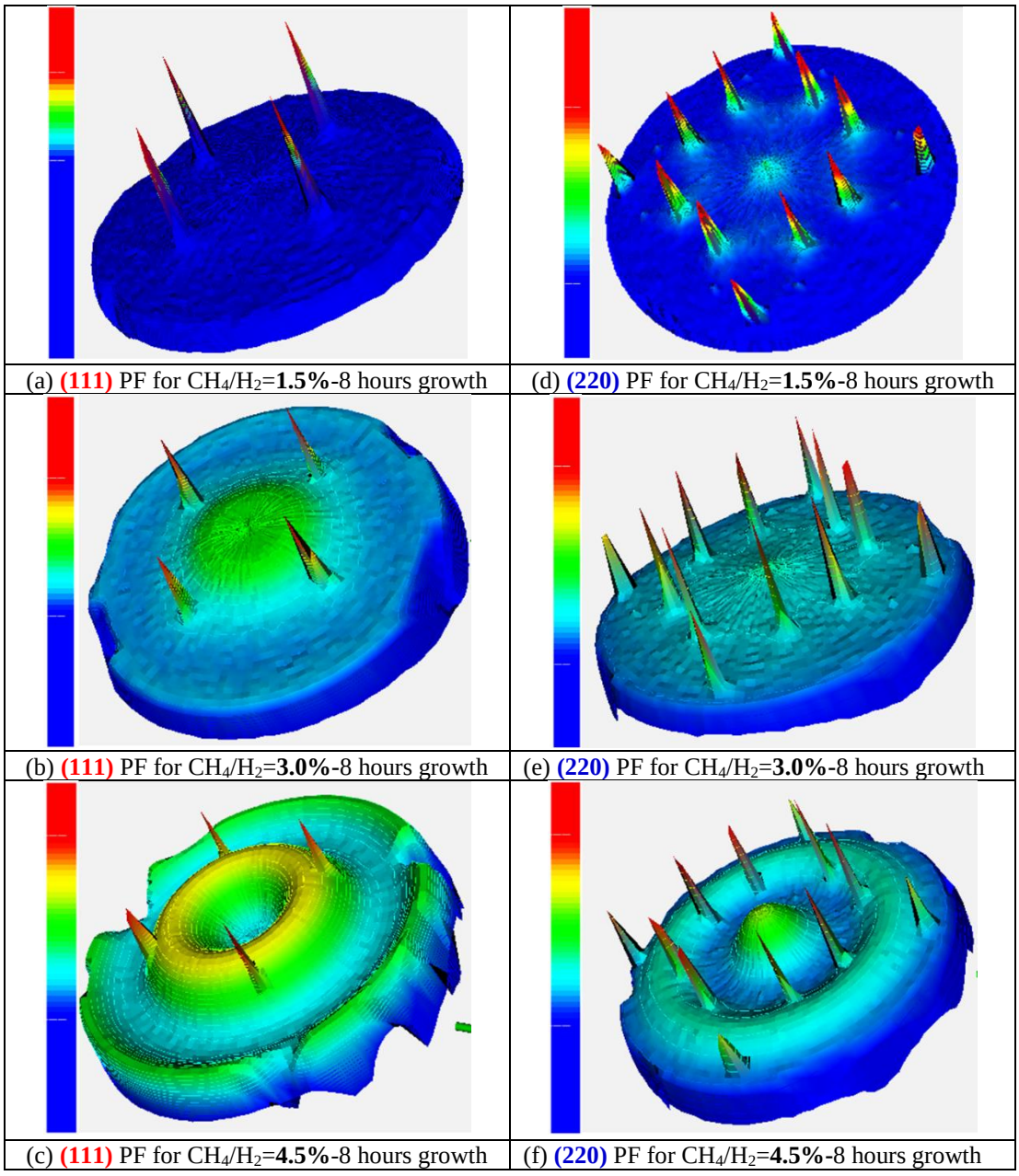

Figure 3. 7. (a)-(c) 3D projection with relative intensity of pole figure (PF) of diamond (111) peaks and; (d)-(f) Pole figure of diamond (220) peaks for films grown with 1.5, 3.0 and 4.5% methane, respectively, for 8 hours.

Pole figure (PF)

To investigate the true texture formation and its dependence on methane concentration, we performed pole figure analysis. It is important to note that pole figure data from these experiments are for observing qualitative differences in texture formation in CVD diamond films due to the change in methane concentration. Therefore, a detailed analysis on inverse pole figure and orientation distribution function are not presented here. Such analysis can be found elsewhere [135] [148] [154][155][156].

In pole figure data collected using Schulz method, reflection of the substrate is always visible for thin film samples because continuous Bremsstrahlung radiation happens to satisfy the diffraction condition. Therefore, very high intensity peaks from the Si substrate are visible in all the pole figures presented. Furthermore, the detector used for pole figure measurement was one dimensional which has an array of detectors and can capture a 2θ spread of around ~ 3^{o}. For pole figure data of diamond (111) shown in Fig.3.7 (a)-(c), high intensity peaks from Si (220) were visible in all samples because its Bragg angle of 47.63° is within 3.74° of the diamond (111) reflection. In the case of diamond (220) pole figure shown in Fig.3.7(d)-(e), Si (331) peaks are visible because the Bragg angle for Si (331) reflection is within 0.5° of diamond (220) [134]. In general, a strong texture in diamond along a certain direction is identified by a sharper peak centered at χ = 0°. Other peaks between χ = 0° and 90° represents tilting of a plane with its surface normal to the substrate. Based on this general convention it is clear from Fig.3.7 (c), (f) and 3.8(c), (f) that these diamond film (4.5% methane) have very strong <220> texture and the (111) plane is ~ 45° tilted with surface normal. On the other hand, only texture along <111> was visible for all other diamond film growth conditions. Texture formation in CVD grown

polycrystalline diamond films have been reported and similar pole figure data for diamond (111) and (220) reflections have been observed in most of those cases [154][157].

Clear texture formation was visible for both (111) and (220) reflection of diamond when methane concentration was 4.5%. However, (111) orientation is tilted ~45^{o} with the surface normal for this sample. Diamond sample with 1.5% methane did not show any texture whereas a weak texture towards diamond (111) were observed for the film grown with 3.0% methane. Notably, no tilting of (111) were observed in this case. No texture was observed for diamond (220) for the sample grown with 3.0% methane. Once again, it is worth mentioning that the thicknesses of these samples were very different and strong texture were observed for sample with highest thickness i.e. film grown with 4.5% methane. Therefore, these results were insufficient to draw any definite conclusion about dependence of texture formation on methane concentration.

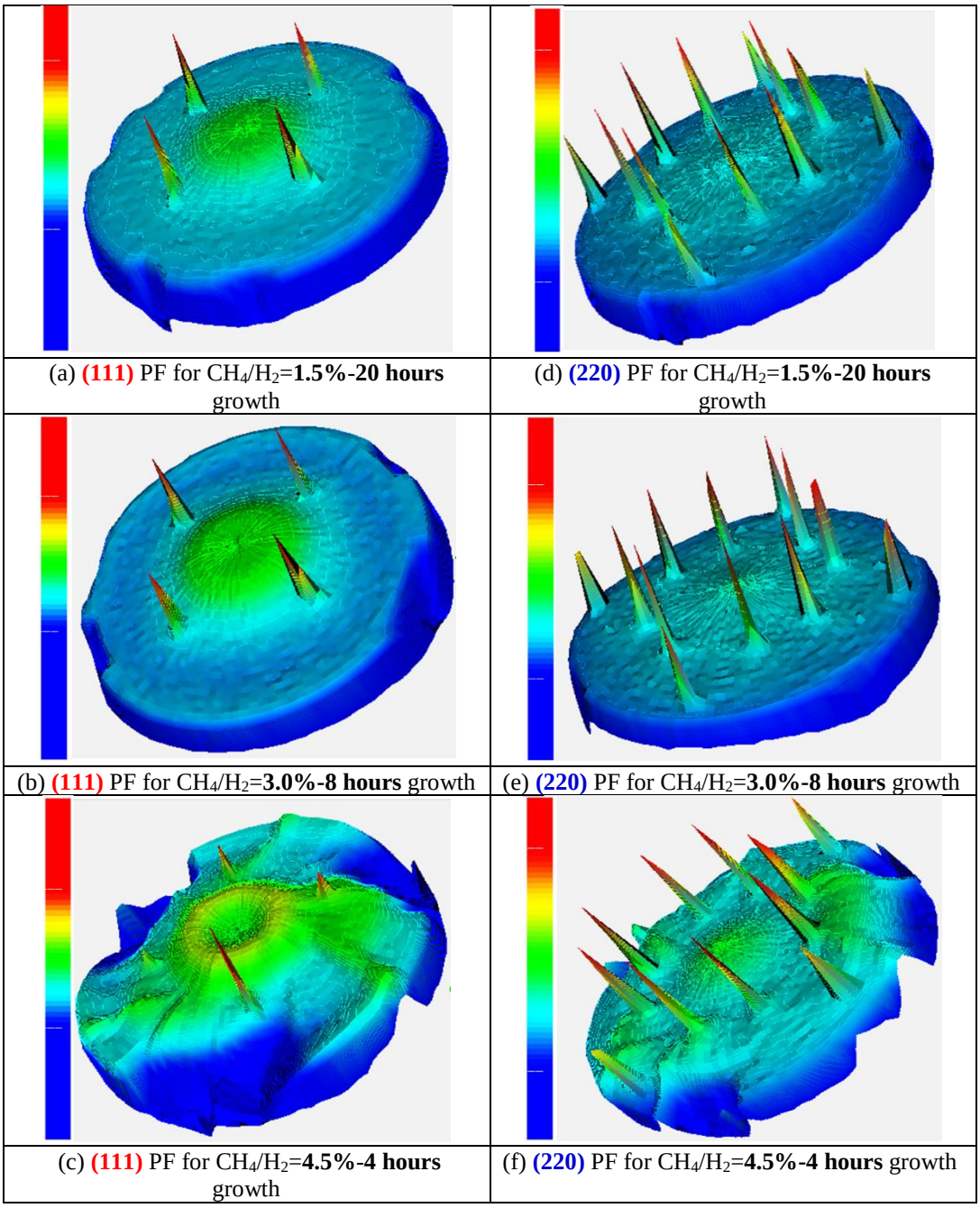

(a) **(111)** PF for CH_4/H_2=**1.5%-20 hours** growth

(d) **(220)** PF for CH_4/H_2=**1.5%-20 hours** growth

(b) **(111)** PF for CH_4/H_2=**3.0%-8 hours** growth

(e) **(220)** PF for CH_4/H_2=**3.0%-8 hours** growth

(c) **(111)** PF for CH_4/H_2=**4.5%-4 hours** growth

(f) **(220)** PF for CH_4/H_2=**4.5%-4 hours** growth

Figure 3. 8. (a)-(c) 3D projection with relative intensity of pole figure (PF) of diamond (111) peaks and; (d)-(f) Pole figure of diamond (220) for diamond films of identical thickness grown with 1.5, 3 and 4.5% methane grown for 20, 8 and 4 hours respectively.

Fig.3.8(a)-(f) show pole figure data collected around diamond (111) and (220) reflections for films with identical thickness. As seen from figure 3.7, the (111) preferred orientation was observed for all three samples but 4.5% methane resulted in a tilt ~ 23° of (111) plane.

Among all films, diamond film with 4.5% methane showed a (220) texture formation. No preferred orientation toward (220) was observed for 1.5 and 3.0% methane. Thus, the primary outcome of these pole figure data is that the increased methane concentration in diamond films results in a preferred (220) texture.

Table 3. 1. Summary of morphology, diamond quality and texture formation data of diamond wafers deposited with three methane concentrations. Deposition time was 8 hours for Experiment 1 wafers and variable deposition were employed in Experiment 2 wafers to achieve similar diamond film thickness.

Experiment	CH_4/H_2 (%)	Deposition time (h)	**Thickness (µm)**			**Average grain size (nm)**		
			center	middle	edge	center	middle	edge
I: Fixed growth time	1.5	8	1.41±0.11	1.06±0.09	0.96±0.09	348±52	300±48	252±21
	3.0		4.69±0.12	3.83±0.15	3.41±0.17	1396±216	1264±257	989±186
	4.5		12.84±0.24	10.95±0.31	9.71±0.45	1412±197	1590±275	1593±291
II. Similar thickness	1.5	20	3.55±0.12	3.38±0.10	3.17±0.17	906±123	918±93	713±77
	3.0	8	4.69±0.12	3.83±0.15	3.41±0.17	1396±216	1264±257	989±186
	4.5	4	4.59±0.23	3.97±0.18	3.52±0.28	1175±163	1174±245	1186±171

			RMS Roughness (nm)			**$I_D/(I_D+I_{DC})$**			**Texture formation**
			center	middle	edge	center	middle	edge	
I: Fixed growth time	1.5	8	99	87	63	0.56	0.57	0.56	None
	3.0		178	163	102	0.54	0.57	0.52	(111)
	4.5		191	187	216	0.14	0.18	0.19	111 and 220
II. Similar thickness	1.5	20	145	139	127	0.71	0.77	0.76	None
	3.0	8	178	163	102	0.54	0.57	0.52	(111)
	4.5	4	147	133	151	0.39	0.36	0.44	111 and 220

3.4 Discussion

Complete diamond coverage of 100 mm Si wafers was observed after 8 hours of growth with all methane concentrations. The uniform coverage and consistent grain size across-

wafer achieved in our research was a result of the combined effects of spin coater based seeding and optimized growth conditions. Dispersing the nano diamond seeds containing photoresist suspension using spin coater resulted in a very uniform seed layer. The key was maintaining consistent thickness of the photoresist which for our process is 500±10nm across the 100 mm wafer. The growth condition of the CVD tool was optimized through a series of growths with various conditions. The morphology results shown in section 3.1 indicate that diamond film with higher methane concentration results in higher growth rate and high surface roughness for a constant growth duration. This is because the higher methane concentration increases the number of activated radicals and diamond growth in certain faces are more than in other face[158]. From the growth model studies reported by several groups it was summarized that to form a stable nucleus of diamond, a different number of carbon atoms are required for different facets[159]–[163]. Specifically, it was reported by Liu et.al.[164] that 1 atom on (100) surface, 2 atoms on (110), and 3 atoms on (111) surface are required to form a stable diamond nucleus. Besides, the hot filament CVD process is a diffusion controlled system where the temperature is sufficiently high and the concentration of methane gas is low [165], and as a result, thickness and roughness follow the methane concentration [141] [142].

Diamond grains with random shapes and relatively small size were observed for 1.5% methane and well faceted pyramid shaped polycrystals were visible in the case of 3.0% methane. Further increasing the methane concentration to 4.5% resulted in films with very large grains but certain faces of the grains exhibited damage which can be a result of etching caused by hydrogen atoms. To understand the etching, it is necessary to understand the chemical reactions that take place during diamond deposition. During the HFCVD

process, clusters of carbon atoms are formed on the nano diamond seeded substrate surface. Thermal energy provided by the hot filament causes a sequence of changes in the chemical bond structure from sp^1 to sp^2 and, eventually, sp^3 [166]. The energetic atomic hydrogen acts as an etch reactant for etching any remaining sp^2 bonded carbon. Therefore, the diamond deposition takes place with simultaneous etching of sp^2 carbon and formation of sp^3 [150]. The observed enhanced etching/ damage on some faces in the 4.5% methane sample can be a result of etch resistance of one face to another due to energetic hydrogen at elevated temperature. Raman spectra shown in Fig.3.4(a) and the volume fraction of diamond in Table 3.1 and Fig.3.5 (D) indicate that the volume fraction of sp^3 diamond is low in films grown with 4.5% methane. Since 4.5% methane results in 80-85% NDC, it is expected that the etching will be predominant in diamond film grown with this condition. Furthermore, the RMS roughness measured from AFM image was also high for this sample.

The cross-section SEM images shown in the insets of the Fig.3.1(a)-(c) show that diamond crystals are very dense in the initial growth stage and a columnar-like growth continues as the film thickness increases. From grain size and grain boundary point of views, diamonds quality gets better as the film thickens and grains grow vertically[167]. For our experiments, at any given methane concentration, better quality diamond is the one that has higher thickness. On the other hand, methane concentration strongly correlates with the non-diamond carbon phase concentration. This can be seen from Fig.3.5 (D).

XRD spectra shown in Fig.3.6(a) shows that there is a slight decrease in diamond (111) peak intensity compared to diamond (220) when methane concentration was increased from 3.0% to 4.5%. The relative change in peak intensity has been reported as

an indication of preferred orientation [135] [141] [144][157]. However, to achieve a complete understanding of texture formation, a pole figure measurement is necessary[148]. Pole figure of diamond (111) and (220) peaks shown in Fig.3.7(a)-(f) indicate strong texture formation in films grown with 3.0% and 4.5% methane. It is worth mentioning that orientation distribution function generated from an inverse pole figure can give complete information about preferential orientation[148]. A detailed description of texture formation in polycrystalline diamond is well understood and has been reported [157][168]. However, since the goal of the present research is to perform a comparative and quick analysis of preferred orientation as a function of gas stoichiometry, we restricted our analysis to pole figure data only. A detailed analysis of texture formation in CVD diamond films grown in similar condition is subject to future research. However, the current data will be explained based on a brief description of texture formation in polycrystalline diamond.

A mechanism of texture formation in polycrystalline films during epitaxial growth was first proposed by Van der Drift [168] based on an evolutionary selection model of specific crystallite orientations. According to this model, randomly oriented nuclei grow freely and uniformly until they impinge. Any given nuclei can prevail in the final film if its fastest growing crystallographic direction is perpendicular to the substrate, because such nuclei overgrow less favorably orientated ones. As a result, crystallographic texture forms in the film [135]. For polycrystalline diamond grown on Si (001), growth on nuclei facing parallel to the substrate are easily overgrown by crystals growing with the diagonal perpendicular to the substrate. Usually, growth rate along the diagonal plane (111) of a cubic crystal is $\sqrt{2}$ times that along the direction perpendicular to its face. Silva et al. [154] have also reported that the film texture is determined by the direction of the fastest growth

corresponding to the largest dimension of the single crystal. As any polycrystalline film thickens, more and more grains are buried by adjacent grains and only the crystals with the highest growth rate direction normal to the substrate survives [154]. The largest dimension of isolated diamond crystal has been reported to be linked with the well-known α parameter, where $\alpha=\sqrt{3}.V_{100}/V_{111}$ and V_{hkl} represents growth rate along the <hkl> direction[157]. The fastest growth direction in polycrystalline diamond varies from <111> to <110> to <100> when α is varied from 1 to 3, respectively. It is worth mentioning that the evolution selection model for texture formation is based on the assumptions of (1) no secondary nucleation and (2) the absence of crystallographic defects, such as twinning. However, in polycrystalline diamond, secondary nucleation and twinning readily occur. Due to secondary nucleation, nano sized diamond grains exhibit elongated growth along the <110> direction after initial nucleation [154]. For CVD diamond, the growth rate of the (110) plane has been reported to be much faster than (111) and (100) [135][144][154]. The microstructure of CVD diamond films presented in Fig.3.1(a)-(c) can be understood by a textured growth with an α value close to 1.5 (cuboctahedra as reported in [154]) that leads to a <110> texture. The observed pyramidal morphology in Fig.3.1(a)-(c) are the result of secondary nucleation and appearance of multi-twinned crystals having their largest dimension along a <110> axis. The effect of fastest growing <110> texture has been observed most clearly from the pole figure data of the 4.5% methane sample (Fig.3.7(f)). However, in the case of 3.0% methane, texture along the <111> plane was visible but no texture along <220> were visible. It is worth mentioning that texture along <111> was visible in diamond film deposited with 4.5% methane but the tilt angle was ~23^{o} with surface normal (the intense circle on Fig.3.7 (f) at ~ 23 ° from the center of the pole figure

data).

After depositing second sets of diamond films in Experiment 2, it was observed that for same methane concentration, growth rate was not a linear function of growth time. As a result, after a series of trial runs, (not all results are presented here) 1.5% methane resulted in a diamond film with thickness in the range of ~3.5μm after depositing for 20 hours. Surprisingly for 4.5% methane, diamond film with thickness ~ 4μm was grown after 4 hours of deposition. The cross wafer non-uniformity in thickness was as high as 1 μm for this sample. Among all samples, diamond deposited with 3.0% methane resulted in the largest grain size while grain size was lowest for diamond deposited with 1.5% methane. The increase in grain size with increasing methane concentration is a result of increased methyl radicals which is the main source of diamond growth. Another model for explaining increased growth rate and grain formation with increasing methane concentration was reported by Jeon et. al [169] which claims that the majority of diamond nuclei clusters become negatively charged due to electrons originated from the hot filament. Clusters formed with lower methane concentration have low energy and higher methane concentration have higher energy. As a result, any increase in methane concentration enhances surface diffusion which assists in transforming cluster masses into well faceted diamond crystals. The decrease in grain size when diamond is deposited with methane concentration above 3.0% was reported by Ali et.al [141]. In their study, highly faceted diamond crystals were achieved with a methane concentration of 3.0% while smaller crystals with pyramidal shape diamond clusters were achieved when the methane concentration was above 3.0%. In other studies, “cauliflower shaped” diamond clusters have been observed when methane concentration was above 4.5%[169] and no preferential

orientation was observed.

Fig.3.8 (a)-(c) shows the pole figure data of diamond (111) for Experiment 2; i.e., diamond films with identical thickness. Fig.3.8 (d)-(f) show corresponding pole figure of the diamond (220) plane. The diamond film grown with 4.5% methane has preferred texture along the <220> direction whereas the films deposited with 1.5% and 3.0% methane showed texture formation along the <111> plane with no indication of tilting to the surface normal. No visible texture was observed along the <220> direction when the film was deposited with 3.0% or 1.5% methane. As stated before, texture along <111> were visible for 4.5% methane but interestingly the tilt angle was ~23° with the surface normal. These results indicate that the increased methane concentration results in a film with strong preferential orientation along <220> and this texture is aligned with the surface normal whereas its texture along <111> changes tilt angle (with surface normal) as film thickens.

At elevated temperature and methane concentration, grain growth parallel to <110> is enhanced while simultaneously suppressing growth along <100> and <111>. In addition, higher methane concentration at high temperature reduces the density of twinning generated from {001} and {111} oriented faces. Chu et.al [170] have reported the growth rate along <110> to be at least double and quadrupole compared to that along <100> and <111>, respectively, for a linear increase in methane concentration. As stated before and seen from SEM images, increasing methane concentration increases the concentration of activated radicals and high consumption rate of methyl radicals prevents further acquisition of new methyl radicals[135]. Therefore, with higher methane concentration, diamond deposition on the (111) plane becomes less favorable compared to other crystallographic planes [171]. It is worth mentioning that increased methane concentration alters the

chemical equilibrium in the gas flow and increases collision frequency of the active radicals with the active surfaces of the diamond crystal. Variation in surface energies of crystal faces with different orientations is the cause of observed texture in our diamond films deposited with higher methane concentration.

3.5 Conclusion

In summary, the effect of methane concentration on morphology, quality and crystal structure of HFCVD diamond has been studied. Higher growth rate and larger diamond grain size primarily results from the increased methyl radical concentration present in the chamber when methane concentration is increased. The volume fraction of sp^3 bonded diamond was dictated by the methane concentration with highest quality diamond (i.e., lowest NDC to diamond ratio) achieved with lower methane concentration (1.5%). Diamond films with pronounced texture were observed only when the thickness of the film was above 3 μm. Diamond films were found to be preferentially oriented along <220> direction when the methane concentration was 4.5% but the volume fraction of diamond phase was lowest at this concentration. A preferential orientation along <111> was observed prominently in diamond films grown with 3.0% methane. Secondary nucleation and twinning has been found to be responsible for the observed high texture formation along <220> when methane concentration was high.

IV. ULTRAVIOLET MICRO-RAMAN STRESS MAP OF POLYCRYSTALLINE DIAMOND GROWN SELECTIVELY ON SILICON SUBSTRATES USING CHEMICAL VAPOR DEPOSITION

In this chapter, ultraviolet micro-Raman stress map of polycrystalline diamond stripes grown on silicon will be discussed. Polycrystalline diamond stripes, with nominal thickness ~ 1.5 μm and various widths, were selectively grown on silicon substrates using chemical vapor deposition. Stress measurements using ultraviolet micro-Raman mapping reveal high compressive stress, up to ~ 0.85 GPa, at the center of the diamond stripe, and moderate tensile stress, up to ~ 0.14 GPa, in the substrate close to the interface with the diamond. Compressive stresses on diamond decrease with decreasing stripe widths. The stress map is well-described using finite element simulation incorporating solely thermal expansion effects.

4.1 Introduction

Thermal management in power electronics is the principal limiting factor to increasing power while reducing size and increasing density of devices. The high thermal conductivity of diamond has motivated work aimed at integrating it with various electronic materials as a passive approach to reduce the effects of local heating in devices[172], [173]. Polycrystalline diamond, which can be grown using chemical vapor deposition (CVD) on diverse substrates, is of great interest as a heat spreading layer due to improvements reported in thermal performance of high power transistors[12][174]. However, the 700-800 °C growth temperature used for hot-filament (HF) CVD diamond and the large difference in coefficient of thermal expansion (CTE) between diamond and the substrate produce high

thermal stresses in both materials[119][175]. In addition to thermal stresses, the diamond CVD process may also produce intrinsic stresses which can have significant deleterious effects on the overall mechanical properties of the diamond and substrate. Stress can affect device performance, through changes in the electronic properties, and even lead to failure, while excessive stresses on the substrate may bow and even shatter the wafer[176].

Wafer stress, due to uniform diamond layer deposition, may be mitigated by producing a patterned diamond structure. Although patterned diamond will not eliminate *local* stresses associated with layer coverage, the presence of open regions permits relaxation of the *global* substrate stress. One approach for producing a patterned diamond layer is blanket CVD following uniform seeding of the substrate, completed by etch removal of selected regions[122]. This "top-down" method does not, however, eliminate the uniform thermal stress produced by the initial diamond layer deposition. Furthermore, it is found that complete removal of the diamond from the substrate is difficult and prospectively destructive to the etched substrate fields[122]. An alternative approach, used here, is based on a "bottom-up" procedure in which diamond seeding is present only in desired regions[77] of a substrate, such as silicon. Subsequent CVD growth takes place only in the seeded areas. We find that this method results in high selectivity and relaxes global stress. Regions covered by diamond, and the silicon substrate itself, are under local mechanical stress as we reveal using ultraviolet (UV) micro-Raman mapping.

4.2 Experimental details

Selective deposition of CVD diamond stripes on 100-mm Si (001) wafers began by patterning the wafer with nano-diamond seeds, which are ubiquitously needed to initiate

growth. Dimethyl sulfoxide based nano-diamond suspension (Adamas Nanotech., 0.5 wt% nano diamond seeds, ~ 4 nm average diameter with 20-30 nm aggregate size) was dispersed in photoresist (Shipley 1813). Approximately 5 mL of the solution was sonicated for 30 min, spun on the wafer and soft baked at 110 °C for 90 s, followed by exposure using a contact I-line photolithography (SUSS MicroTec). Developing the resist then produced regions of seed-laden resist surrounded by cleared silicon fields. To improve selectivity, the wafer is subjected to a plasma processing (dual-power reactive-ion etching and inductively-coupled plasma at 150 and 1500 W, respectively) in 45 sccm of CF_4 and 5 sccm of O_2. This plasma etch helped remove seeds remaining in the opened fields. The resist-patterned wafer was next loaded into a hot filament CVD chamber (Crystallume, Inc.). A 1.5 % mixture of methane (30 sccm) and hydrogen (2 L/min) was used for diamond growth, with substrate temperature in the range 720-750 °C. The resulting morphology and thickness of the diamond films were characterized with scanning electron microscopy (SEM, FEI Helios 400), atomic force microscopy (AFM, Bruker Dimension ICON) and surface profilometer (DektakXT). Good across-wafer uniformity was achieved in diamond growth. Effects due to microloading were not observed.

4.3 Results and discussion

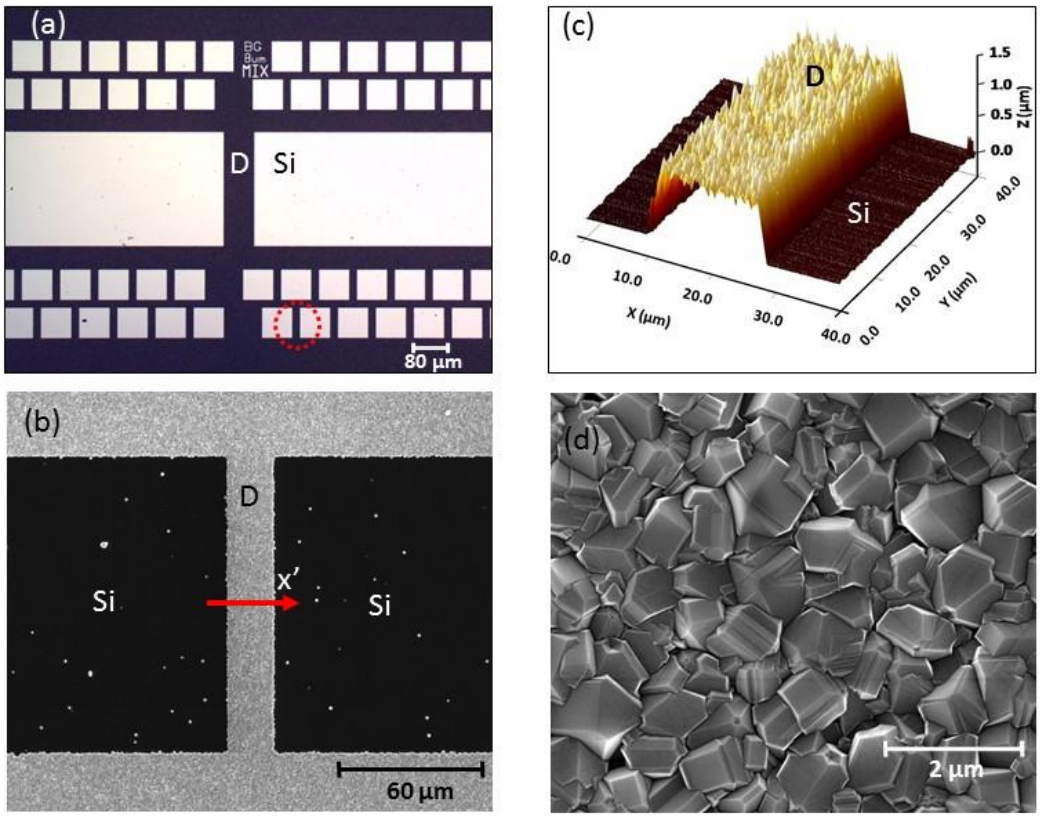

Figure 4. 1.(a) Optical image of selectively grown diamond wafer taken from a region with various size stripes and windows; (b) SEM image exhibiting Si fields, mostly cleared, with occasional diamond nuclei and a 20-µm wide diamond stripe; (c) AFM image of a representative 20-µm wide diamond stripe and (d) Close-up plan-view SEM image of the diamond-covered surface.

Figure 4.1(a) shows a representative optical image from the fully processed wafer. The nominally 20-µm wide diamond stripes and bare Si fields are clearly defined. The SEM image in Fig.4.1(b) is from a representative stripe, as depicted by the circle in Fig.4.1(a). Several ~ 1-µm wide diamonds are observed in the Si fields in the SEM image; these may be a result of nano-diamonds which either remain following the seeding process or which redeposit during the initial diamond growth stage. We find that the unwanted seeding density depends on the resist removal efficacy, supporting the former interpretation but

without ruling out the latter. Stripes are perpendicular to the (110)-oriented flat on the Si wafer so that micro-Raman images, described below, are along a ⟨110⟩ direction that we denote x' = [110]. In Fig.4.1(c) we show an AFM image of a representative 20-μm wide stripe. From AFM images, we determine nominal thickness of 1.5 μm and from 10-μm × 10-μm scan areas (not shown) the root-mean squared (RMS) roughness of the diamond is ~ 80 nm. The micron-scale polycrystals achieved under these growth conditions are shown in Fig.4.1(d) from a close-up plan-view SEM image of the diamond-covered surface.

Micro-Raman spectroscopy is powerful for assessing diamond material quality and for measuring both global and local mechanical stress[111]. Extensive research has been conducted on stress measurements of CVD diamond[177] and Si[178] based on Raman spectroscopy. Here we employ UV micro-Raman imaging, with excitation wavelength 363.8 nm, for two specific reasons. First, the low fluorescence background from diamond allows simultaneous observation of sharp O(Γ)-symmetry phonons in silicon (520 cm^{-1}) and diamond (1332 cm^{-1}), and the broad non-diamond carbon (NDC) spectrum (1450-1600 cm^{-1})[69]. The second reason is the shallow 5-nm penetration depth at this wavelength in Si which permits study of the topmost Si[179], where stress is expected to be most significant. An imaging line focus[118] was implemented to subtend, and thereby simultaneously map, stress along the full lateral width of the diamond stripe in a single acquisition. Spectra collected in this mode generate a 400×1340 pixels image using a charge-coupled device detector. The image spans the stripe in x' direction with the Raman spectra dispersed in the longer dimension of the detector. This approach extensively simplifies performing line maps and obviates concerns of laser heating since the power density at the sample surface is < 10 $\mu W/\mu m^2$. Full line image accumulation required from

1 to 10 min acquisition time.

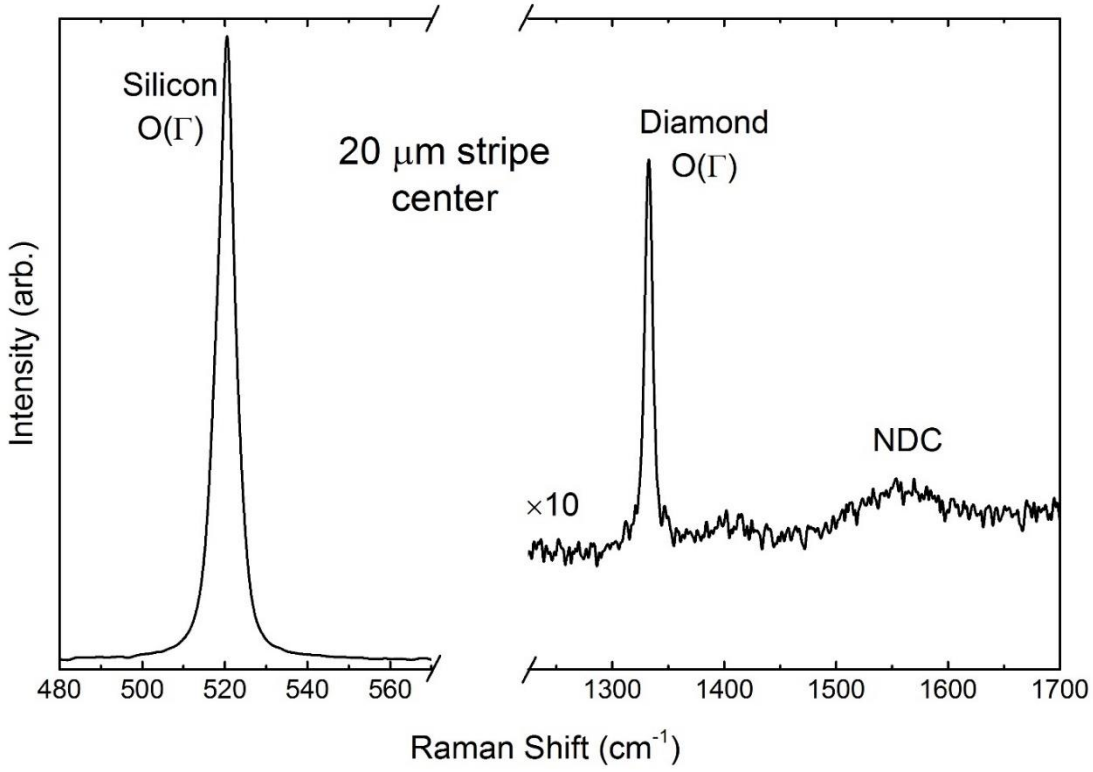

Figure 4. 2. Raman spectrum obtained from the line image at the center of the 20-μm wide diamond stripe.

Figure 4. 2 shows a typical Raman spectrum (polarization not analyzed) extracted from the line image corresponding to the center of the 20-μm wide diamond stripe. Clearly seen are the silicon and diamond phonons and the broad Raman scatter from NDC. The O(Γ)-symmetry phonons are each fit using a single Lorentzian line shape. The line widths near the stripe centers are ~ 6.4 cm^{-1} for silicon and ~ 8.2 cm^{-1} for diamond without correcting for instrumental response. The setup permits observation of shifts ≤ 0.1 cm^{-1} with silicon and diamond position uncertainty of 0.02 cm^{-1} based on fits to the data. In the case of uniform layer coverage, the Raman shift may be used to estimate biaxial stress via

$$\sigma_B = -k_R(\omega - \omega_o) = -k_R\Delta\omega \qquad (4.1)$$

where k_R is the Raman stress factor for either silicon or diamond and $\Delta\omega$ is the frequency shift from the corresponding strain-relaxed material. A red shift in the Raman peak position corresponds to tensile stress ($\sigma_B > 0$), while a blue shift corresponds to compressive stress ($\sigma_B < 0$). Values for ω_0 were obtained immediately prior to each measurement using bulk silicon and natural diamond reference samples.

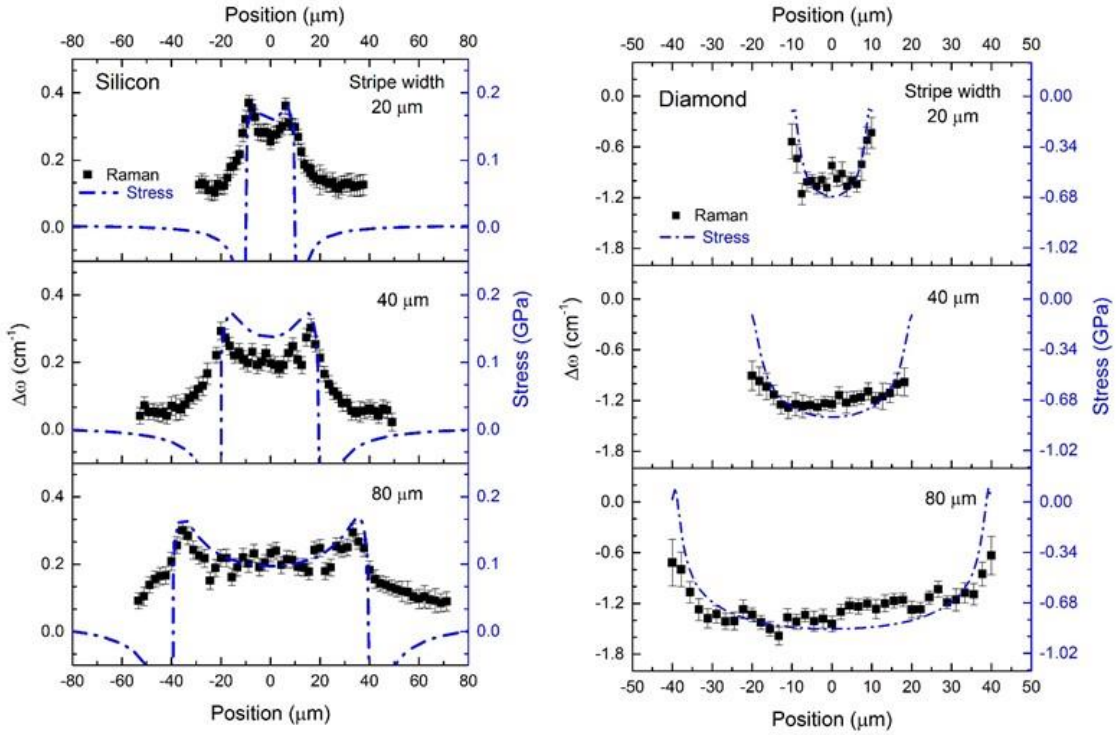

Figure 4. 3. FE simulation (dot-dashed lines) and Raman measurement (discrete points) stress maps of the silicon and diamond as a function of position across three representative widths; 20, 40, and 80 μm.

Mapping transverse to the diamond stripe produces a stress map of the silicon and diamond, as presented in Fig.4.3 as a function of position across three representative widths 20, 40, and 80 μm. The left- and right-hand series of panels are for silicon and diamond, respectively. Note that the scales are different for each panel series. Raw data of change in

Raman shift, $\Delta\omega$, versus position are shown as points. Individual values correspond to an average of five detector pixels, corresponding to a distance of ~ 2.3 μm, which is close to the measured optical resolution of the microscope. A systematic variation in stress is observed in each panel. For the diamond, the maximum shift (compressive stress) occurs near the center of each stripe and diminishes close to the edges due to the available free sidewall surfaces which permit relaxation through less constrained expansion. The relatively smaller shifts observed in Si beneath the diamond correspond to a lower tensile stress. Close to the edge of each stripe an enhancement of the shift (stress) in silicon is observed due to the edge discontinuity. Separate measurements confirm that stress in silicon relaxes far from the diamond stripes.

Thermal stresses due to cooling from the CVD growth temperature and room temperature were simulated using a two-dimensional (2D) finite element (FE) analysis (COMSOL 5.2). To calculate thermal stresses, temperature-dependent CTEs were employed using data published for both silicon[123] and diamond[124]. Other material parameters for CVD diamond were taken from Hess *et al.*[126] and elastic moduli for Si were taken from Hopcroft *et al*.[127] The simulated thermal stress $\sigma_{x'x'}$ is representative of the lateral dependence expected within the diamond and silicon due to the selective growth and is found to compare well with our experimental results.

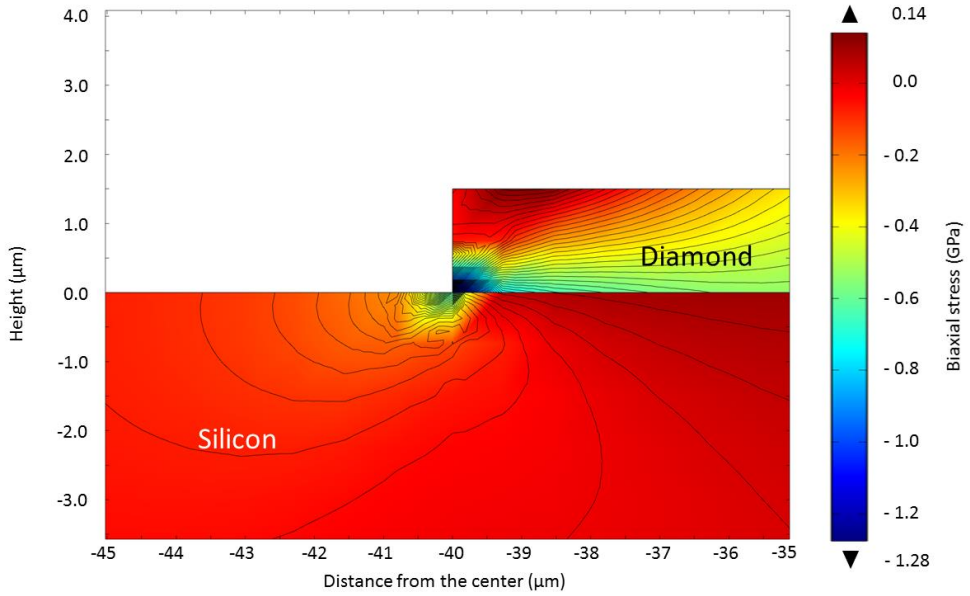

Figure 4. 4. 2D stress simulation results near the edge of an 80μm wide and 1.5 μm thick diamond stripe grown on a 500 μm thick Si substrate.

Figure 4.4 shows a representative 2D simulation of in-plane stress perpendicular to the stripe and near its edge. The diamond stress is enhanced near the edge of the stripe close to the interface with silicon but relaxes in the unconstrained corner region of the diamond. The lateral (x') extent of the relaxed diamond corner is several times the 1.5-μm thickness, as expected for a "hard" stripe on "soft" substrate in the line-force model[180]. Far from the diamond the stress is relaxed in silicon. The stress in the diamond exhibits better uniformity at distances far from the stripe edge. Stress is also present in the silicon immediately beneath the diamond and relaxes by a factor of ~1/3 at a depth of 5 μm (not shown).

To compare computed stress with our measurements, we examine horizontal cut lines at select depths following the simulation. For the transparent diamond, we average the results of cut lines from five depths throughout the diamond. In silicon, optical

attenuation weights the observed stress according to

$$\langle \sigma_{x'x'}(Si) \rangle = \frac{\int_0^\infty \sigma_{x'x'}(z) e^{-z/d_{OPT}} dz}{\int_0^\infty e^{-z/d_{OPT}} dz} \quad (4.2)$$

where z = 0 corresponds to the interface, z > 0 is depth within the silicon, and $d_{OPT} = 1/(\alpha_L + \alpha_S) \approx 5$ nm is the net optical penetration depth. Published absorption coefficients $\alpha_{L(S)}$ are taken at the incident laser (L) and scattered (S) wavelengths[181]. To approximate Eq. (2) we extract cut lines at ten z values spaced 1 nm apart and compute the weighted average. For both diamond and silicon, we perform a horizontal boxcar average with bin size corresponding to the ~ 2-μm resolution of our instrumentation. The boxcar averaging has little effect on the diamond stress profile, while for silicon it has the effect of smoothing the stress enhancement near the stripe edge. The averaging approach has the added benefit of reducing the impact of mesh-related effects in the FE method.

Returning to Fig.4.3, the simulated stresses are shown as dot-dashed lines. Scaling of the shift in Raman position with stress is accomplished by direct application of Eq. (1) and published stress factors k_R = 0.434 GPa/cm^{-1} for Si[178] and 0.57 GPa/cm^{-1} for diamond[122]. The good overall agreement confirms the stress in our diamond stripes to be primarily thermal in origin. The Raman-stress estimate obtained using Eq. (1) is not improved when we apply the more detailed analysis of Ref.[182][183]. We therefore restrict ourselves to the simple approach. For diamond, stress toward the center of each stripe is greatest and decreases with narrower stripe width. This is phenomenologically due to the greater relative factor of available free-surface sidewalls for strain relaxation. There is also a ~ 0.1 GPa discrepancy between simulation and data toward the stripe centers which may be due to slight relaxation into available free volume within the polycrystalline diamond. It is also seen from Fig.4.3 that the tensile stress in Si increases as the width of

the stripes decreases due to the influence of both edges of the diamond stripe which concentrate the tensile stress in the substrate. This concentration of stress increases for smaller stripe width. We note that our measurements did not reveal the simulated compressive stress spikes present in the silicon beneath the stripe edges. This compression compensates for the stress which would otherwise be provided by the diamond in a uniform layer. A possible interpretation of this discrepancy is the relatively ragged diamond stripe edges, which will blur dependences there and even mix stress components due to the local normal to the stripes. To check this possible explanation, a 3D FE model was produced incorporating a simple zigzag edge for the diamond stripe. We average stress in the silicon using a lateral window and Eq. (2) vertically, as described for the sharp diamond stripe simulations. Stress in the diamond and in silicon beneath the stripe are not significantly affected when simulating the zigzag. Furthermore, we obtain a reduction in the compressive stress spike to ~ ¼ the simulated value for a sharp edge. However, the zigzag does not completely eliminate the presence of the spike. We also mention that the $\sigma_{x'z}$ torsion stress, when present during high-temperature processing, is known to enhance dislocation formation in the silicon near a stripe edge[180]. Since our study shows the stresses are resulting from diamond stripe growth are thermal, we rule out formation of dense dislocations at high temperature as a potential stress-relaxation mechanism in silicon beneath the diamond stripe edge.

4.4 Conclusion

In summary, we have applied a bottom-up approach for selective CVD growth of polycrystalline diamond on silicon substrates. Well-defined stripes are demonstrated with

uniform widths as small as ~ 20 μm. UV micro-Raman maps are employed to investigate stress throughout the diamond and in the silicon just beneath the stripes. Measurements are well-described using simulated thermal stress distributions across the diamond stripes with various widths. Both simulation and experimental results indicate that compressive stress on CVD diamond reaches a maximum value in the center of the stripe and relaxes at the edges. Stress in the silicon is highest at the diamond stripe edge interface and drops rapidly with depth. Far from the diamond stripes, the stress in silicon is relaxed.

V. HIGH RESOLUTION SELECTIVE AREA DEPOSITION OF HOT FILAMENT CVD DIAMOND ON 100mm MOCVD GROWN ALGAN/GAN WAFERS

In this chapter, a new technique has been reported for selectively depositing hot filament chemical vapor deposited (HFCVD) polycrystalline diamond on metalorganic chemical vapor deposited (MOCVD) AlGaN/GaN on 100 mm Si(111) wafers without damaging the underlying III-Nitride layers. Photolithography and reactive ion etching based selective seeding of nano diamond were employed before diamond deposition. Significant etching of the AlGaN and GaN layers were observed from scanning electron microscopy (SEM), visible Raman spectroscopy and high-resolution X-ray diffraction (HRXRD) results when no protective layer was implemented prior to diamond deposition and when methane concentration was 1.5% in hydrogen during HFCVD. To mitigate this problem, a thin layer of plasma enhanced CVD SiN_x was deposited on the AlGaN/GaN wafer prior to seeding and diamond deposition. Methane concentration was also increased to 3.0% to achieve increased diamond growth rate and faster surface coverage. Diamond films with excellent selectivity and minimal surface damage were achieved due to the protective layer and faster surface coverage with increased methane concentration. Damage mitigation was confirmed by comparison of atomic force microscopy (AFM), HRXRD and visible Raman spectroscopy data collected before and after diamond deposition, and by SEM images of the final structures. Elimination of surface damage during diamond deposition was confirmed from HRXRD reciprocal space map (RSM) of asymmetric (114) reflections of ~25 nm thick top AlGaN barrier layer. A minimum diamond feature size of ~ 1 μm was confirmed from SEM measurements.

5. 1. Introduction

AlGaN/ GaN based high power and high frequency electronic devices have demonstrated superior performance in terms of power density and operating frequency when compared to other semiconductor materials[1]. The capabilities of these devices are often limited by "self-heating" effects resulting from joule heating at the high carrier channel region because of increased phonon scattering at high applied field[76]. Poor thermal conductivity and high thermal boundary resistance of materials underneath the channel layer is the primary reason for "self-heating"[184][66]. Significant research efforts have been undertaken throughout the last decade and several approaches have been adopted to alleviate this problem, principally by placing an efficient heat spreader such as diamond very close to the heat source[12].

Chemical vapor deposition (CVD) of polycrystalline diamond having thermal conductivity very close to single crystalline diamond has made this technology even more attractive from a manufacturing point of view[132][48][25]. Among the many developed processes to combine GaN-Diamond materials systems, growth of CVD diamond over the processed AlGaN/ GaN HEMT wafer has gained recent popularity due to its scalability and better wafer bow management [76][185]. Significant improvement in terms of power density and operating frequency have been reported when this technique was used to deposit a diamond heat spreader on AlGaN/GaN high electron mobility transistors (HEMT) [78][79]. CVD diamond was deposited via low temperature plasma enhanced CVD (PECVD) and patterning was conducted after diamond deposition in the reported results[76]. From a practical point of view, however, significant challenges still exist in realizing this material system, principally because of damage to the nitride semiconductor

during diamond CVD and the difficulty of patterning diamond on nitride semiconductors[78][79]. For example, hot filament CVD (HFCVD) diamond is better in terms of cost and scalability but has a deteriorating effect on GaN because GaN is decomposed at such environment[75]. HFCVD usually takes place at substrate temperatures above 700 °C with an excess flow of energetic atomic hydrogen through the very hot (2000-2200 °C) filament array [150]. Thermal decomposition of GaN also occurs in such an environment [75]. Furthermore, patterning of CVD diamond films with high energy reactive ion etching can also create damage in the underlying AlGaN/GaN layers. The two dimensional electron gas (2DEG) channel forms in the GaN due to spontaneous and piezoelectric polarization when a thin (20-25nm) AlGaN barrier layer is deposited on top of highly crystalline GaN and this 2DEG resides at only ~15-30 nm from the surface of the HEMT wafer [2][34]. Therefore, it is critical to minimize damage to the AlGaN/GaN layers while selectively depositing diamond in order to leverage the tremendous thermal conductivity for reducing self-heating without deteriorating the AlGaN/GaN 2DEG properties.

Direct growth of diamond on GaN has been reported using HFCVD[75] and PECVD[48], and significant surface damage/etching was observed in both cases. The presence of atomic hydrogen in the plasma was responsible for etching in the case of microwave PECVD. For HFCVD, the etching effect is even more severe because of the simultaneous impacts of the hot filament temperature and energetic hydrogen atoms. A protective layer is therefore necessary to protect the underlying III-Nitride layers during diamond deposition[76]. Al_2O_3, SiO_x and SiN_x are some of the protective layers investigated for this purpose[76]. One drawback of using such protective layers is their

poor thermal conductivity and thermal boundary resistance that hampers the efficient heat removal capability of the deposited diamond[25][185]. Therefore, this layer should be as thin as possible to fully utilize diamond's excellent thermal conductivity[25].

Another potential approach for reducing damage while growing diamond-on-GaN is to use a higher methane concentration[75]. In general, higher methane concentration results in a higher growth rate and, therefore, faster surface coverage due to the increase in available methyl radicals[141]. However, the non-diamond carbon (NDC) percentage increases when methane concentration increases[141]. It has been reported that the best quality diamond, in terms of NDC (or sp^3/sp^2 bonding), occurs when 1-3% methane is used with hydrogen[147]. Therefore, by depositing a thin protective layer on top of the III-Nitride surface before diamond seeding and using a higher methane concentration during diamond deposition, a diamond-on-HEMT wafer may be produced without damaging the underlying layers. Selectively patterning diamond seed should be more effective than patterning and etching a polycrystalline diamond film because the removal of seed from the dielectric-protected exposed region via photoresist and lithography processes is easier to control and utilizes lower-energy processes than removing the coalesced, fully formed, diamond via aggressive etching and, therefore, damage to the III-Nitride layers would be minimal.

In this study, we have demonstrated selective deposition of thin HFCVD diamond on 100 mm AlGaN/GaN HEMT wafers without damaging the thin AlGaN barrier layer or GaN channel layer. Initially, experiments were performed to ascertain surface damage of the III-Nitride layers when no protection layer was used and the methane concentration was low (1.5%) in HFCVD. Increasing methane concentration to 3.0% and utilizing a thin

dielectric layer of PECVD SiN_x resulted in increased selectivity and reduced surface damage. Increased selectivity and elimination of surface damage were confirmed by comparing morphology, and structural and optical characteristics obtained before and after diamond growth.

5. 2. Experimental

5.2.1 Selective area deposition of diamond

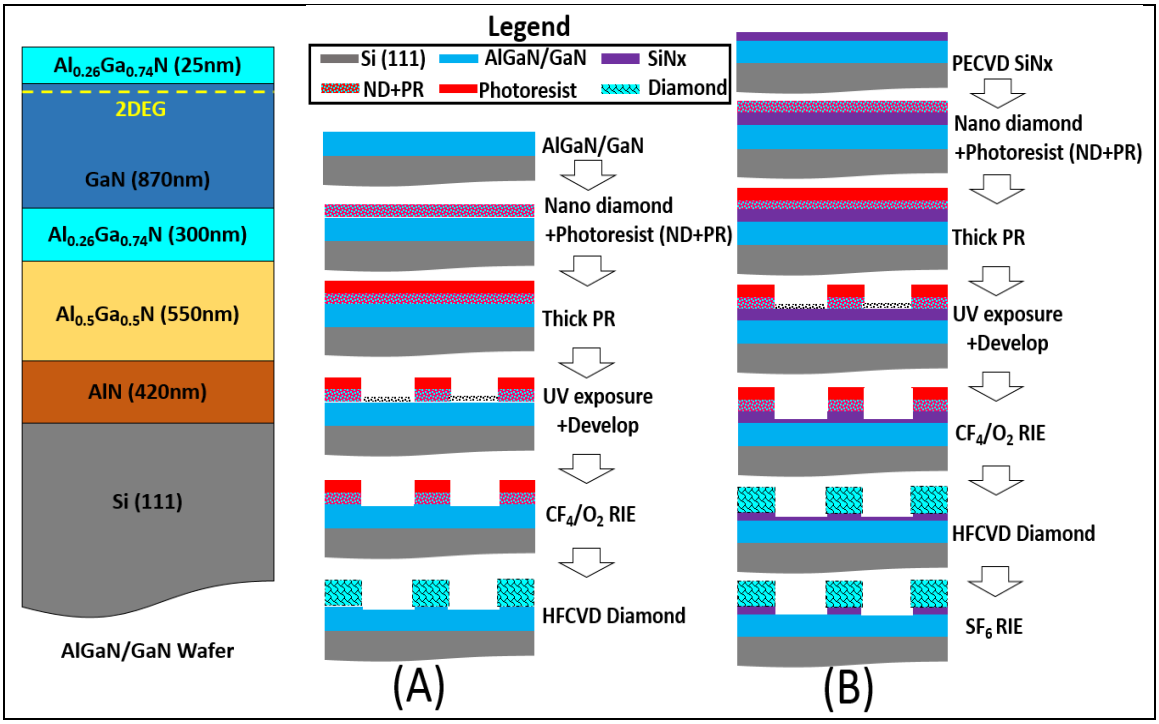

Figure 5. 1. Schematic representations of the AlGaN/GaN structure and selective area diamond deposition process employing, (A) no surface protection layer, and (B) PECVD grown SiN_x protective layer.

Selective deposition of CVD diamond stripes was performed on AlGaN/GaN wafers grown by MOCVD on 100 mm Si(111) wafers. The AlGaN/GaN HEMT structure, shown in Fig.5.1, was grown in a cold wall vertical flow MOCVD system. III-Nitride growth began by depositing a 420 nm AlN nucleation layer followed by two AlGaN alloyed layers of thicknesses ~550 nm and ~300 nm with 50% and 74% GaN, respectively. These layers are

also known as transition layers (TLs) and are mainly responsible for strain relaxation. A thick (~870 nm) GaN buffer layer was deposited to produce reduce dislocation density in the GaN epilayer which is beneficial for high electron mobility. Finally, a 25 nm $Al_{0.26}Ga_{0.74}N$ barrier layer was deposited on the buffer layer which instigates piezoelectric polarization and the formation of a 2DEG near the AlGaN/GaN interface, within the GaN. Finally, a very thin (3-4nm) GaN cap layer (not shown in Fig.5.1) was grown to reduce surface roughness. The growth temperature of the III-Nitride layers ranged from 950 to 1020 °C, while the V/III mole ratio was controlled from 1900 to 8000 and the chamber pressure was 30-100 torr. For all experiments, the III-Nitride growth conditions were held constant.

Selective area diamond growth was conducted via patterning the wafer with nano diamond seeds using standard photolithography techniques as shown in Figs. 1(A) and (B). Dimethyl sulfoxide (DMSO) based nano diamond suspension (ND) with 0.5 wt.% nano diamond seeds (seed size ~4 nm and average aggregate size of 20-30 nm) was used as the seed source which was mixed with S1813 photoresist. A 5 mL photoresist solution containing 3 mL of S1813, 1 mL of DMSO and 1 mL of ND was then sonicated for 30 min. The energy provided by the ultrasonic bath helps break the larger clusters of nano diamond seeds (> 20 nm) [46]. Since DMSO's freezing point is 18.5 °C, the solution was then pre-heated at 60 $^{\circ}$C for 1 min to avoid any non-uniformity or striation effect during spin coating. However, the suspension should not be over heated at this step because this might crosslink the photoresist and make the resist insensitive to UV exposure. It is important to note that the cleanroom temperature and humidity were maintained at 16-22 °C and 65-70%, respectively, because these parameters affect the uniformity of photoresist

dispersion across the wafer. The photoresist was then spun-coated on the wafer and soft baked at 115 °C for 90 seconds. I-line UV exposure was performed using a SUSS Microtech contact aligner. MF CD 26 (Dow Chemical Inc.) developer was used for developing the wafer. The lithography steps for both processes, A and B in Fig.5.1, are identical through this stage, and the photoresist and the majority of ND seeds were cleared from the exposed regions (data not shown).

Continuing with process A, in order to get absolute selectivity and to clear all remaining seeds from the exposed regions, the wafer was then plasma etched in an Oxford Reactive Ion Etching (RIE) chamber. RIE and inductive coupled plasma (ICP) power was 50 W and 500 W, respectively, and the chamber pressure was 20 mTorr. A mixture of 45 sccm of CF_4 and 5 sccm of O_2 was used as etching reagents [98] and the etch time was 30 s. This low energy etching process with short time duration effectively removed nano diamond seeds without incurring damage to the III-Nitride layers. This is primarily due to III-Nitride material not being affected by CF_4 at low plasma power. For comparison, even at high RIE and ICP power (more than 100W and 1000W respectively), the GaN etch rate is less than 1nm/min [186]. The thin, intact and undamaged AlGaN barrier layer was confirmed by x-ray diffraction (discussed later).

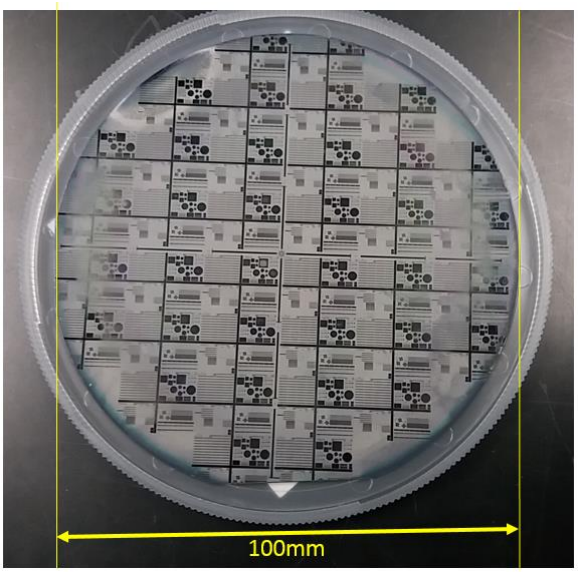

Figure 5. 2. Selectively deposited HFCVD diamond on a 100 mm AlGaN/GaN wafer using process B.

The wafer was then loaded into the HFCVD chamber. The HFCVD system is a custom-built shower head design where 9 tungsten wires with 0.25 mm diameter were used with a separation of 1 cm. The distance between the wafer and filament was kept at 6 mm. At peak power, the hot filament temperature reaches 2200 °C, resulting in a substrate temperature of 720-750 °C. Published data suggests that the best quality diamond (in terms of non-diamond carbon (NDC) percentage) by HFCVD occurs when 1-3% CH_4 is used [42]. It is well known that lower methane concentration results in better quality diamond and, furthermore, our previous Raman measurement results (chapter 3) indicated highest quality diamond with 1.5% methane. Based on these data, we grew diamond in process A using 1.5% methane. The growth conditions were: i=100 A, V= 63 V, 2 slm H_2, 30 sccm CH_4 (1.5%) and 3 sccm of O_2. The growth time was 6 hours to ensure diamond coalescence and complete coverage, based on previous growth rate calibration measurements.

In the second seeding approach, process B, a thin (~100 nm) SiN_x was deposited on the AlGaN/GaN wafer using PECVD to protect the GaN during diamond deposition.

The PECVD conditions were: 3 sccm NH_3 and 1 sccm SiH_4 diluted with 19 sccm H_2. RF power was maintained at 50 W with a temperature of 300 °C and a pressure of 300 mTorr. The SiN_x thickness non-uniformity was < 5% across the 100 mm wafer. The wafer was then seeded in a similar approach as described for process A, and shown in Fig.5.1(B). However, the etch scheme was different for seeding process B. Plasma etching was performed using the same gas chemistry and pressure as process A. However, an ICP/RIE power of 100 W / 1000 W was used to etch 70-75 nm into the SiN_x in 30 s on the photoresist developed regions. A thin layer of unetched SiN_x (25-30 nm) was left after RIE on the exposed region to protect the underlying III-Nitride layers. HFCVD diamond deposition was performed on the process B wafers with 3.0% methane (60 sccm). A 2 hours growth resulted in diamond coalescence and complete coverage across the seeded regions. The higher methane flow was intentional because, as discussed previously, increased methane concentration results in higher growth rate, faster surface coverage and, in principle, reduced damage to the underlying III-Nitride layers. Fig.5.2 shows a 100 mm AlGaN/GaN wafer with ~500-650 nm thick diamond layer selectively deposited. The GaN-diamond wafers using processes A and B will be referred to as GaN-A and GaN-B, respectively, in the remainder of the chapter.

5.2.2 Characterization techniques

The morphology and thickness of the diamond film was characterized with scanning electron microscopy (SEM, FEI Helios 400) an atomic force microscopy (AFM) (Bruker Dimension ICON) and Surface profilometer (Dektak XT). The SEM tool was also used for focus ion beam cross section of the structure. A JEOL JEM 1200 transmission electron microscopy (TEM) was also employed to obtain bright field cross section image

of the AlGaN/GaN structure. The Raman spectroscopy was measured in a Horiba Raman system equipped with a visible laser (λ = 532 nm) and the laser spot size was ~2 μm, utilizing a 100x objective lens. Raman spectra were collected from the same region on the wafers before and after diamond growth. Laser power, spot size and exposure time was kept constant for all measurements. Spectra collection was performed between 450 cm^{-1} and 850 cm^{-1} in order to observe the first order III-Nitride peaks, whereas the range was extended to 1800 cm^{-1} when spectra was collected from the diamond coated region, to capture NDC peaks at ~1450-1600 cm^{-1}.

High resolution XRD (HRXRD) measurements and reciprocal space mapping (RSM) were performed on a SmartLab XRD system (Rigaku Corporation) with Cu Kα radiation (λ = 1.540562 Å) using a Ge (220) 2-bounce monochromator with 0.5 mm incident slit opening. A wide angle θ-2θ HRXRD scan from 25° to 90° and an extended rocking curve (ω scan) from (2θ =) 34° to 37° (around the symmetric (002) reflections) were performed. ω scan of any peak is performed by positioning the XRD source to a specific 2θ angle and then rocking the detector (variation in ω) around that peak. Moving ω while keeping 2θ fixed makes a travel in the reciprocal space that is a circumference around the ideal position of the diffraction peak. The full width at half maxima (FWHM) of peak obtained in such a scan represents how disperse is the orientation of the corresponding planes. A rapid drop of the intensity means small dispersion, and a slow drop indicates a large dispersion. Since the thin AlGaN barrier layer cannot be resolved in the symmetric scan, RSM of the asymmetric (114) reflection in ω-2θ mode was measured [187]. The RSM data was analyzed to determine the degree of etching of the AlGaN barrier layer [34].

5.3. Results

5.3.1 Selective deposition of diamond without a protective layer

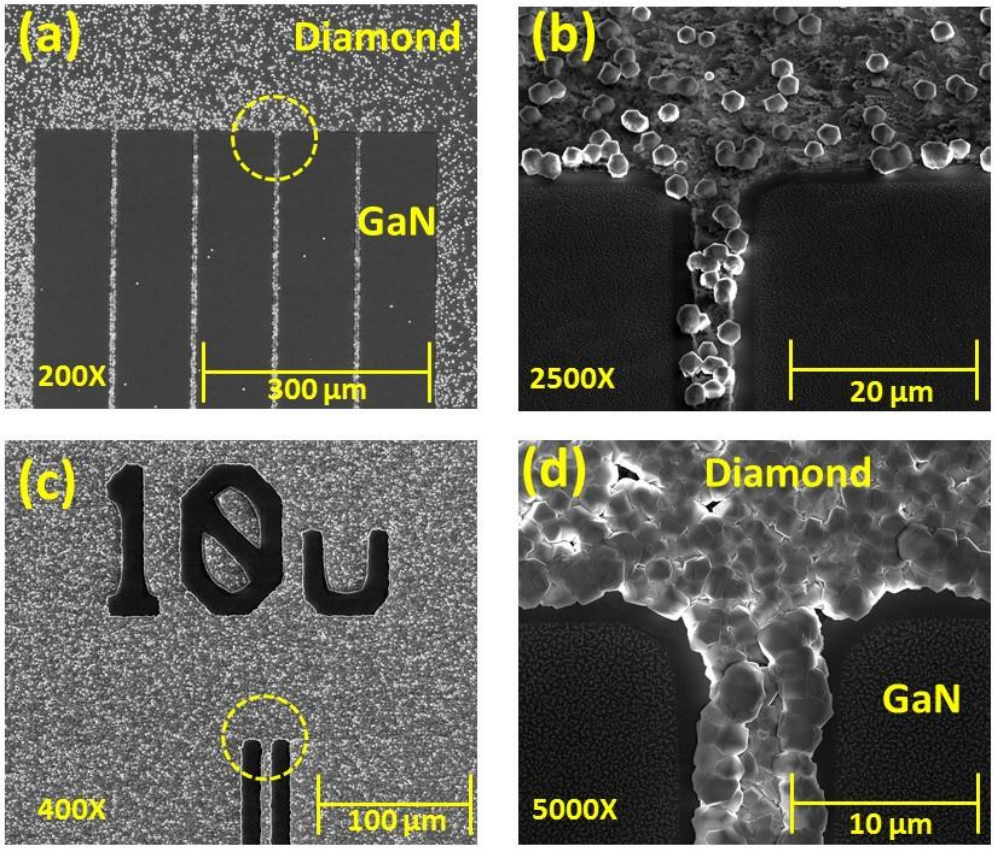

Figure 5. 3. SEM images taken from wafer GaN-A indicating, (a) poor selectivity, (b) close-up view of circled region in (a) exhibiting poor coverage and surface damage to GaN; (c) relatively better coverage region; and (d) closed-up view of circled region in (c) exhibiting non-uniform selectivity and III-Nitride surface damage.

Fig.5.3 shows SEM images taken from two regions at ~ 30 mm from the center of the GaN-A wafer. Significant etching of the III-Nitride layers was observed, as seen in Fig.5.3(a) and from the magnified region in Fig.5.3(b). Diamond coverage was poor in most of the regions on the wafer. The observed poor diamond coverage in Fig.5.3(a) and (b) indicates very poor nucleation of diamond on these regions. Direct nucleation of diamond on GaN has been reported to be very difficult to achieve due to poor adhesion of diamond seeds with GaN surface as a result of surface decomposition in H_2-rich HFCVD environment[76].

Besides, the density of seeds on the center and middle region (0-30mm) of the wafer is relatively low compared to edge region because the spin coating process moves majority of the seed containing photoresist towards the edge region where more seeds accumulates. The observed poor diamond coverage is believed to be due to mainly GaN decomposition and low seeding density to a lower extent. It is interesting to note that relatively better coverage was observed in edge regions of the wafer (~40-48mm from wafer center) but such regions were randomly distributed across the wafer. Figs. 3(c) and (d) shows such a region and its elaborated view. Damaged III-Nitride surface and poor diamond coverage, as shown in Fig.5.3, indicate GaN decomposition is occurring in the CVD diamond deposition environment [74]. Furthermore, while delamination of diamond from the III-Nitride surface was not uniformly observed across the wafer, there were regions where the diamond edges were peeling back from the surface. One such region is observed in Fig.5.3(c) along the diamond edge of "10u" mark. The peeling off is clearly visible in Fig.5.3(d). The observed peeling effect was result of two important effects. The first is excessive thermal stress in diamond-GaN interface due to difference in coefficient of thermal expansion between GaN and diamond. The stress in the edge regions are too high because there was no nearby diamond to mitigate the stress. The second region is micro loading of CVD diamond features. Micro loading occurs during CVD process when active reactant (methyl radicals in case of diamond deposition) reaches the substrate and find very small regions to nucleated. Reactants reaches the substrate at same rate but those who land on a non-seeded region keep traveling until a they find a diamond nucleation site. The reactants make chemical bond as soon as they find any nucleation site. Due to this reason diamond thickness gets higher in the edge region. Due to excessive diamond growth at the

edge regions, more thermal stress is induced and the diamond at the edges try to relax the stress by peeling off from the surface.

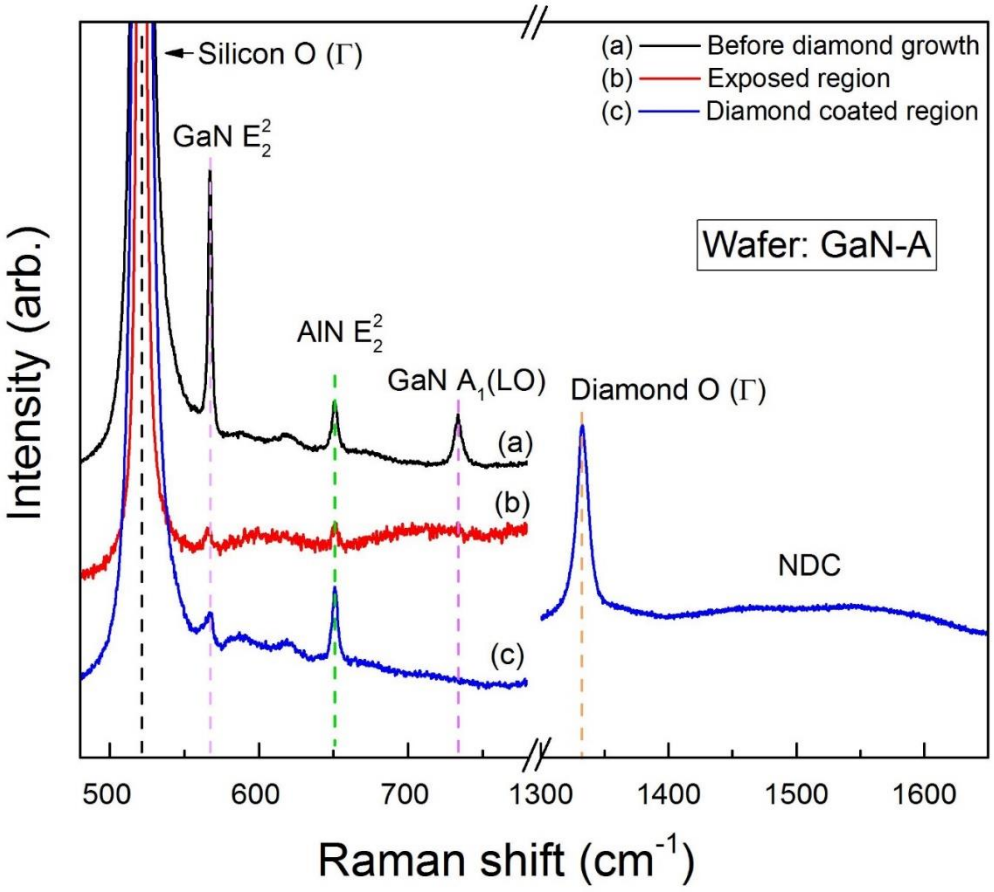

Figure 5. 4. Visible Raman (532 nm) spectra collected from middle region (30mm from the wafer center) of wafer GaN-A: (a) before diamond deposition and, (b) exposed region and (c) diamond coated region after selective diamond deposition for 6 hours with 1.5% methane.

The damage in the underlying III-Nitride layers was also confirmed from Raman measurement results as shown in Fig.5.4. Spectra (a), (b) and (c) on Fig.5.4 represents Raman spectra collected from the middle region (~30 mm from center of wafer GaN-A) before diamond deposition, exposed region after selective diamond deposition and diamond coated region after selective diamond deposition, respectively. Raman spectrum (a), collected before diamond deposition, exhibits Raman peaks for GaN (E_2^2), AlN (E_2^2), and GaN A_1 (LO) phonon at ~ 567.5 cm^{-1}, ~650.3 cm^{-1} and ~733.5 cm^{-1}, respectively.

Here, the superscript 2 of the E_2 phonon represents high frequency phonon. In addition to these peaks, very intense Si O (Γ) peak was also visible at ~520.6 cm^{-1}. Exact peak positions were obtained by fitting the spectra with a Lorentzian function and are noted in Table 5.1. Raman spectra were collected from the same region after selective deposition of CVD diamond for 6 hours with 1.5% methane. Raman spectrum (b) was collected from an exposed (open window) region on the wafer. Only the GaN and AlN E_2^2 peaks were visible while the A_1 (LO) of GaN was no longer present. This is expected because the E_2^2 peak of GaN is the most dominant phonon peak that can be visible in backscatter geometry[188] along the *'c'* axis. Furthermore, the intensities of the III-Nitride peaks were reduced significantly indicating primarily loss of III-Nitride materials from the region examined. Raman spectrum collected from the diamond covered region is shown as spectrum (c). Similar to spectrum (b), only the GaN and AlN E_2^2 peak was visible (the intensity of GaN A1 peak was insignificant compared to other peaks), while a sharp diamond peak at ~1332.7 cm^{-1} and a broad NDC peak at 1450-1600 cm^{-1} were also present. The intensity of the AlN (E_2^2) peak was high compared to the GaN (E_2^2) which is believed to be due to significant etching of the upper GaN layer. Furthermore, comparing the AlN (E_2^2) peaks of the three spectra, it was confirmed that etching and damage of the AlN layer is occurring in the exposed regions, but is not significantly etched or damaged in the diamond coated region.

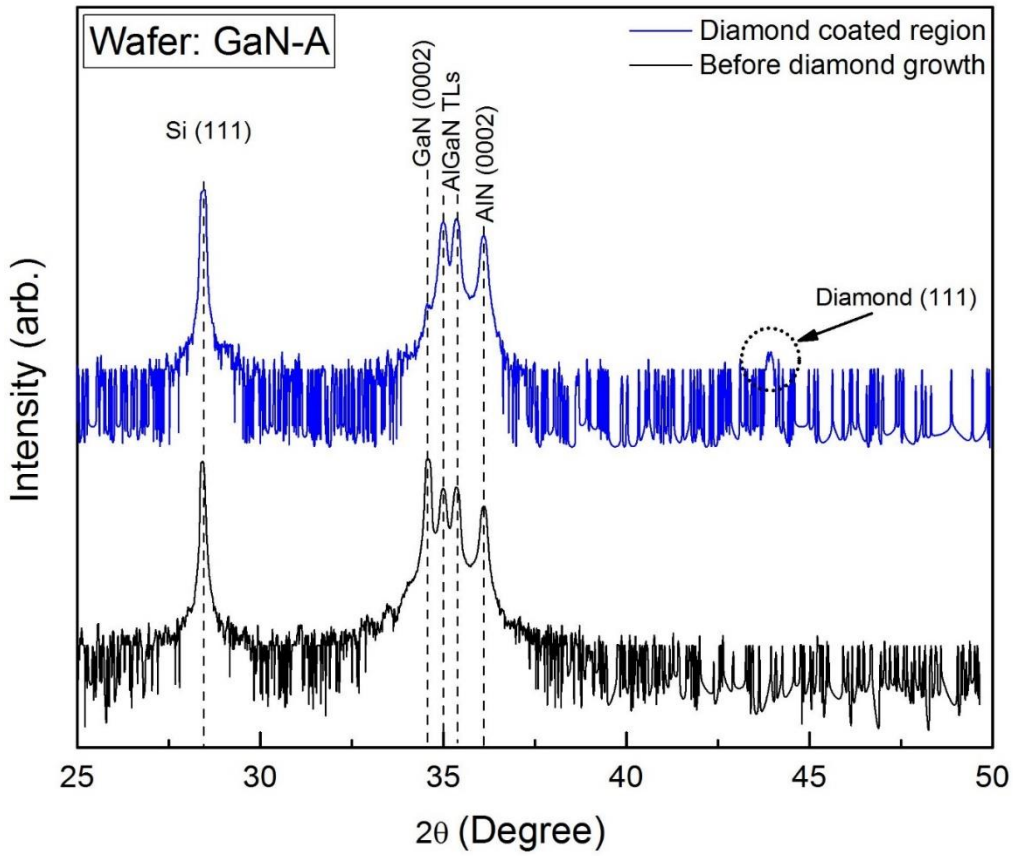

Figure 5. 5. HRXRD spectra collected from the middle region (~30 mm from wafer center) of wafer GaN-A before and after diamond deposition.

HRXRD spectra collected from wafer GaN-A before and after diamond deposition are shown in Fig.5.5. The monochromator, placed in the path of the incident x-ray beam, allows discrimination of the closely spaced (0002) GaN, (0002) AlGaN TLs and (0002) AlN peaks. In addition, the (111) diamond peak was also visible at ~43.9°. While the diamond layer was polycrystalline, the relative diffraction dominance of this crystallographic plane compared to the other diamond planes (e.g., (220) and (311)), coupled with the relatively thin diamond film, resulted in only the (111) orientation having sufficient diffracting x-ray intensity to be detected [144] [189]. The notable difference in the XRD spectrum taken after diamond deposition is the significant reduction of the GaN

(0002) peak intensity, by three orders of magnitude, which is another indication of GaN decomposition/etching during diamond deposition. (Since the GaN peak was severely deteriorated, even under the diamond coated region, no spectra was taken from the exposed region because Raman and SEM already confirmed GaN decomposition/etching.)

The wide angle θ-2θ scan does not provide complete information about any specific crystallographic plane because a plane may have some offset with surface normal and the peak position may reside at a different ω. The intensity of the GaN (0002) peak in the diamond coated region was significantly reduced compared to the AlGaN peak reflections however the peak is still visible in Fig.5.5 as a shoulder of the strong AlGaN peaks. Furthermore, the symmetric (0002) reflections are less sensitive to lattice strain because they solely represent the out of plane crystallographic orientation. The hexagonal III-Nitride crystal is represented by two lattice constants, '*a*' and '*c*'. '*a*' represents the basal (in-plane) lattice constant and 'c' is the unit cell height representing the out of plane lattice constant [190]. Lattice strain typically impacts '*a*' to a much greater extent than '*c*'. Therefore, the (0002) x-ray reflection does not accurately portray lattice strain. Furthermore, this effect also means the (0002) symmetric plane reflection is unable to simultaneous resolve the $Al_{0.26}Ga_{0.74}N$ transition layer and thin $Al_{0.26}Ga_{0.74}N$ barrier layer (see Fig.5.1 for reference) due to their identical alloy compositions. However, these two layers are substantially different in terms of their lattice strain which, again, is greatest in the basal lattice constant '*a*' [190].

Therefore, we have chosen the asymmetric (114) reflection for reciprocal space mapping (coupled 2θ-ω scan). The (114) crystallographic plane carries more information about lattice distortion because it is very close to the basal plane and the lattice constant

'a' found from this peak is very close to its actual value. As a result, RSM of the (114) reflection can detect the thin AlGaN barrier layer, separate and distinct from the AlGaN transition layer. Use of the (114) reflection for determining in-plane lattice strain in the AlGaN/GaN heterostructure is well established [187]. We determined the asymmetric (114) reflections of our III-Nitride structure using diffraction space simulator (DSS) embedded within the Rigaku SmartLab system. The asymmetric (114) reflections for GaN, AlN and their alloys were determined to occur when 2θ is between 82° and 87°. For all RSM measurements, the scan axis was 2θ for each ω in the range of ω = -1° to 2° with an ω step size of 0.03°. The RSM data obtained from wafer GaN-A is shown in Fig.5.6.

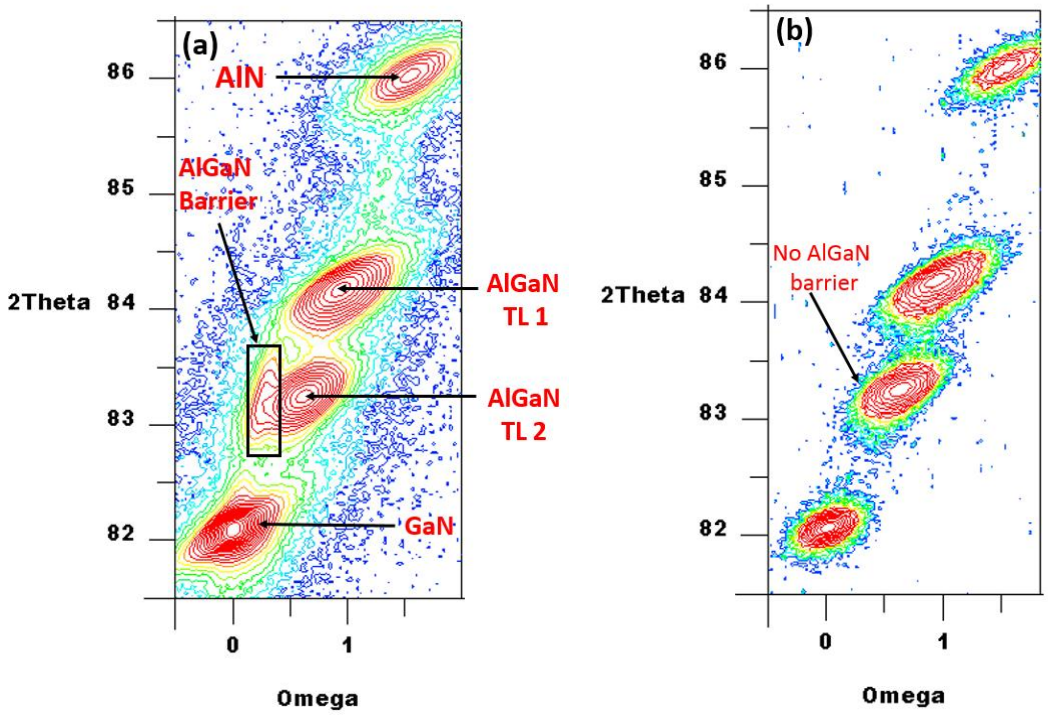

Figure 5. 6. RSM of asymmetric (114) reflection of GaN, AlN and their alloys taken from the middle region of GaN-A wafer obtained (a) before and (b) after diamond growth.

The RSM of GaN-A taken before diamond growth is shown in Fig.5.6(a). All major peaks, i.e. AlN, GaN and AlGaN TLs, along with a clear signature of the thin and strained AlGaN

barrier layer are resolved. To quantify the change in relative intensity and peak width, we calculated a relative integrated intensity ratio of GaN and AlN ($^{I_{GaN}}/_{[I_{GaN}+I_{AlN}]}$) and the results are shown in Table 5.1. RSM after diamond deposition is shown in Fig.5.6(b). No barrier layer is present after diamond deposition. The relative integrated intensity ratio of GaN and AlN has also been reduced as seen in Table 5.1. The integrated intensity of any XRD peak represents mainly crystal quality of that material. Any reduction in integrated intensity of any specific XRD peak indicates presence of defects and significant damage to the crystallinity. For crystalline GaN, defects and surface damage result in reduced integrated intensity of any XRD peak. Although the intensity of asymmetric (114) peaks were three orders of magnitude lower than the symmetric (002) peaks, the relative changes in their integrated intensities before and after diamond growth indicates significant damage to the crystal quality. Corresponding symmetric peaks showed similar trends in terms of integrated intensities indicating damage to the crystal structure of GaN.

At this point, it was clear from SEM, Raman and HRXRD results that the diamond deposition process in the CVD environment has damaged the III-Nitride structure significantly and preventive measures were necessary in order to protect the III-Nitride surface. Preventative measures included depositing a SiN_x protective layer and increasing the methane concentration. Wafer GaN-B was prepared using such an approach, as shown in Fig.5.1(B).

5.3.2 Selective deposition of diamond using SiN_x protective layer

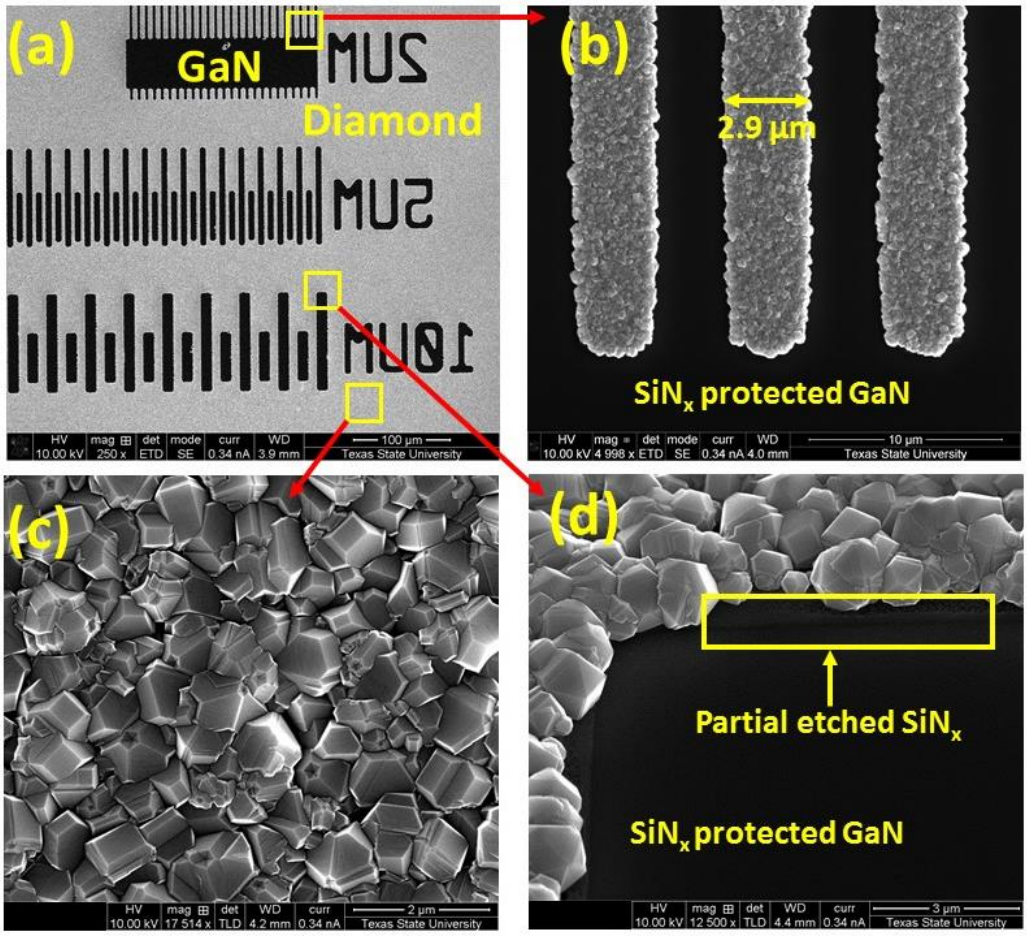

Figure 5. 7. SEM images of wafer GaN-B after diamond deposition showing (a) excellent selectivity (b) close-up view of boxed region in (a) indicating 2.9 µm wide diamond fingers; (c) close-up view of diamond region of (a) exhibiting complete coverage and random grain structure; and (d) close-up view of boxed region in (c) indicating protective SiN_x layer and smooth GaN surface.

Fig.5.7 shows SEM images taken from wafer GaN-B processed according to approach B as shown in Fig.5.1(B). Excellent cross-wafer selectivity was achieved with the smallest resolved feature size of ~1 µm. Diamond features with various shapes and dimensions were deposited successfully and no sign of diamond delamination was observed. To best illustrate the excellent selectivity, the diamond film decorating a ruler on the photolithography mask marked with 10, 5 and 2 µm scale (mirror imaged) is shown in Fig.5.7. Complete coverage of diamond was achieved as seen from Fig.5.7(c). The smooth

surface of SiN_x coated GaN region as seen in Fig.5.7(d) confirms reduced or very small etching on exposed regions during HFCVD process.

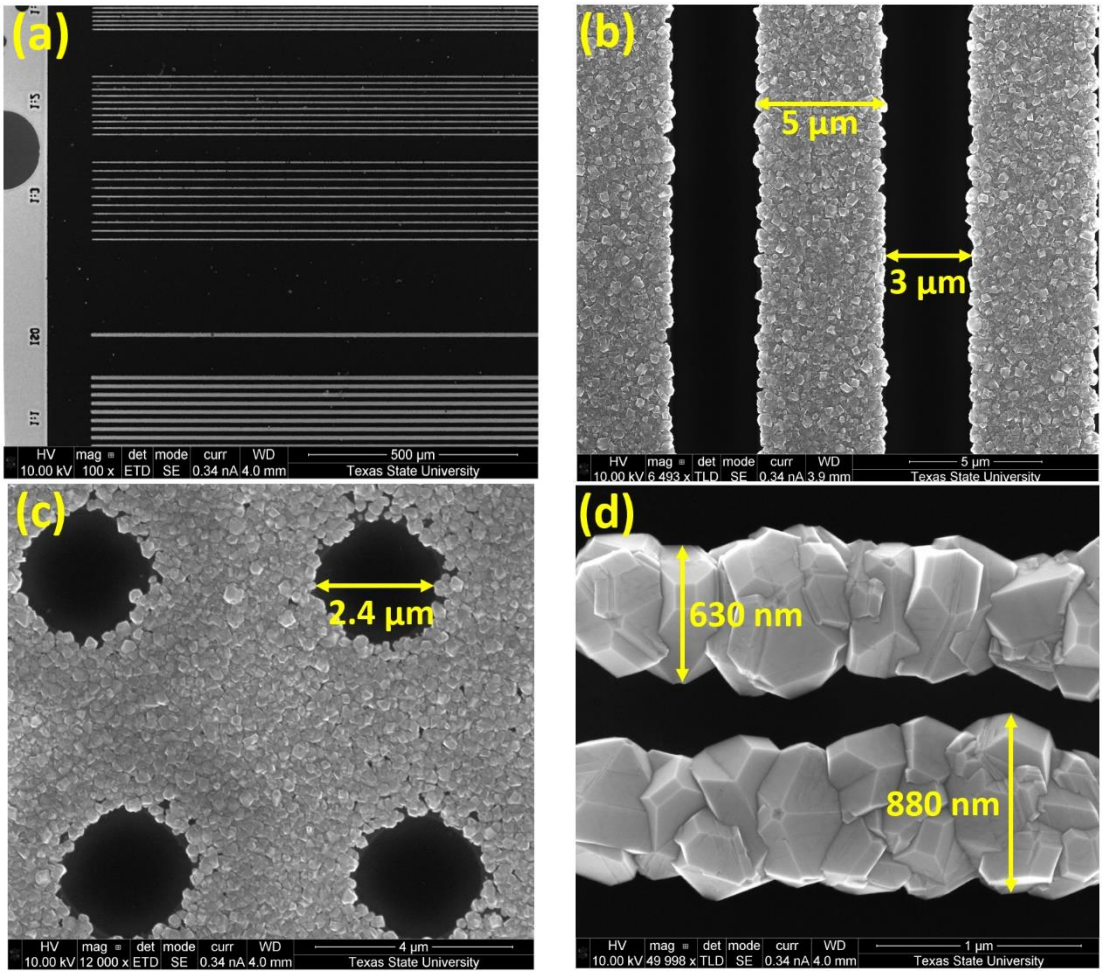

Figure 5. 8. Representative SEM images showing excellent selectivity of diamond grown on wafer GaN-B. (a) Diamond lines with various widths, (b) selectivity of a 5 µm diamond line with 3 µm gap, (c) diamond coated regions with ~2.4 µm diameter openings, and (d) smallest contiguous diamond feature size achieved.

SEM images taken across the 100 mm wafer indicate that very good selectivity was observed consistently across the wafer. Fig.5.8 shows SEM images exhibiting selectivity and various sized features achieved using Process B. Fig.5.8(a) shows diamond lines with various sizes (1-5µm) while Fig.5.8(b) shows 5 µm diamond fingers with 3 µm windows exposing the underlying III-Nitride. Windows with circular shape were also successfully

resolved and Fig.5.8(c) shows an opening with ~2.4 μm diameter. The minimum diamond dimension where a contiguous shape could be resolved was as small as 630-880 nm, as shown in Fig.5.8(d). The damage elimination was then further confirmed from comparing a cross section TEM image of the AlGaN/GaN structure and focus ion beam cross section SEM image of the diamond coated region of wafer GaN-B as shown in Fig. 5.9 (a) and (b) respectively. Comparing Fig 5.9 (b) with 5.9 (a), in addition to all Nitride semiconductor layers, clearly visible diamond layer with thickness ~500nm along with thin layer of platinum (for surface protection during FIB milling) is visible. The thin layer indicated by two parallel dotted horizontal lines in Fig. 5.9 (b) represents the remaining SiN_x and AlGaN barrier layer. The total thickness of these two layers is believed to be ~50-60nm which was not clearly visible in this image. However, GaN layer and its smooth interface with top SiN_x is clearly visible from the fig 5.9 (b).

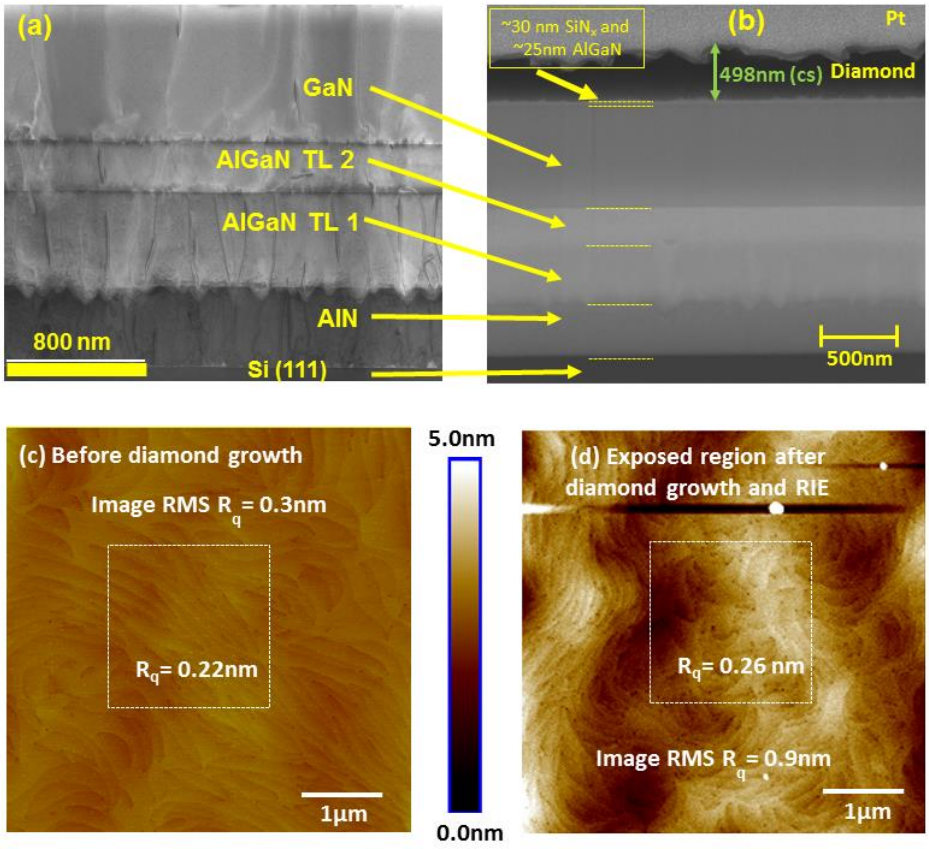

Figure 5. 9. Further confirmation of GaN surface damage elimination through (a) Representative cross section TEM images of AlGaN/GaN wafer (b) FIB cross section SEM image of diamond coated region of wafer GaN-B, (c) representative AFM image of wafer GaN-B before processing and diamond deposition and (d) AFM images taken at exposed region after diamond deposition and SF_6 RIE.

In addition to SEM, Further confirmation of damage elimination of GaN using approach B we performed by AFM of the AlGaN/GaN surface before and after diamond deposition using process B. The SF_6 RIE was performed with a very low power (15W/150W for RIE/ICP) just to remove the thin remaining SiN_x form the exposed region during CVD. Fig. 5.9 (c) and (d) shows the AFM images taken before and after diamond deposition on the exposed region of wafer GaN-B. Isolated diamond crystal is visible in Fig. 5.9 (d) which was a result of some unsuccessful seed clearance form that specific region which resulted in a diamond crystal. However, the density of such isolated diamond crystals on exposed region was not very high and the AFM image was taken from such a region to show the

true effect of diamond growth on the exposed region when diamond is present. Root mean square roughness (RMS R_q) of the 5µm×5µm AFM image has increased from 0.3nm to 0.9nm after diamond deposition but this value is not representing the true roughness because of the isolated diamond crystal. The RMS R_q of the 2µm×2µm boxed region of both images however have very closed roughness (only 0.04nm difference). Overall, the physical appearances of wo AFM images are identical indicating no GaN surface damage on exposed region during the diamond deposition. AFM images and roughness reported in Fig. 5.9 (c) and (d) is a true indication of surface protection during diamond deposition using process B.

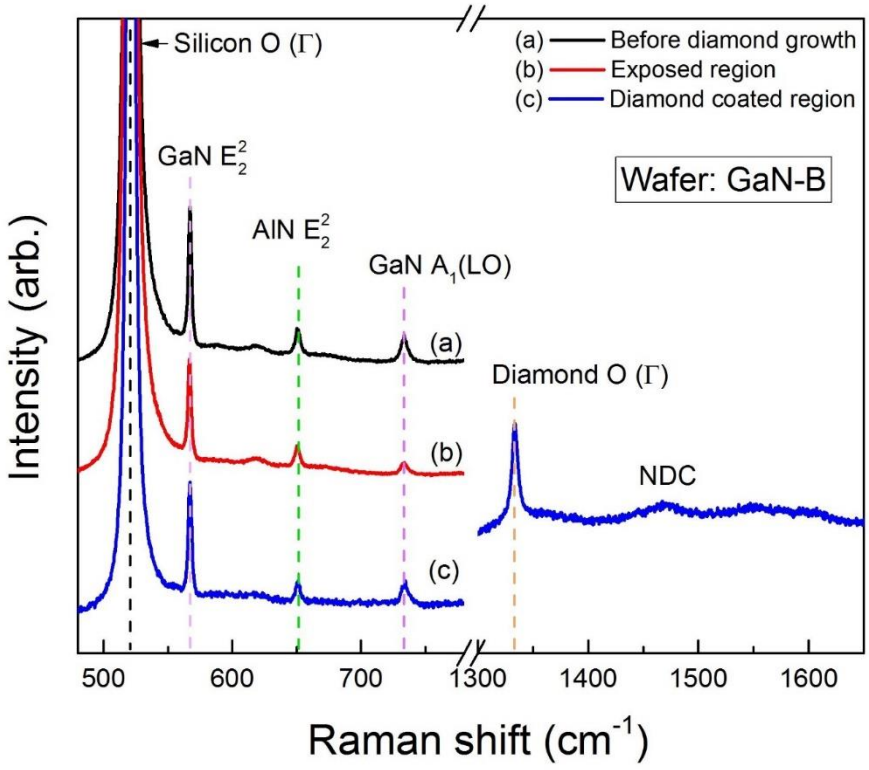

Figure 5. 10. Visible Raman (532 nm) spectra collected from middle region (~30mm from wafer center) of wafer GaN-B: (a) before diamond deposition and, (b) exposed region and (c) diamond coated region after selective diamond deposition for 2 hours with 3% methane.

To ascertain the effectiveness of the SiN_x layer and increased methane protecting the underlying III-Nitride layers, visible Raman measurements were performed on the wafer

before and after diamond deposition. Fig.5.10 represents Raman spectra collected from the middle region (~30 mm from wafer center) (a) before diamond deposition, (b) on exposed region after selective diamond deposition and (c) diamond coated region after selective diamond deposition. The Raman measurement parameters were the same for all spectra, as well as consistent with Raman measurements taken from wafer GaN-A, discussed previously. The differences in GaN-B results, compared with wafer GaN-A, is the consistency of the Raman peaks for GaN (E_2^2), AlN (E_2^2), and GaN A_1 (LO) phonon on all GaN-B spectra. Furthermore, a sharp diamond O (Γ) phonon peak at ~1333.7 cm^{-1} and broad NDC peak at ~ 1450-1650 cm-1 were observed in the diamond coated region of GaN-B. Because no notable difference were observed in the Raman spectra, damage to the III-Nitride layers was expected to be minimal, or mitigated, with Process B.

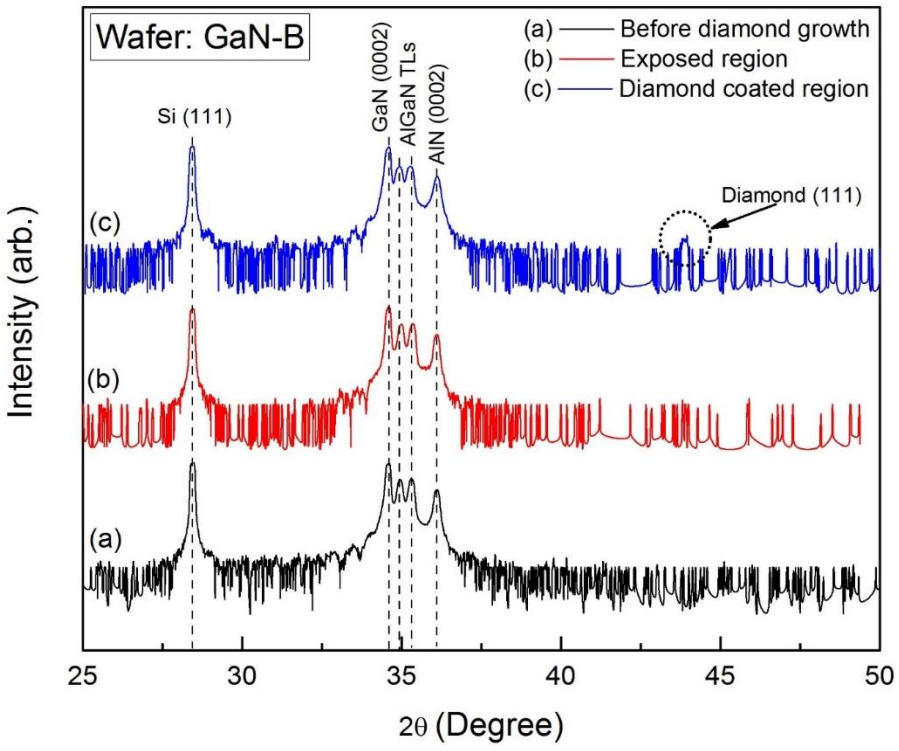

Figure 5. 11. HRXRD spectra collected from middle region (~30mm from center) of wafer GaN-B obtained (a) before diamond deposition, and (b) from exposed region and (c) from diamond coated region after selective diamond deposition.

HRXRD spectra collected from wafer GaN-B before and after diamond deposition are shown in Fig.5.11. Diffraction spectra were collected using the same parameters as described previously for wafer GaN-A. The three spectra shown in Fig.5.11 were collected (a) before diamond growth, and (b) from exposed region and (c) diamond coated region after diamond deposition. (0002) GaN, (0002) AlGaN TLs and (0002) AlN peaks were consistently observed in all three spectra. Furthermore, the (111) diamond peak was resolved in spectra (c), indicating the presence of the polycrystalline diamond layer. Unlike wafer GaN-A, XRD peaks from all planes were visible before and after diamond deposition. Because no discernable differences in the wide angle XRD spectra were observed, RSM of the asymmetric (114) peaks was performed to analyze the thin AlGaN barrier layer before and after diamond deposition. The RSM of wafer GaN-B was collected in the same manner as described for wafer GaN-A and the results are shown in Fig.5.12.

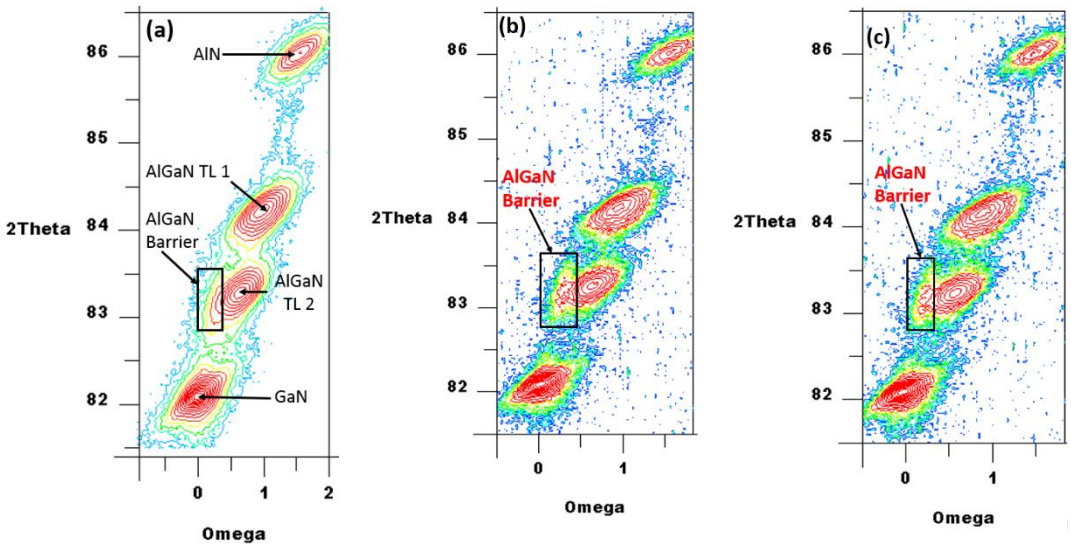

Figure 5. 12. RSM of the asymmetric (114) reflection of GaN, AlN and their alloys taken from the middle region (~30mm from wafer center) of GaN-B wafer (a) before diamond growth, and (b) from the window region and (c) from the diamond coated region, after diamond growth.

The RSM of the (114) reflection collected from GaN-B before diamond deposition is shown in Fig.5.12(a). All layer peaks, i.e., AlN, GaN and both AlGaN TLs (shown in

Fig.5.1), along with the thin, strained AlGaN barrier layer (boxed region) are resolved. The barrier layer was present after diamond deposition on both exposed and diamond coated regions, as indicated in Figs. 5.12(b) and (c), respectively. Thus, the 25 nm AlGaN barrier layer has been preserved after HFCVD diamond. Furthermore, the ratio of integrated intensities of GaN and AlN, tabulated in Table 5.1, were not significantly changed before and after diamond deposition. Based on these results, Process B, with a SiN_x interlayer and increased methane concentration, successfully protected the underlying III-Nitride layers.

Table 5. 1. Visible (532 nm) Raman peak positions of GaN, AlN and Diamond phonons and HRXRD RSM (114) peak intensity ratios of GaN and AlN before and after diamond deposition for wafers GaN-A and GaN-B.

Parameters	GaN-A		GaN-B		
	Before diamond growth	After diamond growth	Before diamond growth	Diamond coated region	Exposed region
GaN E_2^2 (cm^{-1})	567.47±0.01	566.61±0.35	567.28±0.01	566.92±0.04	566.82±0.01
GaN A_1 (LO) (cm^{-1})	733.9±0.1	-	733.60±0.05	733.33±0.16	733.34±0.08
AlN E_2^2 (cm^{-1})	650.38±0.05	650.28±0.4	650.77±0.05	650.64±0.12	650.56±0.04
Diamond O (Γ)(cm^{-1})	-	1332.73±0.05	-	1333.76±0.05	-
$I_{GaN}/(I_{GaN}+I_{AlN})$ (XRD-RSM)	0.97	0.75	0.97	0.96	0.95

5.4. Discussion

The deposition of CVD diamond on GaN without protective measures typically resulted in severe etching of the III-Nitride material due to atomic hydrogen diffusion into the underlying layers [48][75][191], [192]. The decomposition/etching of GaN in the case of Process A observed, for example, from SEM images in Fig.5.3, is substantially identical to other published results. Selective seeding of the wafer accentuated the problem on the exposed regions because there is no diamond growth taking place in these regions to coat

and protect the III-Nitride from the HFCVD environment. In the diamond seeded regions, the surface damage is reduced because of the (eventual) surface coverage by diamond [75]. In the HFCVD process, the etching/decomposition of GaN occurs at ~ 750-800 °C due to excessive energetic hydrogen atoms, even though the standard melting point of GaN is ~2500 °C [193]. The decomposition of GaN can take in the presence of hydrogen through the reverse GaN synthesis reaction or, NH_3 reformation via [74]

$$GaN(s) + {}^{3}/_{2}\, H_2(v) \rightarrow Ga(l) + NH_3(v) \tag{5.1}$$

While the Ga droplet product of reaction (1) was not visible on wafer GaN-A, these droplets may have evaporated during the CVD process. Alternatively, the absence of Ga droplets may indicate a sublimation reaction. GaN sublimation typically occurs at high temperature where the by-products are in the vapor phase and, thus, can be pumped from the reactor. Mastro et. al. [194] reported such a phenomenon for Ga polar GaN at a temperature above 800 °C through the following independent reactions,

$$GaN(s) \rightarrow Ga(v) + {}^{1}/_{2}\, N_2(v) \tag{5.2a}$$

$$GaN(s) + H_2(v) \rightarrow GaH(v) + {}^{1}/_{2}\, N_2(v) + {}^{1}/_{2}\, H_2(v) \tag{5.2b}$$

$$3H_2(v) + N_2(v) \rightarrow 2NH_3(v) \tag{5.2c}$$

GaN etching has been reported to be a strong function of temperature, pressure and hydrogen flow [193]. The temperature range (700-720 °C), pressure (20 Torr) and hydrogen flow (2 slm) in our HFCVD reactor was comparatively less conducive for GaN etching. However, the substrate temperature was measured via pyrometer, aimed at the Molybdenum liner above the wafer. Therefore, the actual substrate temperature may be more than the pyrometer reading. Additionally, the observed diamond delamination from

wafer GaN-A in Fig.5.3(c) can be a result of pinholes created by hydrogen diffusion during GaN decomposition. It is worth mentioning that decomposition of GaN was not the same in all regions across the wafer, especially in the diamond coated regions. GaN underneath the diamond grains was typically less damaged, as observed in the Raman data shown in Fig.5.4(c). On the other hand, GaN was severely etched in the window regions, and in regions between diamond grains (i.e., regions where the diamond did not completely coalesce). GaN etching was further confirmed by the substantial reduction of the (0002) GaN peak in the wide-angle HRXRD scan, shown in Fig.5.5. Most sensitive result was however the RSM of (114) as shown in Fig.5.6 where clear indication of AlGaN barrier etching was observed.

Process B demonstrated excellent selectivity with minimal or no damage to the III-Nitride layers. The SEM images in Fig.5.7 and 5.8 indicate the protection of GaN and uniform diamond coverage. The cross sectional TEM and SEM images of Fig.5.9 (a) and (b) is a clear indication of surface protection during diamond growth using process B. The AFM images shown Fig. 5.9 (c) and (d) taken before and after diamond deposition on exposed region is a true indication of the surface protection because the appearance of the GaN surface after the diamond deposition did not change at all. The curved parallel line shaped features on such AFM images are indication of dislocation that originate during MOCVD and terminate at the surface. Such AFM image of the AlGaN/GaN HEMT surface is very common and is a quick indication of the 2DEG formation. In addition, any damage to the surface more than a nano meters changes the physical appearance of the surface and the RMS roughness increases drastically. Most of the successful HEMT wafer produced by our MOCVD reactor has RMS roughness less than 0.5 nm for a 2μm×2μm. Therefore,

2DEG is believed to be present on the exposed region after diamond deposition.

Similar selectivity, surface protection and diamond coverage was achieved uniformly across the 100 mm substrate and the growth process repeatability has been demonstrated on several wafers (not shown). Careful analysis of the resolved line widths in, e.g., Figs. 5.7 and 5.8, revealed that for some lines, the widths were not exactly the same as defined on the lithography mask. Several reasons can be responsible, such as photoresist over developing, and over etching during RIE etc. Furthermore, lateral growth of diamond poly crystals would create discrepancy due to the diamond crystal three dimensional growth until coalescence [45].

The PECVD grown SiN_x protects the GaN because the Si-N bond dissociation energy (439 kJ mol^{-1} [195]) is much larger than the thermally induced decomposition enthalpy of the Ga-N bond (379 kJ mol^{-1}). However, as noted previously, a dielectric interfacial layer tends to impede the efficient heat flow from the III-Nitride layers. Nevertheless, a thin layer of dielectric is shown to be essential for protecting the underlying layers from etching/decomposition. We also analyzed increasing the methane concentration without a SiNx protective layer, but it was found that even with 3.0% methane there was visible etching of the GaN layer (not shown). The concentration of methane was not increased above 3.0% because NDC increases significantly above this concentration and the film consists of mainly sp^2 bonded carbon. Raman spectra, shown in Figs. 5. 4 and 5. 10, were used to calculate NDC by subtracting the diamond phase volume fraction from unity. The volume fraction of diamond phase is calculated from the ratio of the integrated intensities (area under curve after background correction) of diamond O (Γ) peak (I_D) and summation of I_D and non-diamond carbon peak (I_{NDC}) [114]. For wafer GaN-

A the NDC was ~43% whereas it was ~55% for wafer GaN-B. On the other hand, complete surface coverage was achieved with 3.0% methane in just 2 hours growth whereas 6 hours was required to get incomplete diamond coverage when the methane concentration was 1.5%. The diamond thickness on GaN-A and B was ~1000-1200 nm and ~600-750 nm, respectively, with ~5% variation from center to edge. The diamond thickness was typically higher in the edge region (>30 mm from center) because of higher nucleation density. The high nucleation density resulted from the accumulation of more nano diamond seeds (or, nano-diamond seed containing photoresist) at regions far from the wafer center due to higher kinetic energy of the spin coater. The diamond vertical growth rate was ~200 nm/h and ~300 nm/h for GaN-A and B, respectively, but the lateral growth rate was estimated to be higher for the GaN-B process because of increased methane concentration used in the diamond grown. The higher lateral coverage of diamond with higher methane concentration was due to the greater concentration of methyl radicals in the CVD chamber [45]. Therefore, the 3.0% methane resulted in faster coverage (and with corresponding thinner diamond) compared to 1.5% methane. However, at expense of increased NDC.

In addition to excellent diamond selectivity in wafer GaN-B, the thin AlGaN barrier layer was unchanged from RSM of the (114) asymmetric plane data in Fig.5.12, even on the window regions, where no diamond was seeded or grown. The RSM (114) peak of the strained AlGaN barrier layer is extremely sensitive to the layer thickness and any damage to the barrier layer would substantially convolute its (114) peak with the TL2 (114) peak. The comparatively identical AlGaN barrier layer (114) signatures in Figs. 5.12(b) and (c) indicate that the thin PECVD SiN_x (~25-30nm) effectively protects the underlying III-Nitride layers. This was further confirmed from the ratio of integrated RSM intensities of

GaN and AlN layer as shown in Table 5.1. The GaN layer was substantially unaffected by the diamond deposition process and, thus, it is expected that the 2DEG channel will be unaffected, as well, after diamond deposition in Process B. In addition, the Raman peak position shifts were relatively small after diamond deposition in the case of wafer GaN-B compared to GaN-A as indicated in Table 5.1. The redshift of GaN E_2^2 phonon was ~0.8 cm^{-1} for wafer GaN-A which corresponds to tensile stress. The origin of such stress can be thermal due to the large coefficient of thermal expansion (CTE) mismatch between GaN and diamond [76]. The diamond delamination, indicated in Fig.5.3(c), can also be a result of this stress. Such tensile stress in GaN has been reported for GaN-diamond wafers when diamond was grown on the back side of the GaN [119]. Interestingly, the red shift is reduced to 0.3-0.4 cm^{-1} for wafer GaN-B indicating a relative reduction in the tensile stress with Process B compared to Process A. The MOCVD grown AlGaN/GaN layers normally incur several GPa of biaxial stress in the GaN layer [187]. Therefore, a small added stress due to HFCVD diamond is not likely to adversely affect the AlGaN/GaN structure's mechanical and electrical properties. The presence of the 2DEG after diamond deposition can be confirmed by electrical characterization such as capacitance voltage (C-V) or Hall measurement. Since the main objective of the current study was to reduce/eliminate III-Nitride surface damage, we focused mainly on structural characterization.

Selective CVD diamond deposition on an AlGaN/GaN HEMT wafer has been reported for the first time in this study. In other reported techniques for selective diamond deposition on GaN, the diamond was deposited on top of the fabricated HEMT device [48] [191], [192]. However, any damage to the 2DEG performance at this fabrication stage would result in a substantial increase in the fabrication cost. The technique adopted in the

present research is a novel approach where the diamond deposition has been conducted before electrode formation on HEMT wafer. This process reduces fabrication cost of Diamond-on-GaN wafers significantly. Although thin diamond layers have been utilized in the present research to show the feasibility of the process, thick diamond can also be employed selectively to take further advantage of the vertical heat flow while keeping the GaN region open for subsequent metallization. The selectively deposited diamond coated III-Nitride wafer from this study is ready for thermal characterization and further processing to produce devices with integrated heat spreaders.

5. 5. Conclusion

We have developed a technique to selectively deposit polycrystalline diamond on an AlGaN/GaN HEMT structure using HFCVD which can be transferred to other III-Nitride structures. < 1µm lateral resolution diamond features have been achieved with excellent wafer uniformity across the 100 mm substrate. Significant etching of the GaN layer was observed from morphological and structural characterization when diamond was grown on GaN without protective processes. Increasing the methane concentration from 1.5% to 3.0% and using a 30-100 nm PECVD SiN_x as a protective layer resulted in excellent selectivity and complete protection of the underlying III-Nitride structure. Protection of the top AlGaN (20-25nm) barrier layer was confirmed by HRXRD and RSM data proving the potential of this novel technique. The process can be transferred to large scale GaN wafer production that will yield integrated diamond heat spreaders for thermal management of high power GaN based electronic and optoelectronic devices.

VI. EPITAXIAL LATERAL OVERGROWTH OF GAN ON GAN TEMPLATE PATTERNED WITH CHEMICAL VAPOR DEPOSITED DIAMOND

In this chapter, we report techniques involved and experimental results of growth of single crystal GaN on patterned CVD diamond. Photolithography based selective seeding and hot filament CVD (HFCVD) of polycrystalline diamond with thickness ~600nm was performed on metal organic CVD (MOCVD) grown GaN/AlGaN/AlN/Si substrates at first. The epitaxial lateral overgrowth of GaN on the exposed window of the diamond coated GaN wafers were performed in a vertical flow shower head MOCVD system. Optimization of the growth was performed based on a series of systematic studies by varying ammonia to trimethyl gallium mole ratio (V/III), chamber pressure(P) and temperature(T) in the range of 8000-1330, 40-200torr and 975-1030 ^{o}C respectively. Lower pressure, lower V/III and higher temperature were found to enhance lateral growth of GaN. Effect of GaN to diamond feature area and mask orientation was also studied. Enhanced lateral growth and complete coalescence of vertical $\{11\bar{2}0\}$ GaN facets was observed when GaN window mask openings were along $[1\bar{1}00]$. Complete lateral coverage and coalescence of GaN was achieved over $[1\bar{1}00]$ oriented GaN window on diamond with V/III=7880, P=100torr, T=1030 ^{o}C. Full width at half maxima of x-ray rocking curve of overgrown GaN (0002) plane was found to be less than that of masked GaN region indicating better crystal quality of over grown GaN.

6.1. Introduction

Today's most powerful optoelectronic and power electronic devices are made of wide bandgap semiconductor materials due to their large direct bandgap which facilitates

emission of high energetic light or transmission of high frequency electrical signal[31]. Group III-Nitride semiconductor materials such as Gallium nitride (GaN), Aluminum nitride (AlN) and their alloys can cover very wide energy band and they are superior to other semiconductors for high power electronics[33]. In addition, this class of materials have unique polarization properties which is not available in any other wide bandgap semiconductor materials. Due to piezo electric and spontaneous polarization, a high density ($> 10^{17}$ cm^{-3}) [196] channel of highly mobile electrons called two dimensional electron gas (2DEG) exists in the interface of a wide bandgap (i.e AlGaN) and narrower bandgap (i.e GaN) group III nitride semiconductors)[17]. 2DEG is the heart of III-Nitride based high electron mobility transistors (HEMT)[1]. The presence of 2DEG at the channel has made AlGaN/GaN HEMT an excellent candidate for high power and high frequency electronic and optoelectronic devices. High power operation exceeding 40W/mm has been reported for such a device[53][65]. Due to such high-power operation, excessive heat is generated at the active layer of these devices and this heat is needed to be removed instantly to maintain device performance and reliability. Among many other substrate materials, chemical vapor deposited (CVD) polycrystalline diamond have been used extensively in recent years as substrate material because of its high thermal conductivity (≈ 800-1800 W/m-K)[12][66]. The GaN-on-diamond technology has been incorporated in radio frequency (RF) transistor industry and has already demonstrated excellent scalability, promising electrical and thermal performance[66].

Many literatures and patents have been published on fabrication of GaN-on-diamond devices. In most of the published techniques, GaN is grown on a single crystal substrate and attached to CVD grown diamond substrates using interfacial materials (US

patent no. 8945966B2, 8759134B2, 8674405B1)[197]. In some of the techniques, diamond is grown on GaN and the substrate wafer is then etched from the back side to access the nitrogen faced GaN. Most of these processes involve multiple steps of growth and substrate transfer. Increased chance of wafers damage and thereby reducing throughput is one of the biggest issues in the current state-of-the art for GaN-on-diamond technology. In addition, despite all the advanced approaches, thermal management in GaN-on-diamond devices remains a significant challenge due to two important factors namely thermal boundary resistant (TBR) between different layers and graphitic carbon in the diamond nucleation layer (at the GaN-diamond interface). TBR is inevitable for wafer transfer technology and can only be minimized in GaN devices if they are directly grown on diamond. Since, growing crystalline GaN on foreign substrate (single crystal) is a significant challenge due to lattice mismatch, it is impossible to grow them directly on polycrystalline diamond. In case of CVD diamond growth on GaN, graphitic carbon is unavoidable in diamond nucleation layer during growth and unfortunately it has very poor thermal conductivity. Therefore, an effective way of direct growth of GaN on diamond with active layer residing closest to the diamond substrate would be a compelling material solution to the current problem.

In this chapter, we will demonstrate a novel approach for growing crystalline GaN directly on CVD grown polycrystalline diamond using selective area deposition (SAD) of CVD diamond and epitaxial lateral overgrowth (ELO) of GaN. We have reported selective deposition of CVD diamond on AlGaN/GaN wafers in previous chapters. ELO of GaN using dielectric mask is a well-established growth technique mainly used in optoelectronic research for producing low defect GaN[80][82]. The growth anisotropy of GaN in various

crystallographic orientations is a strong function of four main factors namely group V to group III mole ratio (V/III), pressure, temperature and mask orientations[83]. The lateral growth can be enhanced by using low pressure and high temperature growth. A wide range of V/III (1000-5000) value have been reported for enhanced ELO [83][84].

In a standard ELO process, few micron GaN is grown on Si or SiC at first using trimethyl gallium (TMGa) and ammonia (NH_3), next a few hundred nanometers of dielectric (SiO_2 or SiN_x) is grown using CVD. Standard photolithography and wet/dry etching is performed to open a set of parallel stripes or circles in the mask. GaN is grown on the opening of the masked GaN template at first. Once these openings are filled, GaN grows both laterally and vertically. Under proper conditions, epitaxial lateral growth of GaN over the mask surface takes place and leads to a full coalescence and smooth surface suitable for device fabrication[82][80]. For circular opening, ELO results in hexagonal pyramids with $\{1\bar{1}01\}$ facets[81]. In case of a stripe shaped mask opening, GaN growth in certain direction is dictated by the mask orientation. It is well known for any CVD process that incorporation of reactant molecules on substrate occurs after kinetically controlled diffusion of adsorbed species on the surface. Although molecules are brought to the substrate with uniform flows, the growth rate is controlled by the diffusion of active species through a boundary layer[89]. As a result, any growth anisotropy in MOCVD occurs only when diffusing molecules experience difference surface structure within their mean free path (λ_S)[97]. In case of GaN ELO in MOCVD, growth anisotropy occurs because the diffusing molecular species are preferentially incorporated into different crystallographic sites[82]. It is worth mentioning that due to necessity of growth anisotropy during epitaxial overgrowth of GaN, ELO is only achievable in MOCVD and is very difficult to achieve in

any other growth techniques such as molecular beam epitaxy (MBE)[198].

The effect of pressure, temperature and V/III on the ELO of GaN has been well documented in the literature [80]–[82], [199]. Higher V/III ratio results in higher lateral growth. The lateral growth of GaN on line edge or pyramid sidewall is proportional to the TMGa incorporation probability which is strongly affected by the NH_3 partial pressure[83]. Lateral growth can be enhanced by increasing total NH_3 partial pressure which will enhance the decomposition of NH_3 into surface active nitrogen. Increasing growth temperature can also increase the decomposition of NH_3 resulting in a higher concentration of active nitrogen. Higher concentration of active nitrogen achieved by either higher V/III flow or higher temperature will eventually increase the incorporation probability of TMGa and thus lateral growth[83]. However, it is worth mentioning that excessive increase in NH_3 compared to TMGa would result in excessive atomic hydrogen which will enhance surface etching and therefore no growth at all [200]. Therefore, most of the literature suggest highest lateral growth when the V/III ratio is in between two extreme values for respective reactors[83][201].

Since lateral growth of GaN on CVD polycrystalline diamond mask (never reported before) is the goal of present research, we performed a systematic study of GaN ELO by varying all parameters i.e., V/III, pressure, temperature and mask orientation. The main reason for performing such an elaborate study is that the surface kinetics of Ga and N adatoms on the rough polycrystalline diamond surface is very different that smooth dielectric layers. It is well known that surface mobility of reactant adatoms is strongly dependent on sticking coefficients of adatoms on the substrate[201]. Therefore, the ELO of GaN on polycrystalline diamond is expected to show variation in lateral growth

characteristics. Besides, growth parameters change greatly from reactor to reactor based on reactor size, type of gas flow and pressure range. Therefore, a detailed study involving change in V/III, pressure and temperature were necessary to observe the lateral growth of GaN on polycrystalline diamond mask.

6.2. Experimental

6.2.1 ELO of GaN

The ELO of GaN on diamond mask was started by selectively depositing CVD diamond on MOCVD grown GaN wafer on 100mm Si (111) wafers. The detail of the selective deposition of diamond on GaN can be found in previous chapters (2, and 5). One important modification on the selective growth of diamond on GaN in this chapter compared to that described in chapter 5 was in mask orientation. We intentionally, varied the mask orientation by multiple UV exposure with 90^{o} rotation of the substrate during photolithography based selective seeding of diamond. Each time, a quarter of the full wafer was exposed while rest of the wafer was covered. The goal for this strategy was to achieve both $<11\bar{2}0>$ and $<1\bar{1}00>$ oriented diamond lines and GaN windows on the same diamond coated GaN wafer. Fig. 6.1 shows an image of 100 mm wafer where ELO GaN was deposited on diamond coated GaN wafer. Both $<11\bar{2}0>$ and $<1\bar{1}00>$ oriented mask openings are present in the wafer as seen from the figure.

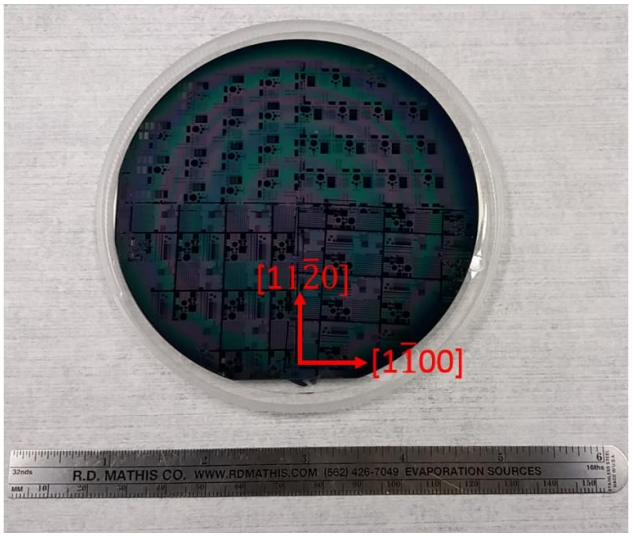

Figure 6. 1. ELO GaN deposited on a diamond coated GaN wafer with GaN window openings along <1$\bar{1}$00> and <11$\bar{2}$0> direction.

The selectively deposited diamond-on-GaN wafers still had a thin layer of SiN_x on the exposed GaN regions. Therefore, we ran another round of reactive ion etching (using same parameters as described in chapter 5) to remove the SiN_x and expose the GaN surface. The second MOCVD growth was performed in the same MOCVD system (donated by Nitronex Corp.). Since this growth involved GaN only, TMGa and NH_3 were only process gases along with carrier gas Hydrogen. Initially, we varied the V/III ratio on a dielectric coated GaN wafer to ascertain the ELO capability of our reactor and to calibrate growth rate. Then, we varied pressure and temperature for ELO of GaN on diamond coated GaN wafers. ELO growth experiments were performed based on literature suggested values[80] [82] of pressure and temperature at first. In most of the published results on ELO of GaN, the temperature range was between 950 and 1050 °C and pressure was between 30 and 200 torr. Relatively large range of V/III ratio have been reported for successful ELO. It is worth mentioning that we varied pressure, temperature and V/III based on our instrument capability. For example, the heater element of our MOCVD reactor could produce maximum of 1030 °C with 1900W power (90% of its highest rating). Therefore, the

maximum temperature used in the present research was 1030 °C. The pressure range of the reactor was 40-500 torr based on the pressure controller system. We varied pressure in the range of 40- 200 torr. The V/III ratio variation was limited by the maximum flow rate of mass flow controllers (MFC). The MFC of the Hydrogen and NH_3 were capable of flowing 1.3 SLM whereas the MFCs for TMGa had a maximum flow of 100 sccm. The V/III values for our research were therefore varied between 1334 and 7880 and corresponding TMGa flows were between 90 sccm and 15 sccm, respectively. Specific growth parameter for various ELO GaN growth is listed in following Table 6.1. It is important to note that the growth parameters were optimized initially by changing TMGa flow (V/III) values for PECVD grown SiN_x masks. The study of V/III was initially done using SiN_x mask because ELO is a quick MOCVD process and patterning dielectric is less time consuming. On the other hand, production of selectively deposited diamond-GaN wafer is very time consuming and more expensive. However, after achieving the best result for V/III, we repeated the study on diamond-GaN wafers. Once study on V/III was successfully done for SiN_x mask, we started to study the effect of pressure and temperature. These studies were performed on selectively deposited diamond-GaN wafers.

Table 6. 1. Growth parameters for ELO GaN optimization

TMGa flow (sccm)	TMGa (µmole/min)	NH_3 flow (sccm)	NH_3 (mole/min)	V/III	P (torr)	T (^oC)	Growth time (min)
90	221.2	6500	0.291	1330	200,100,40	975,1030	4-25
29.5	72.5	6500	0.291	4000	100	975	4
15	36.8	6500	0.291	7880	40, 100	975,1030	4-25

6.2.2 Characterization techniques

The morphology and thickness of the diamond film was characterized with a scanning electron microscopy (SEM, FEI Helios 400) and Surface profilometer (Dektak XT). The Raman spectroscopy of the samples were performed in a Horiba Raman system equipped with a visible laser (λ = 532 nm) and the laser spot size was ~2 μm for a 100x objective lens. Raman spectra were collected on similar region on the wafers after MOCVD growth. Laser power, spot size and exposure time was kept same for all measurement. Spectra collection was performed between 450 cm^{-1} and 850 cm^{-1} to observe first order nitride semiconductor peaks whereas the range was extended to 1800 cm^{-1} when spectra was collected from diamond coated region because non-diamond carbon peaks occurs at ~1450-1600 cm^{-1}. High resolution XRD (HRXRD) measurements the wafers were performed using the SmartLab XRD system (Rigaku Corporation) with Cu Kα radiation (λ = 1.540562 Å) using a Ge (220) 2-bounce monochromator and the incident slit opening was 0.5 mm for all measurements. Initially, a wide angle θ-2θ HRXRD scan from 25° to 90° were performed. Later, a rocking curve (ω scan) around GaN (0002) plane from (ω =) 16.5° to 17.5° (around symmetric (0002) reflections) was performed.

6.3. Results and Discussion

6.3.1 Effect of V/III

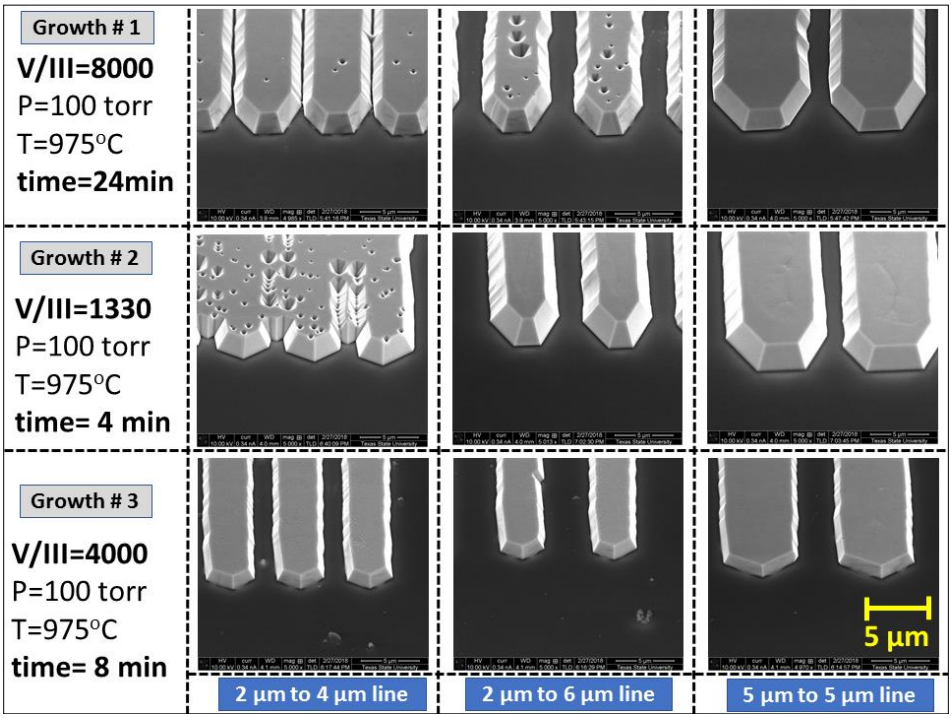

Figure 6. 2. SEM images showing effect of V/III on epitaxial lateral overgrowth of GaN on SiN_x mask (images are taken at ~30 mm from the center of a 100 mm wafer).

The growth rate of ELO GaN is mainly dictated by the amount of reactant present on the surface during the growth[97]. The TMGa (III) and NH_3 (V) flux into the reactor dictates the surface incorporation of GaN on substrate. In general, at any given pressure, higher V to III ratio results in slower vertical growth with very smooth and high quality GaN crystal whereas, a lower value results in enhanced vertical growth due to excessive TMGa flux[33]. We therefore, ran experiments to observe the effect of V/III on lateral growth. To observe the effect of V/III on ELO in our reactor, we first used GaN wafer with SiN_x mask.

Pressure and Temperature were kept the same as our baseline process for GaN growth (100 Torr and 975 °C). Fig. 6.2 shows the effect of V/III on vertical and lateral growth of ELO GaN grown on SiN_x mask. Initially, we used two extreme values of V/III by changing TMGa flow. For V/III ratio of 1330, the TMGa flow was 90 sccm (221 μmole/min) using hydrogen as carrier gas and NH_3 flow rate was 6.5 SLM (0.29 mole/min). For V/III value of 8000, corresponding TMGa flow was 15 sccm (36.8 μmole/min). From our previous experience of standard GaN growth in our MOCVD reactor, we have observed that vertical growth rate is inversely proportional to V/III ratio. Based on previous data of GaN growth rate, we changed the growth time to achieve same thickness of the ELO film so that we can see the lateral growth characteristics for films with same thickness. Clearly visible changes are observed in results as shown in Fig. 6.2. V/III values of 8000 and 1330 both resulted in ELO of GaN with enhanced lateral growth. However, V/III of 1330 seemed to exhibit better lateral coverage despite our initial assumption. To be sure about our finding with first two growths, we grew another wafer with V/III value of 4000 as seen in the bottom panel of Fig. 6.2. Interestingly, lateral growth was reduced in this case. This result indicated that enhanced lateral growth might be possible with lower V/III ratio. It is important to remember that a wide range of V/III values (1000-6000) have been suggested in literatures for GaN ELO[83][201].

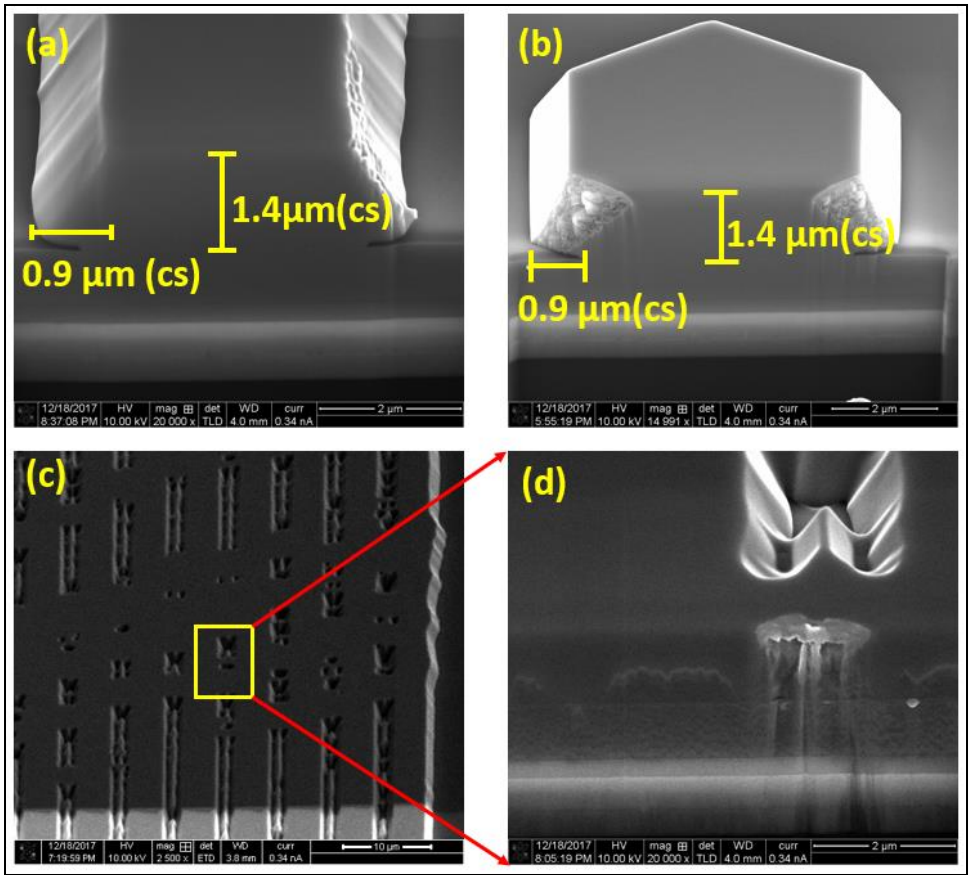

Figure 6. 3. SEM images of vertical and lateral growth of ELO GaN (grown with P=100 torr, T=975 °C and V/III= 1330 using 100 nm thick SiN_x mask) on various SiN_x masks openings (a) 4 µm GaN stripe opening (b) 4 µm GaN circle opening. (c) Complete lateral coverage on a 2 µm mask by 4 µm stripe opening and (d) FIB cross section of the boxed region on (c) showing coalescence of top GaN surface. Images are taken at ~30 mm from the center of a 100 mm wafer.

To identify the vertical to lateral growth ratio for the wafer grown V/III of 1330, we took focus ion beam (FIB) cross section SEM images of the ELO region on the wafer as shown in Fig. 6.3. Fig. 6.3(a) shows a 4 µm GaN stripe opening which grew ~5.8 µm laterally and total vertical thickness was ~1.4 µm. Thus, the lateral to vertical growth ratio was ~0.64 (=0.9/1.4). For a circular opening of 4 µm diameter as shown in Fig. 6.3(b) the ratio was same. However, the lateral coalescence was visible for 2 µm GaN opening separated by 4 µm SiN_x stripe as seen Fig. 6.3(c) and its magnified view in Fig. 6.3(d). This result is expected since the growth rate is extremely dependent on mask to window size. One notable feature in coalesced GaN on Fig 6.3(d) is the poor crystal quality right above the

stripe. Such poor crystal quality above the mask is the result of dislocation formation due to coalescence of two lateral faces. However, such dislocation is expected to reduce as the film thickens above the masked region due to incorporation of newly arrived reactants above this region[202]. In most of the reports of successful ELO GaN, termination of dislocation above mask occurred within one third or half of the total ELO GaN thickness [202]. For our case, GaN has coalesced relatively far above the stripe. However, this result indicates that coalescence of GaN above dielectric mask is achievable within our experimental capabilities when thickness of the regrown region is sufficiently high.

Based on the result of ELO obtained for the SiN_x, we studied other factors i.e. pressure and temperature on diamond coated GaN wafers for using V/III=1330 and they are described in following sections.

6.3.2 Effect of pressure and temperature

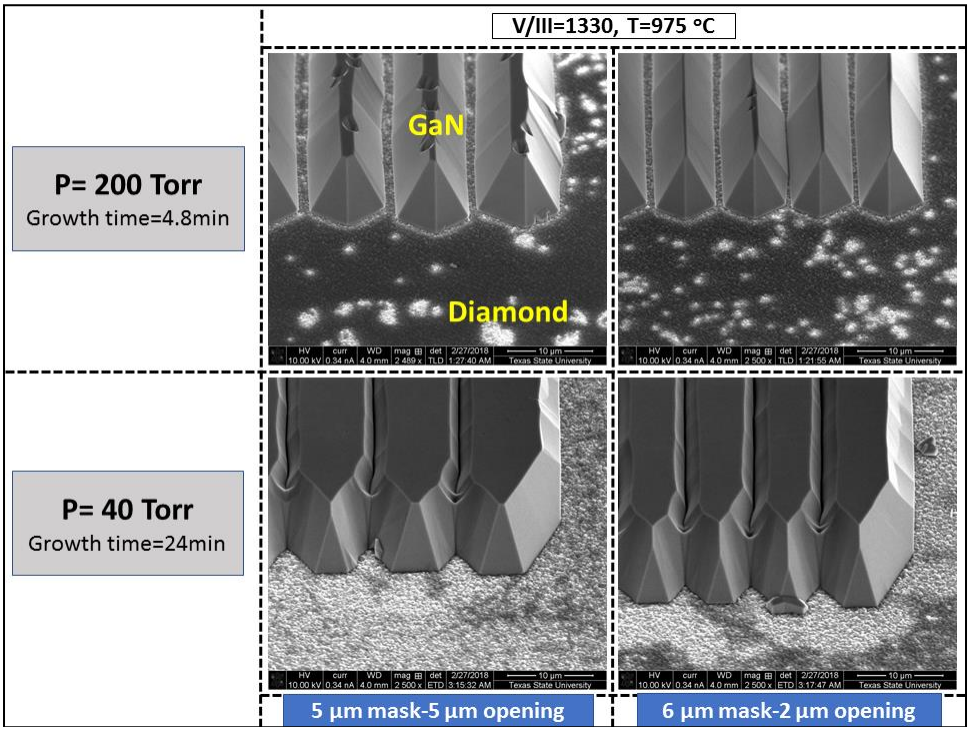

Figure 6. 4. SEM showing effect of pressure on ELO GaN on diamond mask when growth temperature was 975 °C for V/III = 1334 (Images are taken at ~30 mm from the center of a 100 mm wafer).

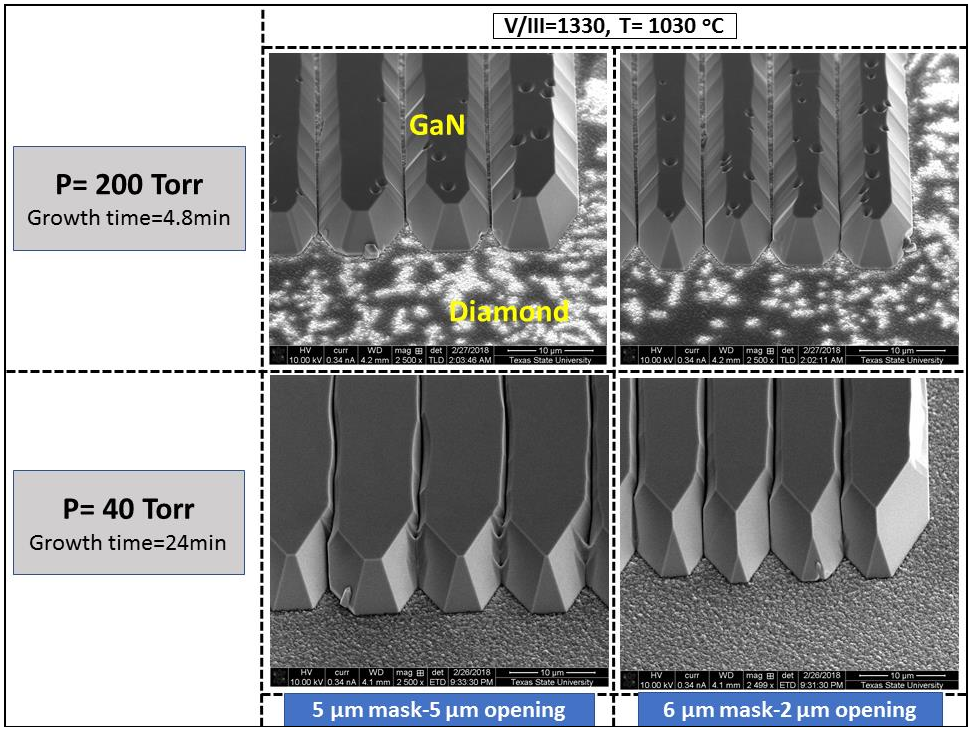

Figure 6. 5. SEM images showing effect of pressure on ELO GaN on diamond mask when growth temperature was 1030 °C for V/III = 1334 (Images are taken at ~30 mm from the center of a 100 mm wafer).

The effect of pressure on lateral growth is shown in SEM images of Fig. 6.4 for ELO GaN on diamond mask when growth temperature was 975 °C for V/III = 1334. A second set of SEM images taken from similar region is shown in Fig. 6.5 when temperature was raised to 1030 °C keeping all other parameters constant for the other set of two wafers. All the images shown here are taken at ~30 mm from the center of a 100 mm wafer. The stripe orientation was along $[1\bar{1}00]$ for all the stripes shown in Figs. 6.4 and 6.5. It is clear from the figure that lower pressure resulted in enhanced lateral growth for both temperatures. The enhanced lateral growth at lower pressure corresponds to increased growth along $(11\bar{2}0)$ face (vertical sidewall of the stripe) compared to $(11\bar{2}2)$ face (face of pyramidal sidewall). The lateral growth along $(11\bar{2}0)$ face has further increased when temperature was higher (1030 °C) as seen in Fig. 6.5. It is worth mentioning that the vertical growth

along <0001> direction has increased with increasing pressure for any given temperature. This is due to increased resident time of gallium and nitrogen reactant [97] inside the boundary layer. Besides, increased coalescences were observed when mask separation was smaller in Figs. 6.4 and 6.5. According to ELO GaN growth model proposed by Hiramatsu et. al. [80], the dependence of growth rate along various faces of Ga faced ELO GaN is shown in Fig. 6.6. This model is helpful to understand various plane formation and effect of growth parameters on relative growth rates along those planes.

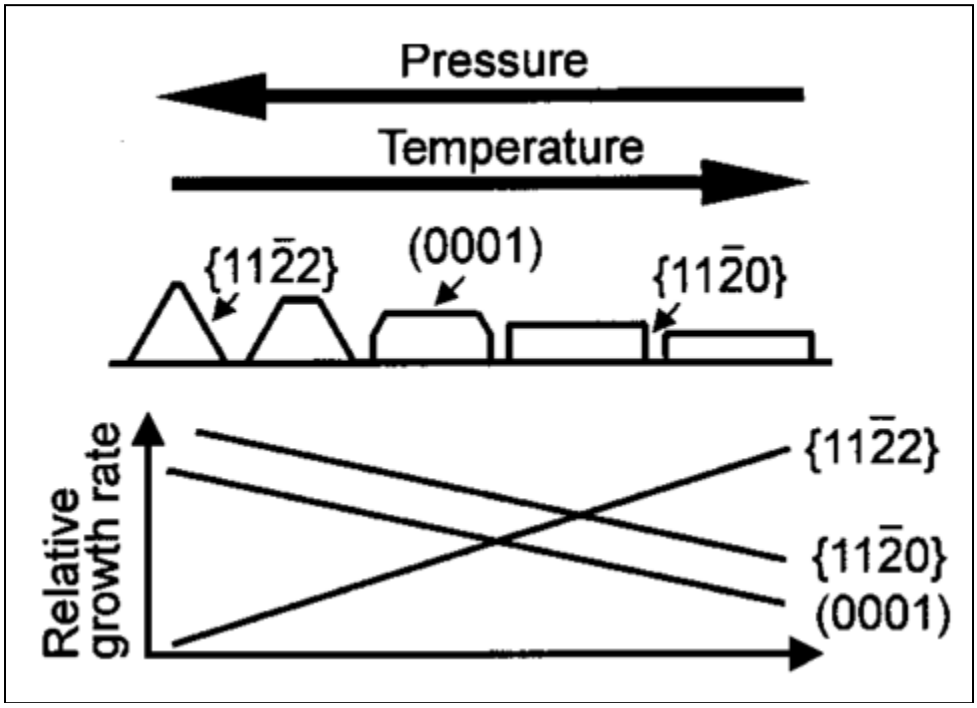

Figure 6. 6. Orientation dependent growth rate of Ga faced ELO GaN based on model proposed by Hiramatsu et. al (image adopted from[80]) for stipes oriented along [1$\bar{1}$00].

According to the model shown in Fig. 6.6, lowering pressure or increasing growth temperature results in increased growth along lateral face {11$\bar{2}$0}. On the other hand, enhanced growth along <0001> with {11$\bar{2}$2} facets are observed when temperature is reduced or pressure is increased. It is clear from the growth model shown in Fig. 6.6 that results shown in Figs. 6.4 and 6.5 follows the growth model proposed by Hiramatsu et al.

[80]. Similar results were also reported by Kapolnek et. al. [83] and Beaumont et.al. [82] for ELO of GaN on dielectric mask.

The poor (0001) plane formation at lower temperature and higher pressure as observed in top panel of Fig. 6.4 is a result of (0001) surface degradation during the MOCVD growth. At this condition, layer by layer formation is not thermodynamically favorable because surface migration of Ga atoms is poor at these condition[82][97]. As a result, we observed poor (0001) plane formation with increased $\{11\bar{2}2\}$ plane formation in Fig. 6.4 and in top panel of Fig .6.5. In contrast, for high temperature and low pressure as seen in Fig. 6.5, surface migration of Ga is increased and results in smooth (0001) plane formation and the $\{11\bar{2}2\}$ plane is replaced by $\{11\bar{2}0\}$ planes. At high temperature and low pressure, $\{11\bar{2}2\}$ plane become unstable because the surface nitrogen atoms of this facet become unstable and the surface become narrow or diminished (bottom left panels of Fig. 6.4 and 6.5). Another possible explanation of the decreased $\{11\bar{2}2\}$ plane formation and increased (0001) and $\{11\bar{2}0\}$ facets is that $\{11\bar{2}2\}$ planes have increased number of dangling bonds per unit area (DB) [82][97]. At high temperature and low pressure, formation of (0001) and $\{11\bar{2}0\}$ facets are favorable because they have smaller DB values (11.4 and 14.0 nm^{-2} respectively) compared to that of $\{11\bar{2}2\}$ plane (17.8 nm^{-2}). Therefore, energetically favorable (0001) and $\{11\bar{2}0\}$ facets formation dominates at such conditions.

At this point, it was clear that increasing temperature and decreasing pressure would result in best lateral coverage of ELO GaN for V/III of 1330. But it was also seen from Fig. 6.2 that the vertical growth was very high for the lower V/III. It is worth remembering that the reason for conducting ELO experiment on diamond was to place GaN active layer as close to diamond as possible. Therefore, our expectation at this point was to get full

coalescence with minimum ELO GaN thickness. For the next set of experiments, we deposited two ELO GaN-diamond wafers with increased V/III (7880 by reducing TMGa flow to 36.8 μmole/min) at 40 Torr and 100 Torr respectively (P = 200 Torr was not chosen because it would result in enhanced vertical growth). To make fair comparison, we deposited one more ELO GaN-diamond wafer with V/III = 1330 but P = 100 Torr. Temperature was 1030 °C for these wafers. The results are discussed in following section.

6.3.3 Effect of V/III and pressure at high temperature

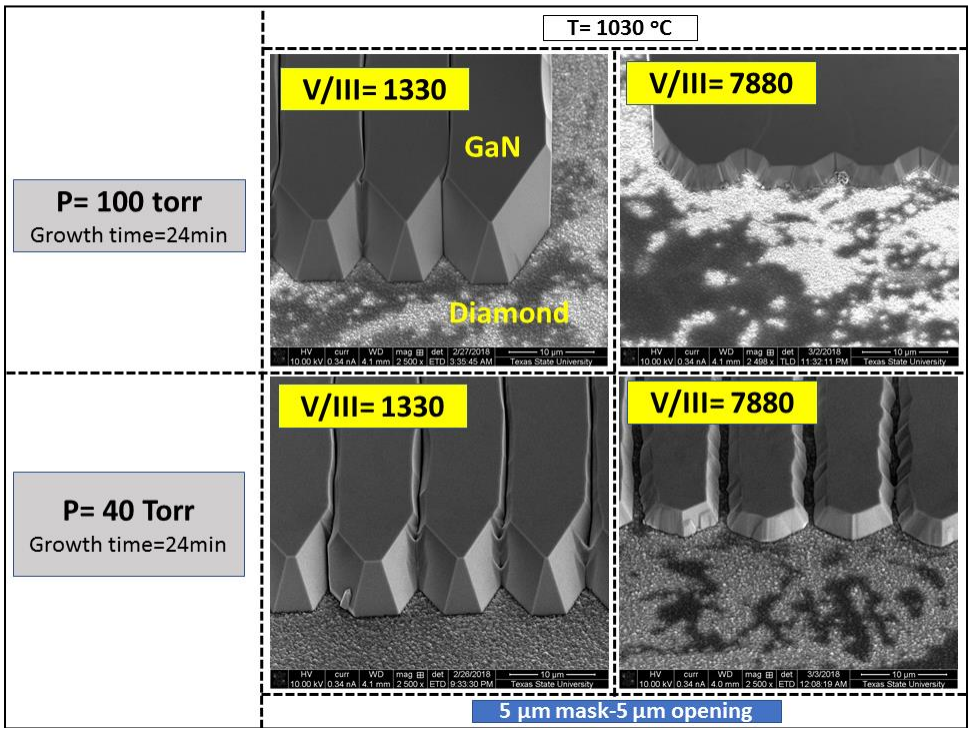

Figure 6. 7. SEM images showing effect of V/III and pressure on lateral growth of GaN at high temperature pressure (T=1030 ºC). Images are taken at ~30mm from the center of a 100mm wafer.

The effect of increasing V/III to 7880 is shown in Fig. 6.7 for P = 100 and 40 torr respectively. As expected, the lateral growth was high when V/III was increased. As described before, the increased lateral growth was due to the increased nitrogen reactant (high V/III) near the lateral faces at higher temperature[83]. However, growth rate was very low for P = 40 Torr when V/III was 7880. This was due to reduced number of reactive Ga molecules present in the gas flux and due to their smaller resident time[97]. Enhanced vertical growth was observed for P = 100 Torr when V/III was 1330.

It is then clear from Fig. 6.7 that P = 100 Torr and V/III= 7880 resulted in best lateral coverage with the least thickness. We performed detail study on this wafer which will be discussed in later sections.

6.3.4 Growth rate anisotropy and micro loading

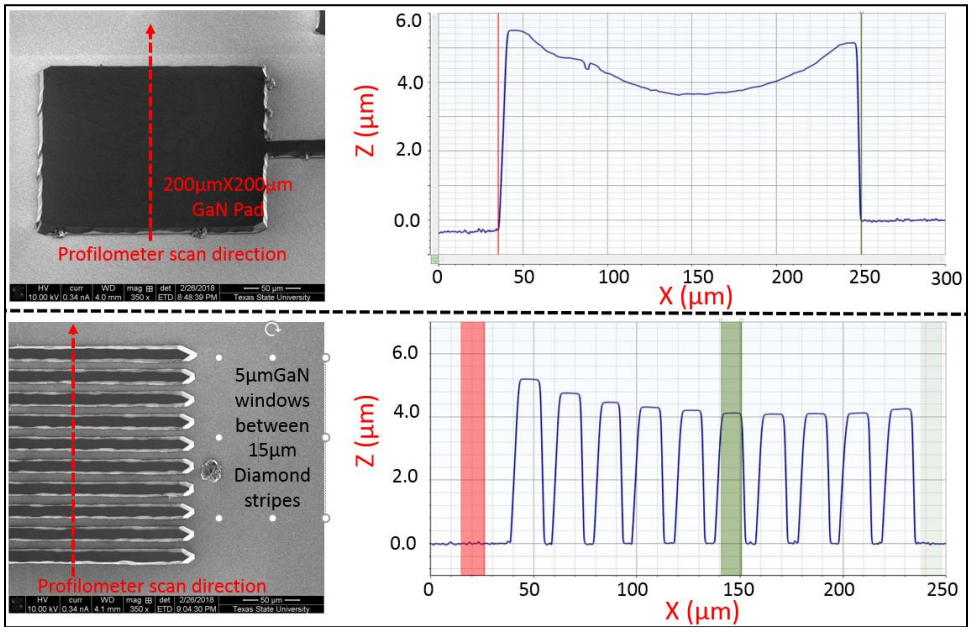

Figure 6. 8. Growth anisotropy resulted from micro loading of GaN on various sizes of GaN openings (for P = 40 torr, T = 975 °C and V/III=1330). The top panel shows SEM images of a 200 µm X 200 µm square GaN ELO region and its profile measured using surface profilometer. The bottom panel shows similar profile for a set of 10 GaN stripes of widths 5 µm separated by 15 µm diamond.

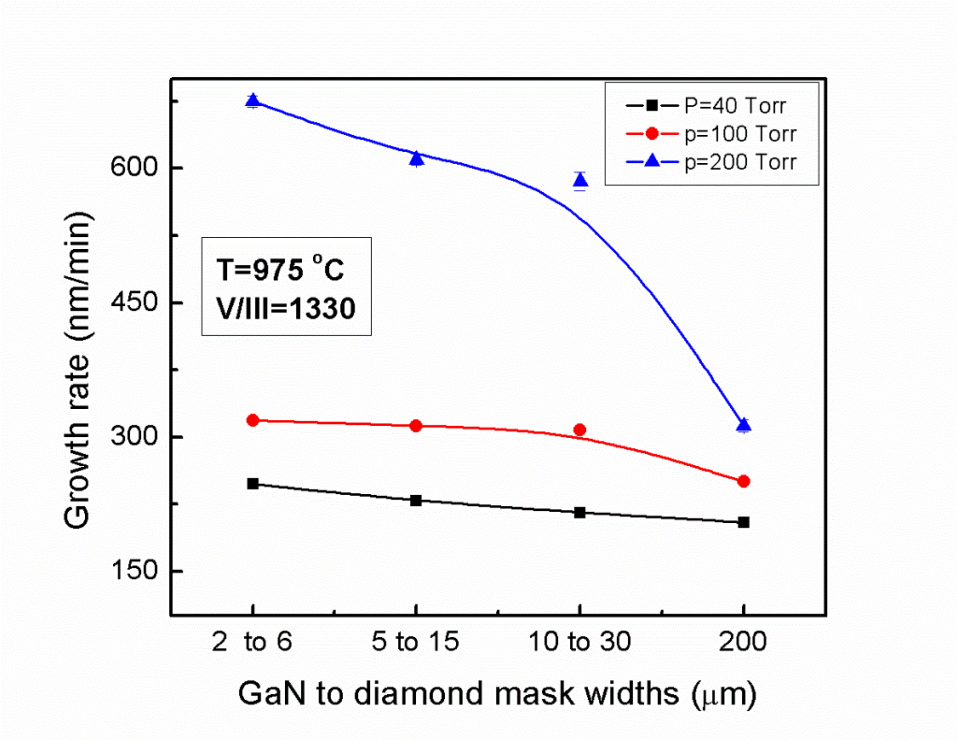

Figure 6. 9. Growth rate anisotropy as a function of mask openings and separations for various pressures. Growth rate was calculated using surface profilometer based on lowest thickness feature at the middle of any panel and average of at least three similar features on various region at ~ 30 mm from the center of a 100mm wafer.

Some very interesting results were observed during the study of ELO GaN on diamond wafer growth experiments. We observed anisotropic growth of ELO GaN for various sized mask openings. Fig. 6.8 shows profilometer thickness of ELO GaN (P = 40 Torr, T = 975 °C and V/III = 1330) grown on a 200 µm opening (top panel) and a series of 10 GaN stripes of widths 5 µm separated by 15 µm diamond. Clearly, growth rate was very high at the edge of each feature and lowest at the middle region of any feature. This is due to micro loading of reactant on the edge of the opening. Energetic reactant migrates on the mask and form bond whenever they find lowest energy position. Reactants coming from diamond mask sees lowest bonding energy at the edge of GaN opening and form a bond there. This process continues during the entire growth and results in growth anisotropy as seen in Fig. 6.8. It is worth mentioning that micro loading reduces (planar surface forms) as the GaN

opening becomes wider because of higher chance of reactant incorporation in wide GaN area.

To quantify the micro loading and calculate growth rate dependence on mask size, we calculated ELO GaN growth rate for various stripe widths with same stripe to mask ratio (1:3) and the results are shown in Fig. 6.9. Growth rates were calculated based on the middle region stripe with lowest thickness. It is clearly seen that growth rate was high when mask opening was small. This result is obvious because higher number of reactants try to incorporate in small space when the reactant flux is same on the same region of the wafer. In our MOCVD reactor, growth uniformity across the wafer was optimized and growth rate was calculated from same region of the wafer (at least 3 sets of stripes from various regions at ~30 mm from center). The observed growth rate anisotropy is the result of micro loading and similar dependencies are expected on the other region of the wafer.

6.3.5 Effect of mask orientation

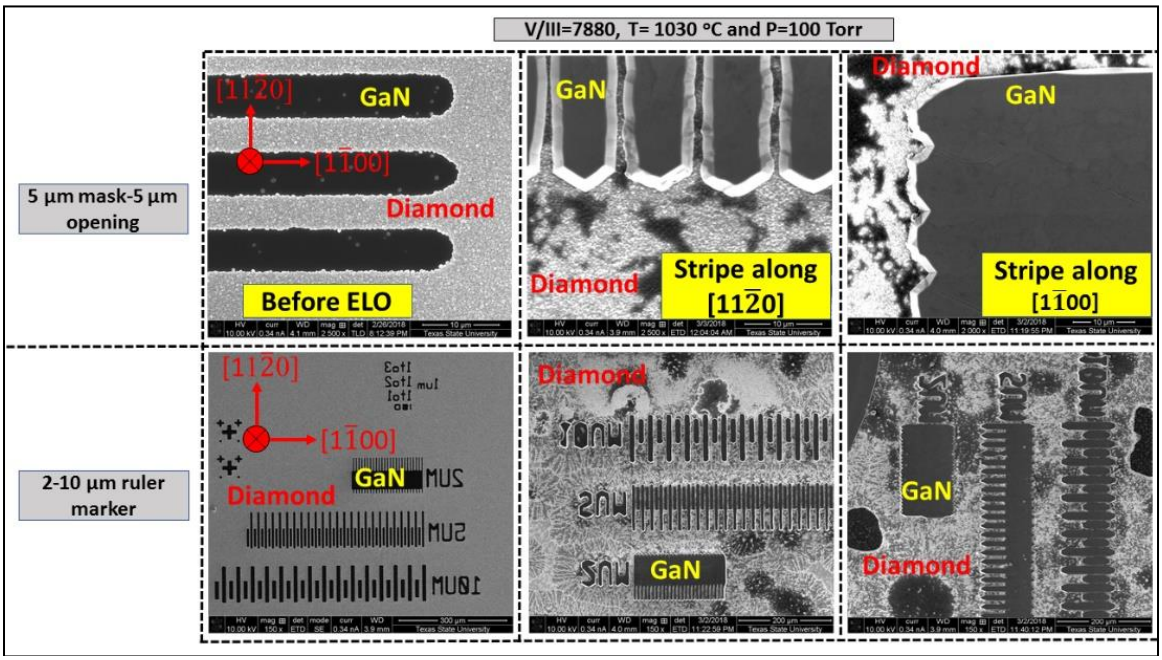

Figure 6. 10. SEM images showing lateral growth anisotropy as a function of mask opening orientation for the wafer grown with T = 1030 °C, P = 100 Torr and V/III = 7880. Top panel represents a 5 µm GaN opening by 5 µm diamond stripes before, and after ELO GaN where enhanced lateral growth and complete coalescence was observed for stripe oriented along [1$\bar{1}$00] direction. Bottom panel shows SEM image of similar growth anisotropy for a 2-10 µm rules marker where GaN was regrown through the markers. Images are taken at ~30 mm from the center of a 100 mm wafer.

The effect of mask orientation on ELO GaN has been well reported by many researchers[82], [84], [203]–[206][81]. To observe this effect, as described in experimental section, we deposited CVD diamond with stripes features along [1$\bar{1}$00] in one half of the wafer and along [11$\bar{2}$0] on another half. Selective seeding technique using photolithography made this possible. Fig. 6.10 shows SEM images taken on same feature before ELO and after ELO GaN growth with distinguishable lateral growth of {11$\bar{2}$0} when stripes are oriented along [1$\bar{1}$00]. According to the growth model as described in Fig. 6.6, under high temperature, increased V/III ratio and lower pressure, growth of {11$\bar{2}$0} is favorable when mask stripes are oriented along [1$\bar{1}$00]. For stripe opening along [11$\bar{2}$0], the pyramidal facets with {1$\bar{1}$01} forms. These facets are reported to be with N face

polarity and have been reported to be less dependent on pressure and temperature[80]. Therefore, despite the low pressure and high temperature, $\{1\bar{1}01\}$ facets were present in ELO GaN when stripes were oriented along $[11\bar{2}0]$.

6.3.6 Details characterization of wafer with successful lateral growth

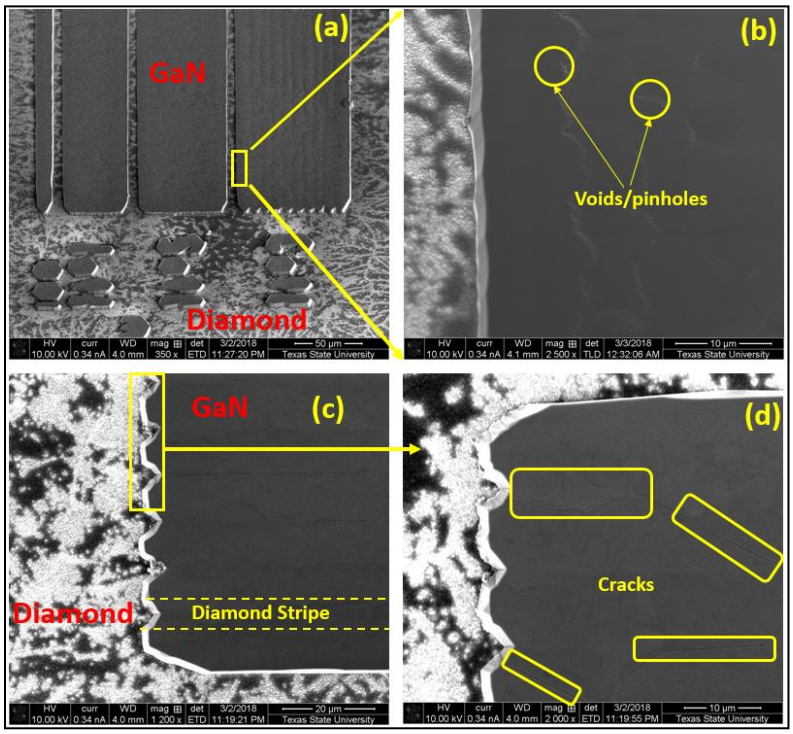

Figure 6. 11. SEM images showing complete coalescence of various features for the ELO with P = 100 Torr, T = 1030 °C and V/III = 7880. A panel of 2 µm GaN stripe opening between various widths diamond lines are shown in (a) and (b) is the magnified version of the boxed region in (a) showing voids/pinholes on ELO surface. Complete coalescence on a 5 µm diamond to 5 µm GaN opening is shown in (c) and its magnified view is shown in (d) where cracks were visible on ELO region. Images are taken at ~30 mm from the center of the wafer.

6.3.6.a Coalescence of GaN on Diamond stripes

Fig. 6.11 shows representative SEM images of ELO GaN grown on diamond mask with P = 100 Torr, T = 1030 °C and V/III = 7880. Clearly visible coalescence of GaN is observed in Fig. 6.11(a) and its magnified view in 6.11(b) for 2 µm sized GaN opening between diamond stripes with various widths. Similar images from a 5 µm GaN opening with 5 µm diamond stripe is shown in Fig. 6.11(c) and its magnified view in Fig. 6.11(d). Although

coalescence was achieved in both types of features, there were several voids, pinholes and cracks visible in the coalescence regions. The pinhole/ voids are believed to form when two faces of GaN coalesced together. The cracking was a result of higher thickness of GaN. Such cracking was visible in other bigger regrown regions (not shown here). Cracks are generated due to the increased thermal stress resulted from quick cooling of the wafer from GaN growth temperature (1030 °C) to room temperature. The thermal expansion coefficient (CTE) mismatch of GaN and Diamond is believed to be the main reason for such thermal stress and cracks[207] on ELO region. On the other hand, the CTE mismatch between GaN and Si was responsible for cracks on the wider window regions.

6.3.6.b ELO GaN-diamond interface

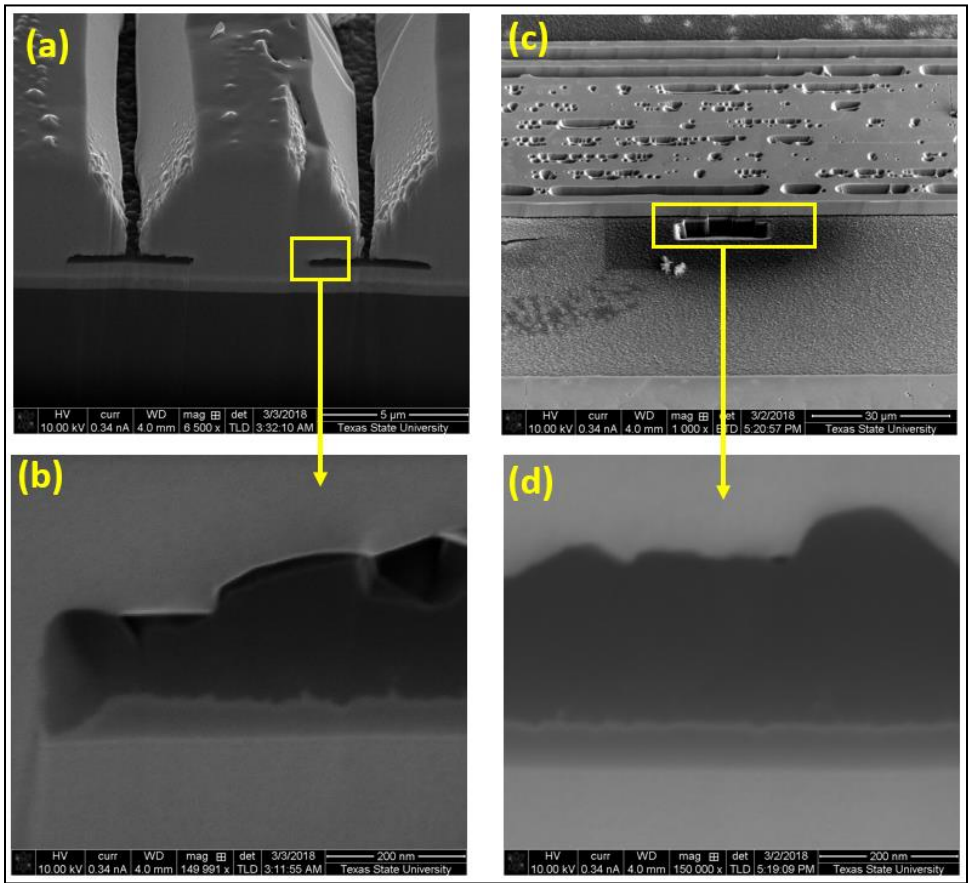

Figure 6. 12. FIB cross section SEM images taken from ELO wafer grown with P = 100 Torr, T = 1030 °C and V/III=7880 (mask orientation [11$\bar{2}$0]). (a) across a 5 µm diamond to 5 µm GaN opening and (b) magnified view of the boxed region in (a). (c) along the side of a panel of 2 GaN stipes with 4 µm diamond line and (d) magnified view of the boxed region in (c).

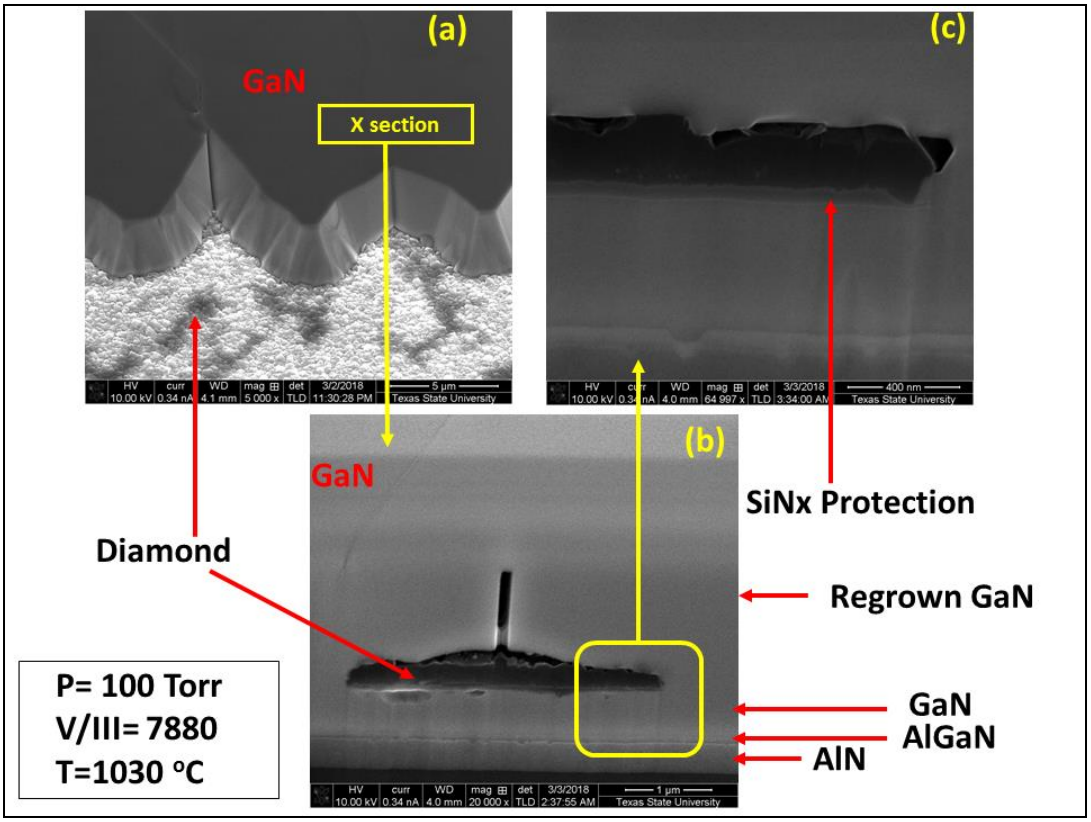

Figure 6. 13. FIB cross section SEM images taken from fully coalesced ELO region of the wafer grown with P = 100 Torr, T = 1030 °C and V/III = 7880 (mask orientation [1$\bar{1}$00]). (a) Fully coalesced 5 µm diamond to 5 µm GaN opening and (b) magnified view of the cross section showing buried diamond stripe and all nitride semiconductor layers and (c) magnified view of the GaN-Diamond interface.

To study the interface of the regrown GaN-diamond, we performed FIB on the successful regrown regions of the ELO GaN grown with P = 100 Torr, T = 1030 °C and V/III = 7880. FIB images taken on region with mask orientation along [11$\bar{2}$0] is shown in Fig. 6.12. Although lateral growth was relatively less when mask orientation was along [11$\bar{2}$0] but we wanted to observe the interface between the GaN and diamond. It is seen from Fig 6.12(a) and its magnified view in Fig. 6.12(b) that there were voids and rough interface between GaN and diamond when cross sections were taken across the stripe. However, in some regions there were good adhesion. We also took a cross section in a region along the stripe on regrown region (6.12(c)) to see the interface and it was found that adhesion was better along the stripe. To understand true interface between these two materials,

transmission electron microscopy (TEM) was necessary. However, TEM was not performed during this research and is subject of future study.

We took cross section SEM images across a fully coalesced GaN stripe (5 μm to 5 μm) on the same wafer as shown in Fig. 6.13(a). It is seen from Fig. 6.13(b) that two adjacent GaN faces did not coalesced until ~1 μm vertical growth. However, clear coalescence was observed above diamond stripe when GaN was grown more that ~1 μm vertically. The GaN-Diamond interface, dielectric protective layer used for selective deposition, initial GaN and regrown GaN are visible in Fig. 6.13(c). Rough GaN-Diamond interface with irregular voids are visible. This is expected because, the roughness of the diamond films was high (<30nm).

It is therefore evident from SEM and cross section SEM images taken from the wafer grown with P = 100 Torr, T=1030 °C and V/III = 7880 that ELO of GaN on diamond is possible and complete coalescence of GaN above diamond stripe is achievable when stripe separation is equal or below 5 μm. We performed x-ray diffraction and Raman measurements on the ELO GaN of this wafer.

6.3.6.c. HRXRD

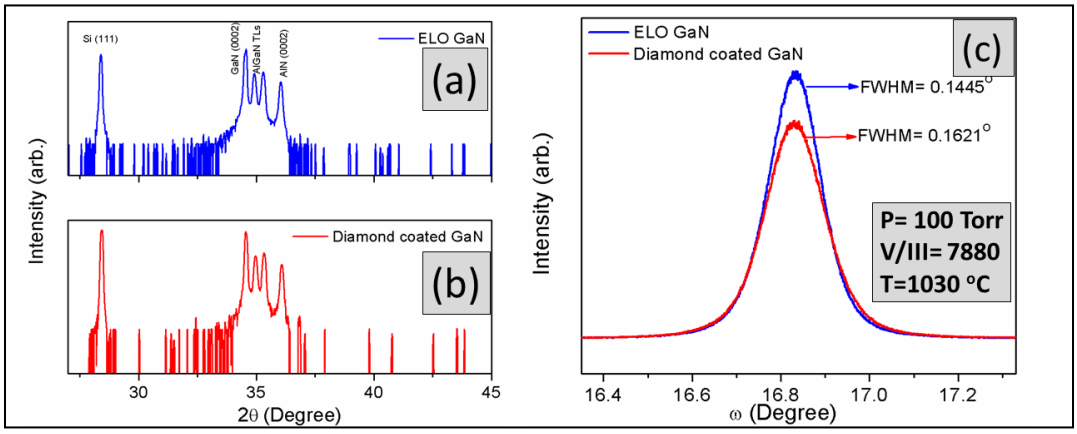

Figure 6. 14. HRXRD spectra of the wafer grown with P=100 Torr, T=1030 °C and V/III=7880 taken from (a) fully coalesced ELO GaN and (b) diamond coated GaN region and (c) Rocking curve of GaN (0002) plane reflection. Spectra collected from ~30mm region from the center of 100mm wafer.

HRXRD spectra of GaN ELO-diamond wafer (grown with P = 100 Torr, T = 1030 °C and V/III = 7880) collected from (a) ELO region and (b) diamond coated region is shown in Fig. 6.14. Spectra were collected for 2θ=25° to 90° but here it is shown for first 20° due to repetitive nature of secondary peaks and most importantly due to absence of any polycrystalline peaks. The absence of polycrystalline peaks on HRXRD patterns confirms formation of (0002) oriented GaN on overgrowth regions. The Ge (220) double bounce monochromator has allowed observation of closely spaced GaN (0002), AlGaN TLs (0002) and AlN (0002) peaks in Fig 6.14. However, diamond (111) peak around ~43.9° [144] was not visible due to its very low thickness. This is because the Ge 2 bounce monochromator reduces the intensity of any peak up to three orders of magnitude. Notable difference in the XRD patterns taken on ELO region compared to diamond coated region is the increase of GaN (0002) peak's integrated intensity which is a result of excessive lateral growth of GaN on ELO region. To understand the true difference between ELO GaN and diamond coated GaN, we took a rocking curve around GaN (0002) as shown in Fig. 6.14(c). The full width

at half maxima (FWHM) of GaN (0002) peak was 0.1445° (520 arc second) and 0.1621° (580 arc second) on ELO and diamond coated region, respectively. Clearly, the ELO GaN has lower FWHM than our baseline GaN wafers (FWHM = ~0.16°) indicating better crystallinity and reduced defect. In general, reduced FWHM of a rocking curve of any peak means more crystal planes are aligned to that specific plane and disorientations or defect density is less in the crystal[208].Such reduction in FWHM have been reported for ELO GaN in many literatures[204][206].

6.3.6d Raman Spectroscopy

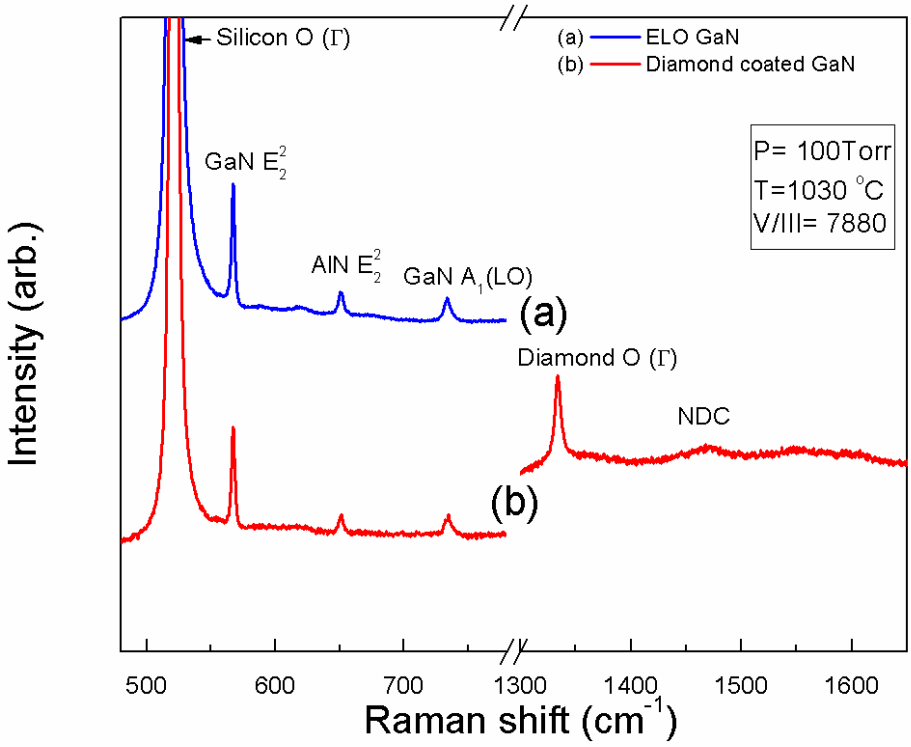

Figure 6. 15. Visible Raman (532 nm) of the ELO wafer grown with P = 100 Torr, T = 1030 °C and V/III = 7880. Spectra collected from (a) fully coalesced ELO GaN and (b) diamond coated GaN region.

The quality of ELO GaN was further confirmed from Raman measurement results as shown

in Fig. 6.15. Spectra (a) and (b) on Fig. 6.15 represents Raman spectra collected (from ~30 mm from center of wafer) on ELO region and diamond coated region, respectively. As seen from Raman spectrum (a), clear Raman peaks were observed for Si O (Γ), GaN (E_2^2), AlN (E_2^2), and GaN A_1 (LO) phonon at ~520.6 cm^{-1}, at ~ 567.5 cm^{-1}, at ~650.3 cm^{-1} and at ~733.5 cm^{-1}, respectively. In case of Raman spectrum collected from diamond coated GaN region, a sharp diamond O (Γ) at ~1333.5 cm^{-1} and broad NDC peak at 1450-1600 cm^{-1} were visible. The observed offset of diamond peaks came from high fluorescence of NDC at 532 nm laser line[209]. Background due to use of visible laser because NDC peaks are more sensitive to visible laser. The peak positions for nitrides semiconductors did not change greatly due to ELO GaN growth. Interestingly, after fitting the peak position (Lorentzian) of GaN Raman peak it was found that the GaN (E_2^2) peak occurred at 566.45±0.1 cm^{-1} on diamond coated region and at 565.7±0.1 cm^{-1} on the ELO region. The 0.75±0.1 cm^{-1} red shift in GaN (E_2^2) Raman peak on ELO region compared to diamond coated region corresponds to ~ 0.22 GPa biaxial tensile stress (σ_{xx}) increase in the ELO GaN according to following equation,

$$\sigma_{xx} = \Delta\omega / k_R \tag{6.1}$$

where, $\Delta\omega$ is Raman shift of GaN(E_2^2) peak and k_R is Raman stress factor and has a value of 3.4±0.3 cm^{-1} /GPa[210]. Other notable difference in Raman spectra between two regions was the higher relative intensity of GaN peak due to higher thickness. Raman spectra observed on ELO region indicated increased tensile stress in GaN resulted due to higher thickness and CTE mismatch between GaN and Silicon.

6.4 Conclusion

We have reported for the first time, the epitaxial lateral overgrowth of crystalline GaN on polycrystalline diamond surface. Experiments were conducted to find out best MOCVD growth parameters and it was found that higher temperature, higher V/III ratio and moderately low-pressure results in best lateral coverage and complete coalescence of overgrown GaN. Diamond mask to GaN opening size and mask orientation plays significant role in lateral growth. Highest lateral growth and complete coalescence can be achieved when stripe shaped mask opening is oriented along $[1\bar{1}00]$. The overgrown GaN-diamond interface exhibited bonding between GaN and diamond along with some irregular voids in some regions. The overgrown GaN was grown along (0002) face and had better crystal quality than initial GaN. Raman spectroscopy result indicated high quality GaN on overgrown region. The technique described in the present research can be a useful for producing large GaN wafers suitable for high power application with better thermal management capability.

VII. CONCLUSIONS AND FUTURE WORKS

The growth of GaN-on-diamond and associated characterization demonstrated in this dissertation is the proof of the concept of successful crystalline semiconductor growth on polycrystalline CVD diamond. The current state-of-the-art process for producing GaN-on-diamond wafers suffers from several issues such that the resultant devices cannot perform to their full potential. The most significant problem associated with fabrication is the complexity of the wafer transfer (or flipped wafer) technology. For the materials, poor thermal conductivity and thermal boundary resistance of the dielectric layer impedes the flow of heat from the active region of the HEMT. An effective solution to all those problems has been presented in this dissertation using a novel approach that has never been reported before. Crystalline GaN grown on polycrystalline diamond using the method developed in this dissertation can revolutionize the nitride semiconductor device technology by increasing its thermal management capability. High power and high frequency GaN based electronic devices such as HEMT, HFET, lasers and LEDs fabricated using this approach is expected to operate at much higher temperature with greater power densities. As stated in the proposed research of Chapter 1, the GaN layer grown directly on diamond using the epitaxial lateral overgrowth (ELO) process developed in this research has the following advantages:

i. The active layer of the GaN based devices is now in direct contact with CVD diamond without any dielectric adhesion layer which will result in very efficient heat removal from the active region.

ii. No poor thermally conductive nucleation layer or graphitic carbon is present adjacent to the GaN surface thereby resulting in no, or very small, thermal resistance between GaN and diamond.

iii. The structure significantly reduces the problems associated with thermal boundary resistance, which is presently the fundamental problem with GaN-on-diamond HEMTs.

iv. No permanent wafer bonding is required which will result in reduced process complexity and overall cost.

v. Significantly simpler replacement of a complex process.

The final goal of depositing GaN directly on diamond was achieved through carefully conducted research at every step of the overall complex process. Invaluable knowledge about materials and growth process was gained through these experiments. Therefore, the research has contributed significant knowledge to the GaN-Diamond research field, in addition to achieving its ultimate goal. The major contributions of this work is summarized below.

7.1 Contributions of this Work

a. A systematic study was performed to understand the effect of CVD growth parameters on the quality and crystal structure of polycrystalline diamond. The motivation for performing this study was to understand the mechanism of texture formation in polycrystalline diamond. Increased methane concentration in hydrogen was found to be responsible for higher growth rate and higher non-diamond carbon in diamond film. Pronounced texture in diamond films were

observed when the film thickness was above 3 μm. Both <220> and <111> oriented diamond films were achieved by changing gas stoichiometry. The outcome of this study can contribute greatly to the realization of growth of semiconductor materials on preferentially oriented diamond films.

b. Having a clear idea about the growth parameters for producing diamond films with desired structural and electronic properties, the research effort was then concentrated to develop selective deposition of diamond. A bottom up approach of selective deposition of CVD diamond with feature size as small as 5 μm was successfully developed. Initially, the process was developed on Si and various dielectric surfaces but later the process was transferred to several other substrates including GaN and AlN. Several modifications to the selective seeding of diamond was implemented to achieve desired selectivity of diamond. The process developed in this step of the research can be used to implement diamond features as local heat spreader very close to the active layer of any electronic device where self-heating is present.

c. To understand the effect of global and local thermal stress associated with diamond growth on any substrate, a thorough study on stress mapping of a diamond-Silicon structure using micro Raman spectroscopy was performed. In addition, finite element model simulations of thermal stress for the grown structure were performed to understand the origin of stress. Excellent agreement between simulations and experimental results confirmed that the stress originates from thermal expansion coefficient mismatch of diamond and substrate materials. Furthermore, global stress of a fully coated diamond wafer can be minimized by depositing selectively.

d. Selective deposition of hot filament CVD diamond on GaN has been achieved without damaging the underlying GaN layer. Lateral resolution of diamond features as small as ~ 1 μm have been achieved with excellent cross wafer uniformity on the 100 mm substrate. The combined effect of a thin SiN_x layer protecting against etching and increased methane concentration for faster surface coverage was proven effective in mitigating damage to the ~25 nm AlGaN barrier layer on top of GaN. Presence of the thin barrier layer observed from HRXRD RSM data taken after diamond growth confirmed the surface protection capability of the developed process. To the best of our knowledge, this is the first report of growing HFCVD diamond on an AlGaN/GaN HEMT structure without damaging the AlGaN barrier layer.

e. Finally, using the knowledge gained from the above studies, ELO of GaN on polycrystalline diamond coated GaN wafers was realized. Selectively deposited diamond wafers produced by the previous steps of the research was utilized to conduct a systematic study of GaN ELO. MOCVD process parameters; i.e., V/III ratio, pressure and temperature, were varied based on literature suggested values for similar processes on other masking materials to achieve complete coverage of GaN on diamond. The effect of mask size and orientation on ELO growth of GaN was also studied. An MOCVD growth recipe for the fastest lateral coverage with minimum GaN thickness has been established.

7.2 Publications

The following invention disclosure form and articles have been prepared/submitted during

this dissertation research at Texas State University:

1. Raju Ahmed and Edwin L. Piner, "Semiconductor device structure on thermally enhanced diamond, and method associated with same", Invention disclosure form (IDF) submitted to Texas State University intellectual property (IP) committee on November 2016.
2. Raju Ahmed, M. Nazari, B. L. Hancock, J. Simpson, C. Engdahl, E. L. Piner, and M. W. Holtz, "Ultraviolet micro-Raman stress map of polycrystalline diamond grown selectively on silicon substrates using chemical vapor deposition", *Applied Physic Letters*, Submitted, March 2018.
3. Raju Ahmed, Anwar Siddique, Jonathan Anderson, Chris Engdahl, Mark Holtz and Edwin Piner, "High resolution selective area deposition of hot filament CVD diamond on 100mm MOCVD grown AlGaN/GaN wafers", In preparation 2018.
4. Raju Ahmed, Anwar Siddique, Jonathan Anderson, Chris Engdahl, Mark Holtz and Edwin Piner, "Effect of precursor stoichiometry on morphology and texture formation in hot filament CVD diamond films grown on Si (100) substrate", In preparation 2018.

7.3 Suggested future works

This dissertation research is proof of the concept for growing crystalline GaN on polycrystalline diamond. There are many research areas associated with this research that need attention. Several exciting areas of study are available as future extensions of the present research. The most interesting future research projects are summarized below:

7.3.1 Study of structural and thermal properties of regrown GaN-Diamond interface

Immediate research should include the study of the interface of the regrown GaN and diamond. Since phonon transport between two materials is greatly dependent on grain structure and crystal orientation[134], a detailed microscopy study involving the crystal quality of regrown GaN and determination of chemical bonding between GaN and diamond is extremely important to realize the full potential of the structure. Measurements of thermal conductivity of the individual layers and thermal boundary resistance of the GaN-Diamond interface should be performed using micro Raman or time domain thermo reflectance (TDTR) with the aid of finite element model simulations of thermal conductivity. In addition, diamond films with various types of preferred orientation can be used to produce GaN on diamond using the processes described in this dissertation. In that way, a true understanding of the effect of diamond crystal orientation on the thermal transport between GaN and diamond interface would be achieved.

7.3.2 Study of the effect of gas stoichiometry on the thermal conductivity of polycrystalline diamond films

The effect of gas stoichiometry on texture formation has been presented in Chapter 3, but no thermal conductivity measurements were performed. To understand the true effect of crystal orientation on thermal conductivity of CVD diamond, measurements of thermal conductivity is necessary. Raman spectroscopy based thermal conductivity measurements requires fabrication of CVD diamond membrane through complex back etching of the wafers. On the other hand, TDTR measurements require a very smooth (RMS roughness < 40 nm) surface which is very challenging to achieve in CVD. To solve this problem, a very thin layer of CVD diamond with complete surface coverage and smaller grain size should

be deposited. Higher methane concentration and shorter growth time can be useful to deposit such films. It is, however, worth mentioning that thermal conductivity is mostly affected by enhanced non-diamond carbons residing within the first few nanometers of the deposited diamond[167]. Therefore, a trade-off between growth process and measurements should be established in order to perform the measurements.

7.3.3 Fabrication and characterization of AlGaN/GaN HEMT on ELO GaN grown on diamond

Future work of this research should include deposition of the AlGaN/GaN HEMT on the regrown GaN regions over diamond. Since ELO produces GaN with better crystal quality, a HEMT with superior performance may be expected when grown on top of this GaN-diamond substrate [206]. Significant research effort will be necessary to optimize the growth conditions of the AlGaN barrier layer on top of the ELO GaN due to micro loading. Micro loading results in a non-uniform surface of ELO GaN which should be planarized in order to deposit the barrier layer. The micro loading issue is inevitable with smaller mask opening. Therefore, diamond coated GaN wafers having wider mask opening with narrow diamond features can be used to mitigate this problem. Another problem associated with HEMT structure growth on a narrow mask region is excessive vertical growth rate which may result in a thicker AlGaN layer with complete relaxation of the layer on top of GaN, even with a very short growth time. If the barrier layer thickness increases significantly above ~30 nm, the layer will relax. No piezo electric polarization is induced and as a result no 2DEG is formed. Possible solutions includes modification of the successful ELO recipe designed in this dissertation by reducing total gas flow into the chamber while keeping the V/III, pressure and temperature constant. In that way, a thin barrier layer can be grown on

top of the ELO GaN.

7.3.4 Growth of AlGaN/GaN HEMT on freestanding polycrystalline diamond

The ELO GaN wafer produced from this research can be used as a starting material to produce an AlGaN/GaN HEMT on a free-standing diamond substrate. The backside of the AlGaN/GaN HEMT wafer on ELO GaN can be etched and all transition layers subsequently removed. After that, diamond can be grown on the backside with higher methane concentration to get faster surface coverage and thicker diamond. The diamond exposed from the backside will act as the nucleation surface and, therefore, no seeding will be necessary for the diamond deposition. Upon successful implementation, this process is expected to produce an AlGaN/GaN HEMT directly grown on CVD diamond which is expected perform with world-record power density, without performance degradation.

7.3.5 Direct growth of nitride semiconductors on selectively deposited diamond-Si (111) wafer

Selective deposition of GaN on Si windows of selectively deposited diamond on Si (111) can produce a GaN-Diamond wafer prepared with further reduced process complexity. Initially, the growth process should be the same as the standard AlGaN/GaN HEMT on the diamond patterned Si wafer. Thickness of the diamond mask should be ~ 2 μm so that the HEMT can grow in the region between the diamond features. However, this process is likely to be affected by micro loading thereby potentially resulting in no barrier layer. A possible alternative is to grow standard AlGaN/GaN until reaching the top of the diamond pillars. At this point, the growth parameters should be switch to the ELO process. If lateral coverage is achieved under this ELO growth, this technique can be a simpler replacement

of the ELO GaN growth process developed in this dissertation. One important difference of this proposed ELO GaN with the reported ELO is the exposure of diamond to AlN precursors. GaN has been shown in this research to not "stick" to diamond but AlN growth on diamond has been observed by our group. ELO of GaN, therefore, can be enhanced due to this directly grown nitride on diamond process. The study of this structure would reveal valuable information about the growth, nucleation and interface of nitride semiconductors on diamond. In addition, the crystalline structure of the polycrystalline nitride layer should be examined using XRD pole figure to observe if a preferred orientation occurs.

REFERENCES

[1] U. K. Mishra, L. Shen, T. E. Kazior, and Y.-F. Wu, "GaN-based RF power devices and amplifiers," *Proc. IEEE*, vol. 96, no. 2, pp. 287–305, 2008.

[2] U. K. Mishra, P. Parikh, Y. F. Wu, Y. Morimoto, Y. Kondo, H. Kataoka, Y. Honda, R. Kozu, J. Sakamoto, J. Nakano, T. Origuchi, T. Yoshimura, and M. Okita, "AlGaN/GaN HEMTs - An overview of device operation and applications," *Proc. IEEE*, vol. 90, no. 6, pp. 1022–1031, 2002.

[3] R. Quay, *Gallium nitride electronics*, vol. 96. Springer Science & Business Media, 2008.

[4] T. Baltynov, V. Unni, and E. M. S. Narayanan, "The world's first high voltage GaN-on-Diamond power semiconductor devices," *Solid. State. Electron.*, vol. 125, pp. 111–117, 2016.

[5] G. Meneghesso, G. Verzellesi, F. Danesin, F. Rampazzo, F. Zanon, A. Tazzoli, M. Meneghini, and E. Zanoni, "Reliability of GaN high-electron-mobility transistors: State of the art and perspectives," *IEEE Trans. Device Mater. Reliab.*, vol. 8, no. 2, pp. 332–343, 2008.

[6] E. F. Schubert, "Light-emitting diodes Cambridge University Press," *New York*, pp. 35–40, 2006.

[7] Z. C. Feng, *III-nitride Devices and Nanoengineering*. World Scientific, 2008.

[8] C. Lu, L. Wang, J. Lu, R. Li, L. Liu, D. Li, N. Liu, L. Li, W. Cao, W. Yang, and others, "Investigation of the electroluminescence spectrum shift of InGaN/GaN multiple quantum well light-emitting diodes under direct and pulsed currents," *J. Appl. Phys.*, vol. 113, no. 1, p. 13102, 2013.

[9] D. Zhu, D. J. Wallis, and C. J. Humphreys, "Prospects of III-nitride optoelectronics grown on Si," *Reports Prog. Phys.*, vol. 76, no. 10, p. 106501, 2013.

[10] Q. Shan, Q. Dai, S. Chhajed, J. Cho, and E. F. Schubert, "Analysis of thermal properties of GaInN light-emitting diodes and laser diodes," *J. Appl. Phys.*, vol. 108, no. 8, p. 84504, 2010.

[11] J.-C. Wang, C.-H. Fang, Y.-F. Wu, W.-J. Chen, D.-C. Kuo, P.-L. Fan, J.-A. Jiang, and T.-E. Nee, "The effect of junction temperature on the optoelectrical properties of InGaN/GaN multiple quantum well light-emitting diodes," *J. Lumin.*, vol. 132, no. 2, pp. 429–433, 2012.

[12] J. D. Blevins, G. D. Via, K. Sutherlin, S. Tetlak, B. Poling, R. Gilbert, B. Moore, J. Hoelscher, B. Stumpff, A. Bar-Cohen, and others, "Recent progress in GaN-on-diamond device technology," in *Proc. CS MANTECH Conf*, 2014, pp. 105–108.

[13] S. Singhal, T. Li, A. Chaudhari, A. W. Hanson, R. Therrien, J. W. Johnson, W. Nagy, J. Marquart, P. Rajagopal, J. C. Roberts, and others, "Reliability of large periphery GaN-on-Si HFETs," *Microelectron. Reliab.*, vol. 46, no. 8, pp. 1247–1253, 2006.

[14] A. Bar-Cohen, J. J. Maurer, and J. G. Felbinger, "DARPA's Intra/Interchip Enhanced Cooling (ICECool) Program," in *CS MANTECH Conference, May 13th-16th*, 2013.

[15] K. D. Malcolm, “Characterization of the Thermal Properties of Chemical Vapor Deposition Grown Diamond Films for Electronics Cooling,” Georgia Institute of Technology, 2016.
[16] M. Nazari, B. L. Hancock, E. L. Piner, M. W. Holtz, M. Nazari, B. L. Hancock, E. L. Piner, and M. W. Holtz, “Self-heating profile in an AlGaN/GaN heterojunction field-effect transistor studied by ultraviolet and visible micro-Raman spectroscopy,” *IEEE Trans. Electron Devices*, vol. 62, no. 5, pp. 1467–1472, 2015.
[17] O. Ambacher, J. Smart, J. R. Shealy, N. G. Weimann, K. Chu, M. Murphy, W. J. Schaff, L. F. Eastman, R. Dimitrov, L. Wittmer, M. Stutzmann, W. Rieger, and J. Hilsenbeck, “Two-dimensional electron gases induced by spontaneous and piezoelectric polarization charges in N- and Ga-face AlGaN/GaN heterostructures,” *J. Appl. Phys.*, vol. 85, no. 6, p. 3222, 1999.
[18] L. F. Eastman and U. K. Mishra, “The toughest transistor yet [GaN transistors],” *IEEE Spectr.*, vol. 39, no. 5, pp. 28–33, 2002.
[19] O. Lancry, E. Pichonat, J. Réhault, M. Moreau, R. Aubry, and C. Gaquière, “Development of time-resolved UV micro-Raman spectroscopy to measure temperature in AlGaN/GaN HEMTs,” *Solid. State. Electron.*, vol. 54, no. 11, pp. 1434–1437, 2010.
[20] A. Wang, M. J. Tadjer, and F. Calle, “Simulation of thermal management in AlGaN/GaN HEMTs with integrated diamond heat spreaders,” *Semicond. Sci. Technol.*, vol. 28, no. 5, p. 55010, 2013.
[21] S. Chhajed, Y. Xi, Y.-L. Li, T. Gessmann, and E. F. Schubert, “Influence of junction temperature on chromaticity and color-rendering properties of trichromatic white-light sources based on light-emitting diodes,” *J. Appl. Phys.*, vol. 97, no. 5, p. 54506, 2005.
[22] Y. Xi and E. F. Schubert, “Junction--temperature measurement in GaN ultraviolet light-emitting diodes using diode forward voltage method,” *Appl. Phys. Lett.*, vol. 85, no. 12, pp. 2163–2165, 2004.
[23] Y. Xi, J.-Q. Xi, T. Gessmann, J. M. Shah, J. K. Kim, E. F. Schubert, A. J. Fischer, M. H. Crawford, K. H. A. Bogart, and A. A. Allerman, “Junction and carrier temperature measurements in deep-ultraviolet light-emitting diodes using three different methods,” *Appl. Phys. Lett.*, vol. 86, no. 3, p. 31907, 2005.
[24] W. Johnson and E. L. Piner, “GaN HEMT technology,” in *GaN and ZnO-based Materials and Devices*, Springer, 2012, pp. 209–237.
[25] J. W. Pomeroy, M. Bernardoni, D. C. Dumka, D. M. Fanning, and M. Kuball, “Low thermal resistance GaN-on-diamond transistors characterized by three-dimensional Raman thermography mapping,” *Appl. Phys. Lett.*, vol. 104, no. 8, 2014.
[26] G. D. Via, J. G. Felbinger, J. Blevins, K. Chabak, G. Jessen, J. Gillespie, R. Fitch, A. Crespo, K. Sutherlin, B. Poling, and others, “Wafer-scale GaN HEMT performance enhancement by diamond substrate integration,” *Phys. status solidi*, vol. 11, no. 3–4, pp. 871–874, 2014.
[27] D. I. Babić, Q. Diduck, P. Yenigalla, A. Schreiber, D. Francis, F. Faili, F. Ejeckam, J. G. Felbinger, and L. F. Eastman, “GaN-on-diamond field-effect transistors: from wafers to amplifier modules,” in *MIPRO, 2010 Proceedings of the 33rd International Convention*, 2010, pp. 60–66.

[28] D. Francis, F. Faili, D. Babić, F. Ejeckam, A. Nurmikko, and H. Maris, "Formation and characterization of 4-inch GaN-on-diamond substrates," *Diam. Relat. Mater.*, vol. 19, no. 2, pp. 229–233, 2010.
[29] F. Ejeckam, D. Babic, F. Faili, D. Francis, F. Lowe, Q. Diduck, C. Khandavalli, D. Twitchen, and B. Bolliger, "3,000+ Hours continuous operation of GaN-on-Diamond HEMTs at 350° c channel temperature," in *Semiconductor Thermal Measurement and Management Symposium (SEMI-THERM), 2014 30th Annual*, 2014, pp. 242–246.
[30] A. Wang, M. J. Tadjer, T. J. Anderson, R. Baranyai, J. W. Pomeroy, T. I. Feygelson, K. D. Hobart, B. B. Pate, F. Calle, and M. Kuball, "Impact of intrinsic stress in diamond capping layers on the electrical behavior of AlGaN/GaN HEMTs," *IEEE Trans. Electron Devices*, vol. 60, no. 10, pp. 3149–3156, 2013.
[31] H. Morkoc, *Nitride semiconductors and devices*, vol. 32. Springer Science & Business Media, 2013.
[32] F. Ren and J. C. Zolper, *Wide energy bandgap electronic devices*. World Scientific, 2003.
[33] O. Ambacher, "Growth and applications of group III-nitrides," *J. Phys. D. Appl. Phys.*, vol. 31, no. 20, p. 2653, 1998.
[34] O. Ambacher, B. Foutz, J. Smart, J. R. Shealy, N. G. Weimann, K. Chu, M. Murphy, A. J. Sierakowski, W. J. Schaff, L. F. Eastman, and others, "Two dimensional electron gases induced by spontaneous and piezoelectric polarization in undoped and doped AlGaN/GaN heterostructures," *J. Appl. Phys.*, vol. 87, no. 1, pp. 334–344, 2000.
[35] T. Hanada, "Basic Properties of ZnO, GaN, and Related Materials," in *Oxide and Nitride Semiconductors*, Springer, 2009, pp. 1–19.
[36] S. Strite and H. Morkoç, "GaN, AlN, and InN: a review," *J. Vac. Sci. Technol. B*, vol. 10, no. 4, pp. 1237–1266, 1992.
[37] S. M. Sze, *Semiconductor devices: physics and technology*. John Wiley & Sons, 2008.
[38] F. Bernardini, V. Fiorentini, and D. Vanderbilt, "Spontaneous polarization and piezoelectric constants of III-V nitrides," *Phys. Rev. B*, vol. 56, no. 16, p. R10024, 1997.
[39] F. Bernardini and V. Fiorentini, "Nonlinear macroscopic polarization in III-V nitride alloys," *Phys. Rev. B (Condensed Matter Mater. Physics)*, vol. 64, no. 8, pp. 85201–85207, 2001.
[40] L. Shen, S. Heikman, B. Moran, R. Coffie, N.-Q. Zhang, D. Buttari, I. P. Smorchkova, S. Keller, S. P. DenBaars, and U. K. Mishra, "AlGaN/AlN/GaN high-power microwave HEMT," *IEEE Electron Device Lett.*, vol. 22, no. 10, pp. 457–459, 2001.
[41] B. G. Streetman and S. Banerjee, *Solid state electronic devices*, vol. 5. Prentice Hall New Jersey, 2000.
[42] P. W. May, "Diamond thin films: a 21st-century material," *Phil. Trans. R. Soc. Lond. A*, vol. 358, no. Tennant 1797, pp. 473–495, 2000.
[43] A. J. Neves and M. H. Nazaré, *Properties, growth and applications of diamond*, no. 26. IET, 2001.

[44] Z. Lin and X. Jiang, “CVD diamond films: nucleation and growth,” *Mater. Sci.*, vol. 25, pp. 123–154, 1999.
[45] M. N. R. Ashfold, P. W. May, C. A. Rego, and N. M. Everitt, “Thin film diamond by chemical vapour deposition methods,” *Chem. Soc. Rev.*, vol. 23, no. 1, p. 21, 1994.
[46] O. Shenderova, S. Hens, and G. McGuire, “Seeding slurries based on detonation nanodiamond in DMSO,” *Diam. Relat. Mater.*, vol. 19, no. 2–3, pp. 260–267, 2010.
[47] M. N. Touzelbaev and K. E. Goodson, “Impact of nucleation density on thermal resistance near diamond-substrate boundaries,” *J. Thermophys. Heat Transf.*, vol. 11, no. 4, pp. 506–512, 1997.
[48] T. Izak, O. Babchenko, V. Jirásek, G. Vanko, M. Vallo, M. Vojs, and A. Kromka, “Selective area deposition of diamond films on AlGaN/GaN heterostructures,” *Phys. Status Solidi*, vol. 251, no. 12, pp. 2574–2580, 2014.
[49] M. Cardona and G. Guntherodt, “LIGHT-SCATTERING IN SOLIDS. 2. BASIC CONCEPTS AND INSTRUMENTATION-INTRODUCTION.” CAMBRIDGE UNIV PRESS 40 WEST 20TH STREET, NEW YORK, NY 10011-4211, 1982.
[50] J. E. Graebner, S. Jin, G. W. Kammlott, J. A. Herb, and C. F. Gardinier, “Large anisotropic thermal conductivity in synthetic diamond films,” 1992.
[51] J. Anaya, S. Rossi, M. Alomari, E. Kohn, L. Tóth, B. Pécz, K. D. Hobart, T. J. Anderson, T. I. Feygelson, B. B. Pate, and M. Kuball, “Control of the in-plane thermal conductivity of ultra-thin nanocrystalline diamond films through the grain and grain boundary properties,” *Acta Mater.*, vol. 103, pp. 141–152, 2016.
[52] Y.-F. Wu, M. Moore, A. Saxler, T. Wisleder, and P. Parikh, “40-W/mm double field-plated GaN HEMTs,” in *2006 64th Device Research Conference*, 2006, pp. 151–152.

[53] D. Liu, H. Sun, J. W. Pomeroy, D. Francis, F. Faili, D. J. Twitchen, and M. Kuball, “GaN-on-diamond electronic device reliability: Mechanical and thermo-mechanical integrity,” *Appl. Phys. Lett.*, vol. 107, no. 25, 2015.
[54] T. Beechem, A. Christensen, D. S. Green, and S. Graham, “Assessment of stress contributions in GaN high electron mobility transistors of differing substrates using Raman spectroscopy,” *J. Appl. Phys.*, vol. 106, no. 11, p. 114509, 2009.
[55] O. Arenas, G. S. Member, É. Al Alam, V. Aimez, A. Jaouad, and A. Self-heating, “Electrothermal mapping of algan gan hemts using microresistance thermometer detectors.pdf,” *IEEE ELECTRON DEVICE Lett.*, vol. 36, no. 2, pp. 2014–2016, 2015.
[56] C. Hodges, J. A. Calvo, S. Stoffels, D. Marcon, and M. Kuball, “AlGaN/GaN field effect transistors for power electronics—Effect of finite GaN layer thickness on thermal characteristics,” *Appl. Phys. Lett.*, vol. 103, no. 20, p. 202108, 2013.
[57] J. Kühn, *AlGaN-GaN-HEMT Power Amplifiers with Optimized Power-added Efficiency for X-band Applications*, vol. 62. KIT Scientific Publishing, 2011.
[58] R. Zhytnytska, J. Böcker, H. Just, O. Hilt, E. Bahat-Treidel, S. Dieckerhoff, J. Würfl, and G. Tränkle, “Thermal characterization of AlGaN/GaN HEMTs on Si and n-SiC substrates,” *Tech. Univ. Berlin, Power Electron. Res. Gr.*, 2015.

[59] O. Hilt, E. Bahat-Treidel, A. Knauer, F. Brunner, R. Zhytnytska, and J. Würfl, "High-voltage normally OFF GaN power transistors on SiC and Si substrates," *MRS Bull.*, vol. 40, no. 5, pp. 418–424, 2015.
[60] G. H. Jessen, J. K. Gillespie, G. D. Via, A. Crespo, D. Langley, J. Wasserbauer, F. Faili, D. Francis, D. Babic, F. Ejeckam, and others, "AlGaN/GaN HEMT on diamond technology demonstration," in *2006 IEEE Compound Semiconductor Integrated Circuit Symposium*, 2006, pp. 271–274.
[61] A. Dussaigne, M. Malinverni, D. Martin, A. Castiglia, and N. Grandjean, "GaN grown on (111) single crystal diamond substrate by molecular beam epitaxy," *J. Cryst. Growth*, vol. 311, no. 21, pp. 4539–4542, 2009.
[62] G. W. G. van Dreumel, J. G. Buijnsters, T. Bohnen, J. J. Ter Meulen, P. R. Hageman, W. J. P. van Enckevort, and E. Vlieg, "Growth of GaN on nano-crystalline diamond substrates," *Diam. Relat. Mater.*, vol. 18, no. 5, pp. 1043–1047, 2009.
[63] K. Hirama, M. Kasu, and Y. Taniyasu, "Growth and Device Properties of AlGaN/GaN High-Electron Mobility Transistors on a Diamond Substrate," *Jpn. J. Appl. Phys.*, vol. 51, no. 1S, p. 01AG09, 2012.
[64] F. Ejeckam, D. Francis, F. Faili, D. Twitchen, B. Bolliger, D. Babic, and J. Felbinger, "S2-T1: GaN-on-diamond: A brief history," in *2014 Lester Eastman Conference on High Performance Devices (LEC)*, 2014.

[65] J. Cho, Z. Li, E. Bozorg-Grayeli, T. Kodama, D. Francis, F. Ejeckam, F. Faili, M. Asheghi, and K. E. Goodson, "Improved thermal interfaces of GaN--diamond composite substrates for HEMT applications," *IEEE Trans. Components, Packag. Manuf. Technol.*, vol. 3, no. 1, pp. 79–85, 2013.
[66] H. Sun, R. B. Simon, J. W. Pomeroy, D. Francis, F. Faili, D. J. Twitchen, and M. Kuball, "Reducing GaN-on-diamond interfacial thermal resistance for high power transistor applications," *Appl. Phys. Lett.*, vol. 106, no. 11, p. 111906, 2015.
[67] P. Chao, K. Chu, and C. Creamer, "A New High Power GaN-on-Diamond HEMT with Low-Temperature Bonded Substrate Technology," *CS MANTECH Conf.*, pp. 179–182, 2013.
[68] J. Cho, K. K. Chu, P. C. Chao, C. McGray, M. Asheghi, and K. E. Goodson, "Thermal conduction normal to thin silicon nitride films on diamond and GaN," *Thermomechanical Phenom. Electron. Syst. -Proceedings Intersoc. Conf.*, pp. 1186–1191, 2014.
[69] M. Nazari, B. L. Hancock, J. Anderson, A. Savage, E. L. Piner, S. Graham, F. Faili, S. Oh, D. Francis, D. Twitchen, and others, "Near-ultraviolet micro-Raman study of diamond grown on GaN," *Appl. Phys. Lett.*, vol. 108, no. 3, p. 31901, 2016.
[70] A. Sarua, H. Ji, K. P. Hilton, D. J. Wallis, M. J. Uren, T. Martin, and M. Kuball, "Thermal boundary resistance between GaN and substrate in AlGaN/GaN electronic devices," *IEEE Trans. Electron Devices*, vol. 54, no. 12, pp. 3152–3158, 2007.

[71] A. Manoi, J. W. Pomeroy, N. Killat, and M. Kuball, "Benchmarking of thermal boundary resistance in AlGaN/GaN HEMTs on SiC substrates: Implications of the nucleation layer microstructure," *IEEE electron device Lett.*, vol. 31, no. 12, pp. 1395–1397, 2010.
[72] J. Cho, Y. Won, D. Francis, M. Asheghi, and K. E. Goodson, "Thermal Interface Resistance Measurements for GaN-on-Diamond Composite Substrates," in *2014 IEEE Compound Semiconductor Integrated Circuit Symposium (CSICS)*, 2014, pp. 1–4.
[73] J. Kuzmik, S. Bychikhin, D. Pogany, E. Pichonat, O. Lancry, C. Gaquière, G. Tsiakatouras, G. Deligeorgis, and A. Georgakilas, "Thermal characterization of MBE-grown GaN/AlGaN/GaN device on single crystalline diamond," *J. Appl. Phys.*, vol. 109, no. 8, pp. 1–4, 2011.
[74] D. D. Koleske, A. E. Wickenden, R. L. Henry, J. C. Culbertson, and M. E. Twigg, "GaN decomposition in H2 and N2 at MOVPE temperatures and pressures," *J. Cryst. Growth*, vol. 223, no. 4, pp. 466–483, 2001.
[75] P. W. May, H. Y. Tsai, W. N. Wang, and J. A. Smith, "Deposition of CVD diamond onto GaN," *Diam. Relat. Mater.*, vol. 15, no. 4–8, pp. 526–530, 2006.

[76] T. J. Anderson, K. D. Hobart, M. J. Tadjer, A. D. Koehler, E. A. Imhoff, J. K. Hite, T. I. Feygelson, B. B. Pate, C. R. Eddy, and F. J. Kub, "Nanocrystalline Diamond Integration with III-Nitride HEMTs," *ECS J. Solid State Sci. Technol.*, vol. 6, no. 2, pp. Q3036–Q3039, 2017.
[77] A. Masood, M. Aslam, M. A. Tamor, and T. J. Potter, "Techniques for Patterning of CVD Diamond Films on Non-Diamond Substrates," *J. Electrochem. Soc.*, vol. 138, no. 11, pp. L67--L68, 1991.
[78] M. J. Tadjer, T. J. Anderson, K. D. Hobart, T. I. Feygelson, J. D. Caldwell, C. R. Eddy, F. J. Kub, J. E. Butler, B. Pate, and J. Melngailis, "Reduced self-heating in AlGaN/GaN HEMTs using nanocrystalline diamond heat-spreading films," *IEEE Electron Device Lett.*, vol. 33, no. 1, pp. 23–25, 2012.
[79] T. J. Anderson, K. D. Hobart, M. J. Tadjer, A. D. Koehler, T. I. Feygelson, J. K. Hite, B. B. Pate, F. J. Kub, and C. R. Eddy, "Nanocrystalline diamond for near junction heat spreading in GaN power HEMTs," *Tech. Dig. - IEEE Compd. Semicond. Integr. Circuit Symp. CSIC*, pp. 8–11, 2013.
[80] K. Hiramatsu, K. Nishiyama, A. Motogaito, H. Miyake, Y. Iyechika, and T. Maeda, "Recent Progress in Selective Area Growth and Epitaxial Lateral Overgrowth of III-Nitrides: Effects of Reactor Pressure in MOVPE Growth," *Phys. Stat. Sol.*, vol. 17672, no. 61, pp. 72–714, 1999.
[81] Y. Kato, S. Kitamura, K. Hiramatsu, and N. Sawaki, "Selective growth of wurtzite GaN and AlxGa1-xN on GaN/sapphire substrates by metalorganic vapor phase epitaxy," *J. Cryst. Growth*, vol. 144, no. 3–4, pp. 133–140, 1994.
[82] B. Beaumont, P. Vennéguès, and P. Gibart, "Epitaxial Lateral Overgrowth of GaN," *Phys. Status Solidi*, vol. 43, no. 1, pp. 1–43, 2001.
[83] D. Kapolnek, S. Keller, R. Vetury, R. D. Underwood, P. Kozodoy, S. P. Den Baars, and U. K. Mishra, "Anisotropic epitaxial lateral growth in GaN selective area epitaxy," *Appl. Phys. Lett.*, vol. 71, no. 9, pp. 1204–1206, 1997.

[84] E. D. Le Boulbar, J. Priesol, M. Nouf-Allehiani, G. Naresh-Kumar, S. Fox, C. Trager-Cowan, A. Šatka, D. W. E. Allsopp, and P. A. Shields, "Design and fabrication of enhanced lateral growth for dislocation reduction in GaN using nanodashes," *J. Cryst. Growth*, vol. 466, pp. 30–38, 2017.
[85] Y.-A. Chen, C.-H. Kuo, L.-C. Chang, and J.-P. Wu, "Void shapes controlled by using interruption-free epitaxial lateral overgrowth of GaN films on patterned SiO2 AlN/sapphire template," *Int. J. Photoenergy*, vol. 2014, 2014.
[86] T. Jiang, S. Xu, J. Zhang, Y. Xie, and Y. Hao, "Spatially resolved and orientation dependent Raman mapping of epitaxial lateral overgrowth nonpolar a-plane GaN on r-plane sapphire," *Sci. Rep.*, vol. 6, 2016.
[87] T. Jiang, S. Xu, J. Zhang, P. Li, J. Huang, Z. Ren, M. Fu, J. Zhu, H. Shan, Y. Zhao, and others, "Spatial distribution of crystalline quality in N-type GaN grown on patterned sapphire substrate," *Opt. Mater. Express*, vol. 6, no. 6, pp. 1817–1826, 2016.
[88] M. Tapajna, S. W. Kaun, M. H. Wong, F. Gao, T. Palacios, U. K. Mishra, J. S. Speck, and M. Kuball, "Influence of threading dislocation density on early degradation in AlGaN/GaN high electron mobility transistors," *Appl. Phys. Lett.*, vol. 99, no. 22, pp. 1–4, 2011.
[89] A. C. Jones and M. L. Hitchman, *Chemical vapour deposition: precursors, processes and applications*. Royal Society of Chemistry, 2009.
[90] S. Matsumoto, Y. Sato, M. Kamo, and N. Setaka, "Vapor deposition of diamond particles from methane," *Jpn. J. Appl. Phys.*, vol. 21, no. 4A, p. L183, 1982.
[91] S. Matsumoto, Y. Sato, M. Tsutsumi, and N. Setaka, "Growth of diamond particles from methane-hydrogen gas," *J. Mater. Sci.*, vol. 17, no. 11, pp. 3106–3112, 1982.
[92] M. N. R. Ashfold, P. W. May, C. A. Rego, and N. M. Everitt, "Thin film diamond by chemical vapour deposition methods," *Chem. Soc. Rev.*, vol. 23, no. 1, pp. 21–30, 1994.
[93] R. H. Wentorf, "Diamond growth rates," *J. Phys. Chem.*, vol. 75, no. 12, pp. 1833–1837, 1971.
[94] J. W. Anderson, "Metalorganic Chemical Vapor Deposition and Investigation of AlGaInN Microstructure," Texas State University, 2014.
[95] G. W. G. van Dreumel, "GaN on Diamond : A Hot Combination ?," Radboud University Nijmegen, 2011.
[96] E. L. Piner, M. K. Behbehani, N. A. El-Masry, F. G. McIntosh, J. C. Roberts, K. S. Boutros, and S. M. Bedair, "Effect of hydrogen on the indium incorporation in InGaN epitaxial films," *Appl. Phys. Lett.*, vol. 70, no. 4, pp. 461–463, 1997.
[97] D. D. Koleske, A. E. Wickenden, R. L. Henry, W. J. DeSisto, and R. J. Gorman, "Growth model for GaN with comparison to structural, optical, and electrical properties," *J. Appl. Phys.*, vol. 84, no. 4, pp. 1998–2010, 1998.
[98] R. J. Shul and S. J. Pearton, *Handbook of advanced plasma processing techniques*. Springer Science & Business Media, 2011.
[99] J. Goldstein, D. E. Newbury, P. Echlin, D. C. Joy, A. D. Romig Jr, C. E. Lyman, C. Fiori, and E. Lifshin, *Scanning electron microscopy and X-ray microanalysis: a text for biologists, materials scientists, and geologists*. Springer Science & Business Media, 2012.

[100] R. F. Egerton, P. Li, and M. Malac, "Radiation damage in the TEM and SEM," *Micron*, vol. 35, no. 6, pp. 399–409, 2004.
[101] P. J. D. Whiteside, J. A. Chininis, and H. K. Hunt, "Techniques and Challenges for Characterizing Metal Thin Films with Applications in Photonics," *Coatings*, vol. 6, no. 3, p. 35, 2016.
[102] Y. Leng, *Materials characterization: introduction to microscopic and spectroscopic methods*. John Wiley & Sons, 2009.
[103] B. D. Cullity, "Elements of X-ray Diffraction," 2001.
[104] C. Kittel, P. McEuen, and P. McEuen, *Introduction to solid state physics*, vol. 8. Wiley New York, 1996.
[105] S. Morita, F. J. Giessibl, E. Meyer, and R. Wiesendanger, *Noncontact atomic force microscopy*, vol. 3. Springer, 2015.
[106] G. Binnig, C. F. Quate, and C. Gerber, "Atomic force microscope," *Phys. Rev. Lett.*, vol. 56, no. 9, p. 930, 1986.
[107] R. Waser, *Nanoelectronics and information technology*. John Wiley & Sons, 2012.
[108] K. J. Stout and L. Blunt, *Three dimensional surface topography*. Elsevier, 2000.
[109] J. R. Dennison, M. Holtz, and G. Swain, "Raman Spectroscopy of Carbon Materials," *Spectroscopy*, vol. 11, no. 8, pp. 38–45, 1996.
[110] W. Hayes and R. Loudon, *Scattering of light by crystals*. Courier Corporation, 2012.
[111] S. Prawer and R. J. Nemanich, "Raman spectroscopy of diamond and doped diamond," *Philos. Trans. R. Soc. London A Math. Phys. Eng. Sci.*, vol. 362, no. 1824, pp. 2537–2565, 2004.
[112] M. Kuball, "Raman spectroscopy of GaN, AlGaN and AlN for process and growth monitoring/control," *Surf. Interface Anal.*, vol. 31, no. 10, pp. 987–999, 2001.
[113] D. S. Knight and W. B. White, "Characterization of diamond films by Raman spectroscopy," *J. Mater. Res.*, vol. 4, no. 2, pp. 385–393, 1989.
[114] M. Nazari, B. L. Hancock, J. Anderson, A. Savage, E. L. Piner, M. Holtz, S. Graham, F. Faili, S. Oh, D. Francis, D. Twitchen, and others, "Near-Ultraviolet micro-Raman study of diamond grown on GaN," *Appl. Phys. Lett*, vol. 31901, no. 3, p. 31901, 2016.
[115] a. Ferrari and J. Robertson, "Interpretation of Raman spectra of disordered and amorphous carbon," *Phys. Rev. B*, vol. 61, no. 20, pp. 14095–14107, 2000.
[116] B. L. Hancock, "Characterization of Devices and Materials for Gallium Nitride and Diamond Thermal Management Applications," Texas State University, 2016.
[117] C.-I. Chang, *Hyperspectral imaging: techniques for spectral detection and classification*, vol. 1. Springer Science & Business Media, 2003.
[118] K. A. Christensen and M. D. Morris, "Hyperspectral Raman microscopic imaging using Powell lens line illumination," *Appl. Spectrosc.*, vol. 52, no. 9, pp. 1145–1147, 1998.
[119] B. L. Hancock, M. Nazari, J. Anderson, E. Piner, F. Faili, S. Oh, D. Twitchen, S. Graham, and M. Holtz, "Ultraviolet micro-Raman spectroscopy stress mapping of a 75-mm GaN-on-diamond wafer," *Appl. Phys. Lett.*, vol. 108, no. 21, 2016.

[120] B. Squires, B. L. Hancock, M. Nazari, J. Anderson, K. D. Hobart, T. I. Feygelson, M. J. Tadjer, B. B. Pate, T. J. Anderson, E. L. Piner, and M. W. Holtz, "Hexagonal boron nitride particles for determining the thermal conductivity of diamond films based on near-ultraviolet micro-Raman mapping," *J. Phys. D. Appl. Phys.*, vol. 50, no. 24, p. 24LT01, 2017.
[121] a. Ferrari and J. Robertson, "Resonant Raman spectroscopy of disordered, amorphous, and diamondlike carbon," *Phys. Rev. B*, vol. 64, no. 7, p. 440, 2001.
[122] V. Jirásek, T. Ižák, M. Varga, O. Babchenko, and A. Kromka, "Investigation of residual stress in structured diamond films grown on silicon," *Thin Solid Films*, vol. 589, pp. 857–863, 2015.
[123] Y. Okada and Y. Tokumaru, "Precise determination of lattice parameter and thermal expansion coefficient of silicon between 300 and 1500 K," *J. Appl. Phys.*, vol. 56, no. 2, pp. 314–320, 1984.
[124] G. A. Slack and S. F. Bartram, "Thermal expansion of some diamondlike crystals," *J. Appl. Phys.*, vol. 46, no. 1, pp. 89–98, 1975.
[125] S. B. Qadri, C. Kim, E. F. Skelton, T. Hahn, and J. E. Butler, "Thermal expansion of chemical vapor deposition grown diamond films," *Thin Solid Films*, vol. 236, no. 1–2, pp. 103–105, 1993.
[126] P. Hess, "The mechanical properties of various chemical vapor deposition diamond structures compared to the ideal single crystal," *J. Appl. Phys.*, vol. 111, no. 5, p. 3, 2012.
[127] M. A. Hopcroft, W. D. Nix, and T. W. Kenny, "What is the Young's Modulus of Silicon?," *J. microelectromechanical Syst.*, vol. 19, no. 2, pp. 229–238, 2010.
[128] R. Hull, *Properties of crystalline silicon*, no. 20. IET, 1999.
[129] O. Auciello and A. V. Sumant, "Status review of the science and technology of ultrananocrystalline diamond (UNCD^{TM}) films and application to multifunctional devices," *Diam. Relat. Mater.*, vol. 19, no. 7–9, pp. 699–718, 2010.
[130] N. Heidrich, D. Iankov, J. Hees, W. Pletschen, R. E. Sah, L. Kirste, V. Zuerbig, C. Nebel, O. Ambacher, and V. Lebedev, "Enhanced mechanical performance of AlN/nanodiamond micro-resonators," *J. Micromechanics Microengineering*, vol. 23, no. 12, p. 125017, 2013.
[131] C. J. Tang, S. M. S. Pereira, A. J. S. Fernandes, A. J. Neves, J. Grácio, I. K. Bdikin, M. R. Soares, L. S. Fu, L. P. Gu, A. L. Kholkin, and M. C. Carmo, "Synthesis and structural characterization of highly 〈1 0 0〉-oriented {1 0 0}-faceted nanocrystalline diamond films by microwave plasma chemical vapor deposition," *J. Cryst. Growth*, vol. 311, no. 8, pp. 2258–2264, 2009.
[132] J. E. Butler, Y. A. Mankelevich, A. Cheesman, J. Ma, and M. N. R. Ashfold, "Understanding the chemical vapor deposition of diamond: recent progress," *J. Phys. Condens. Matter*, vol. 21, no. 36, p. 364201, 2009.
[133] J. J. Alcantar-Pena, J. Montes, M. J. Arellano-Jimenez, J. E. O. Aguilar, D. Berman-Mendoza, R. Garc??a, M. J. Yacaman, and O. Auciello, "Low temperature hot filament chemical vapor deposition of Ultrananocrystalline Diamond films with tunable sheet resistance for electronic power devices," *Diam. Relat. Mater.*, vol. 69, pp. 207–213, 2016.

[134] J. Anaya, T. Bai, Y. Wang, C. Li, M. Goorsky, T. L. Bougher, L. Yates, Z. Cheng, S. Graham, K. D. Hobart, T. I. Feygelson, M. J. Tadjer, T. J. Anderson, B. B. Pate, and M. Kuball, "Simultaneous determination of the lattice thermal conductivity and grain/grain thermal resistance in polycrystalline diamond," *Acta Mater.*, vol. 139, pp. 215–225, 2017.
[135] T. Liu, D. Raabe, and W.-M. Mao, "A review of crystallographic textures in chemical vapor-deposited diamond films," *Front. Mater. Sci. China*, vol. 4, no. 1, pp. 1–16, 2010.
[136] F. J. Himpsel, J. A. Knapp, J. A. VanVechten, and D. E. Eastman, "Quantum photoyield of diamond (111)—A stable negative-affinity emitter," *Phys. Rev. B*, vol. 20, no. 2, p. 624, 1979.
[137] A. K. McCurdy, H. J. Maris, and C. Elbaum, "Anisotropic heat conduction in cubic crystals in the boundary scattering regime," *Phys. Rev. B*, vol. 2, no. 10, p. 4077, 1970.
[138] A. K. McCurdy, "Phonon conduction in elastically anisotropic cubic crystals," *Phys. Rev. B*, vol. 26, no. 12, p. 6971, 1982.
[139] Q. Su, Y. Xia, L. Wang, J. Liu, and W. Shi, "Influence of texture on optical and electrical properties of diamond films," *Vacuum*, vol. 81, no. 5, pp. 644–648, 2007.
[140] H.-J. Bunge, *Texture analysis in materials science: mathematical methods*. Elsevier, 2013.
[141] M. Ali and M. Ürgen, "Surface morphology, growth rate and quality of diamond films synthesized in hot filament CVD system under various methane concentrations," *Appl. Surf. Sci.*, vol. 257, no. 20, pp. 8420–8426, 2011.
[142] P. Mehta, R. E. Clausing, L. Heatherly, C. S. Feigerle, P. M. Menon, R. E. Clausing, L. Heatherly, and C. S. Feigerle, "The morphology of diamond grown by hot filament chemical vapor deposition," *Diam. Relat. Mater.*, vol. 7, no. 8, pp. 1201–1206, 1998.
[143] M. A. Taher, W. F. Schmidt, H. A. Naseem, W. D. Brown, A. P. Malshe, and S. Nasrazadani, "Effect of methane concentration on physical properties of diamond-coated cemented carbide tool inserts obtained by hot-filament chemical vapour deposition," *J. Mater. Sci.*, vol. 33, no. 1, pp. 173–182, 1998.
[144] S. Yang, Z. He, Q. Li, D. Zhu, and J. Gong, "Diamond films with preferred <110> texture by hot filament CVD at low pressure," *Diam. Relat. Mater.*, vol. 17, no. 12, pp. 2075–2079, 2008.
[145] P. K. Bachmann, H.-J. Hagemann, H. Lade, D. Leers, F. Picht, D. U. Wiechert, and H. Wilson, "Diamond chemical vapor deposition: gas compositions and film properties," *MRS Online Proc. Libr. Arch.*, vol. 339, 1994.
[146] C. J. Tang, A. J. S. Fernandes, X. F. Jiang, J. L. Pinto, and H. Ye, "Effect of methane concentration in hydrogen plasma on hydrogen impurity incorporation in thick large-grained polycrystalline diamond films," *J. Cryst. Growth*, vol. 426, pp. 221–227, 2015.

[147] P. W. May, “Diamond thin films: a 21st-century material,” *Philos. Trans. R. Soc. London A Math. Phys. Eng. Sci.*, vol. 358, no. 1766, pp. 473–495, 2000.
[148] K. Nagao and E. Kagami, “X-ray thin film measurement techniques: VII. Pole figure measurement,” *Rigaku J.*, vol. 27, no. 2, pp. 6–14, 2011.
[149] S. C. Ramos, A. F. Azevedo, M. R. Baldan, and N. G. Ferreira, “Effect of methane addition on ultrananocrystalline diamond formation: Morphology changes and induced stress,” *J. Vac. Sci. & Technol. A-vacuum Surfaces Film.*, vol. 28, no. 1, pp. 27–32, 2010.
[150] P. W. May, “Diamond thin films: a 21st-century material,” *Philos. Trans. R. Soc. London A Math. Phys. Eng. Sci.*, vol. 358, no. 1766, pp. 473–495, 2000.
[151] A. C. Ferrari and J. Robertson, “Interpretation of Raman spectra of disordered and amorphous carbon,” *Phys. Rev. B*, vol. 61, no. 20, p. 14095, 2000.
[152] T. Guillemet, Z. Q. Xie, Y. S. Zhou, J. B. Park, A. Veillere, W. Xiong, J. M. Heintz, J. F. Silvain, N. Chandra, and Y. F. Lu, “Stress and phase purity analyses of diamond films deposited through laser-assisted combustion synthesis,” *ACS Appl. Mater. Interfaces*, vol. 3, no. 10, pp. 4120–4125, 2011.
[153] J. Michler, M. Mermoux, Y. Von Kaenel, A. Haouni, G. Lucazeau, and E. Blank, “Residual stress in diamond ® lms : origins and modelling,” vol. 357, pp. 189–201, 1999.
[154] F. Silva, F. Bénédic, P. Bruno, and A. Gicquel, “Formation of 〈110〉 texture during nanocrystalline diamond growth: An X-ray diffraction study,” *Diam. Relat. Mater.*, vol. 14, no. 3–7, pp. 398–403, 2005.
[155] T. Liu and D. Raabe, “Growth rate and EBSD texture analysis of nitrogen doped diamond films,” *arXiv Prepr. arXiv0812.4025*, pp. 1–11, 2008.
[156] K. Helming, S. Geier, M. Schreck, R. Hessmer, B. Stritzker, and B. Rauschenbach, “Texture Analysis of Chemical-Vapor-Deposited Diamond Films on Silicon By the Component Method,” *J. Appl. Phys.*, vol. 77, no. 9, pp. 4765–4770, 1995.
[157] C. Wild, P. Koidl, and W. Müller-Sebert, “Chemical vapour deposition and characterization of smooth {100}-faceted diamond films,” *Diam. Relat. …*, vol. 2, pp. 158–168, 1993.
[158] C. J. Chu, M. P. d’Evelyn, R. H. Hauge, and J. L. Margrave, “Mechanism of diamond growth by chemical vapor deposition on diamond (100),(111), and (110) surfaces: Carbon-13 studies,” *J. Appl. Phys.*, vol. 70, no. 3, pp. 1695–1705, 1991.
[159] J. E. Butler and R. L. Woodin, “Thin film diamond growth mechanisms,” *Phil. Trans. R. Soc. Lond. A*, vol. 342, no. 1664, pp. 209–224, 1993.
[160] D. Huang and M. Frenklach, “Energetics of surface reactions on (100) diamond plane,” *J. Phys. Chem.*, vol. 96, no. 4, pp. 1868–1875, 1992.
[161] B. J. Garrison, E. J. Dawnkaski, D. Srivastava, and D. W. Brenner, “Molecular Dynamics Simulations of Dimer Opening on a Diamond ${$001$}$(2x1) Surface,” *Science (80-.).*, vol. 255, no. 5046, pp. 835–838, 1992.
[162] S. J. Harris, “Mechanism for diamond growth from methyl radicals,” *Appl. Phys. Lett.*, vol. 56, no. 23, pp. 2298–2300, 1990.
[163] K. Larsson, S. Lunell, and J.-O. Carlsson, “Adsorption of hydrocarbons on a diamond (111) surface: An ab initio quantum-mechanical study,” *Phys. Rev. B*, vol. 48, no. 4, p. 2666, 1993.

[164] T. Liu, D. Raabe, and G. Eggeler, “High Resolution Investigation of Texture Formation Process in Diamond Films and the Related Macro-Stresses,” Ruhr-University Bochum Bochum [Germany], 2009.
[165] D. Kweon, J. Lee, and D. Kim, “The growth kinetics of diamond films deposited by hot-filament chemical vapor deposition,” *J. Appl. Phys.*, vol. 69, no. 12, pp. 8329–8335, 1991.
[166] J. Singh, “Nucleation and growth mechanism of diamond during hot-filament chemical vapour deposition,” *J. Mater. Sci.*, vol. 29, no. 10, pp. 2761–2766, 1994.
[167] R. B. Simon, J. Anaya, F. Faili, R. Balmer, G. T. Williams, D. J. Twitchen, and D. M. Kuball, “Effect of grain size of polycrystalline diamond on its heat spreading properties,” *Appl. Phys. Express*, vol. 9, no. 6, pp. 18–22, 2016.
[168] A. der Drift and L. I. B. Rary, “Evolutionary selection, a principle governing growth orientation in vapour-deposited layers,” *Philips Res. Rep*, vol. 22, no. 3, pp. 267–288, 1967.
[169] I. D. Jeon, C. J. Park, D. Y. Kim, and N. M. Hwang, “Effect of methane concentration on size of charged clusters in the hot filament diamond CVD process,” *J. Cryst. Growth*, vol. 223, no. 1–2, pp. 6–14, 2001.
[170] C. J. Chu, R. H. Hauge, J. L. Margrave, M. P. D’evelyn, G. N--j-, C. J. Chu, R. H. Hauge, J. L. Margrave, and M. P. D’evelyn, “Growth kinetics of (100),(110), and (111) homoepitaxial diamond films,” *Appl. Phys. Lett.*, vol. 61, no. 12, pp. 1393–1395, 1992.
[171] H.-X. Zhu, W.-M. Mao, H.-P. Feng, F.-X. LU, V. II, and R. VG, “Influence of methane concentration on crystal growing process in CVD free standing diamond films,” *J. Inorg. Mater.*, vol. 22, no. 3, pp. 570–576, 2007.
[172] M. Kuc and R. P. Wasiak Michałand Sarzała, “Impact of Heat Spreaders on Thermal Performance of III-N-Based Laser Diode,” *IEEE Trans. Components, Packag. Manuf. Technol.*, vol. 5, no. 4, pp. 474–482, 2015.
[173] Y. Han, B. L. Lau, G. Tang, and X. Zhang, “Thermal management of hotspots using diamond heat spreader on Si microcooler for GaN devices,” *IEEE Trans. Components, Packag. Manuf. Technol.*, vol. 5, no. 12, pp. 1740–1746, 2015.
[174] Q. Wu, Y. Xu, J. Zhou, Y. Kong, T. Chen, Y. Wang, F. Lin, Y. Fu, Y. Jia, X. Zhao, and others, “Performance Comparison of GaN HEMTs on Diamond and SiC Substrates Based on Surface Potential Model,” *ECS J. Solid State Sci. Technol.*, vol. 6, no. 12, pp. Q171--Q178, 2017.
[175] C. Hua, X. Yan, J. Wei, J. Guo, J. Liu, L. Chen, L. Hei, and C. Li, “Intrinsic stress evolution during different growth stages of diamond film,” *Diam. Relat. Mater.*, vol. 73, pp. 62–66, 2017.
[176] M. J. Edwards, C. R. Bowen, D. W. E. Allsopp, and A. C. E. Dent, “Modelling wafer bow in silicon--polycrystalline CVD diamond substrates for GaN-based devices,” *J. Phys. D. Appl. Phys.*, vol. 43, no. 38, p. 385502, 2010.
[177] H. Windischmann and K. J. Gray, “Stress measurement of CVD diamond films,” *Diam. Relat. Mater.*, vol. 4, pp. 837–842, 1995.
[178] I. De Wolf and I. De Wolf, “Micro-Raman spectroscopy to study local mechanical stress in silicon integrated circuits,” *Semicond. Sci. Technol.*, vol. 11, no. 2, p. 139, 1996.

[179] M. Holtz, J. C. Carty, and W. M. Duncan, “Ultraviolet Raman stress mapping in silicon,” *Appl. Phys. Lett.*, vol. 74, no. 14, p. 2008, 1999.
[180] S. M. Hu, “Film-edge-induced stress in substrates,” *J. Appl. Phys.*, vol. 50, no. 7, pp. 4661–4666, 1979.
[181] D. E. Aspnes and A. A. Studna, “Dielectric functions and optical parameters of si, ge, gap, gaas, gasb, inp, inas, and insb from 1.5 to 6.0 ev,” *Phys. Rev. B*, vol. 27, no. 2, p. 985, 1983.
[182] E. Anastassakis, A. Pinczuk, E. Burstein, F. H. Pollak, and M. Cardona, “Effect of static uniaxial stress on the Raman spectrum of silicon,” *Solid State Commun.*, vol. 8, no. 2, pp. 133–138, 1970.
[183] I. De Wolf, H. E. Maes, and S. K. Jones, “Stress measurements in silicon devices through Raman spectroscopy: bridging the gap between theory and experiment,” *J. Appl. Phys.*, vol. 79, no. 9, pp. 7148–7156, 1996.
[184] J. Pomeroy, M. Bernardoni, A. Sarua, A. Manoi, D. C. Dumka, D. M. Fanning, and M. Kuball, “Achieving the best thermal performance for GaN-on-diamond,” *Tech. Dig. - IEEE Compd. Semicond. Integr. Circuit Symp. CSIC*, pp. 1–4, 2013.
[185] Y. Zhou, R. Ramaneti, J. Anaya, S. Korneychuk, J. Derluyn, H. Sun, J. Pomeroy, J. Verbeeck, K. Haenen, and M. Kuball, “Thermal characterization of polycrystalline diamond thin film heat spreaders grown on GaN HEMTs,” *Appl. Phys. Lett.*, vol. 111, no. 4, 2017.
[186] R. Chu, C. S. Suh, M. H. Wong, N. Fichtenbaum, D. Brown, L. McCarthy, S. Keller, F. Wu, J. S. Speck, and U. K. Mishra, “Impact of CF4 Plasma Treatment on GaN,” *IEEE Electron Device Lett.*, vol. 28, no. 9, pp. 781–783, 2007.
[187] S. K. Jana, P. Mukhopadhyay, S. Ghosh, S. Kabi, A. Bag, R. Kumar, and D. Biswas, “High-resolution X-ray diffraction analysis of AlxGa1- xN/InxGa1- xN/GaN on sapphire multilayer structures: Theoretical, simulations, and experimental observations,” *J. Appl. Phys.*, vol. 115, no. 17, p. 174507, 2014.
[188] H. Harima, “Properties of GaN and related compounds studied by means of Raman scattering,” *J. Phys. Condens. Matter*, vol. 14, no. 38, p. R967, 2002.
[189] M. Marinelli, E. Milani, M. Montuori, A. Paoletti, P. Paroli, and J. Thomas, “Effect of gas composition on texture of diamond films,” *Appl. Phys. Lett.*, vol. 65, no. 22, pp. 2839–2841, 1994.
[190] O. Ambacher, J. Smart, J. R. Shealy, N. G. Weimann, K. Chu, M. Murphy, W. J. Schaff, L. F. Eastman, R. Dimitrov, L. Wittmer, M. Stutzmann, W. Rieger, and J. Hilsenbeck, “Two-dimensional electron gases induced by spontaneous and piezoelectric polarization charges in N- and Ga-face AlGaN/GaN heterostructures,” *J. Appl. Phys.*, vol. 85, no. 6, pp. 3222–3233, 1999.
[191] M. Alomari, M. Dipalo, S. Rossi, M. A. Diforte-Poisson, S. Delage, J. F. Carlin, N. Grandjean, C. Gaquiere, L. Toth, B. Pecz, and E. Kohn, “Diamond overgrown InAlN/GaN HEMT,” *Diam. Relat. Mater.*, vol. 20, no. 4, pp. 604–608, 2011.
[192] M. Dipalo, Z. Gao, J. Scharpf, C. Pietzka, M. Alomari, F. Medjdoub, J. F. Carlin, N. Grandjean, S. Delage, and E. Kohn, “Combining diamond electrodes with GaN heterostructures for harsh environment ISFETs,” *Diam. Relat. Mater.*, vol. 18, no. 5–8, pp. 884–889, 2009.

[193] A. Koukitu, M. Mayumi, and Y. Kumagai, “Surface polarity dependence of decomposition and growth of GaN studied using in situ gravimetric monitoring,” *J. Cryst. Growth*, vol. 246, no. 3–4, pp. 230–236, 2002.
[194] M. A. Mastro, O. M. Kryliouk, T. J. Anderson, A. Davydov, and A. Shapiro, “Influence of polarity on GaN thermal stability,” *J. Cryst. Growth*, vol. 274, no. 1–2, pp. 38–46, 2005.
[195] J. G. Speight and others, *Lange’s handbook of chemistry*, vol. 1. McGraw-Hill New York, 2005.
[196] A. Reznik, G. Zhang, and P. R. Chitrapu, “III-V NITRIDE SEMICONDUCTOR LAYER-BONDED SUBSTRATE AND SEMICONDUCTOR DEVICE,” 2008.
[197] F. Ejeckam et. al., “GALLIUM-NITRIDE-ON-DIAMOND WAFERS AND DEVICES, AND METHODS OF MANUFACTURE,” 8,759,134, 2014.
[198] Z. Yu, “EPITAXIAL LATERAL OVERGROWTH OF GaN ON SiC AND SAPPHIRE SUBSTRATES ZHONGHAI YU*. MAL JOHNSON’, JD BROWN*. NA EL-MASRY**, JF MUTH‘, JW COOK. JR.*, JF SCHETZINA’, KW HABERERN*’. HS KONG*". AND JA EDMOND,” in *GaN and related alloys: symposium held November 29-December 4, 1998, Boston, Massachusetts, USA*, 1999, vol. 537, p. 3.
[199] D. Kapolnek, R. D. Underwood, B. P. Keller, S. Keller, S. P. Denbaars, and U. K. Mishra, “Selective area epitaxy of GaN for electron field emission devices,” *J. Cryst. Growth*, vol. 170, no. 1–4, pp. 340–343, 1997.
[200] P. Gibart, “Metal organic vapour phase epitaxy of GaN and lateral overgrowth,” *Reports Prog. Phys.*, vol. 67, no. 5, pp. 667–715, 2004.
[201] O.-H. Nam, T. S. Zheleva, M. D. Bremser, and R. F. Davis, “Lateral epitaxial overgrowth of GaN films on SiO2 areas via metalorganic vapor phase epitaxy,” *J. Electron. Mater.*, vol. 27, no. 4, pp. 233–237, 1998.
[202] T. S. Zheleva, O. Nam, M. D. Bremser, and R. F. Davis, “Dislocation density reduction via lateral epitaxy in selectively grown GaN structures Dislocation density reduction via lateral epitaxy in selectively grown GaN structures,” *J. Cryst. Growth*, vol. 22, pp. 706–718, 2001.
[203] H. J. Lee, S. Y. Bae, K. Lekhal, A. Tamura, T. Suzuki, M. Kushimoto, Y. Honda, and H. Amano, “Orientation-controlled epitaxial lateral overgrowth of semipolar GaN on Si(001) with a directionally sputtered AlN buffer layer,” *J. Cryst. Growth*, vol. 468, no. December 2016, pp. 547–551, 2017.
[204] C. He, W. Zhao, K. Zhang, L. He, H. Wu, N. Liu, S. Zhang, X. Liu, and Z. Chen, “High-Quality GaN Epilayers Achieved by Facet-Controlled Epitaxial Lateral Overgrowth on Sputtered AlN/PSS Templates,” *ACS Appl. Mater. Interfaces*, vol. 9, no. 49, pp. 43386–43392, 2017.
[205] T. Zhu, C. F. Johnston, M. J. Kappers, and R. A. Oliver, “Microstructural, optical, and electrical characterization of semipolar ($11\bar{2}2$) gallium nitride grown by epitaxial lateral overgrowth,” *J. Appl. Phys.*, vol. 108, no. 8, p. 83521, 2010.
[206] K. Hiramatsu, K. Nishiyama, M. Onishi, H. Mizutani, M. Narukawa, A. Motogaito, H. Miyake, Y. Iyechika, and T. Maeda, “Fabrication and characterization of low defect density GaN using facet-controlled epitaxial lateral overgrowth (FACELO),” *J. Cryst. Growth*, vol. 221, no. 1–4, pp. 316–326, 2000.

[207] B. L. Hancock, M. Nazari, J. Anderson, E. Piner, F. Faili, S. Oh, D. Francis, D. Twitchen, S. Graham, and M. W. Holtz, "Ultraviolet and visible micro-Raman and micro-photoluminescence spectroscopy investigations of stress on a 75-mm GaN-on-diamond wafer," *Phys. Status Solidi Curr. Top. Solid State Phys.*, vol. 14, no. 8, 2017.
[208] B. D. Culity and S. R. Stock, "Elements of X-ray Diffraction," *2nd, Addit. MA, London*, 1978.
[209] R. W. Bormett, S. A. Asher, R. E. Witowski, W. D. Partlow, R. Lizewski, and F. Pettit, "Ultraviolet Raman spectroscopy characterizes chemical vapor deposition diamond film growth and oxidation," *J. Appl. Phys.*, vol. 77, no. 11, pp. 5916–5923, 1995.
[210] I. Ahmad, M. Holtz, N. N. Faleev, and H. Temkin, "Dependence of the stress--temperature coefficient on dislocation density in epitaxial GaN grown on $α$-Al 2 O 3 and 6H--SiC substrates," *J. Appl. Phys.*, vol. 95, no. 4, pp. 1692–1697, 2004.